Transition metal doped phosphors for LEDs

A study of temperature dependent luminescence of manganese and chromium

Overgangsmetaalgedoteerde fosforen voor LEDs

Een studie naar temperatuurafhankelijke luminescentie van mangaan en chroom

Proefschrift

Ter verkrijging van de graad van doctor aan de Universiteit Utrecht op gezag van Prof. Dr. H.R.B.M. Kummeling, ingevolge het besluit van het college voor promoties in het openbaar te verdedigen

op maandag 9 oktober 2023
des middags te 12:15 uur

door

Arnoldus Jacobus van Bunningen

Geboren op 21 december 1992 te Maastricht

Promotor

Prof. Dr. Andries Meijerink

Co-promotor

Dr. Atul D. Sontakke

Het onderzoek beschreven in dit proefschrift werd gefinancierd door NICHIA corporation (日亜化学工業株式会社) te Japan.

Contents

Chapter 1.	Introduction	5
Chapter 2.	Theory	17
Chapter 3.	Thermal luminescence quenching in Mn^{2+}phosphors	37
Chapter 4.	NIR emission in highly concentrated $MgAl_2O_4:Mn^{2+}$	79
Chapter 5.	New Hexagonal KRSF	99
Chapter 6.	Temperature quenching of Cr^{3+} in solid solutions	125
Chapter 7.	Conclusion and Outlook	153
Chapter 8.	Nederlandse Samenvatting	163
Chapter 9.	Appendices	175

Acknowledgements
List of publications
List of presentations
Over de auteur

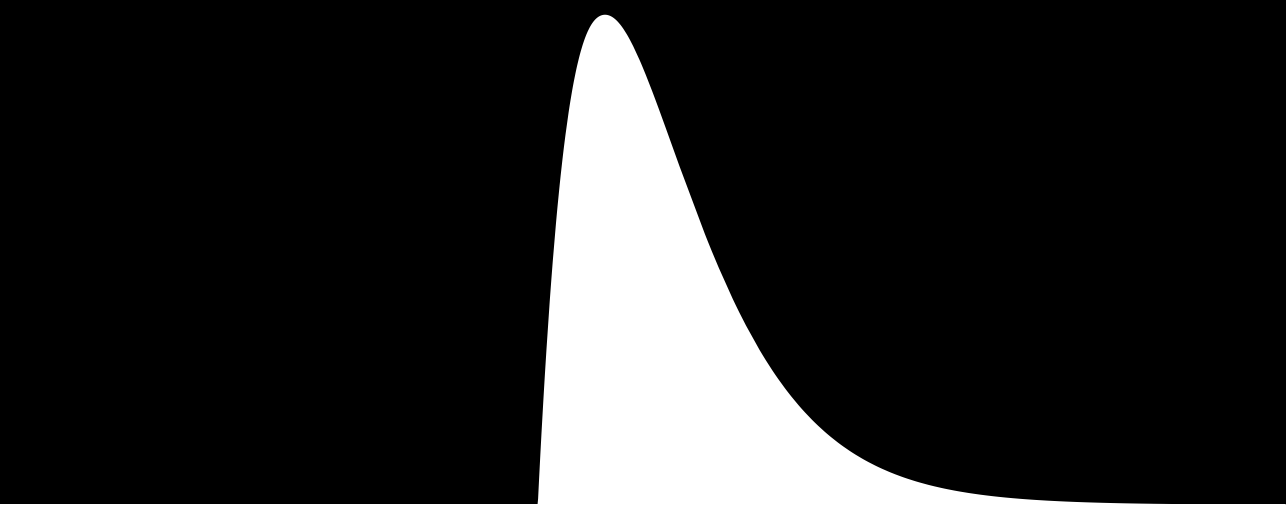

Chapter 1

Introduction

“Κακής απ' αρχής γίγνεται
τέλος κακόν”

*“A bad beginning makes a
bad ending.”*

Euripides

One of the pressing issues at the forefront today's society is the global climate crisis. Improving the energy efficiency of devices is vital in the battle against it. An excellent example of technology advancing energy efficiency is the use of LEDs for lamps and displays. It is projected that by 2030, LEDs will dominate the entire lighting market, resulting in a decrease in global electricity consumption. In the United States of america, for instance, lighting application's share of total energy consumption is projected to drop from 15% in 2014 to 6.4% by 2030.[1] This shift is due to the low energy efficiency of traditional lighting sources, such as incandescent and fluorescent lamps. In addition, they are bulky and have limited lifespans. In comparison, LEDs consume 2-3 times less energy than fluorescent tubes, are over 10 times more efficient than incandescent lighting and have a lifespan of over 40,000 hours, whereas fluorescent tubes and incandescent lights have spans of 10,000 and 1,000 hours, respectively. Still, while LEDs have made significant progress in improving efficiency, lifespan, and color quality, there is room for further advancements. Understanding the science and technology behind LED-based lighting is vital if we want to achieve further improvements.

A LED, or light emitting diode, is created by combining two semiconductor materials: one **p**-doped and the other **n**-doped. The 'p' and 'n' designations indicate that one type of semiconductor has positive charge carriers while the other has negative ones. The p-doped semiconductor has holes in the valence band, while the n-doped semiconductor has electrons in the conduction band. When these two materials are brought together, the electrons and holes can recombine, often in an undoped intermediate layer between the p- and n-doped semiconductors. When a voltage is applied, a continuous supply of electrons via the n-doped side and holes via the p-doped side results in recombination in the interface layer where the recombination energy is released by emitting photons. The photon energy (and thus the color of light) emitted depends on the size of the band gap of the material, and thus the color can be controlled by altering the bandgap of a material.[2]

Nick Holonyak, Jr. created the first commercial LED from (Ga,As)P in 1962 while working at General Electric.[3] These red LEDs were mainly used for numeric displays. In 1972, M. George Craford discovered the first green LED while employed at Monsanto, which then became the first company to mass-produce LEDs. Finally, in 1991, Shuji Nakamura, working at Nichia, contributed to the discovery of the blue (In, Ga)N LED, for which Akasaki, Amano and he were awarded the Nobel Prize in Physics in 2014.[4] With the Blue LED invention, the complete visible spectrum was covered and white light could be generated by the combination of **R**ed, **G**reen, and **B**lue LEDs in one device, known as an RGB LED. These RGB LEDs can not only generate white light but any desired color by altering the intensity of the three individual LEDs.

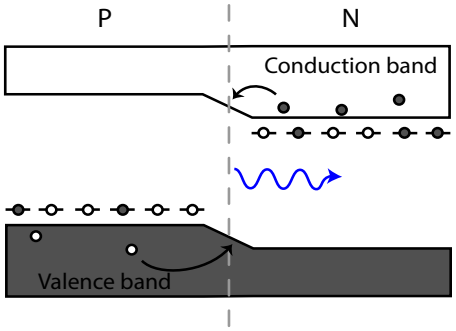

Figure 1-1. This diagram depicts a p-type and n-type semiconductor, with white dots representing electron holes and black dots representing electrons. When a sufficient voltage is applied, electrons and holes will diffuse into the depletion region, leading to recombination, resulting in photon emission.

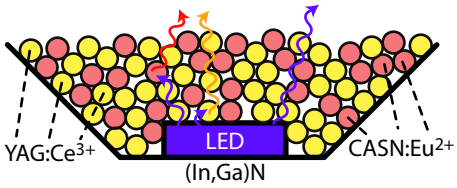

Figure 1-2. Schematic illustration of a pcLED, where the blue light is generated by a (In,Ga)N semiconductor chip. Part of the blue light is converted to yellow and red light is by the YAG:Ce^{3+} and CASN:Eu^{2+} phosphors. The resulting combined light output will have a warm white and the colour temperature can be varied from cool to warm white changing the amount and composition of the phosphor mixture .

LED manufacturers face difficulties in creating RGB LEDs for white light applications. Consistency in the light intensity ratio of the three LEDs over thousands of hours is hard to ensure, since the three different chips require varying operating voltages, in turn complicating the electronics. Additionally, the reproducibility of emission color for LEDs is challenging. Common variations of several nanometers between LEDs lead to notable differences in shades of white for the 'same' white LED, which is undesirable. Additionally, as the green LEDs have relatively poor electrical efficiency, the RGB LED concept also results in an overall lower efficiency.[5] An alternative to create white light LEDs (wLEDS) is to use phosphor-converted LEDs (pcLEDs). In a pcLED, one or multiple phosphors above the blue LED chip convert part of the blue light to green, yellow, and/or red. The combined light output of the transmitted blue LED light and the phosphor's emission is perceived as white. With only one blue LED and highly stable and reproducible emission of the phosphor, the color of the lamp will be the same for all wLEDs and will not change, even if the light output of the chip degrades over time. Due to its simplicity, the pcLED outcompetes the RGB-LED for most applications, although the RGB concept is used in variable color LED lighting such as the Philips Hue lamps.

Variation in luminescence properties of different phosphors enables flexibility in the performance of pcLEDs. The yellow $Y_3Al_5O_{12}$: Ce^{3+} (YAG) phosphor was the first successful wLED phosphor and is still widely used for pcLEDs. It has a broad emission range spanning the green to red regions of the visible spectrum. Combining YAG with blue (In,Ga)N produces a white light, however with a bluish appearance (cold white), which is often undesired for residential lighting. To create a warmer ambiance, a red component needs to be added. This is achieved by introducing $CaSiAlN_3$:Eu^{2+} (CASN) or $Sr[LiAl_3N_4]$:Eu^{2+} (SLA) phosphors, which emit red light and enable wLEDs with a warmer white color.[6,7]

CASN and SLA are two examples of phosphors with optical properties that are suitable to make warm white LED lamps. Lighting applications vary in the requirements for phosphors. The main applications are in lighting and displays. In liquid crystal displays (LCDs), wLEDs serve as backlight for blue, green and red light that is transmitted (or not) at any desired pixel in the display to generate a color image. Here, backlight wLEDs with narrow emission bands are preferred. The white light produced by the wLED backlight is filtered by red, green and blue color filters that only transmit in a window of wavelengths. A good match of the narrow band emission from the phosphors that overlaps with the transmission window results in high color quality without sacrificing light intensity. The blue emission from the LED chip is already narrow enough, but green and red phosphors used in displays often have a broad band emission extending over tens of nanometers, which is broader than desired.

For lighting applications the narrow band emission is desired to improve the efficiency as to reduce power consumption. The efficiency of lamps is often expressed in lumen/W where the lumen is a measure of the number of photons emitted corrected for the eye response curve. Many of the available red phosphors have a broad band emission, even extending into the near infrared (NIR) region of the electromagnetic spectrum. As the eye is less sensitive to wavelengths closer to the infrared, it is preferable to have a red emitter with a narrow emission centered around 610-630 nm, where eye response is still high and enhances the lumen/W efficiency. The efficiency is not the only important parameter for wLEDs. Other aspects such as color rendering and more recently, health benefits related to lighting are receiving increasing attention. The color rendering index reflects how well colors are reproduced under artificial light sources compared to the colors under natural sunlight. Human centric lighting considers the impact of lighting on well-being.

An interesting example of human centric lighting involves the effect light has on the sleep pattern. Over the past decade, pcLEDs include lamps that adjust to the circadian rhythm. Melatonin production is inhibited by a protein activated in the eye, which is sensitive to 480 nm light. By regulating melatonin production through variation of the intensity of 480 nm emission in the spectrum of wLEDs during the day, sleepiness and dozing off can be reduced and a healthy sleep pattern can be stimulated. In 2020, Nichia introduced the Vitasolis LED, which automatically adjusts its light output based on the time of day without changing the color temperature.[8]

Color rendering is generally important as it is preferred to see colors of objects as close to their natural color as possible. To determine how closely a light source represents natural sunlight, the color rendering index (CRI) provides a value that indicates how similar pigments appear under a light source compared to a blackbody light source. For example, in cloth stores it is important when matching colors to have lighting with high color rendering index. Art museums strive to display artwork as it was intended by the artist.

As different pigments absorb specific parts of the electromagnetic spectrum, conventional lighting is designed to activate our three color sensors. However, a specific pigment may absorb a portion of the sunlight but not a certain color of lamp light, resulting in the artwork appearing different under various light sources. Companies such as LumiLed, Soraa, and Nichia now produce pcLEDs with high CRI values, ensuring that the light source accurately represents natural sunlight and faithfully reproduces the artwork's colors.[9,10,11]

The flexibility offered by phosphor conversion in LED lighting continues to initiate new developments in the field of LED lighting. In addition to developments discussed above, emerging areas for LED lighting involve automotive, horticulture and sensing. In the automotive field high brightness wLEDs are important. The use of NIR applications for pcLEDs is on the rise for plant growth. The amount of NIR light can be used to control the direction of growth and impact crop yield.[12] Plants use the NIR to red ratio to assess the presence of other nearby plants, determining whether to grow upwards or focus on producing offspring. Therefore, precise control of blue, red, and infrared light is critical for indoor horticulture applications.[12,13,14]

Another emerging technology involving NIR phosphors is the use of pcLEDs for rapid and accurate sensing of the chemical compositions of food and crops. This can be used for ensuring food safety. This technique involves sending a broad band in the NIR spectrum to a product, which absorbs specific wavelengths related to vibrational overtones of organic molecules. The reflected spectrum then shows distinct absorption features that can be analyzed using advanced computer algorithms to detect compounds such as sugar, fat or ethanol. Such a technique can be used for quick and efficient quality control of products. To create a device for this application, a NIR detector and a source of NIR radiation are necessary. A broadband NIR emitting phosphor can be added to a blue or red LED chip to create a compact and efficient NIR radiation source that is vastly superior to the old alternative, incandescent lighting. As of now, OSRAM is a leading manufacturer of NIR pcLEDs.[15]

Most of the currently used LED phosphors have a lanthanide as the active luminescent ion, phosphors mentioned above include CASN:Eu^{2+}, SLA:Eu^{2+}, and YAG:Ce^{3+}. Another commonly used phosphor is β-$Si_4Al_2O_2N_6$: Eu^{2+} (β-SiAlON), which emits green light. A commercially relevant LED phosphor not based on lanthanides is K_2SiF_6:Mn^{4+}, which produces a bright red emission and is excellent for display technologies. Before LED-based lighting, phosphors contained activators from a wide variety of elements in the periodic table, with Mn^{2+} being a widely used ion for its green luminescence (e.g. in Zn_2SiO_4:Mn^{2+}), orange emission (e.g. in the famous $Ca_5(PO_4)_3F$:Sb^{3+},Mn^{2+} halophosphate) and red luminescence (e.g. in $Ca_3(PO_4)_2$:Sb^{3+},Mn^{2+}). However, modern LED-based lighting require the active ion to be excited by blue light, which is challenging for Mn^{2+} as it has only very poorly absorbing forbidden transitions in the blue part of the spectrum. To resolve this, sensitizer ions can be added to a phosphor to absorb blue light and transfer the energy to Mn^{2+}, enabling it to

emit light.[16–20]Incorporating a sensitizer into a phosphor would expand the possibilities for using Mn^{2+}-based phosphors in wLED applications.

Novel phosphors are required to enable emerging technologies and improve existing technologies. The lumen/W efficacy, CRI of lighting, energy efficiency and color gamut of displays can be improved by using narrower band red and green emitting phosphors. New broad band NIR emitting phosphors with high luminescence quenching temperature are desired for emerging applications such as sensing and lighting for horticulture. To design a new phosphor, it is important to understand the properties of the luminescent ion and how they are influenced by the host material. This thesis will focus on transition metal ions with a partly filled 3d-shell, specifically Mn^{2+} ($3d^5$) Mn^{4+} ($3d^3$) and Cr^{3+}($3d^3$). The luminescence properties of these ions are strongly affected by the host material and better insight in the relation between host lattice and optical properties is crucial to optimize performance for the various applications.

When designing a new LED phosphor, it is important to consider the temperature dependence of the luminescence. The local environment at the position of the phosphor just above the blue (In,Ga)N LED chip can reach temperatures up to 150°C during operation.[21,22] Thus, studying the changes in luminescence properties at elevated temperatures is essential. Temperature induced spectral shifts in the emission spectrum can alter the wLED's color. The emitted light intensity can decrease rapidly at elevated temperatures, known as thermal quenching, and negatively impacts the wLED's performance. Moreover, the excited state lifetime of the phosphor can vary with temperature, which is relevant for high-intensity applications where a shorter lifetime can increase the turnover rate, reducing saturation effects (sublinear increase of emission intensity with excitation power, also known as 'droop').[23,24] These temperature-dependent properties are affected by the interaction between luminescent center and local environment in the embedding host material. This thesis focuses on studying the temperature-dependent optical properties of transition metals, namely manganese and chromium, considering both the host material and the local environment. The aim is to improve our understanding of phosphor materials and improve the quality of LEDs for applications in lighting, displays and NIR sensing.

Scope of thesis

Chapter 2 of this thesis aims to provide the necessary theoretical background for readers to understand the research described in this thesis. It covers various topics related to luminescence spectroscopy with a focus on $3d^n$ transition metal ions. The chapter discusses the energy level structure for the $3d^n$ configuration and includes explanations of important concepts such as term symbols and crystal field splitting, which combine to Tanabe-Sugano

diagrams for the $3d^n$ transition metal ions. The origin of Stokes shift will be explained. Additionally, different mechanisms that can cause luminescence quenching at high temperatures will be evaluated, as well as how thermal quenching can be reduced. Energy transfer and energy migration and their role in understanding and optimizing the performance of luminescent materials will be explored. Defects play a crucial role in luminescence but are poorly understood. In relation to defects, the Kröger-Vink notation and self-diffusion of ions are discussed. The basic knowledge outlined in this introductory chapter will be essential in understanding optical properties and synthesis of phosphors featuring chapters 3 to 6.

Chapter 3 of the thesis discusses the mechanism behind thermal luminescence quenching of Mn^{2+} in phosphors. The Mn^{2+} ion can give efficient narrow band green or red emission, depending on the local coordination. Despite the long history and recent increasing popularity of Mn^{2+}-based phosphors, the luminescence quenching temperature is often neglected in research papers, despite its crucial importance in practical applications. Understanding the mechanism behind luminescence quenching is essential for designing new phosphors with higher luminescence quenching temperatures. This chapter studies twenty Mn^{2+}-based phosphors and measures their quenching temperature by analyzing both intensity and luminescence decay time as a function of temperature. Additionally, thermally stimulated luminescence (TSL) curves of different phosphors are measured following illumination at various charging temperatures. A positive correlation is found between a rise in TSL signal and the temperature where thermal quenching of the luminescence sets in. This indicates that thermally activated photo-ionization is the luminescence quenching mechanism. Support for this mechanism is obtained by comparing the bandgap of different Mn-doped host materials to the quenching temperature of Mn within these hosts, showing that a wider bandgap helps to increase the quenching temperature.

In **Chapter 4** the origin of near infrared (NIR) emission in host materials with high Mn concentrations is investigated. Recent publications reported efficient NIR emission in concentrated Mn^{2+} phosphors and attribute the NIR emission to exchange coupled Mn^{2+}-Mn^{2+} pairs at high Mn^{2+} concentrations. This chapter shows that this explanation for the NIR emission is not correct and proposes an alternative and plausible theory. Careful experiments (optical and magnetic) in the last century have shown that exchange coupling in Mn^{2+} is more than ten times weaker than what is required to explain the very large (~5000 cm^{-1}) redshift of NIR emission from Mn-pairs. An alternative explanation is energy migration over the Mn^{2+} sublattice to NIR emitting centers in highly doped systems. To test this model, $MgAl_2O_4$ was doped with

concentrations up to 50 mol% Mn and the 'normal' green and NIR emissions were measured as a function of Mn-concentration, temperature and synthesis conditions. All steady state and time resolved luminescence measurements are consistent with energy migration to a NIR emitting trap center. At cryogenic temperatures the sample with 50 mol% Mn showed an increase in 'normal' green Mn^{2+} emission and decreased NIR emission, consistent with energy migration being hampered by small energy differences between Mn^{2+} neighbours but not with the exchange-coupled pair model as the Mn-Mn pair concentration is not temperature dependent. Additionally, attempts were made to identify the origin of the NIR emission by synthesizing $MgAl_2O_4$ with different relative amounts of MgO and Al_2O_3 precursors. Based on the results Mn^{3+} is identified as a potential NIR emitting trap center.

In **Chapter 5** we present the discovery of a new phase related to K_2SiF_6:Mn^{4+}(KSF) As discussed above, KSF is a popular phosphor for display technologies because of its sharp red line emission around 620 nm. However, because of the long lived Mn^{4+} emission KSF suffers from saturation effects. To reduce this limitation and to improve the efficiency, we synthesized M_2SiF_6:Mn^{4+} were M is a mixture of K, Rb, and Cs, with the goal of shortening the lifetime of the Mn^{4+} emission so that saturation would occur at higher photon fluxes. During the synthesis of $KRbSiF_6$, we accidentally produced a hexagonal polymorph (h-KRSF) that is different from the commonly found cubic KSF or KRSF (c-KRSF). The hexagonal crystal structure gives a deviation from inversion symmetry at the Mn^{4+} site and this causes the optical performance to be superior to that of cubic KSF (higher lm/W efficacy, shorter luminescence life time, stronger absorption). The formation mechanism of h-KRSF was studied by monitoring the Mn^{4+} emission during the phase transition from the initially formed nanocrystalline c-KRSF to h-KRSF. The transformation shows an unexpected behavior: after a long induction period of about 15 hours, the appearance and rise of a zero-phonon line is observed (characteristic of h-KRSF) and followed by an exponential increase in the transformation to h-KRSF with time until all c-KRSF is converted.

To understand and optimize the performance of a novel broad band NIR phosphor **Chapter 6** investigates the Cr^{3+} emission in (Li/Na)$Sc(Si_{1-x}Ge_x)_2O_6$, a broad band NIR phosphor with a high luminescence quenching temperature. Cr^{3+} has potential as an excellent NIR emitter. Often the thermal quenching temperature is low but not in $LiScSi_2O_6$ and $NaScSi_2O_6$ with a quenching of the Cr^{3+} NIR emission around 500 K. To further improve the performance as NIR phosphor it is attractive to broaden the spectral width of the emission band. This was successfully realized by creating disorder in Si/Ge coordination sphere. However, for practical applications, it is crucial that the luminescence quenching temperature remains high. Upon partly replacing Si by Ge the quenching temperature of Cr^{3+} emission is lowered. An optimized per-

formance was realized for $LiSc(Si_{1-x}Ge_x)_2O_6:Cr^{3+}$ with a Ge content x = 0.2-0.4. This redshifts the NIR band maximum close to 900 nm and increases the FWHM bandwidth to 180 nm, while keeping the thermal quenching temperature high enough for application in NIR-LEDs, showing that this phosphor has potential for application as emitter in NIR-LEDs.

Finally **Chapter 7** provides a summary of the previous chapters and presents the main conclusions. Additionally, an outlook is provided on scientific questions that emerged during the four-year project. These questions provide a guide and inspiration for future researchers who wish to delve further into the field of transition metal luminescence.

References

[1] E. and M. National Academies of Sciences, *Assess. Solid-State Light. Phase Two* **2016**, 1.

[2] Biasing of P-N Junctions, http://hyperphysics.phy-astr.gsu.edu/hbase/Solids/pnjun2.html, accessed: **Nov., 2022.**

[3] T. S. Perry, *IEEE Spectr.* **1995**, *32*, 52.

[4] The 2014 Nobel Prize in Physics - Press release, https://www.nobelprize.org/prizes/physics/2014/press-release/, accessed: Feb., **2023.**

[5] Getting to grips with the green gap - News, https://compoundsemiconductor.net/article/101325/Getting_To_Grips_With_The_Green_Gap, accessed: Feb., 2023.

[6] P. Pust, V. Weiler, C. Hecht, A. Tücks, A. S. Wochnik, A. K. Henß, D. Wiechert, C. Scheu, P. J. Schmidt, W. Schnick, *Nat. Mater.* **2014**, *13*, 891.

[7] K. Uheda, N. Hirosaki, Y. Yamamoto, A. Naito, T. Nakajima, H. Yamamoto, *Electrochem. Solid-State Lett.* **2006**, *9*, H22.

[8] Vitasolis™ Lighting | NICHIA CORPORATION, https://led-ld.nichia.co.jp/en/product/lighting_vitasolis.html, accessed: **Nov., 2022.**

[9] Optisolis™ Lighting | NICHIA CORPORATION, https://led-ld.nichia.co.jp/en/product/lighting_optisolis.html, accessed: **Nov., 2022.**

[10] Lumileds Expands LUXEON CoB Family with Industry Leading High CRI LEDs | Lumileds, https://lumileds.com/lumileds-expands-luxeon-cob-family-with-industry-leading-high-cri-leds/, accessed: **Nov., 2022.**

[11] SORAA VIVID MR16 - GU5.3, https://www.soraa.com/products/18-MR16-GU5-3.php, accessed: **Feb., 2023.**

[12] J. J. Casal, *Arab. B.* **2012**, *10*, e0157.

[13] Horticultural lighting for sustainable food production | Signify Company Website, https://www.signify.com/global/our-company/blog/sustainability/horticultural-lighting-sustainable-food, accessed: **Nov., 2022.**

[14] S. Fang, T. Lang, M. Cai, T. Han, *J. Alloys Compd.* **2022**, *902*, 163825.

[15] OSLON® P1616, SFH 4737, https://www.osram.com/ecat/OSLON® P1616 SFH 4737/com/en/class_pim_web_catalog_103489/prd_pim_device_10751075/.

[16] A. D. Sontakke, A. J. van Bunningen, F. T. Rabouw, S. Meijers, A. Meijerink, *J. Phys. Chem. C* **2020**, *124*, 13902.

[17] A. D. Sontakke, A. J. van Bunningen, S. Wakui, A. Meijerink, *Mater. Adv.* **2021**, *2*, 2075.

[18] T. F. Soules, R. L. Bateman, R. A. Hewes, E. R. Kreidler, *Phys. Rev. B* **1973**, *7*, 1657.

[19] J. Si, L. Wang, L. Liu, W. Yi, G. Cai, T. Takeda, S. Funahashi, N. Hirosaki, R. J. Xie, *J. Mater. Chem. C* **2019**, *7*, 733.

[20] H. Masai, Y. Hino, T. Yanagida, Y. Fujimoto, Y. Tokuda, J. S. Kim, P. E. Jeon, J. C. Choi, H. L. Park, S. I. Mho, G. C. Kim, *Opt. Mater. Express, Vol. 5, Issue 3, pp. 617-622* **2015**, *5*, 617.
[21] A. Sarua, J. Hangfeng, M. Kuball, M. J. Uren, T. Martin, K. P. Hilton, R. S. Balmer, *IEEE Trans. Electron Devices* **2006**, *53*, 2438.
[22] M. Kuball, J. M. Hayes, M. J. Uren, T. Martin, J. C. H. Birbeck, R. S. Balmer, B. T. Hughes, *IEEE Electron Device Lett.* **2002**, *23*, 7.
[23] J. W. de Wit, T. P. van Swieten, M. A. van de Haar, A. Meijerink, F. T. Rabouw, *Adv. Opt. Mater.* **2023**,*11*, 2202974.
[24] M. A. van de Haar, M. Tachikirt, A. C. Berends, M. R. Krames, A. Meijerink, F. T. Rabouw, *ACS Photonics* **2021**, *8*, 1784.

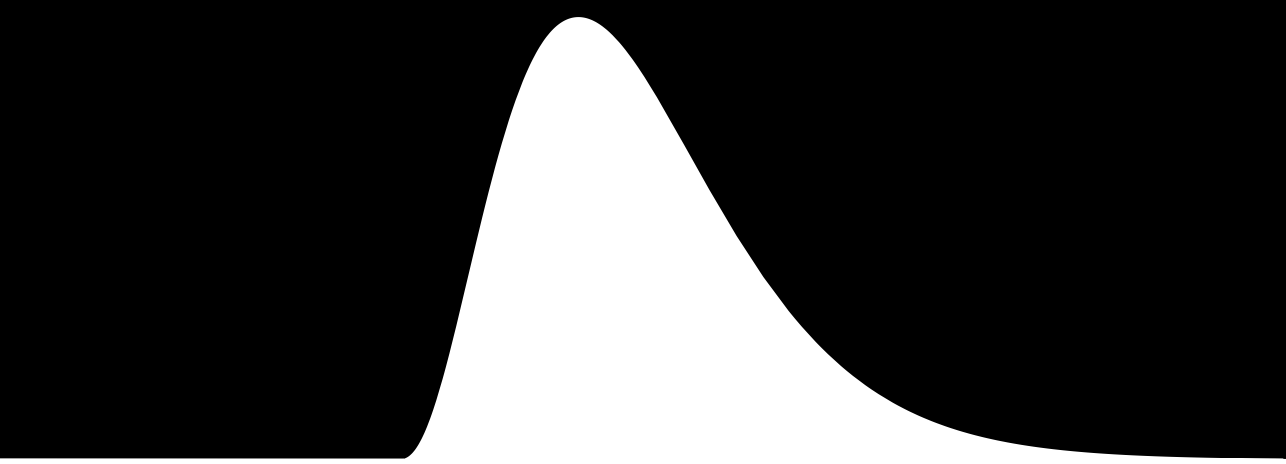

Chapter 2

Theory

“ If ignorance is bliss, then knock the smile off my face.”

Zack de la Rocha

This thesis focuses on the study of the luminescence of transition metal ions in various hosts, their temperature-dependent emission properties and the implications for practical applications, especially in blue-LED pumped light sources where they serve as colour converters in luminescent materials (phosphors). Transition metals are elements from group 3 to 12 in the periodic Table, and when incorporated into host lattices, their oxidation states can vary from +1 to +8, depending on the element, host matrix, and synthesis conditions. Among the transition metals, those in the fourth row are the most widely studied for commercial applications due to their abundance in the earth's crust and existing knowledge. In this group of elements the 3*d* shell is filled with up to ten electrons. This chapter explains the origin of the energy levels for 3*d* transition metal ions in both free ions and the ions embedded in a crystalline matrix and how this can be related to the luminescence properties. In addition, an introduction to vacancies, defects, and the Kröger-Vink notation is provided.

Free ion

In order to understand the luminescence of transition metal ions, it is necessary to understand the origin of different energy levels within the ions. For the free ion the partly filled 3d shell with *n* electrons gives rise to a rich energy level structure as a result of Coulomb interactions. Both spin- and orbital magnetic moments of electrons interact and this gives rise to multiple energy levels. The ground state represents the energetically most favourable arrangement of 3*d* electrons and can be determined using Hund's rules:

$$1)\ S = \max\ \Sigma_i m_{s,i}$$

$$2)\ L = \max\ \Sigma_i m_{l,i}$$

where *S* and *L* are the total spin and orbital magnetic moments (summed over those of all 3d electrons). In the ground state the electron spins are as much as possible aligned to maximize *S*. The total of different electron configurations results in multiple energy levels. Many higher energy levels arise for electron configurations with less favourable alignment of the magnetic moments. The energy levels are labelled using Russell-Saunders term symbols (also known as *LS* term symbols) that provide information on the total spin and total orbital momentum. The term symbols that serve as labels for the free ion energy levels are written as ^{2S+1}L. The upper label 2*S*+1 is known as the spin multiplicity (number of possible orientations for the total spin magnetic moment). Letters are used instead of numbers for *L*, with the notation S, P, D, and F for *L*=0, 1, 2 and 3, as an analogy to the *s*, *p*, *d*, and *f* notations for *l*=0, 1, 2 and 3 of the single electron orbitals. The energy of each level can be described with three parameters, known as Racah parameters A, B, and C. Here A accounts for a constant average Coulomb repulsion, while B and C vary

Table 2-1. Free ion term symbols and their splitting in a crystal field of octahedral symmetry.

Term	Degeneracy	Splitting in octahedral symmetry
S	1	A_1
P	3	T_1
D	5	$E+T_2$
F	7	$A_2+ T_1+T_2$
G	9	$A_1+E+T_1+T_2$
H	11	$E+T_1+T_1+T_2$
I	13	$A_1+A_2+E+T_1+T_2+T_2$

for the different energy levels and are responsible for the energy separation between the energy levels labelled by the term symbols. Energy differences between states of the same spin multiplicity (same *S*) depend only on B, while for states with different *S* it depends on both B and C. Typically, the ratio C/B is around 4.5.

Crystal field splitting

A transition metal ion is typically embedded in a crystalline host where it is surrounded by negatively charged anions known as ligands. These ligands have an impact on the energy levels of the transition metal ion. This influence is explained by the crystal field theory, which takes into account the shape and orientation of the d-orbitals with respect to the ligands. Figure 2-1 shows the electron density distribution of the five *d* orbitals. In the case of an octahedral coordination of six anions, interaction between the negatively charged ligands and the d-electron in orbitals in the directions of the ligands will raise the energy. It is more favourable for electrons to occupy d-orbitals that have the electron density between the ligands. This results in the z^2 and x^2-y^2 (e_g) *d*-orbitals to be higher in energy, whereas the xy, xz, and yz (t_{2g}) d-orbitals, oriented in between the ligands, will be lower in energy. The energy difference for a *d*-electron in a t_{2g} and e_g orbital is known as the crystal field splitting Δ_O or 10 D_q. The crystal field splitting increases with higher negative charge of the ligands and with smaller distance to the ligands.

The crystal field splitting causes a splitting of the free ion energy levels. The orbital degeneracy of $2L+1$ is partially lifted when the five 3d orbitals do no longer have the same energy (as was the case in the free ion). Using group theory, the splitting can be determined for free ion levels in any point group symmetry. An insightful description of how group theory can be used to derive the splitting of free ion term symbols into crystal field levels can be found in the book 'Chemical Applications of Group Theory' of Cotton [1] but is

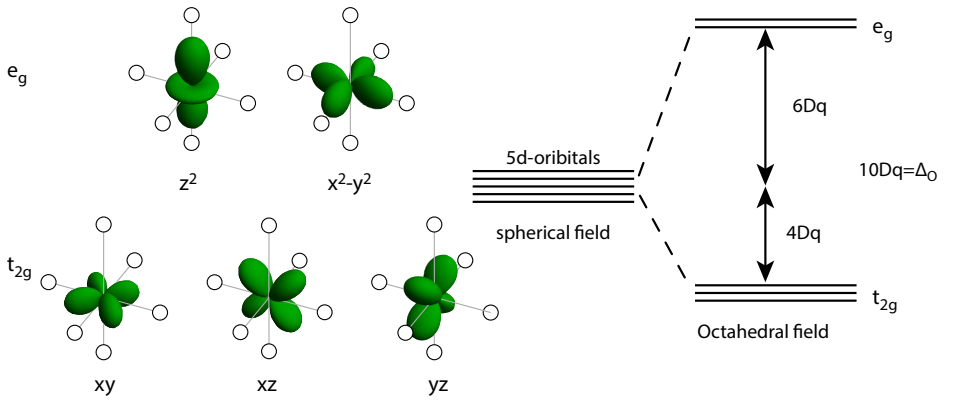

Figure 2-1. Schematic illustration of the orientation of the five d orbitals in an octahedral crystal field, with hollow spheres representing negative ligands. The z2 and x2-y2 d-orbitals are oriented directly towards the point charges, making them less favourable than the xy, xz, and yz d-orbitals. On the right hand side of the Figure, a schematic representation shows the splitting of the energy levels due to an octahedral crystal field.

not further discussed here. In Table 2-1 the crystal field terms arising from an octahedral crystal field are shown. The energy levels are labelled by Mulliken symbols of the irreducible representation that describe the symmetry of crystal field levels. Symbols A and B are singly, E doubly and T triply degenerate crystal field levels. Subscripts 1 or 2, g or u and superscripts ' or " give information on the symmetry properties. Note that the total degeneracy before and after splitting is the same.

Tanabe Sugano diagram

In a Tanabe Sugano (TS) diagram the free ion energy levels arising from Coulomb interaction in the $3d^n$ configuration and the crystal field splitting of the five d-orbitals by the ligands are combined to give the energy levels structure of $3d^n$ transition metal ions as a function of the (octahedral) crystal field splitting Δ_O. These diagrams are named after their creators Tanabe and Sugano[2]. On the x-axis the crystal field splitting (given as Δ_O/B or D_q/B) increases from left to right and the y-axis gives the energy (E/B). Tanabe Sugano diagrams were developed to explain 3d transition metal ion absorption spectra for an octahedral coordination. The ground state by definition coincides with the x-axis and serves as the zero-energy reference. On the left, at the position of the y-axis where there is no crystal field splitting (Δ_O=0), the energy levels of the free ion states are given and the TS diagram shows the associated Russell-Saunders term symbols.

Upon incorporation in a crystal or solution, the transition metal ion is surrounded by negative ligands. This gives rise to a splitting of the five d-orbitals as outlined above. The orbital degeneracy is lifted and splitting into crystal field levels occurs. The total degeneracy of the new crystal field levels that

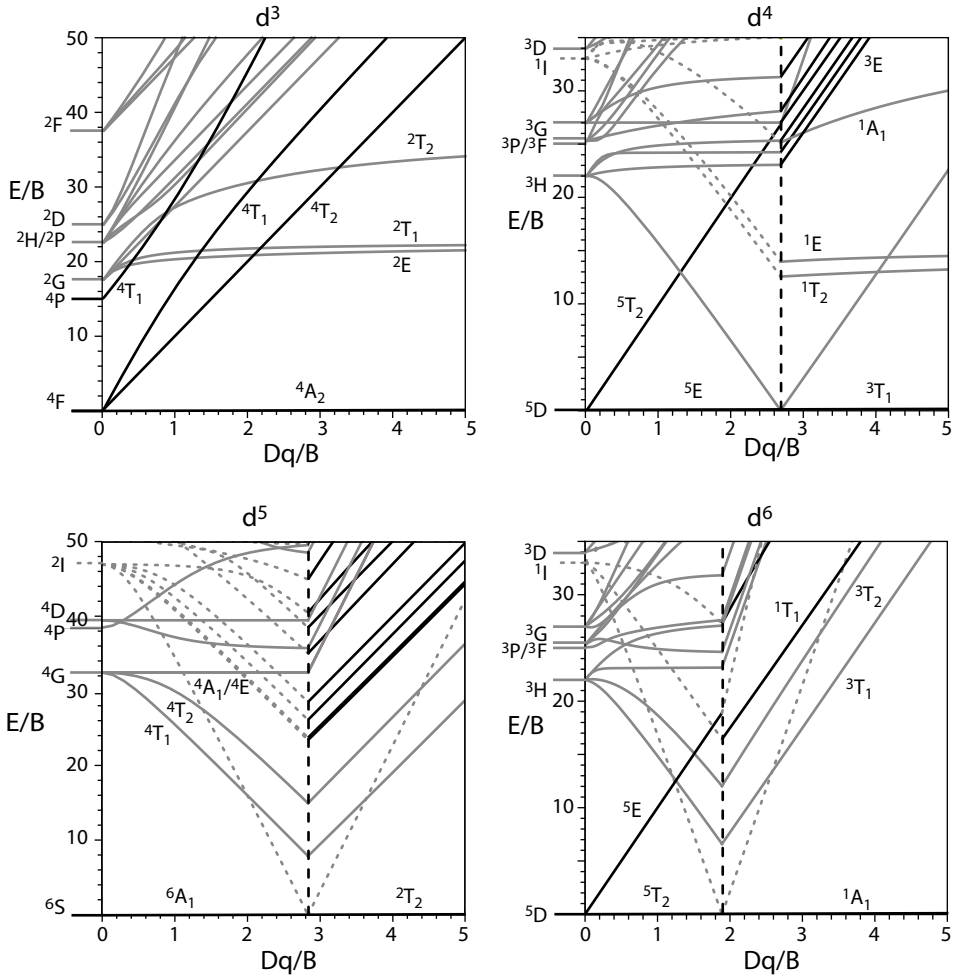

Figure 2-2. The Tanabe Sugano diagrams for d^3 to d^6 are presented depicting the energy as a function of crystal field splitting in octahedral coordination. The free ion term symbols on the left split into crystal field levels and the evolution as function of Dq/B is plotted. Black lines show the energy levels with the same S as the ground state, while the grey lines represent those with a difference in S of one and the dotted grey lines represent those with a ΔS of two. The value of C/B is 4.5 for all diagrams

emerge from a term symbol is the same as the orbital degeneracy $2L+1$ of the free ion level. Tanabe Sugano diagrams for the d^3 until d^6 electron configurations are shown in Figure 2-2. The free ion term symbols for these configurations, their crystal field splitting and how the energy of all crystal field levels varies with respect to the ground are plotted in a TS diagram. In certain electron configurations, such as those with 4 or 5 electrons, a strong crystal field can cause a transition from a high spin to a low spin ground state, as indicated by the dashed black line in Figure 2-2. At this transition point the crystal field splitting becomes higher than the spin-spin interaction energy and it becomes energetically favourable to have electrons as much as possible in the lower energy t_{2g} orbitals with spins paired.

The strength of the crystal field is determined by the nature of the ligands. Higher negatively charged anions and shorter distances give rise to a larger crystal field splitting. In the so-called spectrochemical series the ligands are arranged from small to high crystal field splitting Δ_O:

$$I^- < Br^- < S^{2-} < Cl^- < NO_3^- < F^- < OH^- < H_2O < NH_3 < NO_2^- < CN^- < CO$$

The chemical properties of both ligand and transition metal ion are also important. Charge delocalization of the 3d electron density over the anions occurs. In crystal field theory, the ligands are treated as point charges, and this approximation is more accurate for ionic ligands when charges are more localized. However, for more covalent ligands, when the charges become more delocalized, the 3d electron density spreads out, reducing the repulsion between the d-electrons and decreasing the energy difference between (free ion) energy levels which can be expressed as a reduction in Racah parameters B and C. This phenomenon is known as the nephelauxetic effect, derived from the Greek words for "cloud expanding." The extent of the effect depends on the ionic character of the anion, with larger anions and ions with lower electronegativity (more covalent bonding) resulting in a greater nephelauxetic effect. Depending on the type of ligand, the Racah parameter B is reduced to 0.6 - 0.8 of the free ion values.

With the considerations outlined above, the TS diagrams in Figure 2-2 can be used to understand the optical properties of transition metal ions in solids and solutions. The energy level structure is determined by the crystal field splitting and can be found by drawing a vertical line at the position of Δ_O/B or D_q/B that is valid for the transition metal ion in a specific host matrix. The order in which the higher energy levels are positioned with respect to the ground state can be used to assign absorption bands to transitions from the ground state. Emission typically corresponds to a transition from the lowest excited state back to the ground state. Note that both the x- and y-axis have the /B term. By dividing by B for both the x- and y-axis the TS diagram can be used for any ion with the same specific $3d^n$ configuration but with different B (due to differences in ligands or type of element). For example, both Mn^{4+} and Cr^{3+} discussed in this thesis have the $3d^3$ configuration and the luminescence of both can be understood using the $3d^3$ TS diagram, albeit with a different

value for B (B being larger for Mn^{4+}).

Although originally designed for octahedral coordination, the TS diagrams can also be applied to tetrahedral and cubic coordination by using the TS diagram for 10-*n* electrons, where '*n*' is the number of electrons in the d-shell. However, it is important to note that the crystal field splitting is smaller compared to that for octahedral coordination. For the same ligands at the same distances the crystal field strength for tetrahedral and cubic coordination are $\Delta_T=4/9\ \Delta_O$ and $\Delta_C=8/9\ \Delta_O$, respectively.

Line shape and selection rules

The TS diagrams present the energies of states within the partly filled $3d^n$ configuration as a function of the crystal field strength, as outlined in the previous section. In addition, they provide information on line shape (sharp lines or broad bands) and oscillator strengths (strong or weak absorption, short or long emission life time) of transitions within the $3d^n$ configuration. As the electron configuration for the $3d^n \rightarrow 3d^n$ transitions in the TS diagrams does not change, all transitions are formally parity forbidden. For $3d^n$ ions in inversion symmetry this selection rule is more strict than for ions not in a site with inversion symmetry. Odd parity crystal field components can admix opposite parity states into the $3d^n$ states to relax the parity selection rule. For ions in inversion symmetry there are no static odd parity CF components and only coupling with odd-parity vibrations can induce dynamic CF components to partially break the selection rule. The parity forbidden character results in molar extinction coefficient ε of typically 10-100 $M^{-1}.cm^{-1}$. Luminescence life times for parity forbidden d-d transitions are also affected by the forbidden nature of the transition and are around several µs, with longer life times observed for $3d^n$ ions in inversion symmetry. Note that these values are much smaller than for fully allowed transitions with ε around 10^4-10^5 $M^{-1}.cm^{-1}$ and emission life times in the ns range.

Some d-d transition are not only parity forbidden but also spin-forbidden. If the value of *S* changes in the transition from the initial to the final state, transitions are spin forbidden as light cannot induce a spin flip. In the TS diagram the spin forbidden character can be derived from the value of 2*S*+1 in the left upper corner of the Mulliken symbols of the crystal components. Note that these are the same as for the *LS* term symbols from which they originate: the crystal field splitting does not affect *S*. For spin forbidden transition the molar extinction coefficients are usually smaller than 1 $M^{-1}.cm^{-1}$ and the luminescence life time is of the order of ms. A well-known spin-forbidden transition is the $^2E \rightarrow {}^4A_2$ transition in the $3d^3$ configuration. The TS diagram in Figure 2-2 shows that for high crystal field the ^2E state is the lowest excited state (with *S*=1/2) and the transition back to the $^4A_2$ ground state (with *S*=3/2) is spin forbidden. For ruby, Cr^{3+} in Al_2O_3, this transition is responsible for the deep red emission and the forbidden nature of the transition was instrumental in realizing population inversion in the first laser[3]. In the well-known red

LED phosphor $K_2SiF_6:Mn^{4+}$ the $^2E \rightarrow {}^4A_2$ transition is responsible for the narrow band red emission that is widely used in LCD displays.[4]

In the absorption and emission spectra of $3d^n$ ions both broad band and sharp line emission can be observed. Again, this can be understood with the TS diagrams in Figure 2-2. If a transition occurs between two states for which the lines in the TS diagram run parallel, a sharp absorption or emission line is observed. For transitions between states with lines that have a different slope as a function of Δ_O broad bands are expected. A simple way to understand this is to realize that the crystal field is not constant. Variations in the ligand-$3d^n$ ion distance during vibrations (even the zero point vibration at 0 K) will cause Δ_O to fluctuate. For two parallel lines the energy difference does not change with variations in Δ_O (or D_q) and a sharp absorption or emission line is observed. For lines with different slopes the energy difference varies with Δ_O and broad band absorption or emission results.

An alternative (but not fundamentally different) way to explain the line shape is using the configurational coordinate diagram. In this diagram the energy of the ground and excited state are plotted as a function of the configuration coordinate, the ion-ligand distance. Both electronic and vibrational (phonon) energies are considered. In Figure 2-3 equidistant vibrational levels are plotted for the ground state and excited state. The curves have a parabolic shape as the potential energy varies with the square of the deviation from the equilibrium distance for a harmonic oscillator. The Franck-Codon principle dictates that optical transitions (absorption or emission of light) are drawn as vertical lines since the time scale is much faster than that of the motion of nuclei (vibrations) and thus occur at a fixed ion-ligand distance. Absorption occurs typically from the lowest vibrational level in the ground state. The overlap with different vibrational wave functions in the excited state determines the relative intensity of the various vibronic transitions. A larger change in equilibrium distance between ground and excited state (*R*-*R*') results in broader absorption bands. Similarly, emission occurs from the lowest vibrational level in the excited state back to different vibrational levels in the ground state. The energy of the maximum of absorption (blue arrow in Figure 2-3) is higher than the maximum of emission (green arrow) and the energy difference is called the Stokes' shift. A stronger variation in equilibrium bond length (*R*-*R*') increases the Stokes' shift. For electronic transitions that induce a change in bond strength (for example by an excitation involving a transition of an electron from a bonding to an anti-bonding orbital) broad absorption and emission bands and large Stokes' shifts are expected. For electronic transitions that do not induce a change in ion-ligand bonding (i.e. *R*=*R*') sharp absorption and emission lines between the zero-vibrational levels of ground and excited state are observed. These so-called zero-phonon lines are at the same energy in excitation and emission.

The two ways of understanding line shape may seem different but are equivalent if the electronic configurations for states in the TS diagrams are consid-

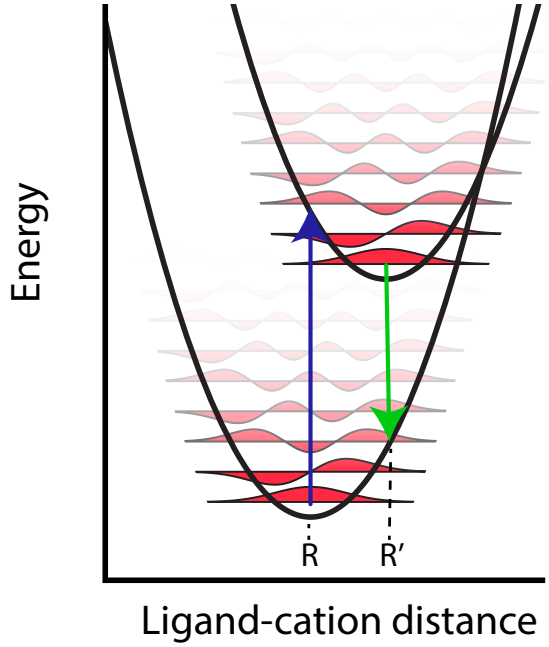

Figure 2-3. Configuration coordinate diagram showing the energies for a luminescent ion in both its ground and excited state as a function of ion-ligand distance. The equilibrium ion-ligand distance (minimum of the parabolas) is indicated by R (ground state) and R' (excited state). The horizontal lines within the parabolas represent the vibrational levels and the red curves give their wave functions. Absorption and emission are shown as blue and green lines, respectively. The wave function overlap varies for transitions between different vibronic levels and is determined by the offset between the parabolas. A larger change in bond strength induced by an electronic transition gives in a larger offset R-R'. A larger offset results in a larger spread of transition energies (wider range of vibronic levels) and broader absorption and emission bands. The absorption maximum (blue arrow) is at higher energie than the emission maximum (green line). The energy is known as the Stokes' shift, which is commonly observed in luminescent materials. The Stokes' shift increases with a larger difference R-R'.

ered and knowing that the t_{2g} orbitals are non-bonding while the e_g orbitals have an anti-bonding character. Parallel lines in the TS diagrams correspond to states with the same electron distribution over t_{2g} and e_g orbitals while lines with a different slope differ in the distribution over t_{2g} and e_g. For example, the $^4A_2$ and ^2E state of Cr^{3+} both correspond to the t_{2g}^3 configurations and the energy difference results from a spin flip while the $^4T_2$ state has the $t_{2g}^2e_g^1$ configuration and the higher energy of the $^4T_2$ state is a result of the transition from one electron from the non-bonding t_{2g} to the anti-bonding e_g (energy difference Δ_O). A larger change in bond strength corresponds to stronger electron-phonon coupling and is not only important in understanding line shape and Stokes shift but also thermal quenching behavior.

Thermal quenching

At elevated temperatures, luminescent materials show temperature quenching of their emission. Quenching can be reversible or irreversible. Irreversible quenching is typically associated with the degradation of the host material or a change in oxidation state of luminescent ions. In reversible quenching processes, the luminescent centres remain the same, but the efficiency for emission of light decreases at elevated temperatures. When an ion in an excited state returns to the ground state, it may do so by emitting a photon (radiative) or by competing non-radiative pathways. The internal quantum yield (Φ_I) quantifies the fraction of absorbed photons that is converted to the desired emitted photons and ranges from 0 to 1. Φ_I is determined by the ratio of the average rate of radiative transitions to the average rate of non-radiative transitions (P_r and P_{nr}, respectively). The temperature dependence of the quantum yield is typically the result of an increase in non-radiative transition probability with increasing temperature, which causes luminescence quenching. The radiative decay rate can also be temperature dependent but is mostly less affected. The luminescence quenching temperature T_Q or T_{50} is defined as the temperature at which the radiative and non-radiative decay rates are equal, i.e. the temperature at which Φ_I has dropped to 0.5. The relationship between the temperature and the quantum yield can be described by the following equation:

$$\Phi_{\mathrm{I}}(T) = \frac{P_{\mathrm{r}}}{P_{\mathrm{r}} + P_{\mathrm{nr}}(T)} \qquad (2.1)$$

The increase in non-radiative transition probability with increasing temperature is a well-established phenomenon. To explain this behavior, three well-known temperature-dependent quenching processes will be discussed in this section: multi-phonon relaxation, thermally activated crossover, and thermally assisted photon ionization. The different processes are depicted in Figure 2-4.

Multi-phonon relaxation is a mechanism in which an excited state returns to the ground state by exciting multiple phonons or vibrations in the surrounding environment. The rate of energy transfer to vibrations depends on the number of vibrations that is required to bridge the energy gap between the excited and ground states, the energy of these vibrations and the temperature. Multi-phonon relaxation is often considered for transitions where R-R' = 0 such as f-f transitions in lanthanides and sharp line d-d transitions for 3d transition metal ions. The average rate of non-radiative decay by multi-phonon relaxation, can be calculated using:[5]

$$P_{\mathrm{nr}} = Ae^{-\beta p} \qquad (2.2)$$

Where the prefactor A is typically 10^{12} to 10^{13} s^{-1} and β is approximately 3. The variable p represents the number of phonons required for the transition. To

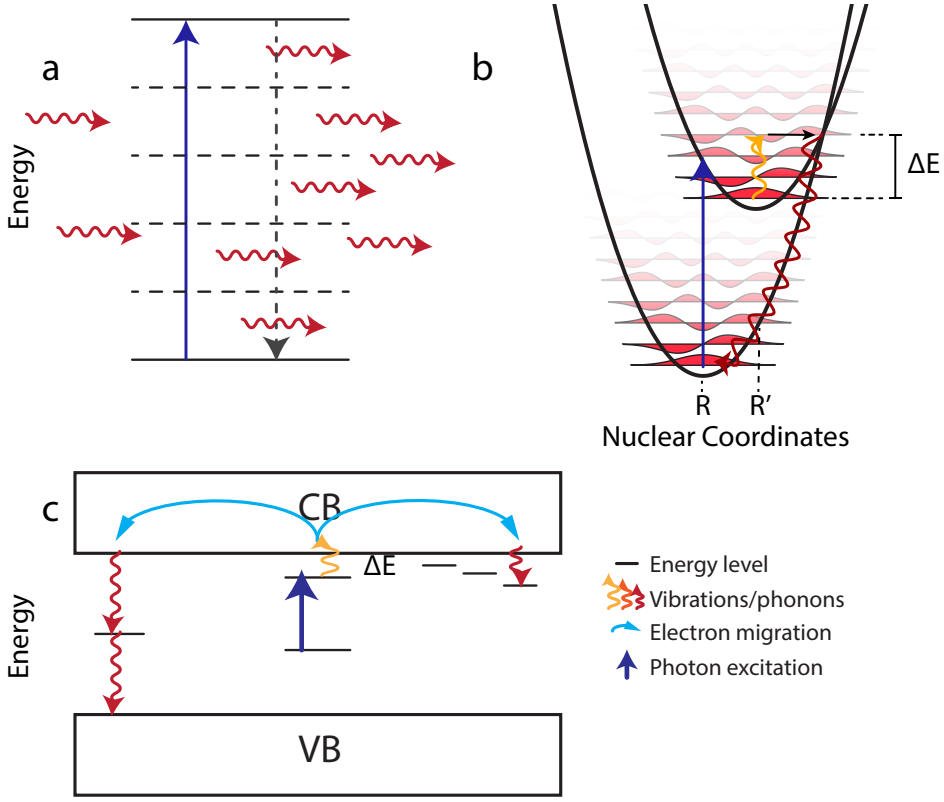

Figure 2-4. Schematic illustration of the three different non-radiative pathways for a luminescent centre. The blue arrows represents the excitation of the system by an incoming photon. The yellow lines show thermal excitation, while the red arrows indicate the non-radiative decay and loss of excitation energy to heat in the system. (a) Multi phonon relaxation: the rate of returning to the ground state through exciation of multiple vibrations decreases with the number of vibrations needed to bridge the gap but increases upon thermal population of the phonon modes involved (b) Thermal cross-over from the excited state to the ground by thermal population of a higher vibronic in the excited state followed by a resonant transition to a very high vibrational level in the ground state (c) Thermally assisted photon ionization of an electron from the excited state to the conduction band. From there, the electron can either fill a trap state or fall back via a killer site (shown in light blue arrows) causing quenching of the luminescence.

ensure a high quantum yield, it is preferable to have a high number of phonons (above 5) required for multi-phonon relaxation. Thermal population of phonon modes involved in multi-phonon relaxation enhances the non-radiative relaxation rate:

$$P_{\mathrm{nr}}^{(p)}(T) = P_{\mathrm{nr}}^{(p)}(0)(1 + n(T))^{p} \qquad (2.3)$$

with n(T) representing the phonon occupation number at temperature T:

$$n(T) = \frac{1}{e^{\hbar\omega/kT} - 1} \tag{2.4}$$

ħω is the phonon energy of the mode involved in multi-phonon relaxation. Thermal occupation of vibrational modes thus enhances non-radiative relaxation and the temperature at which this occurs depends on the energy of the modes involved, typically multi phonon relaxation happens via the highest energy vibrations in the lattice as these correspond to the smaller value of *p*, phonons needed, to bridge the gap.

A second mechanism for non-radiative relaxation is thermal crossover. For a luminescent center as depicted in Figure 2-4 the excited state parabola is offset from the ground state parabola. This causes higher vibrational levels in the luminescent center to overlap with a very high vibrational levels of the ground state. Upon thermal population of the higher vibrational levels in the excited state, a resonant transition to a very high vibrational level of the ground state can occur. This is followed by fast relaxation to the zero-vibrational level in the ground state and quenches the luminescence. A widely used description of the temperature dependence of this mechanism is Arrhenius behavior as the cross-over to the ground state requires overcoming an energy barrier *ΔE* (see Figure 2-4b). A more correct mathematical model considering the wavefunction overlap in thermally occupied excited state vibrational levels and high ground state vibrational levels was derived by Struck and Fonger [6] and shows that the activation barrier description is a good approximation. The average rate of non-radiative relaxation can be expressed by the following equation:

$$P_{\mathrm{nr}}(T) = Ae^{-\Delta E/kT} \tag{2.5}$$

where *A* is the attempt rate (usually around 10^{12}-10^{14} Hz), *ΔE* is an effective energy barrier corresponding to the energy difference to vibrational modes that overlap with the edge of the ground state parabola, where the very high vibrational wavefunction have their highest probability and k is the Boltzmann constant. Often the energy barrier is depicted as the energy difference between the zero-vibrational level of the excited state and the crossing point of the ground state and excited state parabola. Although this is not correct (the effective *ΔE* is smaller) it does help to illustrate that *ΔE* becomes smaller when the offset between the parabola (*R*-*R*') becomes larger. By substituting Equation (2.5) into Equation (2.1) and dividing both the numerator and denominator by P_r, we obtain:

$$\Phi_{\mathrm{I}}(T) = \frac{1}{1 + \frac{A}{P_{\mathrm{r}}} e^{-\Delta E/kT}} \tag{2.6}$$

For the thermally activated cross-over mechanism the thermal quenching temperature is strongly dependent on the relaxation induced by the electronic transition. If there is a considerable change in bonding induced by

the electronic transition (large change in equilibrium distance) the thermal quenching temperature will lowered. As the *R*-*R*' offset is also related to the bandwidth of absorption and emission bands, this quenching mechanism can be identified by a correlation between bandwidth and T_Q and shows a lowering of T_Q for increasing bandwidth.

Thermally assisted photon ionization is the third mechanism by which luminescence can be quenched. To understand this mechanism, we need to consider the energy levels of the excited state relative to the conduction band. If the excited state is close to the conduction band, following excitation an ion can thermally release an electron to the conduction band. In the conduction band, the electron is mobile and can find a trap state or move to a killer site, resulting in a non-radiative decay. A similar process is possible for thermally activated escape of a hole to the valence band and is not usually considered but it is fully equivalent. The origins of trap states and killer sites are often due to crystal defects or impurities in the crystal. The rate of the electron to escape into the conduction band is determined by ΔE, which is the energy difference between the excited state and the bottom of the conduction band. The equation for the Φ_I is then identical to that of thermally activated crossover discussed above. Both quenching processes show Arrhenius type temperature dependent behavior and it is not easy to distinguish between the two processes.

To investigate thermal quenching processes of luminescence two methods are available: luminescence intensity or lifetime measurements. While measuring intensity changes with temperature seems the logical choice to monitor and understand thermal quenching behavior, it can produce misleading results due to various factors. For instance, changes in the oscillator strength of the absorption transition or spectral broadening or shifting can cause variations in intensity unrelated to thermal quenching but caused by changes in the number of photons absorbed. Furthermore, trivial aspects such as variations in alignment, collection efficiency, or excitation source intensity can also impact the reliability of intensity measurement. Lifetime measurements provide a more robust and reliable approach as it is not influenced by the aforementioned factors. The luminescence lifetime (τ) is determined by the sum of radiative and non-radiative decay rates. Changes in the radiative decay rate as a function of temperature can complicate the analysis but are often well understood and are easier to correct for than the complications related to luminescence intensity measurements.

Energy transfer and Energy migration

As discussed above, a luminescent ion in the excited state can return to the ground state by emission of light (radiative decay) or conversion of the energy to heat (non-radiative decay). A third option is energy transfer to another luminescent species. Energy transfer can occur through non-radiative energy transfer via dipole-dipole interaction (known as Förster energy transfer) or via exchange interaction (Dexter energy transfer). Radiative energy transfer (photon emission followed by reabsorption) is also possible but usually not efficient. For energy transfer to occur, interaction between a donor ion D (also called sensitizer) and an acceptor ion A (also called activator) are considered. The probability for Förster energy transfer for dipole-dipole interaction is given by:[7]

$$W_{\mathrm{DA}}^{\mathrm{d\text{-}d}} \propto \frac{f_{\mathrm{D}} \cdot f_{\mathrm{A}}}{R^6} \times \int SO \qquad (2.7)$$

where f_D and f_A are the oscillator strengths of the transitions involved in the energy transfer for the donor and acceptor, *R* is the donor-acceptor distance and the last term SO is the spectral overlap, defined as $g_D(E)\, g_A(E)\, dE$. Where g_D and g_A are the donor emission and acceptor absorption spectrum. As the radiative decay rate on the donor also scales with f_D, the energy transfer efficiency primarily dependent on the absorption strength of the acceptor and the degree of resonance between donor emission and acceptor absorption (spectral overlap integral) and very strongly on the donor-acceptor distance with an R^{-6} dependence. When one or both ions have a low oscillator strength, energy transfer via exchange interaction is more likely to occur, but only when ions are in close proximity, as it requires wave function overlap to allow for energy transfer through direct electron exchange. This is known as Dexter energy transfer. Unlike Förster energy transfer, the oscillator strengths of transitions on either ion do not play a role in this type of transfer. The Dexter energy probability therefore scales as:[8]

$$W_{\mathrm{DA}}^{\mathrm{ex}} \propto e^{-R/L} \times \int SO \qquad (2.8)$$

and has an exponential distance dependence where *L* is the effective Bohr radius, determined by the wavefunctions involved in the energy transfer process. Dexter energy transfer is highly effective when donor and acceptor are in close proximity to one another, such as a nearest neighbour pair, but becomes insignificant when distances exceed ~5 Å. In contrast, despite the R^{-6} distance dependence energy transfer via dipole-dipole interaction can be efficient even for distances exceeding 10 Å.

If the donor and acceptor ions are the same, the acceptor can serve as a new donor and transfer its energy to another nearby ion. This sequential energy transfer where energy is transferred to the same excited state of the same

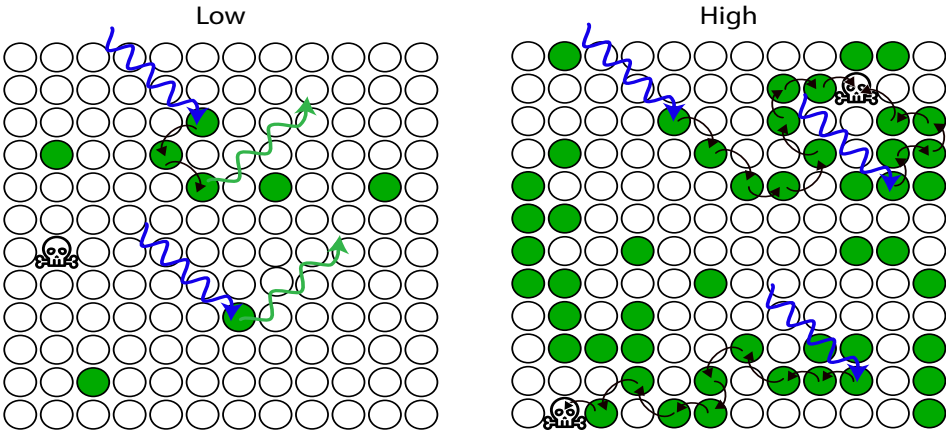

Figure 2-5. Illustration of energy migration in a periodic crystal lattice. Dopant ions (depicted as green) facilitate energy transfer when the concentration becomes high and multiple energy transfer steps between nearest neighbor optically active ions become possible. Absorption of a photon (represented by blue arrows) excites a specific ions in the lattice. Quenching centers (indicated by skulls) are potential sinks where energy is lost when an excited dopant ion is in close proximity and transfers its energy. With higher dopant ion concentrations, energy migration becomes more efficient and the migrating excitation energy probes a large volume of the crystal. This increases the risk of encountering a quenching site where the energy is lost by energy transfer to the quenching centers followed by non-radiative relaxation (lattice vibrations or heat).

type of ions is known as energy migration. The efficiency of energy migration is determined by the concentration of donor ions and the distance between ions. For a high enough concentration the percolation point can be reached where a three dimensional network is formed over which the excitation energy can migrate through the crystal lattice. As a result, the excitation energy probes a large volume. As the excited state travels through the crystal, it may encounter impurities or imperfections that can act as a sink or quenching center for the excited state, leading to a loss of emission intensity. This phenomenon is known as concentration quenching. Concentration quenching occurs even for low concentrations of quenching sites. Energy migration can also be used to enhance the efficiency of energy transfer to an intentionally included acceptor ion with a desired emission wavelength. Extensive research has been done on energy migration in concentrated Eu^{3+}, Gd^{3+} and Tb^{3+} host lattices,[9][10] but also for Mn^{2+} energy migration in concentrated Mn^{2+} phosphors has been studied.[11]

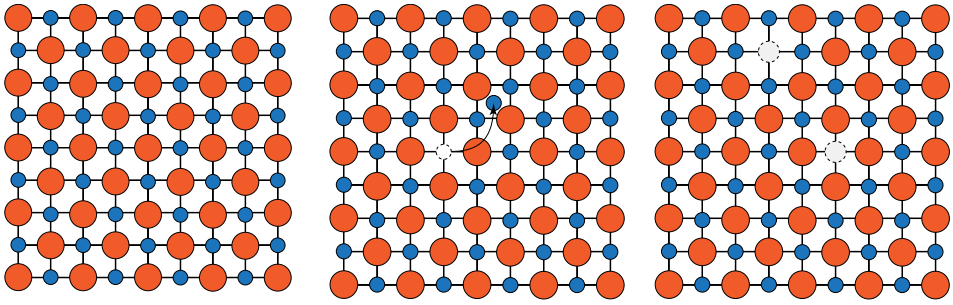

Figure 2-6. Schematic representation of different crystal defects. On the left is a perfect ionic crystal with smaller cations shown in blue and larger anions in red. In the middle, a Frenkel defect is shown where a cation moves from its original lattice site to an interstitial site, resulting in a vacancy and an interstitial atom. On the right, a Schottky defect is formed where both a cation and an anion are missing. Note that for these types of defects charge neutrality is maintained.

Defects and Kröger Vink notation

In crystalline materials, the atoms or ions arrange themselves in a repetitive pattern. In a perfect crystal, the unit cell in which atoms or ions are positioned at well-defined lattice sites repeats itself in all directions and builds up the crystal. However, a crystal is never perfect. Thermodynamics dictates that defects occur. Possible defects are vacancies or interstitials, while also impurities or variations in valence state are considered as defects. Next to these point defects also more extended dislocations from the perfect lattice positions can occur in for example line defects. Defects have a significant impact on solid-state chemistry and physical properties of a material. Indeed, in the semiconductor industry the control over the defect chemistry is crucial in the design of materials with the desired functionalities. The Kröger-Vink notation was developed to provide a clear description of various types of point defects and the formation and annihilation of defects. A vacancy is an empty site in the crystal structure where an atom or ion should have been, whereas an interstitial atom occupies a space that is typically unoccupied in the regular crystal lattice.

In the Kröger-Vink notation defects are described by putting the species in the middle. This can be an element but also a vacancy. The right hand subscript gives the position in the type of lattice site where the species is located. The right hand superscript gives the effective charge of the species relative to the charge expected for the normal occupancy of that lattice site. The charge difference is denoted by the symbol × if there is no change in charge, • represents one relative positive charge, and ’ represents one relative negative charge. The Kröger-Vink notation will be illustrated with the NaCl crystal lattice. A well-known defect is a Schottky defect which involves a cation vacancy and anion vacancy. In the Kröger-Vink notation the formation of a Schottky defect is given by:

$$\mathrm{Na}_{\mathrm{Na}}^{\times} + \mathrm{Cl}_{\mathrm{Cl}}^{\times} \rightleftharpoons \mathrm{V}_{\mathrm{Cl}}^{\bullet} + \mathrm{V}'_{\mathrm{Na}} + \mathrm{NaCl}$$

This can be read as a Na^+ ion on a Na^+ site and Cl^- ion on a Cl^- site (both charge neutral!) convert to a vacancy on a Cl^- site (note that this neutral vacancy is 1+ with respect to 1– charge expected on this site, hence the • superscript), a vacancy on a Na^+ site and NaCl added to the crystal. Another type of defect is the Frenkel defect which involves the combination of an interstitial and vacancy of the cation while an anti-Frenkel defect is the same for an anion. In the Kröger-Vink notation the formation is described by:

$$\mathrm{Na}_{\mathrm{Na}}^{\times} + \mathrm{V}_{\mathrm{i}}^{\times} \rightleftharpoons \mathrm{V}'_{\mathrm{Na}} + \mathrm{Na}_{\mathrm{i}}^{\bullet}$$

Impurity ions can also be described using the Kröger-Vink notation and aliovalent impurities can give rise to additional defects. For example, when AgCl is doped with Zn^{2+}, two Ag^+ ions can be replaced by one Zn^{2+} to preserve charge neutrality. In the Kröger-Vink notation this is described by:

$$Zn\mathrm{Cl}_2 \rightleftharpoons Zn_{Ag}^{\bullet} + \mathrm{V}'_{Ag} + 2\mathrm{Cl}_{\mathrm{Cl}}^{\times}$$

All types of other point defects can also be described using the Kröger-Vink notation in a manner that avoids confusion and is more concise and descriptive than other defect notation schemes. It is worth noting that the formation of all these defects can be considered as chemical reactions. The equilibrium for the reactions follows thermodynamics and involve an entropy term and an enthalpy term. The formation of defects is always energetically unfavourable (i.e. endothermic) and it increases the entropy of the system. The formation reactions follow the chemical equilibrium equation and the equilibrium constant *K* depends on the temperature, as given by the Van 't Hoff equation. For example for the formation of Schottky defects the equilibrium constant K_S is given by:

$$K = \frac{[\mathrm{V}'_{\mathrm{Na}}] \cdot [\mathrm{V}_{\mathrm{Cl}}^{\bullet}]}{[\mathrm{Na}_{\mathrm{Na}}^{\times}] \cdot [\mathrm{Cl}_{\mathrm{Cl}}^{\times}]} = e^{-\Delta G/kT} \tag{2.9}$$

where ΔG is the Gibbs free energy for the formation of the defect. In a state of equilibrium, the concentration of any point defect increases exponentially with temperature:[12]

$$c_{\mathrm{D}} = Ae^{-\Delta H/kT} \tag{2.10}$$

The variable c_D represents the equilibrium fraction of defects, while A is a constant that equals $e^{\Delta S/k}$, where Δ*S* is the change in entropy upon defect formation. Equation (2.10) has a significant implication: at any temperature above 0 K, it is theoretically impossible to have a defect-free material. The high formation enthalpy of defects makes that equilibrium concentrations are low and often actual defect concentrations are determined by small

amounts of impurities, synthesis conditions and freezing in of non-equilibrium concentrations of defects upon cooling. Although defects play an important role in the luminescence properties of phosphors it is notoriously difficult to identify defects and the role and nature of defects in luminescent materials remains one of the great challenges in the field.

References

[1] F. A. Cotton, Chemical Applications of Group Theory, *John Wiley And Sons Inc, New York,* **1963**.

[2] Y. Tanabe, S. Sugano, *J. Phys. Soc. Japan* **1954**, *9*. 766

[3] T. H. Maiman, Nature **1960**, *187*, 493.

[4] H. F. Sijbom, R. Verstraete, J. J. Joos, D. Poelman, P. F. Smet, *Opt. Mater. Express* **2017**, *7*, 3332.

[5] B. Henderson, I. G. F., Optical Spectroscopy of Inorganic Solids, *Oxford University Press*, **1989**.

[6] C. W. Struck, W. H. Fonger, *J. Lumin.* **1975**, *10*, 1.

[7] T. Förster, *Ann. Phys.* **1948**, *437*, 55.

[8] D. L. Dexter, *J. Chem. Phys.* **1953**, *21*, 836.

[9] A. J. de Vries, M. F. Hazenkamp, G. Blasse, *J. Lumin.* **1988**, *42*, 275.

[10] J. P. M. van Vliet, D. van der Voort, G. Blasse, *J. Lumin.* **1989**, *42*, 305.

[11] A. J. Warren, C. B. Thomas, H. S. Reehal, P. R. C. Stevens, *J. Lumin.* **1983**, *28*, 147.

[12] A. R. West, Solid State Chemistry and Its Applications, *John Wiley & Sons, Ltd, New York,* **2014**.

Chapter 3

Thermal luminescence quenching in Mn^{2+} phosphors

Abstract

Narrower band red and green emission in phosphor converted white light LEDs (wLEDs) can improve the efficacy and color gamut in lighting and display applications. A promising luminescent ion is Mn^{2+} that can have both narrow band green (tetrahedral coordination) or red (octahedral coordination) emission. Unlike in earlier lighting applications of Mn^{2+} phosphors, temperature quenching is important in wLEDs. Until now insight in the thermal quenching behaviour of Mn^{2+} luminescence is lacking. Here we report systematic research for a variety of Mn^{2+}-doped phosphors and reveal a huge variation in the luminescence quenching temperature T_{50}, ranging from 50 K for Mn^{2+} in ZnTe to 1200 K in $MgAl_2O_4$. The value of T_{50} shows a positive correlation with the bandgap of the host but no correlation with the FWHM of the emission band, indicating that thermally activated photoionization and not thermal cross-over is the operative quenching mechanism. This is confirmed by thermally stimulated luminescence (TSL) measurements that show a clear rise in TSL signal following photo-excitation at temperatures around T_{50} providing evidence that quenching is correlated with generation of free charge carriers. Based on these findings a design rule is obtained that for temperature stable Mn^{2+} luminescence in (high power) LEDs a wide bandgap host material is required.

「ドーナツの穴を空白として捉えるか、あるいは存在として捉えるかはあくまで形而上的な問題であって、それでドーナツの味が少しなりとも変わるわけではないのだ。」

"Whether you take a doughnut hole as a blank space or as an entity unto itself is purely a metaphysical question and does not affect the taste of the doughnut one bit. "

Haruki Murakami

Introduction

Light emitting diodes (LED) have been a revolution in the lighting industry. Since the discovery of the blue (In,Ga)N chip, LED based technology is rapidly taking over the lighting industry. LED based lighting has a superior efficiency and lifespan compared to incandescent and fluorescent lighting. Most lighting applications rely on phosphor converted LED (pcLED). In pcLEDs a luminescent material (phosphor) is combined with a blue chip to convert part of the blue light to green, yellow and/or red light. The combination of the blue light with the phosphor converted light is perceived as white light. By varying the composition of the phosphor mix, any desired spectral distribution can be obtained to meet the needs of specific applications. For example, for indoor housing applications there is a demand for warmer white light, requiring a stronger red component. In spite of the wide range of available phosphor materials, there is a still need of better materials to convert blue light into narrow band red and green emission. Presently used red LED phosphors have a spectrum that extends into the deep red/NIR region where the eye sensitivity is lower thus reducing the lumen/W efficacy. Narrow band red phosphors can mitigate this problem. Narrow band green phosphors are especially advantageous for display applications to improve filter transmission efficiency and extend the colour gamut. In the last decade several new commercially interesting narrow band emitters have been discovered. For example β-SiAlON:Eu^{2+} emitting in the green around 535nm with a Full Width Half Maximum (FWHM) of 55 nm is suitable for display and lighting applications. Very popular for displays is the red narrow line emission around 630nm of $K_2SiF_6:Mn^{4+}$ (KSF) but it has issues for high power lighting (fast saturation and low stability). [1] For indoor lighting $Sr[LiAl_3N_4]: Eu^{2+}$ (SLA) is a good red component emitting at 650 with a FWHM of 50nm. [2]

A promising activator ion for narrow band red and green emission is Mn^{2+}. Mn^{2+} luminescence has been used extensively in the past in lighting and display applications. It has a tuneable emission wavelength ranging from green to the near infrared (500 to 700nm) depending on the type of ligand and coordination symmetry. Typically, Mn^{2+} emits in the green in tetrahedral coordination and in the red in octahedral coordination. Additional tuning is possible through covalency to redshift the emission to longer wavelengths for more covalent ligands/host lattices through the nephelauxetic effect. Early applications involve willemite $Zn_2SiO_4:Mn^{2+}$, a famous green emitting material named after the Dutch King William that has been applied in displays and fluorescent tubes. [3] The most widely used phosphor in early fluorescent tubes was the halophosphate $Ca_5(PO_4)_3X:Sb^{3+}$, Mn^{2+} (X=F,Cl) discovered in 1942 by McKeag et al. [4] It replaced the highly toxic $(Zn,Be)_2SiO_4:Mn^{2+}$ phosphor in white light fluorescent tubes and is still used in inexpensive fluorescent

tubes. By adjusting the Sb^{3+}: Mn^{2+} ratio the colour temperature could easily be adjusted by varying the contribution of blue Sb^{3+} and orange Mn^{2+} emission. ZnS:Mn^{2+} has been widely applied in electroluminescent displays. A more recent example of an efficient and narrow band green phosphor with Mn^{2+} is $BaMg_2Al_{16}O_{27}$: Eu^{2+}, Mn^{2+} that was used in fluorescent tubes.

In the various applications of Mn^{2+} emission the excitation involved high energy UV photons or fast electrons. For application in white light LEDs excitation in the near UV or blue spectral region is required. This poses a problem for Mn^{2+}. The d-d transitions in the visible and near-UV region for Mn^{2+} are both parity- and spin-forbidden, resulting in extremely low absorption coefficients for these transitions. A possible solution is sensitization with for example Eu^{2+} or Ce^{3+}, relying on energy transfer to Mn^{2+}. This requires close proximity of Mn^{2+} and the sensitizer ion. [5,6]

In addition to the sensitization issues, thermal quenching may pose a problem for Mn^{2+} phosphors in LED application where the temperature around the chip can reach up to 150 °C, which is higher than in earlier applications of Mn^{2+} phosphors mentioned above. At elevated temperatures phosphors show thermal quenching of the luminescence. Most commercially used phosphors in LEDs have Ce^{3+}, Eu^{2+} or Mn^{4+} incorporated. For these ions the luminescence quenching mechanism has been widely studied and is well-understood. The ^2E emission from Mn^{4+} quenches via thermal crossover via the $^4T_2$ excited state. [7] Ce^{3+} and Eu^{2+} often quench via thermally assisted photo ionization (PI). [7-9] Surprisingly, research on thermal quenching of Mn^{2+} has been very limited and the thermal quenching mechanism of Mn^{2+} emission has gained little attention and is therefore still poorly understood. For future applications of Mn^{2+} phosphors in wLEDs insight in the thermal quenching behaviour of Mn^{2+} is crucial. A few articles mention the thermal quenching and/or a quenching mechanism but lack systematic measurements to provide evidence for the suggested quenching mechanism. Both thermally activated photoionization [10] and thermal cross-over (TC) [11] have been suggested but no evidence for either mechanism is provided. In phosphors were Mn^{2+} emission is sensitized, for example by Ce^{3+} or Eu^{2+}, the quenching temperature of the sensitizer is important as well. If the sensitizer has a lower quenching temperature than Mn^{2+} the quenching of the sensitizer will be the dominant and determine thermal quenching behaviour of the Mn^{2+} phosphor.

The two possible quenching mechanisms for Mn^{2+} are thermal crossover and thermally assisted photo ionization and are depicted in Figure 3-1. For TC thermal excitation to a higher vibrational level in the excited state can induce cross-over to the ground state. For Mn^{2+} this involves a high vibrational level of the $^4T_1$ excited state which overlaps with a very high vibrational level of the $^6A_1$ ground state. The probability for cross-over scales with the overlap of the vibrational wavefunctions which increases as higher vibrational levels are thermally occupied (see Figure 3-1). Following cross-over, the system will relax non-radiatively down the ladder of vibrational energy

levels in the ground state. Thermally activated photo-ionization occurs when Mn^{2+} is in the $^4T_1$ excited state and thermal energy is sufficient to promote an electron from the excited state to the conduction band. The electron in the CB has increased mobility and will be trapped at an impurity or defect sites in the material that function as 'killer sites' that facilitate non-radiative emission. The mechanism of temperature quenching by thermally activated photoionization has been widely investigated and clearly established in Eu^{2+}- and Ce^{3+}-doped phosphors. [8,9] Still, the details on the quenching mechanism following ionization of the electron to the conduction band and the nature of the quenching centres remains unknown and identification of defects and impurities that play a role in luminescence quenching in phosphors remains one of the great challenges in the field.

In this paper we systematically investigate the thermal quenching of Mn^{2+} luminescence in a variety of host lattices. The luminescence properties are measured over a wide temperature range, up to temperatures as high as 1200K. We observe that the quenching temperatures of the Mn^{2+} emission vary strongly from 50K up to a record high 1190K. To determine the mechanism for thermal quenching, thermally stimulated luminescence (TSL) measurements were done for Mn^{2+} in a selection of host materials. It was concluded that the dominant quenching mechanism of the Mn^{2+} emission is thermally assisted photo ionization. Further research into the correlation of the quenching temperature with either the bandgap of the host (indicating PI) or the full width at half maximum (FWHM) of the emission band (indicating TC) shows a clear correlation with the bandgap but not the FWHM, which confirms that thermally activated photo ionization is the universal quenching mechanism for Mn^{2+} luminescence. This is consistent with the narrow bandwidth of Mn^{2+} emission reflecting a small off-set between ground- and excited state parabola which results in a high activation barrier for thermal cross-over.

Methods

Two classes of materials were synthesized via typical solids state synthesis methods (see SI Table S3-1 for specific synthesis conditions). In the first group of host lattices the Mn^{2+} ion occupies a well-defined tetrahedal site. In the second group Mn^{2+} occupies one or more (close to) octahedral sites. The first group contains: AlN, $Ba_2MgSi_2O_7$, $MgAl_2O_4$, $MgGa_2O_4$, Na_2MgGeO_4, $ZnAl_2O_4$, $ZnGa_2O_4$, Zn_2SiO_4 and Zn(S,Se) (wurtzite) and ZnS-zb (zincblende). The second group of Mn^{2+}-doped materials includes $Ba_3MgSi_2O_8$, $Ba_2Ca(BO_3)_2$, $Ba_2Mg(BO_3)_2$, $Ca_3MgSi_2O_8$, α-$Ca_3(PO_4)_2$, β-$Ca_3(PO_4)_2$, $CaSiO_3$-pwo (pseudo wollastostonite), $CaSiO_3$-wo (wollastonite), $LiScSi_2O_6$ and $Sr_3MgSi_2O_8$. To check phase purity of the synthesis products a Philips X-ray diffractometer was used. The *K*α radiation of Cu was used (λ= 1.5401 Å). The machine was operated at 40 kV and 20 mA current.

All spectroscopic measurements were done using an Edinburgh Instruments

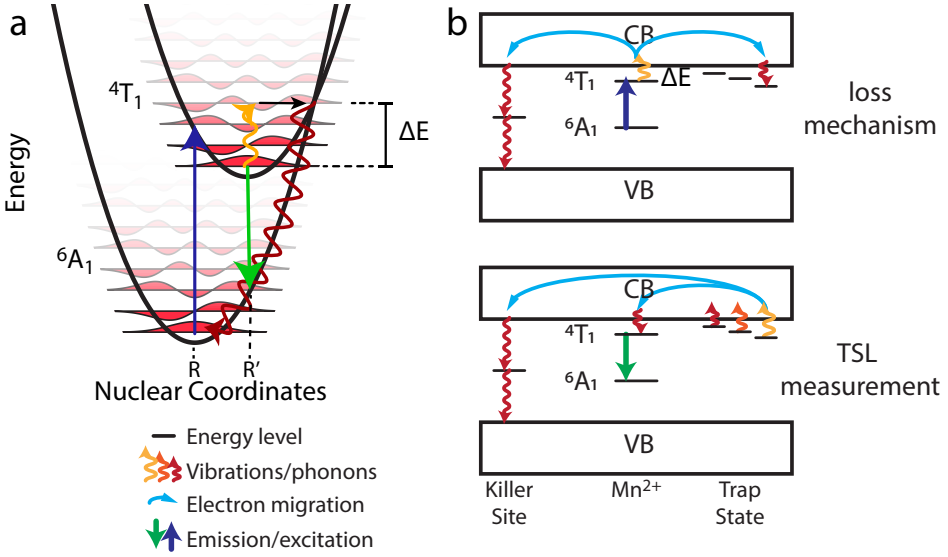

Figure 3-1. Potential quenching mechanisms for Mn^{2+} emission **a.** Diagram of thermal cross-over (TC). After Mn^{2+} is excited to the $^4T_1$ level at elevated temperatures higher vibrational levels are populated. Overlap with a very high vibrational level of the ground state allows cross-over followed by non-radiative relaxation to the zero-vibrational level of the ground state. **b.** Diagram of thermally assisted photo ionization (PI). Thermal excitation of an electron from the $^4T_1$ excited state to the conduction band results in luminescence quenching. Thermally stimulated luminescence (TSL) can be used as a probe for PI. In case of PI part of the thermally released electrons can be trapped, leaving behind Mn^{3+}. Heating the sample in the dark, causes trap states to thermally empty and part of the electrons will recombine with Mn^{3+} resulting in Mn^{2+} in the excited $^4T_1$ state and Mn^{2+} emission.

FLS 920 spectrofluorometer. As an excitation source a 450W Xenon lamp was used for recording excitation and emission spectra. Alternatively, for luminescence decay measurements, an Opetek Opolette HE355L tunable laser was used, with a variable repetition rate between 1 and 20Hz and ~10 ns pulse width. For PL and PLE and most decay curves measurements a R928 Hamamatsu PMT was used as a detector. For other decay curves a H74220 Hamamatsu PMT was used. For the time resolved measurements the signal of the detector was recorded with a Pico Quant Timeharp 260 card. For temperature dependent measurement as well as TSL measurements a Linkam THMS600 was used with a temperature range from -190 °C to 600 °C. Some materials were measured up to even higher temperatures with a Linkam TS1000, with a temperature limit of 1000 °C.

As discussed above, the process that is responsible for PI quenching can also fill traps giving rise to a TSL signal upon heating in the dark. If PI is the luminescence quenching mechanism, filling of traps should occur in the same temperature region where temperature quenching of the luminescence is observed. In Figure 3-2 the strategy to unravel the quenching mechanism

through TSL measurements is shown and is similar to the approach pioneered by Ueda and Tanabe for YAG:Ce. [9] Prior to the TSL experiment the sample is illuminated at variable temperatures. The wavelength of the illuminating light is chosen to be at long wavelengths, exciting Mn^{2+} into a low excited state to ensure that no direct escape from a high excited (charge transfer, CT) state can occur. Typically this means exciting with wavelengths longer than 420 nm. Excitation in a high energy CT state can give rise to direct escape to the conduction band, competing with relaxation to the emitting $^4T_1$ state resulting in ionization (and a TSL response) unrelated to thermal quenching. For excitation in a low energy $3d^5$ state well below the conduction band fast relaxation to the emitting state occurs. Now, the illumination temperature will determine the probability to be thermally excited from the $^4T_1$ state to the conduction band and a subsequent observation of TSL serves as a signature for PI luminescence quenching.

It is important that after illumination at elevated temperatures, the sample is cooled rapidly to limit detrapping. Once the sample is cooled the sample is gradually heated in the dark and the thermally stimulated Mn^{2+} emission is recorded. This TSL signal originates from the emptying of the traps. Thermally excited electrons in the CB can recombine with Mn^{3+} and give rise to the Mn^{2+} ions in the $^4T_1$ excited state and Mn^{2+} emission. The more traps that were initially filled during the illumination stage, the higher the TSL signal detected during the heating step will be. This allows probing of thermally activated photoionization at different illumination temperatures to check if there is a correlation between thermal quenching of the Mn^{2+} emission and photo ionization.

The samples were excited for 5 to 20 minutes (depending on the host material) with a wavelength corresponding to a d-d transition of the Mn^{2+} ion (no wavelengths shorter than 420 nm were used). The excitation was done while the sample was kept at various fixed temperatures. After the sample was excited at elevated temperature it was rapidly cooled down before the TSL measurement started. The samples were then heated in the dark (no illumination/excitation) and the Mn^{2+} luminescence was measured as a function of temperature.

Results and Discussion

To elucidate the temperature quenching mechanism of Mn^{2+} emission, a wide variety of host lattices was investigated to vary covalency, local coordination symmetry and bandgap. Temperature dependent properties of the Mn^{2+} luminescence were studied in AlN, $Ba_2MgSi_2O_7$, $Ba_3MgSi_2O_8$, $Ba_2Ca(BO_3)_2$, $Ba_2Mg(BO_3)_2$, $Ca_3MgSi_2O_8$, α-$Ca_3(PO_4)_2$, β-$Ca_3(PO_4)_2$, $CaSiO_3$-pwo (pseudo wollastostonite), $CaSiO_3$-wo (wollastonite), $LiScSi_2O_6$, $MgAl_2O_4$, $MgGa_2O_4$, $NaMgGeO_4$, $Sr_3MgSi_2O_8$, $ZnAl_2O_4$, $ZnGa_2O_4$, Zn_2SiO_4 Zn(S,Se) (wurtzite) and ZnS-zb (zincblende). For $ZnGa_2O_4$ and AlN doped with Mn^{2+} the luminescence properties

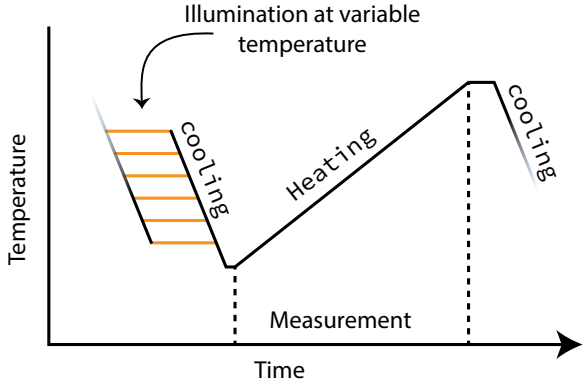

Figure 3-2. Schematic diagram of the temperature profile for the temperature dependent TSL measurements. The samples were illuminated at various temperatures for 5-20 minutes. After the lamp was turned off the sample were rapidly cooled and a thermally stimulated luminescence curve was recorded

will be discussed in more detail. The luminescence spectra and decay curves for Mn^{2+} in the other materials are shown in the SI.

The emission of Mn^{2+} in tetrahedral coordination in the oxide samples is in the green spectral region, around 510-520nm, and has a fairly narrow bandwidth with a FWHM of 0.1 to 0.2 eV. The emission of AlN:Mn^{2+} is around 600nm and for Zn(S,Se) around 580 nm. All these emission bands correspond to the $^4T_1 \rightarrow {}^6A_1$ transition. The shift in the emission wavelength is mainly caused by the stronger nephelauxetic effect of the more covalent anions (N^{3-}, S^{2-}) coordinating Mn^{2+} in the different host materials while also a higher crystal field splitting for N^{3-} ligands shifts the Mn^{2+} emission to longer wavelengths. The emission of Mn^{2+} in the octahedral coordination in the oxide samples is in the red/deep red spectral region ranging from 600-700nm The FWHM ranges from 0.3 to 0.6 eV. The shift in the emission wavelength with respect to the tetrahedal symmetry is due to the stronger crystal field strength of Mn^{2+} in octahedral cooridination.

$ZnGa_2O_4:Mn^{2+}$

To investigate the thermal quenching behavior of Mn^{2+}, the temperature dependent optical properties for Mn^{2+} in $ZnGa_2O_4$ were studied. The emission spectra of $ZnGa_2O_4:Mn^{2+}$, excited with 290nm light, are shown in Figure 3-3a. At low temperatures (around 100K) a sharp peak is observed at 500 nm with structured side bands on the longer wavelength side, showing sharp features around 502, 509 and 517nm. The 500 nm line is assigned to a zero-phonon line and the longer wavelength features to vibronic lines. The presence of individual vibronic lines at low temperature is often observed for Mn^{2+} and is typical for a luminescent ion with limited relaxation in the excited state (small Huang-Rhys factor S, indicating a small off-set between the ground-

and excited state equilibrium distance, R-R' in Figure 3-1) . [7,9] This small relaxation is directly related to the narrow bandwidth (small FWHM) that is typically observed for Mn^{2+} emission. As the temperature rises the vibronic peaks widen and merge into one broader band that continues to broaden with increasing temperature, as is typically observed for emission bands. The total emission intensity drops gradually with increasing temperature from 100 to 300K. Between 325 and 400 K the emission drops rapidly and at 500K the emission is at only 2% of the maximum intensity. The intensity of the emission is proportional to the quantum yield (ratio of radiative decay rate and total decay rate) and can be described by:

$$I(T) \propto \frac{P_{\mathrm{r}}(T)}{P_{\mathrm{r}}(T) + P_{\mathrm{nr}}(T)} \tag{3.1}$$

Here P_r and P_{nr} are the probability of radiative and non-radiative decay as a function of T. The thermal quanching temperature T_{50} is defined as the temperature at which $P_r = P_{nr}$ and thus the intensity is at 50% of its low temperature value . When we assume that P_r is constant as a function of temperature (which we will see below is not always the case) and that P_{nr} as a function of temperature can be aproximated by the Arrhenius equation we obtain:

$$I(T) = \frac{I_0}{1 + \frac{A}{P_{\mathrm{r}}} e^{-\Delta E/kT}} \tag{3.2}$$

Where ΔE is an activation barrier for non-radiative decay and A is a constant pre-factor. Measuring emission intensity as function of temperature to probe thermal quenching can show variations in intensity that are not related to thermal quenching, for example when the oscillator strength of the absorption transition is temperature dependent or when spectral broadening or shift of the absorption line reduces absorption at the excitation wavelength. This gives rise to intensity variations that are not related to thermal quenching. [7,11] In addition to fundamental problems also trivial aspects such as changes in alignment, collection efficiency or excitation source intensity can give rise to intensity variations. The decrease in intensity observed between 100 and 300 K for $ZnGa_2O_4:Mn^{2+}$ is probably related to these types of effects. A fast and reliable method to determine T_{50} is measuring the emission lifetime as a function of temperature. As non-radiative decay sets in, the emission lifetime shortens. To determine the lifetime the luminescence decay curves are fitted with a single exponential function. The observed emission decay time τ is dependent on the radiative rate P_r as well as the non-radiative rate P_{nr}:

$$\tau(T) = \frac{1}{P_{\mathrm{r}}(T) + P_{\mathrm{nr}}(T)} \tag{3.3}$$

Comparison of equations (3.3) and (3.1) reveals they have the same denominator (sum of radiative and non-radiative decay rate) which shows that I(T)

and $\tau(T)$ vary in the same way with temperature, if the radiative decay rate is temperature independent: $I(T) \propto \tau(T)$. When thermally activated non-radiative decay sets in, both the luminescence intensity and decay time decrease proportional to the quantum yield. For Mn^{2+} luminescence (and also other luminescent ions) often temperature dependent decay measurements give a more reliable determination of the quenching temperature as intensity fluctuations related to other causes (e.g. change in absorption strength, alignment) can affect intensity but not the luminescence decay.

To probe the thermal quenching temperature of the Mn^{2+} emission in $ZnGa_2O_4$ also temperature dependent life time measurements were done. Figure 3-3b shows the luminescence decay curves of the Mn^{2+} emission as a function of temperature, while excited with a 420nm laser, and monitored at 520nm. The decay curves are largely single exponential with a faster initial decay (~first ms). This faster decay is ascribed to emission from Mn^{2+} nearby a quenching center and energy tansfer to the quenching sites results in a faster decay. In the single exponential fitting procedures this faster initial decay is not considered and single exponential fits starting after 1 ms results in the temperature dependent decay times that are plotted in the inset of Figure 3-3b. Between 100 and 300 K the lifetime remains constant at 4ms and above 325 K it starts to drop, very similar to the temperature region where the fast drop in emission intensity is observed. Similar to the Arrhenius behavior of the emission intensity, the change of the lifetime as a function of temperature can be described by the following equation:

$$\tau(T) = \frac{\tau_r(T)}{1 + Ae^{-\Delta E/kT}} \qquad (3.4)$$

where $\tau_r(T)$is the raditiave life time at temperature T ($\tau_r(T) = 1/P_r(T)$). By fitting the measured lifetime to this equation it was possible to determine the T_{50} at 360 K for $ZnGa_2O_4$:Mn^{2+}, very similar to the 375 K determined from the temperature dependent intensity measurements.

The results discussed above show that the quenching temperature can be determined accurately and consistently but it does not give information on the quenching mechanism. For both quenching mechanisms (PI and TC) Arrhenius type behavior is expected. In the case of TC the energy barrier (ΔE) is often considered as the energy difference between the zero-vibrational state of the excited $^4T_1$ level and the cross-over point between the $^6A_1$ and $^4T_1$ parabolas. [12] For PI ΔE is the energy gap from the $^4T_1$ to the CB. [8] To distinguish between the two quenching mechanisms, PI or TC, TSL measurements can help. As outlined above, in this procedure TSL is measured following long wavelength excitation at various temperatures. In the case of $ZnGa_2O_4$:Mn^{2+} the sample was illuminated with 450nm for 5 minutes. The results for $ZnGa_2O_4$:Mn^{2+} are shown in Figure 3-3c. When a TSL signal is observed, this indicates that electrons have been released during photoexcitation of Mn^{2+} and are subsequently trapped. The TSL peaks at certain temperatures reflect the trap depth

for the trapped electrons where deeper traps give rise to a TSL peak with a maximum at higher temperatures. For $ZnGa_2O_4:Mn^{2+}$ the TSL curves show at least two distinct traps, one corresponding to the TSL peak around 320K and one around 500K. At even higher temperatures, above ~650K, the TSL curves show a rise which is caused by blackbody radiation. When comparing the TSL curves recorded after different charging temperatures it can be seen that the peak at 320K increases steadily until a charging temperature of 350/370K. This coincides with the temperature region where thermal quenching of the Mn^{2+} emission is observed. At even higher temperatures the TSL peak intensity declines but remains visible even at the highest charging temperatures. The peak at 500K shows a similar trend and rises starting at 320 K until a charging temperature of 450K after which it declines. The integrated intensities of the peaks at 350K and 500K are shown in Figure 3-3d as 'TSL trap1' and 'TSL trap2' respectively. The rise of both peaks is attributed to an increase of traps filled due to thermal ionization of the Mn^{2+}. At elevated temperature the detrapping rate starts to compete with the trapping rate and the signal drops, first for the shallower TSL trap1 and then for the deeper TSL trap2.

The two traps correspond to different defects in the structure. The peak at 300K is well known for persistence in $ZnGa_2O_4:Cr^{3+}$ but has also been observed for $ZnGa_2O_4:Ni^{2+}$. The peak here is caused by an antisite pair defect, Zn'_{Ga} and $Ga^{\bullet}_{Zn}$ capturing an electron and hole, forming $Zn^{\times}_{Ga}$ and $Ga^{\times}_{Zn}$. These electron and hole will be released around 300K. [13,14] The peak at 500K is not observed in $ZnGa_2O_4:Cr^{3+}$. [15] Our sample do not include Cr, but are doped with Mn instead. This would indicate that the trap at 500K is either induced or created by the incorporation of Mn.

Figure 3-3d shows a combined picture of the temperature dependent luminescence properties of $ZnGa_2O_4:Mn^{2+}$. In red the total emission, in green the luminescence lifetime and in dark and light blue the integrated signal for the two peaks in the TSL curves are shown as a function of illumination temperature. The total emission and TSL intensity were normalised to allow for better comparison with the lifetime. The coincidence between the temperature region where thermal quenching of the Mn^{2+} emission observed (drop in intensity, decrease luminescence life time) and the filling of traps provide evidence that thermally activated photoionization is responsible for the thermal quenching of the Mn^{2+} emission in $ZnGa_2O_4$.

AlN:Mn^{2+}, $Zn_2SiO_4:Mn^{2+}$ and $MgGa_2O_4:Mn^{2+}$

Next to $ZnGa_2O_4:Mn^{2+}$ temperature dependent emission, lifetime and TSL measurements were done for AlN:Mn^{2+}, $Zn_2SiO_4:Mn^{2+}$ and $MgGa_2O_4:Mn^{2+}$. The results for AlN:Mn^{2+} are shown in Figure 3-4 while for $Zn_2SiO_4:Mn^{2+}$ and $MgGa_2O_4:Mn^{2+}$ the experimental data can be found in the supporting information (Figure S3-13 and S3-17) and only the combined plots of temperature dependence of intensity, luminescence life time and TSL signal are shown. The temperature dependent emission of AlN:Mn^{2+} is shown in Figure 3-4a for

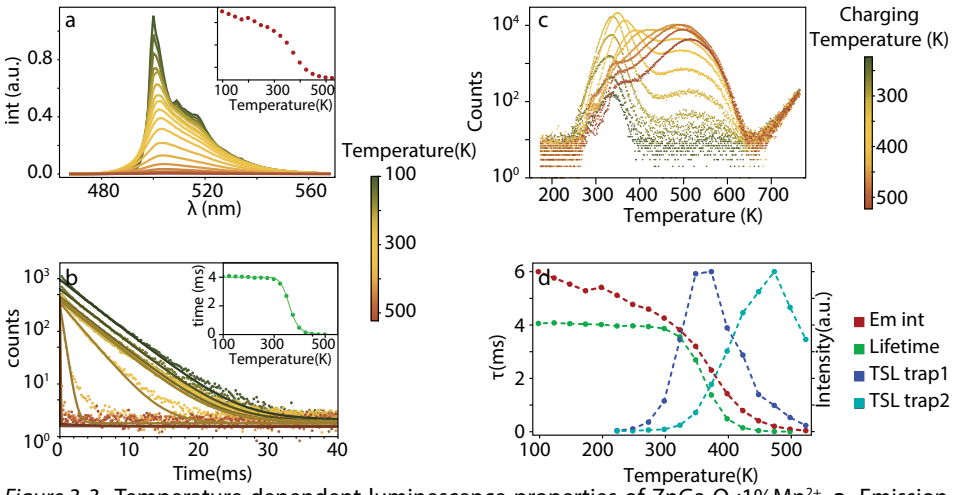

Figure 3-3. Temperature dependent luminescence properties of $ZnGa_2O_4$:1%Mn^{2+}. **a.** Emission spectra and intensity (inset) at various temperatures for excitation at 290nm. **b.** Luminescence decay curves and decay times (inset) at various temperatures for pulsed excitation at 450nm and observing the emission at 520nm. **c.** TSL curves after the sample was excited with 450nm for 5 minutes at different temperatures, followed by cooling to 300 K. The TSL was subsequently monitored. **d.** The three figures a-c are combined in a single graph to show the relation between the drop in emission lifetime, drop inemission intensity and increase of the TSL signal in the temperature range where the Mn^{2+} emission is quenched between 320 and 420 K.

a wide temperature range, from RT up to 1123K. The Mn^{2+} emission is centered around 610nm and slowly widens with increasing temperature. Around 700K a rapid drop in total emission intensity is observed. When the temperature reaches 1000K strong blackbody radiation appears in the spectrum at longer wavenlength. The temperature dependent luminescence decay curves for Mn^{2+} in AlN are shown in Figure 3-4c. The decay time remains constant at 1.2ms until ~700K and then rapidly drops. The T_{50} quenching temperatures as derived from the temperature dependence of the emission intensity and decay times are in good agreement, 852 and 824 K, respectively. In Figure 3-4b the TSL curves of the Mn^{2+} emission after 520 nm illumination at different temperatures are shown. All TSL curves show a broad TSL band between 400 and 700 K. No distinct peaks are visible which implies the existence of a wide variety of traps. The TSL intensity starts to increase for illumination temperatures above 600 K. The TSL curve continuously shifts to higher temperatures as the charging temperature is increased, consistent with a variety of traps with different trap depths. The shallower traps are thermally emptied during illumination at the higher temperatures. As a result, charging the traps at higher temperatures changes the distribution of filled traps towards deeper traps. This explains the decrease of the TSL signal on the low temperature side and shift of the maximum to higher temperatures where the deeper traps are emptied. Clear black body radiation is observed in the TSL curves. The black body background was subtracted to obtain the TSL signal as a function of illumination temperature. These results are plotted together

with the temperature dependent emission intensity and luminescence decay times in Figure 3-4d. Similar to the results for $ZnGa_2O_4:Mn^{2+}$ the rise in TSL signal coincides with the drop in emission intensity and decay time for the Mn^{2+} emission and provides evidence that thermally activated photo ionization is responsible for the thermal quenching of the Mn^{2+} emission in AlN:Mn^{2+}.

For $Zn_2SiO_4:Mn^{2+}$ and $MgGa_2O_4:Mn^{2+}$ the temperature dependent emission intensity and lifetime are shown in Figures 3-4 e and f, together with the TSL signal after varying illumination temperatures. Again, the emission intensities and luminescence lifetimes show a sharp drop at elevated temperatures that coincide with the onset for an increase in TSL signal at elevated illumination temperatures.

The results shown in the SI Figure S3-13 for $MgGa_2O_4:Mn^{2+}$ show that the emission intensity is dropping gradually while the lifetime is slowly declining between 300 and 700K, rather than the steeper drop observed for Mn^{2+} emission in AlN and $ZnGa_2O_4$. $MgGa_2O_4$ has a spinel structure but is characterized by substantial disorder, i.e. some Ga^{3+} occupying tetrahedral sites and some Mg^{2+} on octahedral sites. [16] This disorder causes a variation in local surrounding for Mn^{2+} ions as a result can give rise to variations of the energy gap from the $^4T_1$ level to the conduction band. This explains the more gradual change drop in emission intensity. The partial inversion can also explain the discrepancy between temperature dependence of the lifetime (green curve in Figure 3-4e) and the emission intensity (red curve). Ions that are quenched give less signal and the signal in the decay curves is thus dominated by emission from unquenched ions with longer emission life times. For an alternative comparison we summed the total counts of each life time measurements, divided by the intensity at t=0 to correct for changes in the alignment or fluctuation in the laser power. The temperature dependence of the intensity of the integrated intensity for the luminescence decay curves (light green curve in Figure 3-4e) now shows very good overlap with the emission intensity.

The temperature dependence of emission intensity, lifetime and TSL signal for $Zn_2SiO_4:Mn^{2+}$ are shown in Figure 3-4f. A clear coincidence of the onset temperature for the drop in intensity and lifetime and increase in TSL signal around 500 K is observed. In the temperature region where quenching occurs, the luminescence decay curves show some afterglow and this complicates the analysis of the decay curves and gives rise to an extra multi-exponential component in the decay curves (see SI Figure S3-17). This afterglow is ascribed to traps that are filled as a result of thermally activated photoionization at temperatures above 500 K, but there are also shallow traps that empty on a ms time scale above 500K. In general, it has to be realized that the TSL-based method described to identify PI as quenching mechanism relies on the presence of traps with a suitable trap depth: the traps should be deep enough to be stable at the illumination/charging temperature but not so deep that heating to high temperatures with (too) strong black body radiation is required or require such high temperatures that the re-ionization of Mn^{2+}

cannot compete with emission. The dominant traps in Zn_2SiO_4:Mn^{2+} are relatively shallow, similar to TSL trap 1 in $ZnGa_2O_4$:Mn^{2+}.

In addition to the extensive characterization for the four host lattices discussed above, temperature dependent emission as well as luminescence lifetime measurements were performed for variety of other Mn^{2+} doped materials. The results can be found in the supporting information (Figures S3-3 to S3-20). T_{50} values were determined for Mn^{2+} emission in $Ba_2MgSi_2O_7$, $MgAl_2O_4$, $NaMgGeO_4$, $ZnAl_2O_4$, ZnS (both zincblende and wurtzite), Zn(S,Se) solid solutions and ZnSe. In all these materials, Mn^{2+} typically occupies well defined tetrahedral sites. The T_{50} of Mn^{2+} in octahedral sites was also determined in $Ba_3MgSi_2O_8$, $Ba_2Ca(BO_3)_2$, $Ba_2Mg(BO_3)_2$, $Ca_3MgSi_2O_8$, α-$Ca_3(PO_4)_2$, β-$Ca_3(PO_4)_2$, $CaSiO_3$-pwo (pseudo wollastostonite), $CaSiO_3$-wo (wollastonite), $LiScSi_2O_6$ and $Sr_3MgSi_2O_8$. Here Mn^{2+} occupies one or more octahedral sites. For most materials the T_{50} could be determined by decay measurements.

As discussed above, the more reliable T_{50} values are obtained from temperature dependent lifetime measurements. Typically, the T_{50} can be found by determining at what temperature the lifetime of Mn^{2+} is half of the lifetime at low temperatures. This is however only correct if the radiative rate of Mn^{2+} is independent of temperature. This is not always the case, especially when Mn^{2+} is located in a highly symmetry environment (inversion symmetry) . [17] The parity selection rule is more strict for d-d transitions in inversion symmetry as a prominent mechanism to relax the parity selection rule is admixture of opposite parity states by odd-parity crystal field components. These are absent in inversion symmetry. Coupling with odd-parity (ungerade symmetry) vibrations serves now as a main mechanism to relax the selection rule as is evidenced by strong vibronic lines and a weak zero-phonon line in the emission spectrum. Thermal occupation of these vibrational modes enhances this mechanism and thus increases the radiative decay rate. The change in the lifetime due coupling to odd-parity phonons is described by: [7,17]

$$\tau_r(T) = \frac{\tau_r(0)}{\coth(h\nu/2kT)} \qquad (3.5)$$

Here 'hν' is the effective odd-parity vibration energy. For Mn^{2+} emission in host lattices with high symmetry coordination the emission life time is long and correction for the temperature dependence of the radiative life time is needed to find the correct T_{50}. This includes all host lattices where Mn^{2+} is in octahedral coordination. For some tetrahedral coordination hosts this correction was done as well, specifically: $MgAl_2O_4$ $ZnAl_2O_4$ and Zn_2SiO_4. In all these hosts the lifetime of the Mn^{2+} emission is longer than 10ms at room temperature indicating that the local symmetry is high and coupling with odd-parity vibrations can be expected to significantly contribute to the radiative life time.

To test the hypothesis of photo ionization as the dominant quenching mechanism, also TSL measurements were attempted for other Mn^{2+}-doped hosts,

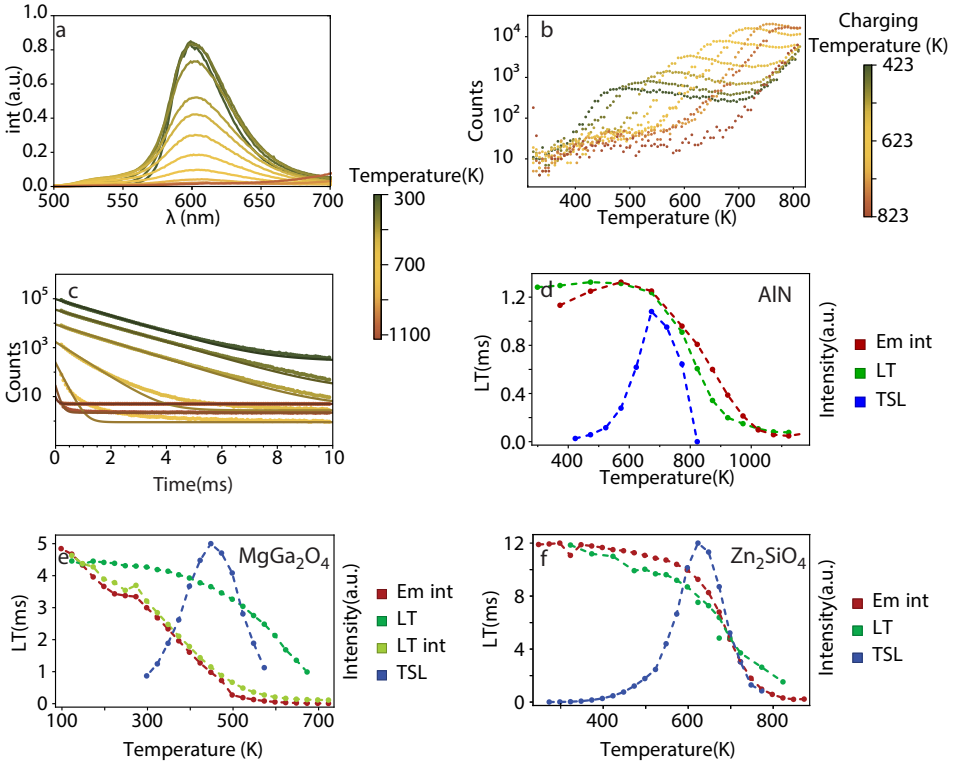

Figure 3-4. Temperature dependent luminescence properties of AlN:1%Mn^{2+}, $MgGa_2O_4$:1% Mn^{2+} and Zn_2SiO_4:1% Mn^{2+} **a.** Emission spectra at various temperatures for excitation at 300nm. **b.** TSL curves after the sample was excited at 520nm for 5 minutes at different temperatures. **c.** Luminescence decay curves at various temperatures after pulsed excitation at 515nm for emission at 630nm. **d.** The three figures a-c are combined in a single graph to show the relation between the drop in emission lifetime, emission intensity and increase of the TSL signal. **e.** and **f.** Temperature dependent luminescence properties of $MgGa_2O_4$:1% Mn^{2+} and Zn_2SiO_4:1% Mn^{2+} respectivly, showing the relation between the drop in emission lifetime, emission intensity and increase of the TSL signal and (see SI Figure S3-13), The light green curve shows the total counts during the lifetime measurements

viz. $Ba_2MgSi_2O_7$, Na_2MgGeO_4, $MgAl_2O_4$, $ZnAl_2O_4$, ZnS wz, ZnSe. No TSL signal was observed. For $MgAl_2O_4$ and $ZnAl_2O_4$ this is not surprising as the Mn^{2+} emission in these materials is stable up to extremely high temperatures (T_{50} of 1127 K and 1190K , respectively). This means that high temperatures will be necessary to thermally excite the electron from the $^4T_1$ state to the conduction band, deep and stable traps are needed to later verify the occurrence of photo ionization. Even if sufficiently deep traps exist, the temperature necessary to empty this trap will cause strong blackbody radiation that obscures a possible TSL signal. As discussed above, a more general requirement is the presence of traps with a trap depth that is high enough to limit detrapping during the illumination step and not so deep that the temperature necessary for ther-

mal release also cause immediate quenching of the Mn^{2+} emission. If no such trap exist in the material no TSL signal will be measured even when PI is the quenching mechanism.

For thermal ionization to occur the energy gap between the conduction band and the $^4T_1$ level of Mn^{2+} is crucial and determines the quenching temperature. It can be expected that this energy difference will be larger for wider bandgap materials. We therefore compared the T_{50} Mn^{2+} in different materials with the band gap. The materials that are investigated are insulators and have bandgap typically above 5 eV. Measurements in this range pose challenges for most absorption spectrometers. For AlN, $MgAl_2O_4$ and ZnS, ZnSe and ZnTe reliable values were found in Refs. [18–22] For solid solutions of wurtzite Zn(S,Se) the bandgap varies between and 2.7 and 3.6 eV. [23] ZnS zinc blende has a bandgap of 3.8eV. [27] ZnTe has a bandgap of 1.98eV.[22] For AlN there are multiple sources consistently mentioning a bandgap between 6 to 6.3 eV.[19] In $MgAl_2O_4$ the band gap was determined via synchrotron radiation to be 8.2 eV.[20] For most other materials a value for the bandgap was found in literature, but was based on absorption measurements. For the materials that lacked any source, the band gap was determined by the materials project. [24] The materials project uses DFT calculations to determine the band gap. Calculating the band gap by DFT often gives a large deviation from the real experimental band gap. The deviation between the calculated band gap and the measured band gap for AlN, $MgAl_2O_4$, ZnS, ZnSe and ZnTe were compared. For this series reliable experimental values for the bandgap have been reported and a clear trend is observed showing a factor of 1.6 difference between the experimental (actual) bandgap and the calculated bandgap (See SI Figure S3-22). For the materials that lack an experimentally determined band gap we multiplied the calculated band gap by 1.6 to have a better estimate of the actual band gap of the materials. The bandgaps of the host materials and the T_{50} values for the Mn^{2+} emission are collected in Tables 3-1, 3-2 and 3-3 and are plotted in Figure 3-5.

The results in Figure 3-5 show a clear trend that with increasing bandgap the luminescence quenching temperature of the Mn^{2+} increases. There is one outlier: Mn^{2+} in $Ba_2MgSi_2O_7$ where the T_{50} is lower compared to the other host materials with similar bandgaps. This may be due to an error in the bandgap as only the theoretical bandgap is known. Comparison between theoretical bandgaps and experimentally determined bandgaps shows that the theoretical estimate of bandgaps is not always accurate. Overall, the clear correlation between band gap and T_{50} quenching temperature confirms that PI is the dominant quenching mechanism for Mn^{2+} both in tetrahedral and octahedral coordination. It is important to realize that deviations from the expected correlation between bandgap and T_{50} can be expected as it is not only the absolute value of the bandgap, but also the position of the Mn^{2+} ground state in the gap (relative to the conduction band) that determines the activation barrier for photo ionization. This can explain also some deviations from the expected trend, for example for the fluorides where the low energy of the

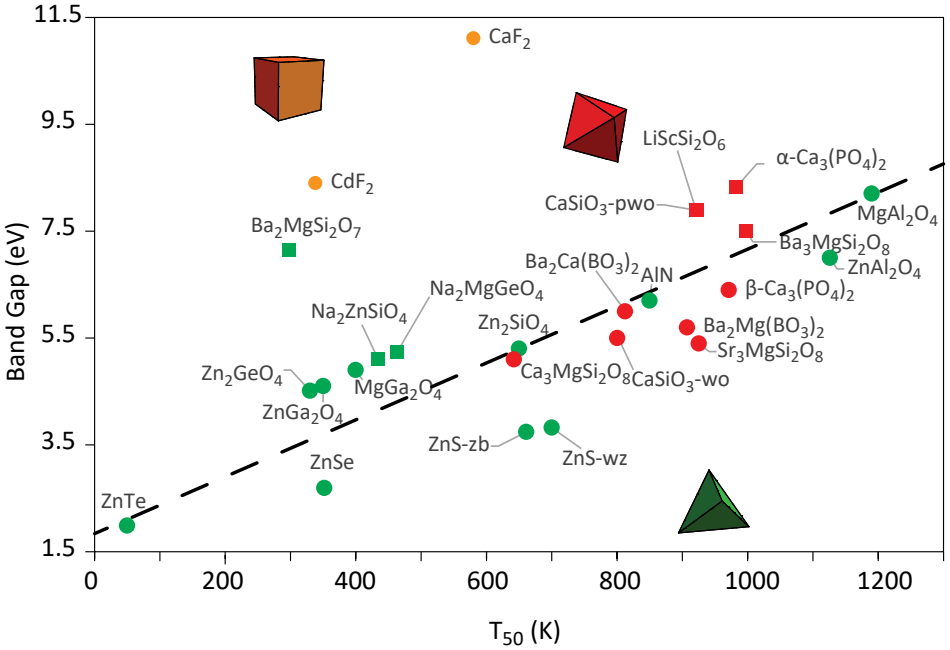

Figure 3-5. Luminescence quenching temperature of Mn^{2+} emission in various host lattices vs. the band gap of the host. The red data points are for Mn^{2+} in an octahedral site, green for Mn^{2+} in a tetrahedral site and orange in a cubic site. The dots indicate experimentally determined bandgaps, squares indicate theoretical bandgaps based on calculations by the materials project [24] (see also text), the dashed lines is added to indicate the trend.

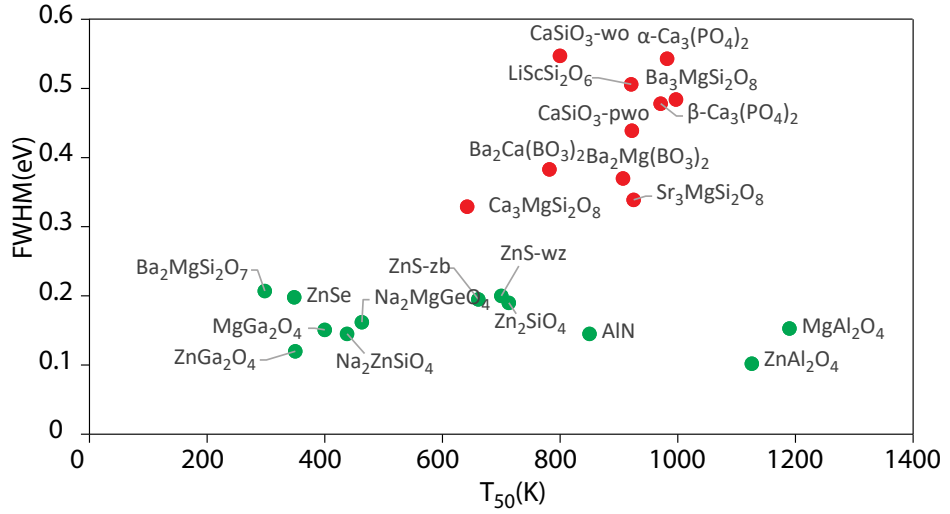

Figure 3-6. Luminescence quenching temperature of Mn^{2+} emission in various host lattices vs. the FWHM of the emission at 300 K of the Mn^{2+} emission in these hosts. Red data points are for Mn^{2+} in an octahedral site, green for Mn^{2+} in a tetrahedral site.

F(2p) valence band contributes to the large bandgap. Similarly, the higher T_{50} values than expected based on the bandgap for Mn^{2+} in ZnS, ZnSe and ZnTe may be explained by a higher energy position of the valence band. For the two modifications of ZnS and the solid solutions Zn(S,Se) a clear correlation is found between bandgap and T_{50} (see SI Figures S3-18 to S3-21 and Table S3-2).

Despite some deviations, the results in Figure 3-5 clearly show a consistent trend of increasing T_{50} for higher bandgaps for oxides, fluorides and chalcogenides. For the smaller bandgap oxides (gallates and germanates) this leads to undesired quenching at the operating temperature of high power LEDs of around 150 °C but in most oxides the quenching temperature is sufficiently high for application in wLEDs. If for specific applications higher thermal stability of the luminescence is required, wider bandgap oxides are needed.

It is also interesting to relate the width of the Mn^{2+} emission bands to the luminescence quenching temperatures. For the thermal crossover mechanism a clear correlation is expected. A larger offset between ground and excited state parabola will give rise to a broader emission band and a lower luminescence quenching temperature. For decades this has been the standard model to explain trends in luminescence quenching temperatures. Limiting expansion (or contraction) in the excited state relative to the ground state in stiff lattices and well-designed coordination was used to raise luminescence quenching temperatures. Only when this model failed to explain low quenching temperatures of e.g. Eu^{2+} or Ce^{3+} emission in host lattices where the emission band width was narrow, the alternative model of photo ionization was found to provide an alternative and frequently occurring quenching mechanism.[8,9,37] To investigate the role of TC quenching, in Figure 3-6 the FWHM at RT for the Mn^{2+} emission is plotted vs. the T_{50} values. The results show no correlation. This provides further evidence that thermally activated photo ionization is the dominant thermal quenching mechanism for Mn^{2+} emission and not TC quenching. The FWHM and Stokes shift of emission bands are both determined by the offset of ground and excited state parabolas.[8-10] A larger FWHM and Stokes shift is expected with increasing offset of the ($^4T_1$) excited state parabola with respect to the ($^6A_1$) ground state parabola. A larger offset leads to a lower activation barrier ΔE (see Fig. 1) and thus a lower quenching temperature. Clearly, no correlation between FWHM and quenching temperature is observed for an extremely wide range of T_{50} values (300-1200 K). This confirms that the dominant quenching mechanism is not thermally activated cross-over from the excited state to the ground state. Based on the narrow bandwidth of Mn^{2+} emission this is not unexpected. A narrow bandwidth is indicative of a small relaxation in the excited and a correspondingly high TC quenching temperature. It cannot be excluded that the mechanism for thermal quenching for Mn^{2+} in the two aluminates with T_{50} values above 1000 K is TC although the higher T_{50} (1191 K) is observed for Mn^{2+} emission in the host where the Mn^{2+} emission band has a broader FWHM at 300 K ($MgAl_2O_4$). Three host of the octahedrally coordinated Mn can emit from multiple sites (α -$Ca_3(PO_4)_2$, β-$Ca_3(PO_4)_2$ and $CaSiO_3$ –wo). This will increase the measured

Table 3-1. The quenching temperature of Mn^{2+} in tetrahedral coordination in various host materials together with the bandgap (experimentally observed or calculated) and the full width half maximum of Mn^{2+} emission in these hosts. For the theoretical bandgap the bandgap was taken as determined by DFT calculations by the materials project (values shown in the parentheses) and this was multiplied by 1.6 (see also text).

Material	Experimental Bandgap (eV)	Theoretical Bandgap (eV)	T_{50}(K)	FWHM at 298K (eV)
$MgAl_2O_4$	8.2 [20]	8.2 (5.12)	1191	0.153
$ZnAl_2O_4$	7.0 [25]	6.16 (3.85)	1126	0.102
AlN	6.12 [19]	6.49 (4.05)	824	0.145
Zn_2SiO_4	5.3 [26]	4.41 (2.76)	729	0.190
ZnS-wz	3.82 [27]	3.32 (2.08)	700	0.200
ZnS-zb	3.74 [27]	3.76(2.35)	661	0.195
Na_2MgGeO_4	-	5.23(3.27)	463	0.162
Na_2ZnSiO_4	-	5.11(3.19)	434	0.145
$MgGa_2O_4$	4.9 [28]	3.9(2.44)	400	0.151
ZnSe	2.69 [21]	2.58(1.61)	352	0.198
$ZnGa_2O_4$	4.6 [29]	3.73 (2.33)	360	0.120
Zn_2GeO_4	4.51[30]	3.16(1.97)	330 [30]	0.210
$Ba_2MgSi_2O_7$	-	7.15 (4.47)	298 [5]	0.207
ZnTe	1.98 [22]	1.73(1.08)	50 [31]	-

FWHM of the emission of these compounds and therefore for octahedrally coordinated Mn^{2+} TC cannot yet be fully excluded.

Note that the emission FWHM for Mn^{2+} in octahedral coordination is consistently larger than for Mn^{2+} in tetrahedral coordination. The larger FWHM for Mn^{2+} emission in octahedral symmetry can be explained by the steeper slope of the $^4T_1$ excited state line in the $3d^5$ Tanabe Sugano diagram at stronger crystal fields. The much smaller crystal field splitting in tetrahedral coordination compared to octahedral or cubic coordination ($\mathbf{\Delta}_T=-4/9\Delta_O$; $\Delta_C= -8/9\Delta_O$) indicates that tetrahedral Mn^{2+} is in the region where $\mathbf{\Delta}/B$ is smaller than 10 where the $^4T_1$ slope is reduced in comparison to the constant and steep slope in the region with $\mathbf{\Delta}/B>15$.

Table 3-2. The quenching temperature of Mn^{2+} in octahedral coordination in various host materials together with the bandgap (experimentally observed or calculated) and the full width half maximum of Mn^{2+} emission in these hosts. For the theoretical bandgap the bandgap was taken as determined by DFT calculations by the materials project (values shown in the parentheses) and this was multiplied by 1.6 (see also text).* emission from multiple different Mn^{2+} sites is possible.

Material	Experimental Bandgap (eV)	Theoretical Bandgap (eV)	T_{50}(K)	FWHM at 298K (eV)
$Ba_3MgSi_2O_8$	-	7.51 (4.69)	997	0.484
α -$Ca_3(PO_4)_2$	-	8.32 (5.20)	982	0.543*
β -$Ca_3(PO_4)_2$	6.4 [32]	8.77 (5.48)	971	0.478*
Sr_3MgSiO_8	5.4 [33]	7.5 (4.69)	925	0.339
$CaSiO_3$ -pwo	-	7.89 (4.93)	922	0.439*
$LiScSi_2O_6$	-	7.89 (4.93)	921	0.506
$Ba_2Mg(BO_3)_2$	5.7 [34]	7.26 (4.54)	907	0.370
$CaSiO_3$ -wo	5.5 [35]	7.57 (4.73)	800	0.547*
$Ba_2Ca(BO_3)_2$	6.0 [34]	6.53 (4.08)	782	0.383
$Ca_3MgSi_2O_8$	5.1 [36]	6.12 (3.82)	642	0.329

Table 3-3. Quenching temperature of Mn^{2+} emission for cubic 8-coordination in two fluorides together with the bandgap (experimentally observed and calculated) and the full width half maximum of Mn^{2+} emission. For the theoretical bandgap the bandgap was taken as determined by DFT calculations by the materials project (values shown in the parentheses) and this was multiplied by 1.6 (see also text).

Material	Experimental Bandgap (eV)	Theoretical Bandgap (eV)	T_{50}(K)
CaF_2	11.1 [37]	11.6(7.25)	580 [38]
CdF_2	8.4 [39]	4.91(3.07)	338 [38]

Conclusion

The temperature dependent luminescence properties of Mn^{2+} have been studied in over 20 host lattices to gain insight in the thermal quenching behaviour and mechanism. A huge variation in T_{50} quenching temperatures is observed, from quenching around room temperature ($Ba_2MgSi_2O_7$:Mn^{2+}) or even below room temperature (ZnSe:Mn^{2+}, ZnTe:Mn^{2+}) to record high quenching temperatures around 1200 K ($MgAl_2O_4$:Mn^{2+}). Temperature dependent emission intensity and lifetime measurements have been related to thermally stimulated luminescence signals after illumination at different temperatures. In four

different hosts the onset temperature for the drop in Mn^{2+} emission intensity and emission life time coincides with illumination temperature at which an onset of TSL signal is recorded. This provides strong evidence for thermally activated photo ionization as the dominant quenching mechanism. A clear relation between bandgap of the host materials and the T_{50} quenching temperature confirms that photoionization is responsible for thermal quenching of Mn^{2+} emission. No correlation was found between the emission bandwidth (FWHM) and T_{50}, where a lower T_{50} would be expected for larger bandwidths if the alternative quenching mechanism (thermal cross-over from the excited $^4T_1$ to the $^6A_1$ ground state) would be operative. Based on these observations we conclude that luminescence quenching in Mn^{2+}-doped phosphors occurs by thermally activated photoionization and that the thermal quenching behaviour can be optimized by choosing wide bandgap hosts. Still, for most host lattices the thermal quenching temperatures are sufficiently high to prevent thermal quenching in (high power) white LED applications while for specialty applications requiring extremely high thermal quenching can be realized well over 1000 K.

References

[1] M. A. van de Haar, M. Tachikirt, A. C. Berends, M. R. Krames, A. Meijerink, F. T. Rabouw, *ACS Photonics* **2021,** *8*, 1784.

[2] L. Gan, Z. Y. Mao, X. H. Zeng, Y. Q. Zhang, Y. Zhao, F. F. Xu, Y. C. Zhu, X. J. Liu, *Mater. Res. Bull.* **2014**, *51*, 205.

[3] Willemite, https://www.mindat.org/min-4292.html, accessed: **Aug., 2022**.

[4] W. M. Yen, S. Shionoya, H. Yamamoto, Phosphor Handbook, *CRC Press*, **2018**.

[5] A. D. Sontakke, A. J. van Bunningen, F. T. Rabouw, S. Meijers, A. Meijerink, *J. Phys. Chem. C* **2020**, *124*, 13902.

[6] A. D. Sontakke, A. J. van Bunningen, S. Wakui, A. Meijerink, *Mater. Adv*. **2021**, *2*, 2075.

[7] T. Senden, R. J. A. van Dijk-Moes, A. Meijerink, *Light Sci. Appl*. **2018**, *7*, 2047.

[8] P. Dorenbos, *J. Phys. Condens. Matter* **2005**, *17*, 8103.

[9] J. Ueda, P. Dorenbos, A. J. J. Bos, A. Meijerink, S. Tanabe, *J. Phys. Chem. C* **2015**, *119*, 25003.

[10] S. H. M. Poort, D. Cetin, A. Meijerink, G. Blasse, *J. Electrochem. Soc*. **1997**, 144, 2179.

[11] D. Böhnisch, J. Rosenboom, A. García-Fuente, W. Urland, T. Jüstel, F. Baur, *J. Mater. Chem. C* **2019**, *7*, 6012.

[12] C. W. Struck, W. H. Fonger, *J. Lumin*. **1975**, *10*, 1.

[13] D. Gourier, A. Bessière, S. K. Sharma, L. Binet, B. Viana, N. Basavaraju, K. R. Priolkar, *J. Phys. Chem. Solids,* **2014**, *75*, 826.

[14] V. Castaing, L. Giordano, C. Richard, D. Gourier, M. Allix, B. Viana, *J. Phys. Chem. C,* **2021**, *125*, 10110.

[15] S. K. Sharma, A. Bessière, N. Basavaraju, K. R. Priolkar, L. Binet, B. Viana, D. Gourier, *J. Lumin*. **2014**, *155*, 251.

[16] T. Ito, A. Yoshiasa, T. Yamanaka, A. Nakatsuka, H. Maekawa, *Zeitschrift fur Anorg. und Allg. Chemie* **2000**, *626*, 42.

[17] A. J. van Bunningen, A. D. Sontakke, S. Wakui, A. Meijerink, *Opt. Mater.*. **2022**, *128*, 112433.

[18] O. Brafman, I. T. Steinberger, *Phys. Rev.* **1966**, ***143***, 501.

[19] M. E. Levinshtein, S. L. Rumyantsev, M. S. Shur, Properties of Advanced Semiconductor Materials GaN, AlN, InN, BN, SiC, SiGe, *John Wiley And Sons,* **2001**.

[20] E. Feldbach, I. Kudryavtseva, K. Mizohata, G. Prieditis, J. Räisänen, E. Shablonin, A.

Lushchik, *Opt. Mater.* **2019**, *96*, 109308.
[21] S. Adachi, T. Taguchi, *Phys. Rev. B* **1991**, *43*, 9569.
[22] R. E. Dietz, D. G. Thomas, J. J. Hopfield, *Phys. Rev. Lett.* **1962**, *8*, 391.
[23] M. A. Avilés, J. M. Córdoba, M. J. Sayagués, F. J. Gotor, *Inorg. Chem.* **2019**, *58*, 2565.
[24] A. Jain, S. P. Ong, G. Hautier, W. Chen, W. D. Richards, S. Dacek, S. Cholia, D. Gunter, D. Skinner, G. Ceder, K. A. Persson, *APL Mater.* **2013**, *1*, 011002.
[25] R. E. Rojas-Hernandez, F. Rubio-Marcos, I. Romet, A. del Campo, G. Gorni, I. Hussainova, J. F. Fernandez, V. Nagirnyi, *Inorg. Chem.* ***2022***, *61*, 11886.
[26] H. Amekura, K. Kono, N. Kishimoto, C. Buchal, *Nucl. Instr. and Meth. in Phys. Res. B* **2006**,*242*, 96
[27] O. Brafman, I. T. Steinberger, *Phys. Rev.* **1966**, *143*, 501.
[28] Z. Galazka, D. Klimm, K. Irmscher, R. Uecker, M. Pietsch, R. Bertram, M. Naumann, M. Albrecht, A. Kwasniewski, R. Schewski, M. Bickermann, *Phys. status solidi* **2015**, *212*, 1455.
[29] Z. Galazka, S. Ganschow, R. Schewski, K. Irmscher, D. Klimm, A. Kwasniewski, M. Pietsch, A. Fiedler, I. Schulze-Jonack, M. Albrecht, T. Schröder, M. Bickermann, *APL Mater.* **2019**, *7*, 022512.
[30] F. Chi, X. Wei, B. Jiang, Y. Chen, C. Duan, M. Yin, *Dalt. Trans.* **2018**, *47*, 1303.
[31] L. v. Khoi, *J. Supercond.* **2003**, *16*, 427.
[32] E. Feldbach, M. Kirm, A. Kotlov, H. Mägi, n.d.,
[33] P. Dewangan, D. P. Bisen, N. Brahme, R. K. Tamrakar, S. Sharma, K. Upadhyay, *Opt. Quantum Electron.* **2018**, *50*, 1.
[34] S. Jayakiruba, S. S. Chandrasekaran, P. Murugan, N. Lakshminarasimhan, *Phys. Chem. Chem. Phys.* **2017**, *19*, 17383.
[35] H. Nagabhushana, B. M. Nagabhushana, M. Madesh Kumar, Chikkahanumantharayappa, K. V. R. Murthy, C. Shivakumara, R. P. S. Chakradhar, *Spectrochim. Acta Part A Mol. Biomol. Spectrosc.* **2011**, *78*, 64.
[36] V. Singh, G. Lakshminarayana, A. Wagh, N. Singh, *Optik (Stuttg).* **2020**, *206*, 164240.
[37] T. Tomiki, T. Miyata, *J. Phys. Soc. Japan* **1969**, *27*, 658.
[38] P. J. Alonso, R. Alcalá, ***J. Lumin.*** **1981**, *22*, 321.
[39] C. Raisin, J. M. Berger, S. Robin-Kandare, *J. Phys. C Solid State Phys.* **1980**, *13*, 1835.

QR-Codes

Link to paper

Supporting Information

Supplementary information

Synthesis Methods

Synthesis methods: all samples were synthesized with a solid state synthesis. The samples were annealed in tube oven in a 10/90 H_2/N_2 atmosphere. Except for the Zn containing compounds which were made in a N_2 atmosphere. The samples contained 0.5 to 7% Mn respective to their host ion.

Table S3-1. Synthesis conditions for the different samples

compound	Max T (°C)	total dwell time (hour)	regrinds	Extra step
AlN	1650	5		
$Ba_2Ca(BO_3)_2$	900	5		
$Ba_2Mg(BO_3)_2$	1100	8		pre annealing 1 hour at 800°C
$Ba_3MgSi_2O_8$	1125	5		
α $Ca_3(PO4)_2$	1400	8		precursors were made by precipitation*
β $Ca_3(PO_4)_2$	1250	4		precursors were made by precipitation*
$Ca_3MgSi_2O_8$	1200	5		pre annealing 1 hour at 800°C
$CaSiO_3$pw	1300	10		
$CaSiO_3$wo	1100†	96	3	
$LiScSi_2O_6$	1200	12		
$MgAl_2O_4$	1400	16	1	
$MgGa_2O_4$	1200	8		
$Sr_3MgSi_2O_8$	1200	5		pre annealing 1 hour at 800°C
Zn_2SiO_4	1250	5		
$ZnAl_2O_4$	1400	16		second reduction step 12 h at 850°C 10% H_2
$ZnGa_2O_4$	1200	8		second reduction step 12 h at 850°C 10% H_2

compound	Max T (°C)	total dwell time (hour)
ZnSe	800	12
ZnS wurtzite	1200	4
ZnS zinc blende	800 ‡	12

*Sol gel precursors for the phosphate were made by dissolving nitrate salts of the cation in water. This solution was added to a ammonium dihydrate solution. Precipitation is visible. 25% Ammonia was added to keep the pH value over 10. This emulsion was stirred for 30 minutes. After this the precipitate was filtered.

†Above 1125°C $CaSiO_3$ has a phase transition from wollastonite to pseudo wollastonite therefore to synthesize the wollastonite phase the synthesis was done at 1100°C.

‡ ZnS has a phase transition from zinc blende to wurtzite around 1020 °C[1] , therefore to maintain the zinc blende structure the sample was annealed at 800°C to prevent any phase transition.

XRD patterns

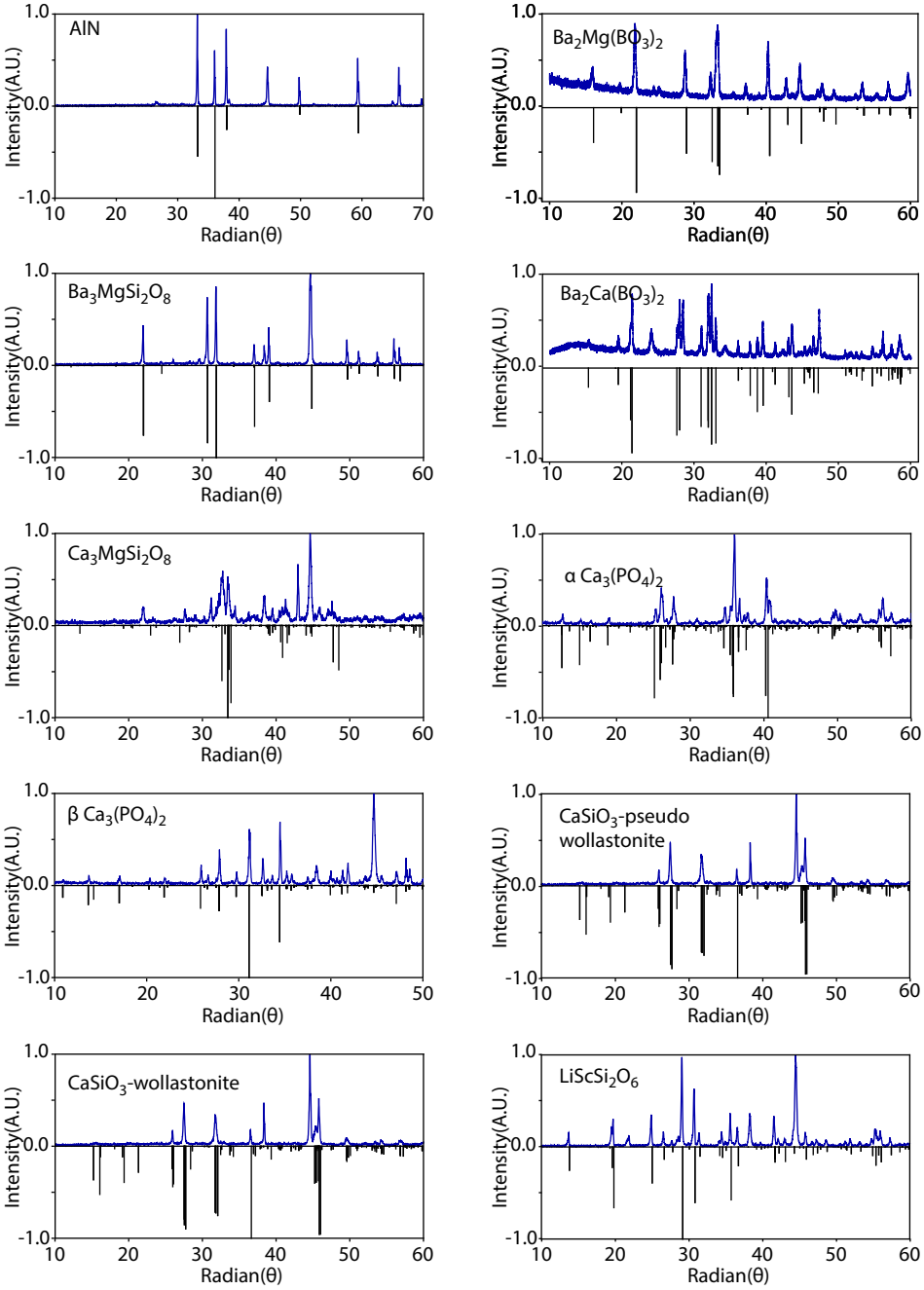

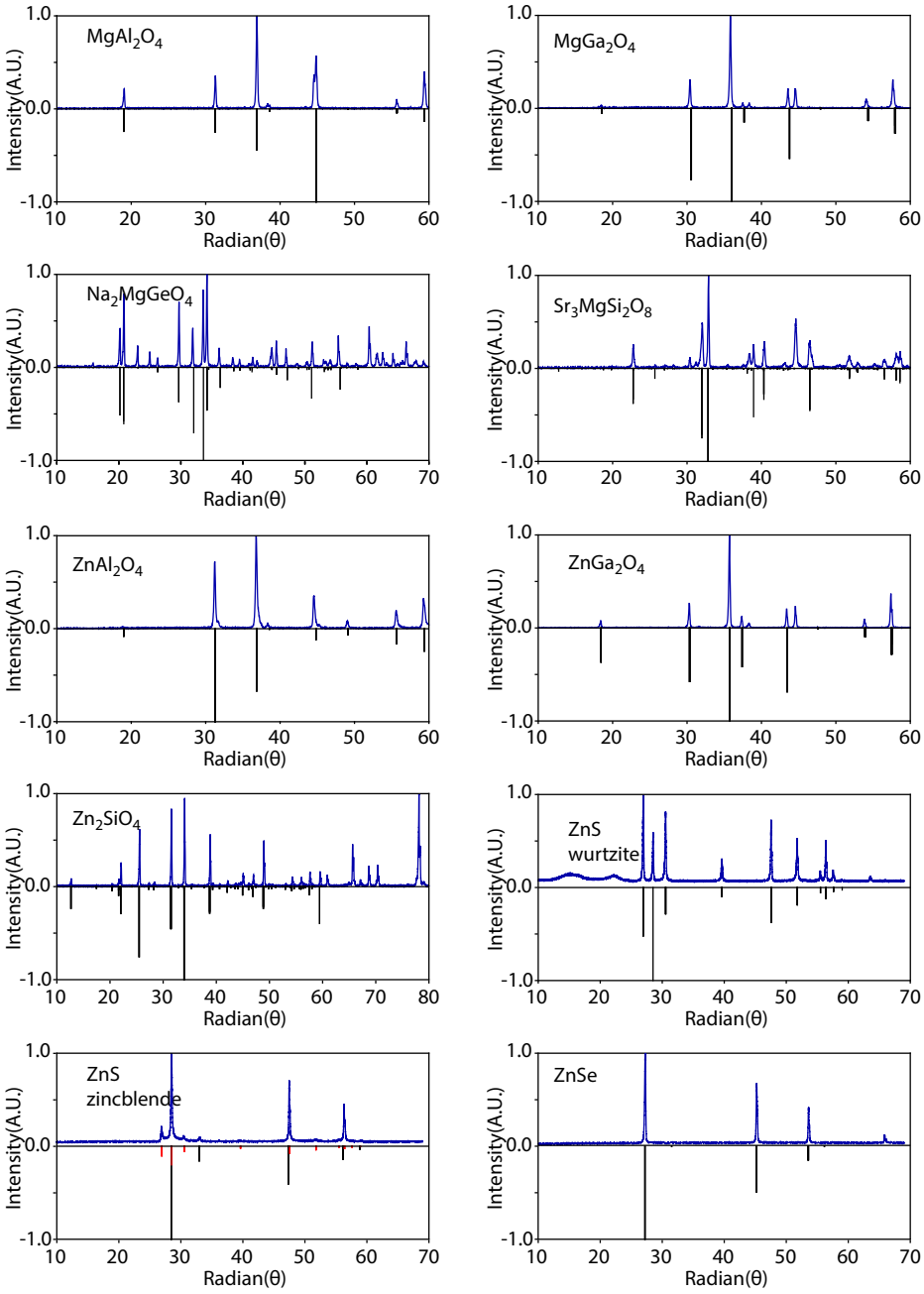

Figure S 3-1. XRD Diffractograms of synthesized compounds in blue. In black the respective reference is shown underneath. Peaks visible at 38 and 45 ^{0} are caused by the aluminium sample holder. For ZnS –zincblende some ZnS wurtzite structure was present as indicated in red

PL and PLE

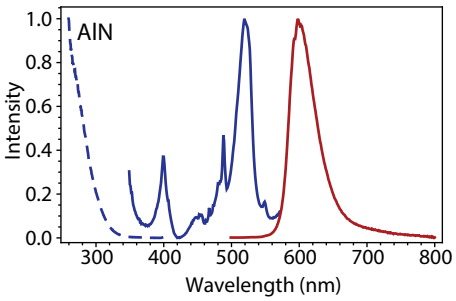
AlN
Intensity
Wavelength (nm)

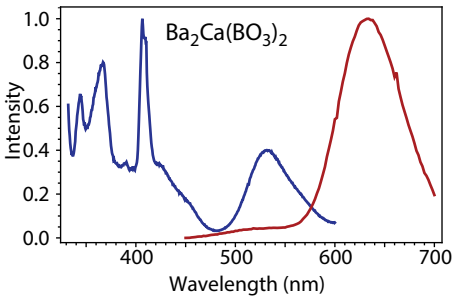
$Ba_2Ca(BO_3)_2$
Intensity
Wavelength (nm)

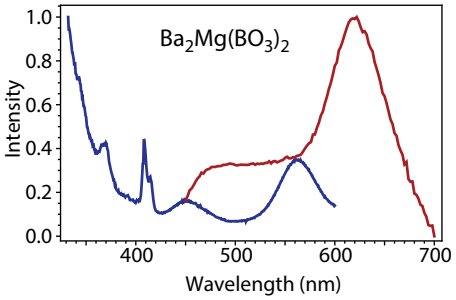
$Ba_2Mg(BO_3)_2$
Intensity
Wavelength (nm)

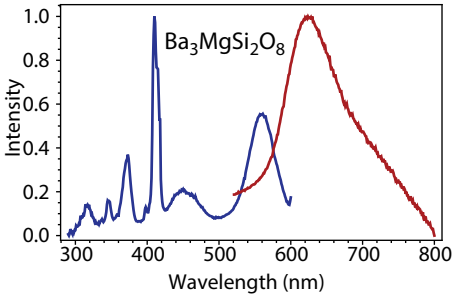
$Ba_3MgSi_2O_8$
Intensity
Wavelength (nm)

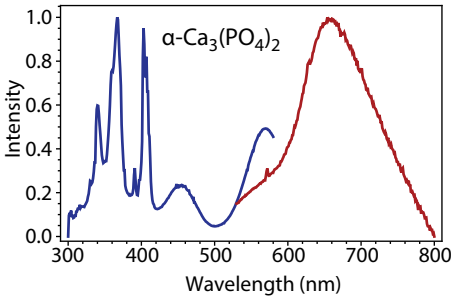
α-$Ca_3(PO_4)_2$
Intensity
Wavelength (nm)

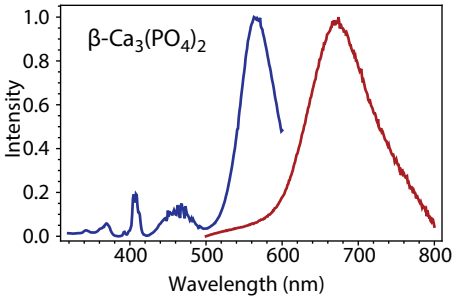
β-$Ca_3(PO_4)_2$
Intensity
Wavelength (nm)

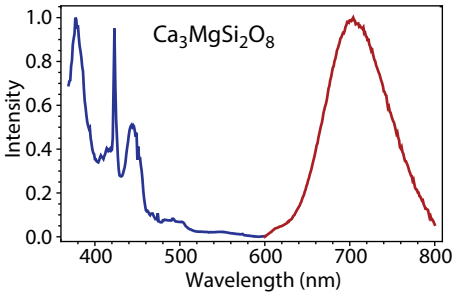
$Ca_3MgSi_2O_8$
Intensity
Wavelength (nm)

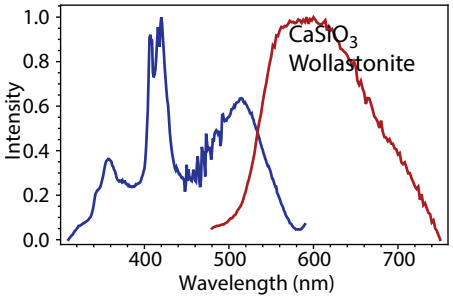
$CaSiO_3$
Wollastonite
Intensity
Wavelength (nm)

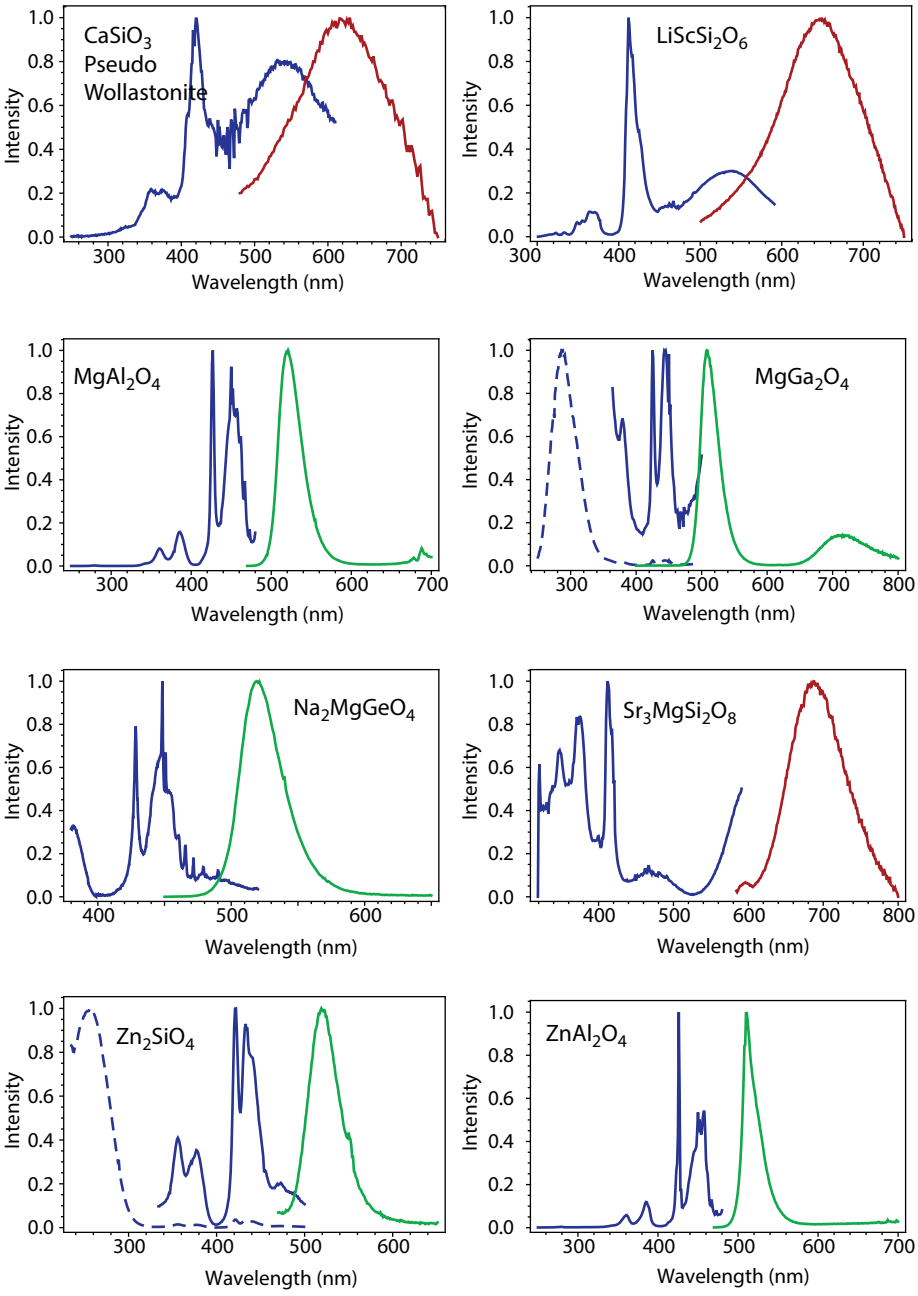
CaSiO3
Pseudo
Wollastonite
LiScSi2O6
MgAl2O4
MgGa2O4
Na2MgGeO4
Sr3MgSi2O8
Zn2SiO4
ZnAl2O4
Intensity
Wavelength (nm)

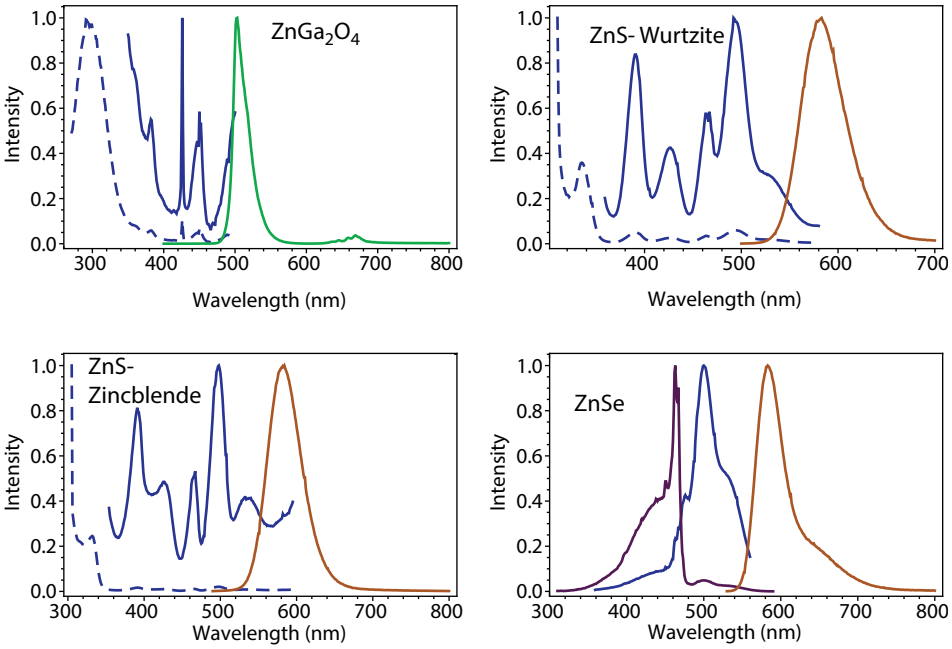

Figure S3-2. PL and PLE spectra of Mn^{2+} in different host materials. PLE in blue and PL in the respective emission colour. The dotted PLE is scaled down. In ZnSe two PLE are shown, one for the emission at 600nm (blue) and one for the emission at 650nm (purple)

Temperature dependent luminescent properties

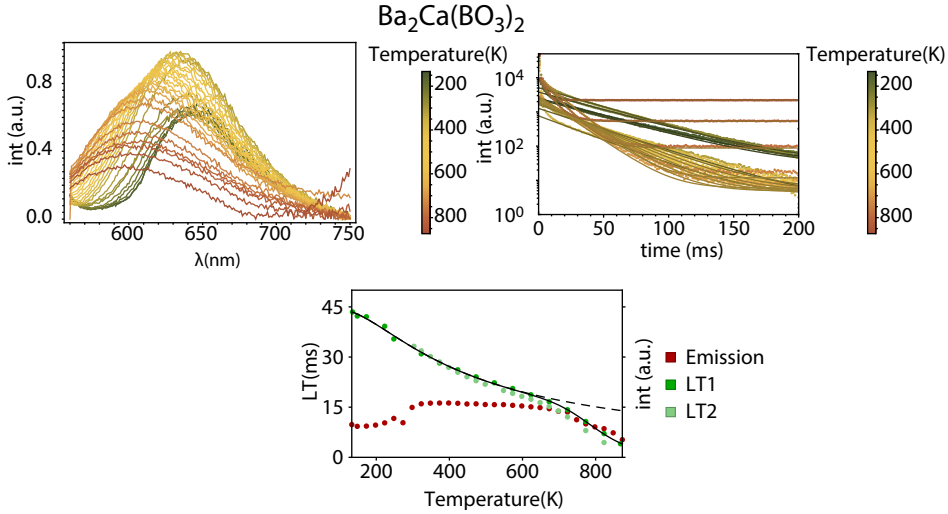

Figure S3-3. Temperature dependent luminescent properties of Mn^{2+} doped $Ba_2Ca(BO_3)_2$. In the top left Figure the emission spectra at various temperatures are shown. The top right shows the decay curves with their respective fit. The bottom shows the change in lifetime and emission intensity as a function of temperature, the lifetime has been measured and fitted on two different dates.

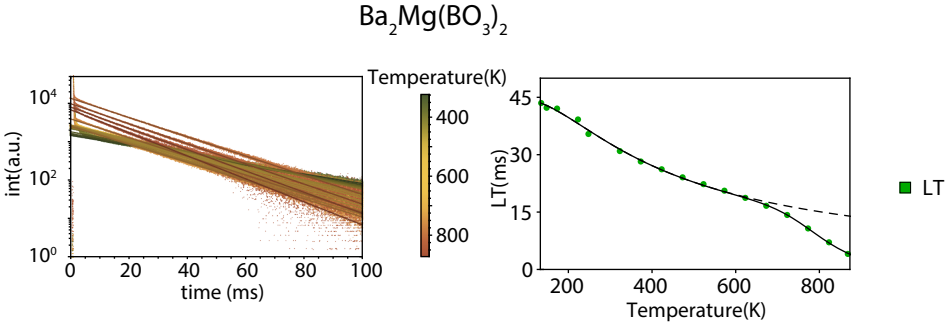

Figure S3-4. Temperature dependent Decay curves of Mn^{2+} doped $Ba_2Mg(BO_3)_2$. The top left shows the decay curves with their respective fit. The right shows the change in lifetime intensity as a function of temperature.

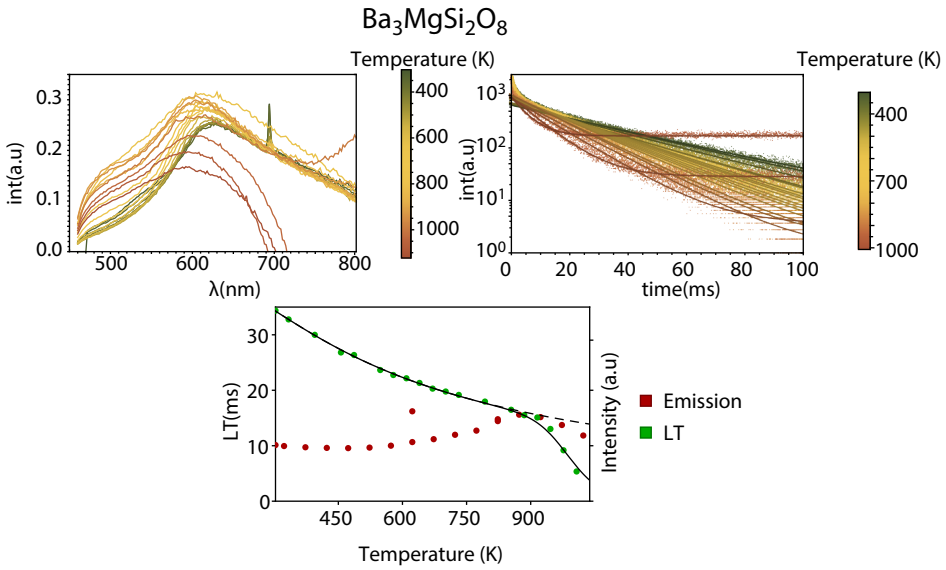

Figure S3-5. Temperature dependent luminescent properties of Mn^{2+} doped $Ba_3MgSi_2O_8$. In the top left Figure the emission spectra at various temperatures are shown(for the three highest spectra the blackbody radiation was subtracted). The top right shows the decay curves with their respective fit. The bottom shows the change in lifetime and emission intensity, up to 650 nm, as a function of temperature.

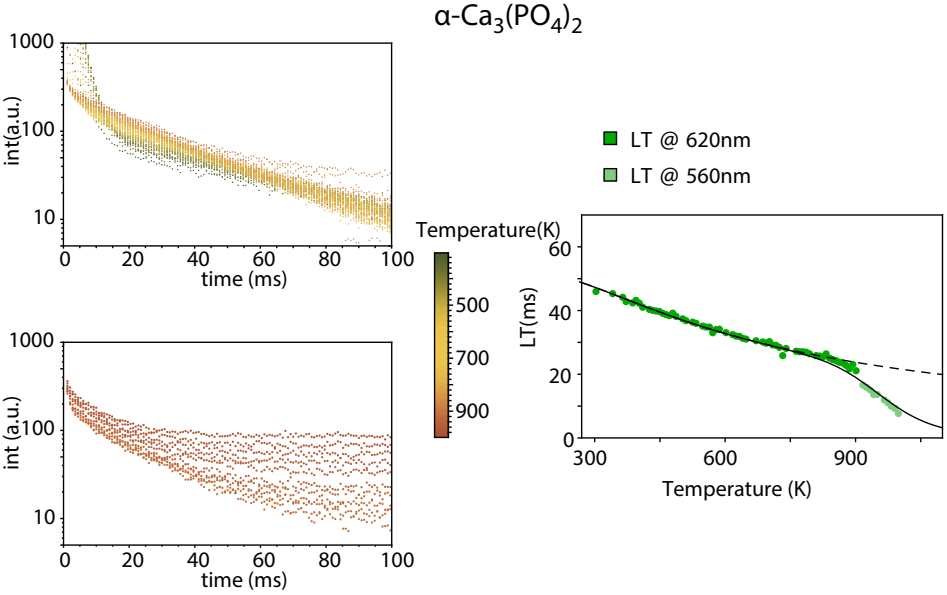

Figure S3-6. Temperature dependent luminescent properties of Mn^{2+} doped α -$Ca_3(PO_4)_2$. In the top left Figure the lifetime was recorded at 620 nm emission. At higher temperature the blackbody radiation is problematic so the lifetime was recorded at 560 nm emission. The combination of both measurements series is shown in the right Figure.

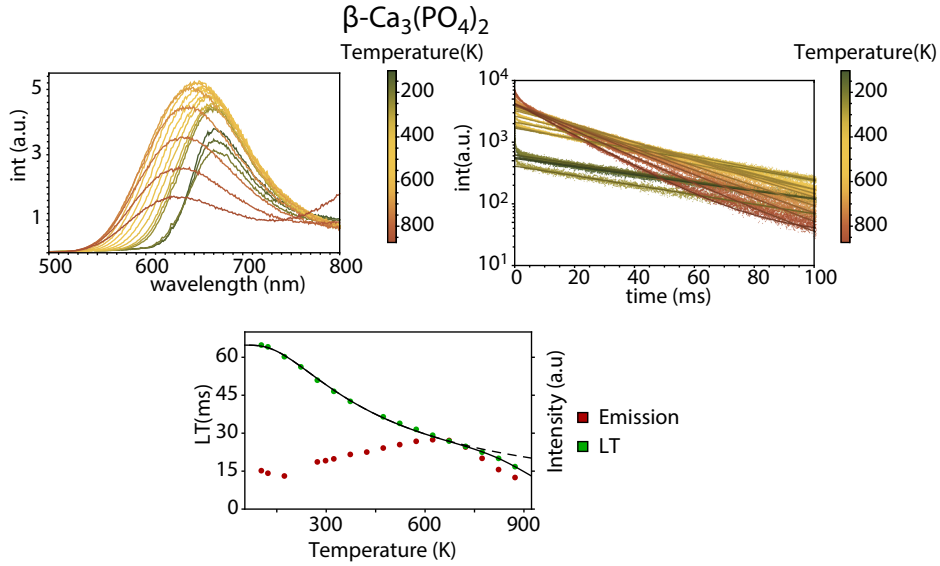

Figure S3-7. Temperature dependent luminescent properties of Mn^{2+} doped β -$Ca_3(PO_4)_2$. In the top left Figure the emission spectra at various temperatures are shown. The top right shows the decay curves with their respective fit. The bottom shows the change in lifetime and emission intensity as a function of temperature.

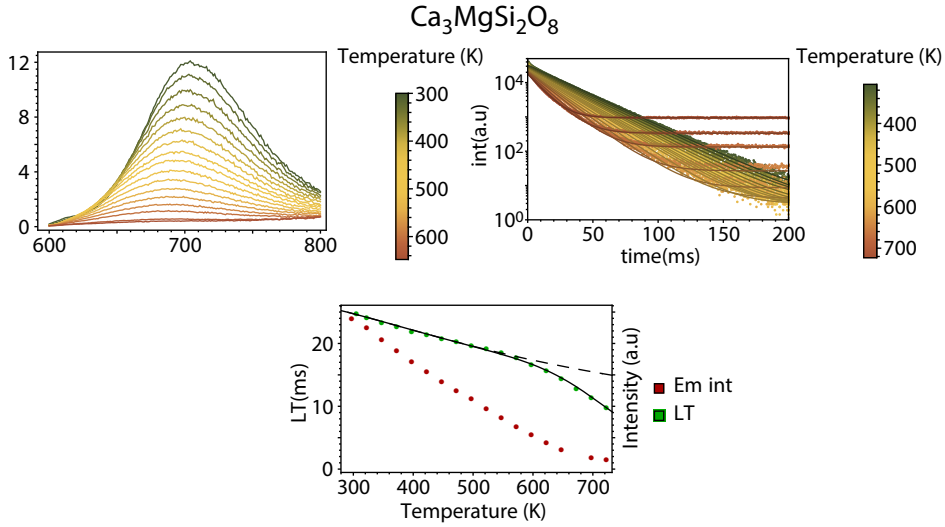

Figure S3-8. Temperature dependent luminescent properties of Mn^{2+} doped $Ca_3MgSi_2O_8$. In the top left Figure the emission spectra at various temperatures are shown. The top right shows the decay curves with their respective fit. The bottom shows the change in lifetime and emission intensity as a function of temperature.

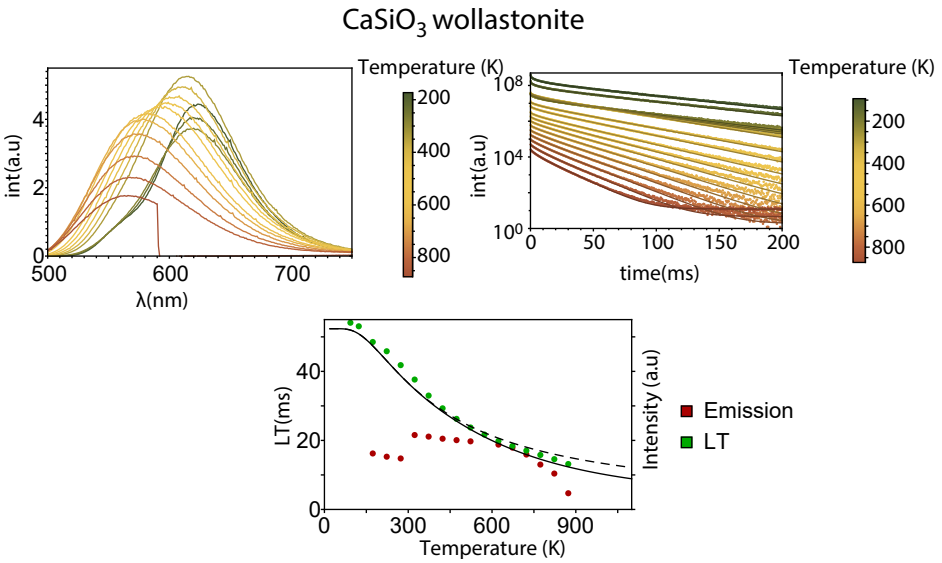

Figure S3-9. Temperature dependent luminescent properties of Mn^{2+} doped $CaSiO_3$ -wollastonite. In the top left figure the emission spectra at various temperatures are shown. The top right shows the decay curves with their respective fit. The bottom Figure shows the change in lifetime and emission intensity as a function of temperatur

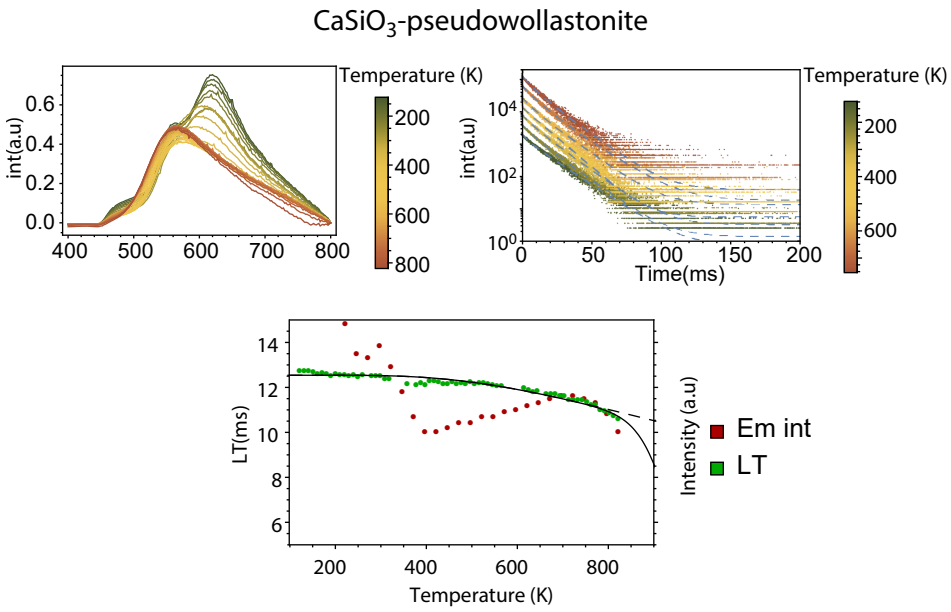

Figure S3-10. Temperature dependent luminescent properties of Mn^{2+} doped $CaSiO_3$ - Pseudowollastonite. In the top left Figure the emission spectra at various temperatures are shown. The top right shows the decay curves with their respective fit. The bottom shows the change in lifetime and emission intensity as a function of temperature.

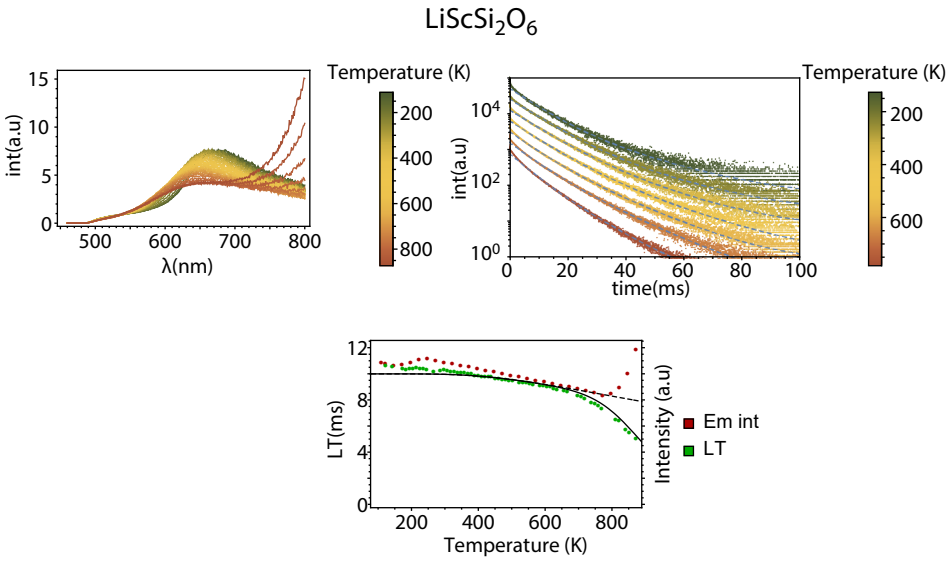

Figure S3-11. Temperature dependent luminescent properties of Mn^{2+} doped in $LiScSi_2O_6$. In the top left Figure the emission spectra at various temperatures are shown. The top right shows the decay curves with their respective fit. The bottom Figure shows the change in lifetime and emission intensity as a function of temperature.

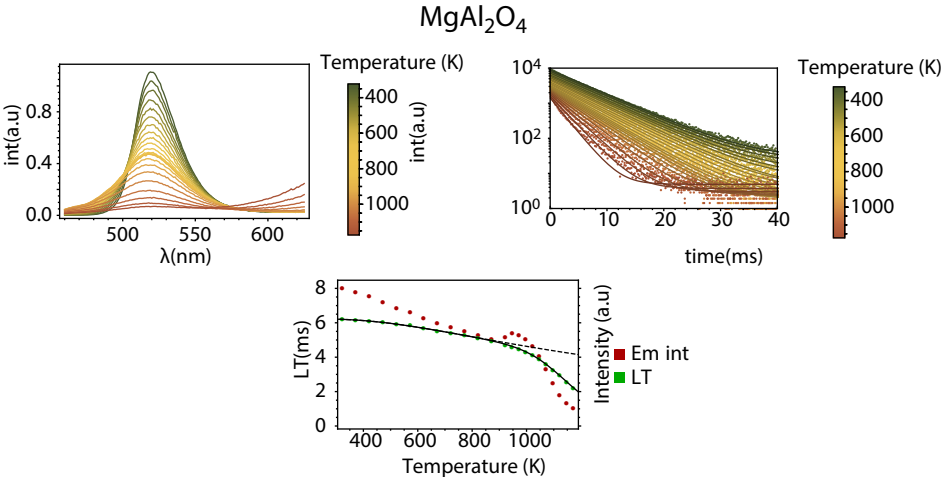

Figure S3-12. Temperature dependent luminescent properties of Mn^{2+} doped in $MgAl_2O_4$. In the top left Figure the emission spectra at various temperatures are shown. The top right shows the decay curves with their respective fit. The bottom shows the change in lifetime and emission intensity as a function of temperature.

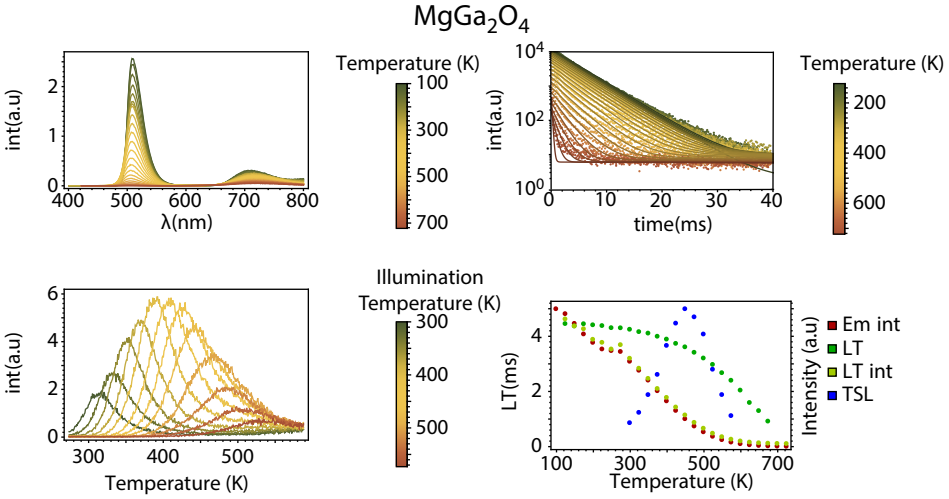

Figure S3-13. Temperature dependent luminescent properties of Mn^{2+} doped in $MgGa_2O_4$. In the top left Figure the emission spectra at various temperatures are shown. The top right shows the decay curves with their respective fit. The bottom left shows some of the TSL curves. The Figure in the bottom right corner shows the change in lifetime and emission intensity and TSL intensity as a function of temperature.

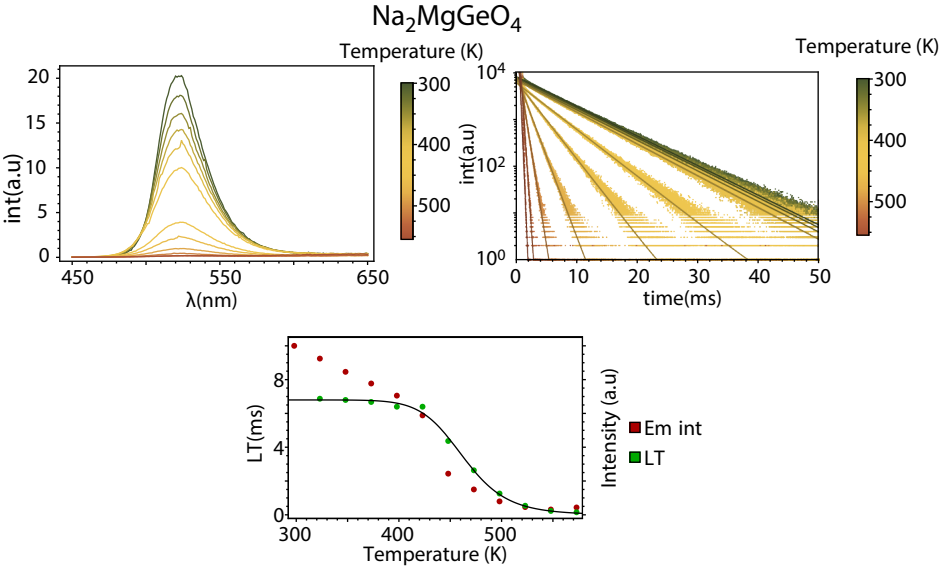

Figure S3-14. Temperature dependent luminescent properties of Mn^{2+} doped in Na_2MgGeO_4. In the top left Figure the emission spectra at various temperatures are shown. The top right shows the decay curves with their respective fit. The bottom shows the change in lifetime and emission intensity as a function of temperature.

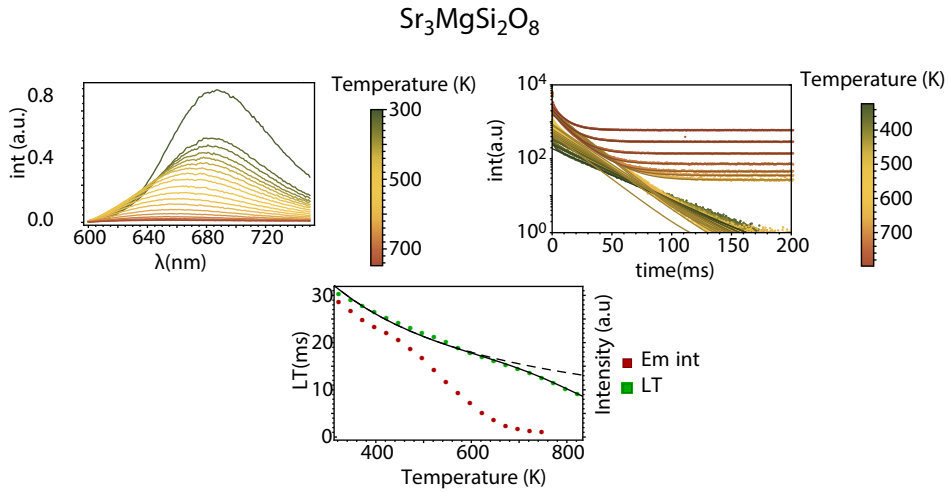

Figure S3-15 .Temperature dependent luminescent properties of Mn^{2+} doped in $Sr_3MgSi_2O_8$. In the top left Figure the emission spectra at various temperatures are shown. The top right shows the decay curves with their respective fit. The bottom shows the change in lifetime and emission intensity as a function of temperature.

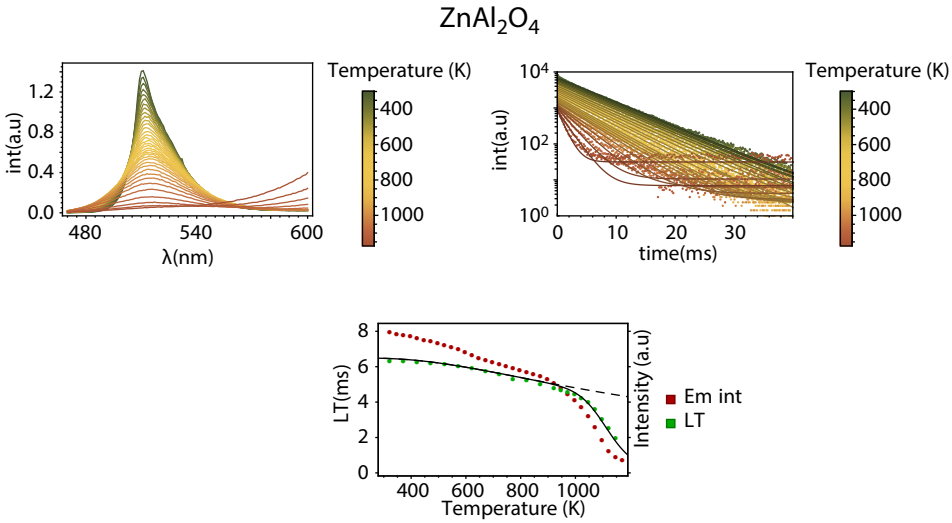

Figure S3-16. Temperature dependent luminescent properties of Mn^{2+} doped in $ZnAl_2O_4$. In the top left Figure the emission spectra at various temperatures are shown. The top right shows the decay curves with their respective fit. The bottom shows the change in lifetime and emission intensity as a function of temperature.

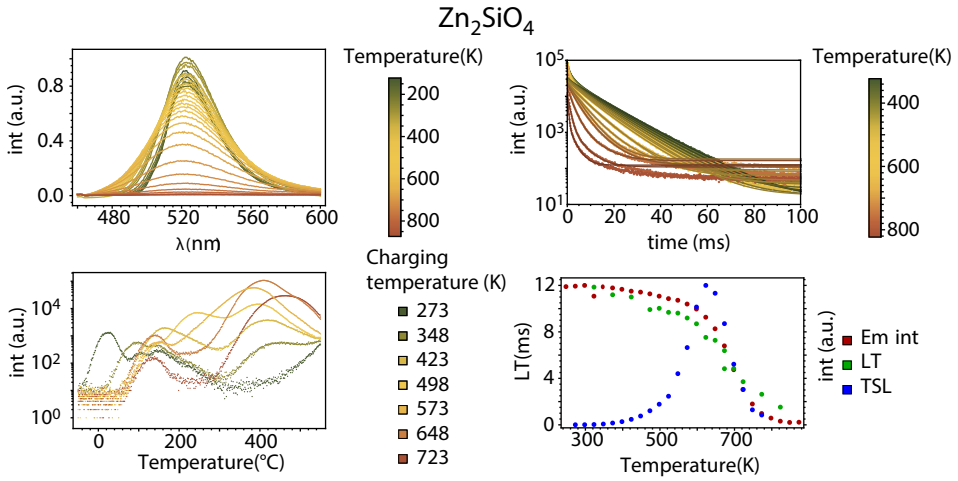

Figure S3-17. Temperature dependent luminescent properties of Mn^{2+} doped in Zn_2SiO_4. In the top left Figure the emission spectra at various temperatures are shown. The top right shows the decay curves with their respective fit. The bottom left shows some of the TSL curves. The bottom right corner shows the change in lifetime and emission intensity and TSL intensity as a function of temperature.

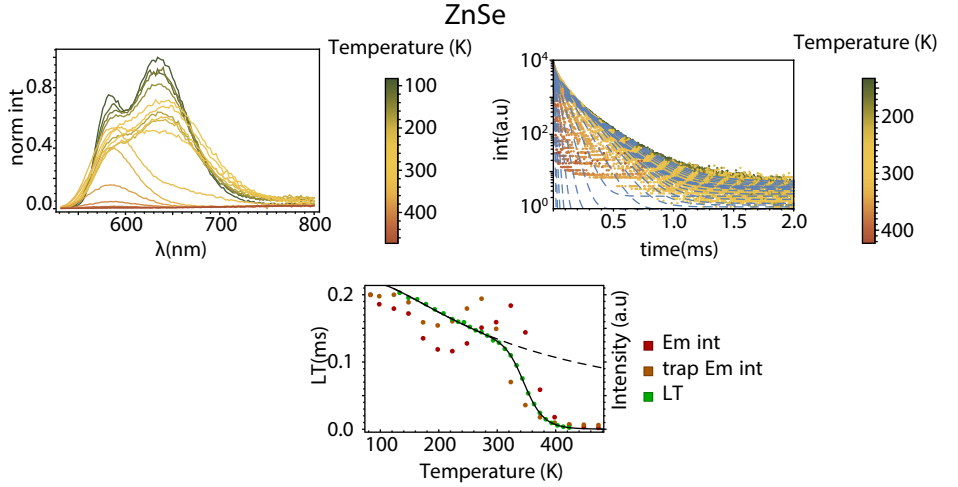

Figure S3-18. Temperature dependent luminescent properties of Mn^{2+} doped in ZnSe. In the top left Figure the emission spectra at various temperatures are shown. The top right shows the decay curves with their respective fit. The bottom shows the change in lifetime and emission intensity, both of the host emission and the Mn^{2+} emission, as a function of temperature.

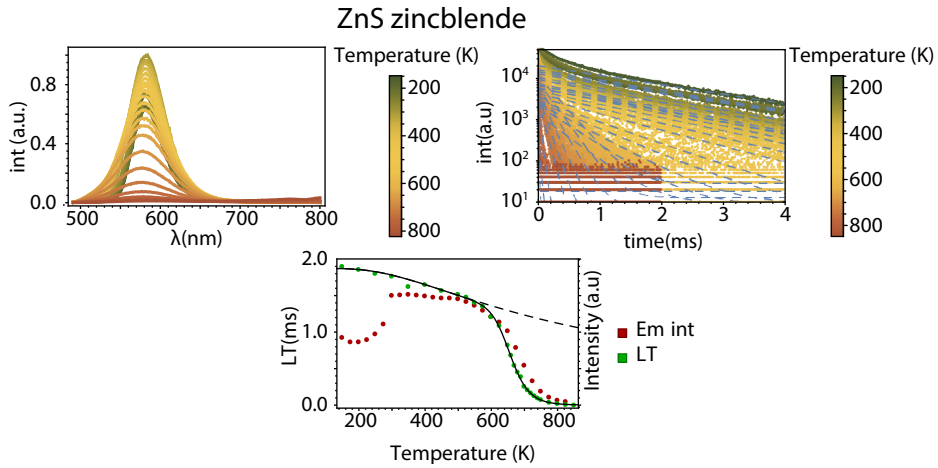

Figure S3-19. Temperature dependent luminescent properties of Mn^{2+} doped in ZnS zincblende. In the top left Figure the emission spectra at various temperatures are shown. The top right shows the decay curves with their respective fit. The bottom shows the change in lifetime and emission intensity as a function of temperature.

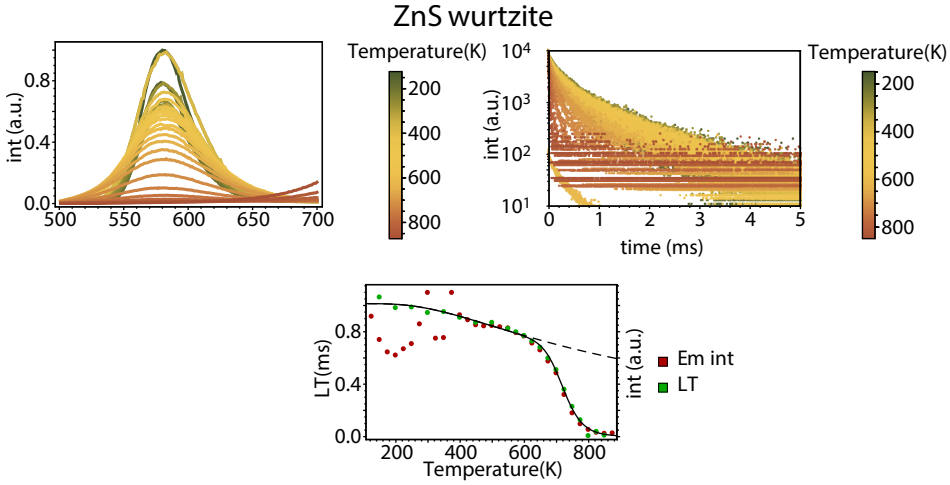

Figure S3-20. Temperature dependent luminescent properties of Mn^{2+} doped in ZnS zincblende. In the top left Figure the emission spectra at various temperatures are shown. The top right shows the decay curves with their respective fit. The bottom shows the change in lifetime and emission intensity as a function of temperature.

$ZnS_{1-x}Se_x$:Mn solid solutions

Table S3-2. luminescence quenching temperature of Mn^{2+} in different $ZnS_{1-x}Se_x$:Mn solid solutions. The bandgap was estimated based on the article by Miguel et al [2]

Compound	T_{50} (K)	Estimated bandgap (eV)
ZnS	661	3.6
$ZnS_{0.41}Se_{0.59}$	473	2.9
$ZnS_{0.26}Se_{0.74}$	435	2.8
ZnSe	348	2.6

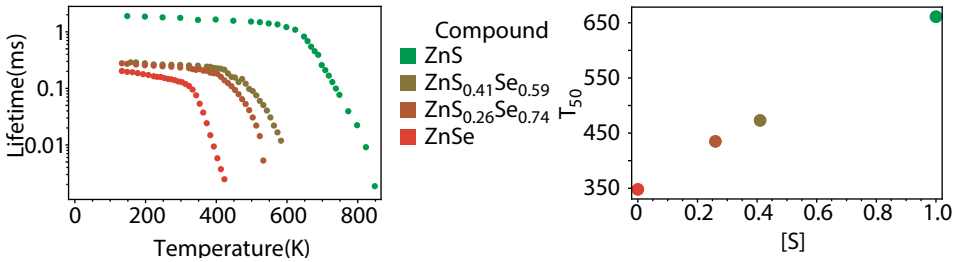

Figure S3-21. Left; Life time of Mn^{2+} in different $ZnS_{1-x}Se_x$:Mn solid solutions at various temperatures. On the right the T_{50} of the Mn^{2+} in these solid solutions against the fraction of sulphur anions.

Calculated bandgap to experimental bandgap

Table S3-3. Compounds with the experimental bandgap as compared to the experimental bandgap

Compound	Bandgap Calculated (eV)	Experimental bandgap (eV)	Source
$MgAl_2O_4$	5.122	8.2	[3]
AlN	4.054	6.2	[4]
ZnS Zincblende	2.35	3.82	[5]
ZnS Wurtzite	2.08	3.74	[5]
ZnSe	1.614	2.69	[6]
ZnTe	1.078	1.97	[7]

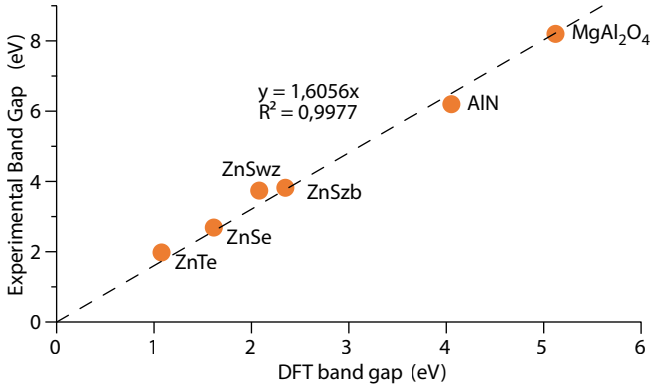

Figure S3-22. Calculated bandgap as calculated by the materials project [8] compared to the experimental bandgap. As shown in Table S3-3. A linear trend is seen and the deviation between calculated and experimental seems to be 60%.

FWHM of Mn^{2+} in Spinel structures

In more detail the FWHM of Mn^{2+} in four spinel structures $MgAl_2O_4$, $MgGa_2O_4$, $ZnAl_2O_4$ and $ZnGa_2O_4$ as a function of temperature was studied, as shown in Figure S3-23 here we see that for all four hosts that the FWHM increases with temperature. The width " "as a function of temperature can effectively be described with the following function:

$$\Gamma(T) = 2.35\sqrt{S \cdot coth\, h\nu/kT} \qquad \text{(S 3-1)}$$

Here Γ is the FWHM as a function of temperature, hν is the effective phonon energy and S is the Huang-Rhys factor. The Huang-Rhys factor gives an indication how big the stokes shift is. [9] What this equation shows is that at elevated temperatures higher vibrational levels get occupied. Emission from higher vibrational state becomes possible while at the same time emission to higher vibrational levels is enhanced resulting in a broader emission peak at elevated temperature.

What is peculiar is that the FWHM of the Mn^{2+} emission in $MgAl_2O_4$ overlaps with $MgGa_2O_4$. Similarly for $ZnAl_2O_4$ and $ZnGa_2O_4$.

A clear distinction is seen for th Zn containing spinels and the Mg containing spinels. The size of Zn is 0.6, Mg 0.57 and Mn 0.66Å. there therefore is a smaller mismatch between Zn and Mn and Mg and Mn. [10] The larger mismatch causes a larger stokes shift. We thus expect a distinct S for the Mg spinels and a different S for the Zn spinels. Since there is good voerlap is similar aswell for the spinels with the same divalent cation. This is peculiar as the phonon

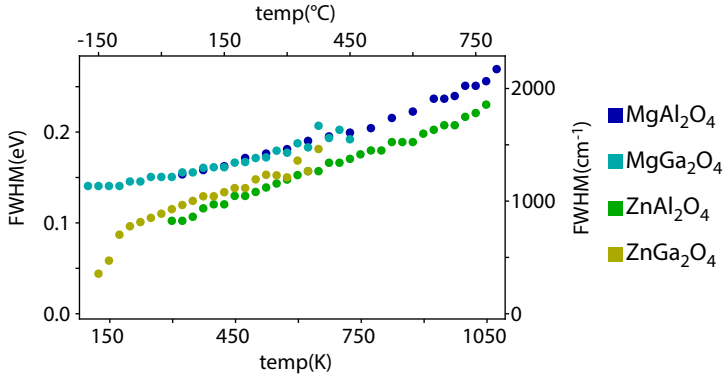

Figure S3-23. FWHM of Mn^{2+} emission as a function of temperature incorporated in four different Spinel structures, expressed in eV as well as cm^{-1}

energy of gallates needs to be considerably lower than for the aluminates. What this indicates is that widening of Mn^{2+} at elevated temperatures is not caused by coupling to phonons in the host materials but is more likely caused by the local isolated vibrations of the Mn^{2+} with the surrounding oxygen ligands.

It is also interesting to relate the width of the Mn^{2+} emission bands to the luminescence quenching temperatures. For the thermal crossover mechanism a clear correlation is expected. A larger offset between ground and excited state parabola will give rise to a broader emission band and a lower luminescence quenching temperature. For decades this has been the standard model to explain trends in luminescence quenching temperatures. Limiting expansion (or contraction) in the excited state relative to the ground state in stiff lattices and well-designed coordination was used to raise luminescence quenching temperatures. Only when this model failed to explain low quenching temperatures of e.g. Eu^{2+} or Ce^{3+} emission in host lattices where the emission band width was narrow, the alternative model of photo ionization was found to provide an alternative and frequently occurring quenching mechanism. To investigate the role of TC quenching, in Figure x the FWHM at 300 K for the Mn^{2+} emission is plotted vs. the T_{50} values. The results show no correlation. This provides further evidence that thermally activated photo ionization is the dominant thermal quenching mechanism for Mn^{2+} emission. Based on the narrow bandwidth of Mn^{2+} emission this is not unexpected. A narrow bandwidth is indicative of a small relaxation in the excited and a correspondingly high TC quenching temperature. It cannot be excluded that the mechanism for thermal quenching for Mn^{2+} in the two aluminates with T50 values above 1000 K is TC although the higher T_{50} (1191 K) is observed for Mn^{2+} emission in the host where the Mn^{2+} emission band has a broader FWHM at 300 K ($MgAl_2O_4$).

[1] J. Baars, G. Brandt, *J. Phys. Chem. Solids* **1973**, *34*, 905.
[2] M. A. Avilés, J. M. Córdoba, M. J. Sayagués, F. J. Gotor, *Inorg. Chem.* **2019**, *58*, 2565.
[3] E. Feldbach, I. Kudryavtseva, K. Mizohata, G. Prieditis, J. Räisänen, E. Shablonin, A. Lushchik, *Opt. Mater.* **2019**, *96*, 109308.
[4] M. E. Levinshtein, S. L. Rumyantsev, M. S. Shur, Properties of Advanced Semiconductor Materials GaN, AlN,InN, BN, SiC, SiGe, *John Wiley And Sons,* **2001**.
[5] O. Brafman, I. T. Steinberger, *Phys. Rev.* **1966**, *143*, 501.
[6] S. Adachi, T. Taguchi, *Phys. Rev. B* **1991**, *43*, 9569.
[7] R. E. Dietz, D. G. Thomas, J. J. Hopfield, *Phys. Rev. Lett.* **1962**, *8*, 391.
[8] A. Jain, S. P. Ong, G. Hautier, W. Chen, W. D. Richards, S. Dacek, S. Cholia, D. Gunter, D. Skinner, G. Ceder, K. A. Persson, *APL Mater.* **2013**, *1*, 011002.
[9] B. Henderson, I. G. F., Optical Spectroscopy of Inorganic Solids, *Oxford University Press*, **1989**.
[10] R. D. Shannon, *Acta Crystallogr. Sect. A* **1976**, *32*, 751.

Chapter 4

NIR emission in highly concentrated $MgAl_2O_4:Mn^{2+}$

Abstract

Broad band near infrared (NIR) emission has recently been reported for a wide variety of concentrated Mn^{2+} phosphors. Typically, Mn^{2+} emits in the green to red spectral region, depending on local coordination. The enormous redshift to the NIR was explained by exchange coupling between Mn^{2+} neighbours at high Mn^{2+} dopant concentrations. However, the reported redshifts are an order of magnitude larger than expected for exchange coupling and also the absence of a shift in excitation spectra suggests that exchange coupling cannot explain the observations. Here, extensive concentration, temperature and time dependent luminescence studies are reported for $Mg_{1-x}Mn_xAl_2O_4$ (x=0.01-0.5). The results show that the broad band NIR emission originates from NIR emitting trap centers, possibly Mn^{3+}. High Mn^{2+} dopant concentrations enable efficient energy migration over the Mn^{2+} sublattice to these traps, consistent with the same excitation spectra for the green Mn^{2+} and NIR trap emission. Upon cooling to cryogenic temperatures energy migration is hampered and the green Mn^{2+} emission increases, especially in the most concentrated systems. Finally, the relative intensity of the NIR emission was varied by changing synthesis conditions to favour or suppress Mn^{3+} formation providing further support that the NIR emission in concentrated Mn^{2+} phosphors originates from Mn^{3+} and not exchange coupled Mn^{2+} pairs.

"If we don't understand the mechanism, we blame it on the defects"

Andries Meijerink

Introduction

The development of new luminescent materials (phosphors) is crucial for improving white light LEDs for lighting and displays and also for enabling new applications. Important current topics in the LED phosphor industry concern narrow band red and green phosphors to improve the light quality, colour gamut and efficacy.[1-5] New applications are emerging and include human centric lighting and lighting for horticulture [6-11]human-centric lighting considers the visual and non-visual effects of light in support of positive human outcomes. At its worst, it is a marketing phrase used to healthwash lighting products or lighting design solutions. There is no doubt that environmental lighting contributes to human health, but how might one practice human-centric lighting given both the credible potential and the implausible hype? Marketing literature is filled with promises. Technical lighting societies have summarized the science but have not yet offered design guidance. Meanwhile, designers are in the middle, attempting to distinguish credible knowledge from that which is dubious to make design decisions that affect people directly. This article is intended to: (1. An interesting spectral region is the near infrared (NIR). In addition to applications in horticulture (controlling plant growth) and human centric lighting (adding NIR to the lamp spectrum for health benefits), NIR emitters are now gaining attention for chemical sensing.[12,13] For both narrow band phosphors and NIR emitters there is increasing interest in phosphors relying on the luminescence of the Mn^{2+} ion.[14,15]

Mn^{2+} has a long history of applications in a variety of phosphors for lighting and displays.[16, 17] The luminescence properties of Mn^{2+} are versatile and can be understood based on the Tanabe-Sugano diagram for the $3d^5$ configuration. Mn^{2+} typically yields narrow band green emission in tetrahedral coordination and red emission in octahedral coordination resulting from the $^4T_1 \rightarrow {}^6A_1$ transition. The luminescence quenching temperature can be very high, making Mn^{2+} phosphors attractive for applications where high temperatures are reached, e.g. in white light LEDs (wLEDs) [18] Drawbacks are the weak absorption ($\varepsilon < 1 M^{-1}.cm^{-1}$) and long luminescence life time ($\tau >$ ms) as all transitions within the $3d^5$ configuration are spin- and parity forbidden. The weak absorption can be mitigated by combining Mn^{2+} with a strongly absorbing sensitizer and the emission life time can be shortened by incorporation in a host lattice with heavier elements (stronger spin-orbit coupling) or through magnetic interactions, e.g. in Mn^{2+} pairs (partially lifting the spin selection rule).[19-25] In the past decade a new emission was reported for Mn^{2+}: NIR emission from exchange coupled Mn^{2+}-pairs [26–35] an anomalous near-infrared (NIR. This broad band NIR emission was observed in a variety highly doped Mn^{2+} phosphors and deemed promising for applications in both lighting and sensing.

Before considering these recent findings of NIR emission in highly-doped Mn^{2+} phosphors, it is good to discuss early work on the optical properties of exchange-coupled Mn^{2+} pairs. In an insightful review in 1988 McCarthy and Güdel summarize experimental findings and theoretical explanations for the role of exchange coupling in redshifting the Mn^{2+} emission and shortening the emission life time.[20] The spectral shifts are determined by the exchange coupling parameter J in the ground state and J_{ex} in the excited state. Depending on distance, geometry and bridging ligands, values for J and J_{ex} vary and are typically tens of cm^{-1}. The redshift and shortening of decay time are explained using an energy level diagram (Figure 4-1) in which the total spin for the pair in the ground state can vary from 0 to 5 (with steps of 1) depending on the relative orientation of the S=5/2 spins of the exchange coupled Mn^{2+} ions and of the S=5/2 and S=3/2 spins for the pair with one ion in the excited state. The total spin magnetic moments for the pair can thus be 0, 1, 2, 3, 4 or 5 in the ground state and 1, 2, 3 or 4 in the excited state, giving rise to partially spin-allowed transitions between pair states with the same total spin. In the review several examples of exchange coupled pairs are discussed, showing redshifts of typically 10-100 cm^{-1}, for example for Mn^{2+} pairs in $CsMgCl_3$, $KMgF_3$ and for Cr^{3+} pairs in ruby ($Al_2O_3:Cr^{3+}$) .[20,21,36,37] For several commercial phosphors the concentration dependent redshift was later also experimentally observed, theoretically explained and related to phosphor performance. In the famous green willemite phosphor $Zn_2SiO_4:Mn^{2+}$ the emission maximum shifts from 520 to 529 nm (~250 cm^{-1}) upon raising the concentration from 0.5 to 20% Mn^{2+}.[38,39] In the electroluminescent $ZnS:Mn^{2+}$ phosphor similar Mn-concentration dependent shifts are observed as well NIR emission.[40,41] The NIR emission was explained by energy migration to NIR emitting centers of which the nature was not known. In an overview of luminescence properties of exchange coupled pairs of transition metal (TM) ions in 2001 also Mn^{2+}-Mn^{2+} pairs were discussed and a spectral shift from 519 to 528 nm accompanied by life time shortening from 7.2 to 4.5 ms was reported for $MgAl_2O_4$ doped with 0.2 to 10% Mn^{2+}.[21] Even though not all aspects of exchange coupling can be quantitatively explained, the influence of exchange coupling on the Mn^{2+} (and other TM ions) luminescence properties are well documented.

In the past decade unexpected NIR emission for heavily doped Mn^{2+} phosphors was reported for a wide variety of materials, including $KZnF_3$, $MgGa_2O_4$, MnS, CaO, $MgAl_2O_4$, $CsMnF_3$, $(Gd,Y)_3(Ga,Al)_5O_{12}$ and Li_2ZnSiO_4 [26–35]. In 2014 the first papers reported a strongly redshifted NIR emission band in addition to the 'normal' Mn^{2+} emission in $KZnF_3$ and $MgGa_2O_4$.[26,27] In $KZnF_3$ the normal 585 nm emission intensity decreased upon raising the Mn^{2+} concentration above 10% and a strong NIR emission at 770 nm appeared. Similar observations in $MgGa_2O_4$ revealed green emission shifting from 507 to 518 nm for Mn^{2+} concentrations of 1 to 20%. This green emission intensity strongly decreased upon raising the Mn^{2+} concentration and was accompanied by a strong increase of a broad 770 nm NIR emission band, gaining intensity for Mn^{2+} concentrations above 10%. In both cases the visible Mn^{2+} emission was assigned to the $^4T_1 \rightarrow {}^6A_1$ transition on isolated Mn^{2+} while the NIR emission band was

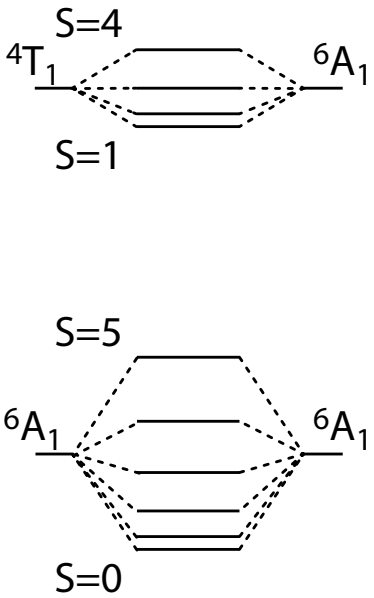

Figure 4-1. Schematic of exchange coupling between Mn^{2+} neighbours in the $^6A_1$ ground state (S=5/2) giving rise to total spin S varying from 0 to 5 while exchange coupling with one ion in the $^4T_1$ excited state (S=3/2) gives rise to total spin S varying from 1 to 4. [20, 21] In case of anti-ferromagnetic interaction S=0 is the lowest state while for ferromagnetic interaction S=5 will be the ground state for the exchange coupled pair. Note that the actual exchange splitting is much smaller than the splitting in the schematic Figure

assigned to exchange coupled Mn^{2+} pairs, in the case of $KZnF_3$ Mn^{2+} in adjacent octahedral sites and in the case of $MgGa_2O_4$ to Mn^{2+} ions in edge-sharing neighbouring tetrahedral and octahedral sites. The exchange coupling theory, as outlined in Refs [19,20,41], was cited to explain the redshift. In the years following many more examples were reported and included on reviews of Mn^{2+} doped phosphors. For example, in MnS deep red emission at 710 nm was assigned to isolated Mn^{2+} and two NIR 900 and 1380 nm emission bands were explained by emission from next-nearest and nearest neighbour exchange coupled pairs.[28] DFT calculations were done to support similar assignments in CaO:Mn^{2+}[29]In a recent paper a difference in thermal quenching behavior of the two emission bands in heavily Mn-doped Li_2ZnSiO_4 was used for temperature sensing.[34]

The vast number of papers and host lattices showing broad band NIR emission at high Mn^{2+} doping concentrations seems convincing but the redshifts reported for the exchange-coupled Mn^{2+} pairs are very large, varying from 3400 cm^{-1} in $(Gd,Y)_3(Ga,Al)_5O_{12}$ and Li_2ZnSiO_4 to 6800 cm^{-1} in $MgAl_2O_4$ and MnS. [28,32] These shifts are more than ten times larger than those reported in earlier work [20,21,36,37,40,42], where clear evidence was presented for the magnitude of the exchange splitting parameters J and J_{ex} based on temperature dependent luminescence and decay measurements as well as experiments in magnetic

fields. In fact, the small shifts of the visible emission bands of Mn^{2+} upon raising the concentrations (e.g from 507 to 518 nm in $MgGa_2O_4$) are consistent with earlier results on redshifts expected for exchange coupled Mn^{2+} pairs. In addition, no large shifts are observed in the excitation spectra which is unexpected for high concentrations of exchange coupled Mn-pairs with a strongly distorted energy level scheme that would be expected based on the enormous redshifts reported for the emission. It is the aim of this work resolve the discrepancies between the recent papers and earlier work on exchange coupled Mn-pairs.

To find the origin for the NIR emission in heavily Mn^{2+} doped phosphors, here the luminescence properties of $Mg_{1-x}Al_2O_4:Mn_x$ (x = 0.01 to 0.5) are investigated in detail. The $MgAl_2O_4:Mn^{2+}$ phosphor is well studied and serves as a model system to provide insight. As Mn^{2+} doping is raised, a prominent NIR emission appears, consistent with the results reported in.[32] However at low temperatures (< 100K), this NIR emission decreases, while the typical green emission of Mn^{2+} ($^4T_1 \rightarrow {}^6A_1$) reappears. In addition, the relative intensity of the NIR emission is shown to depend on synthesis conditions and host stoichiometry. Based on our experimental findings, we propose a different origin for the NIR emission: it does not originate from exchange coupled Mn^{2+} pairs but from NIR emitting traps. At high doping concentrations efficient energy migration between excited Mn^{2+} ions facilitates energy transfer to this NIR luminescent center, which we tentatively assign to trace amounts of Mn^{3+}. Energy migration is hampered at cryogenic temperatures, explaining the reappearance of the green Mn^{2+} emission. Synthesis conditions favoring incorporation of Mn^{3+} result in a higher NIR emission intensity and are consistent with our assignment.

Methods

For the synthesis of microcrystalline $Mg_{1-x}Mn_xAl_2O_4$ the starting materials MgO (99.99%,Sigma Aldrich), Al_2O_3 (99.99%,chempur), and $MnCO_3$ (99.99%,Sigma Aldrich) were mixed in stoichiometric amounts in an agate mortar and pestle. The mixture was wetted with a few drops of acetone (to prevent microparticle aggregation), and ground manually for 15 minutes. The mixtures were then annealed twice in a tube oven for a total of 18h at 1500°C in a reducing atmosphere (H_2/N_2 20/80) and were reground in between.

The powders were examined using powder X-ray powder diffraction for phase purity. A Phillips PW1729 X-ray generator, Cu Kα source was used at 40 kV operating voltage and 20 mA current. The step size resolution was 0.02° 2θ. Photoluminescence (PL) spectroscopy was performed using an Edinburgh Instruments FLS-920 fluorescence spectrometer. The photoluminescence (PL) and PL excitation (PLE) measurements were recorded using a 450 W Xe lamp as excitation source and a Hamamatsu R928 PMT or a Hamamatsu N7422 PMT detector for the visible and NIR spectral region, respectively. To prop-

erly compare the intensity of the NIR with the VIS detector the spectra were normalised on the 650-700 nm peaks that were measured with both detectors. Spectra are corrected for the instrumental response. PL decay measurement were performed by using a tuneable optical paramagnetic oscillator (OPO) Opotek Opolette HE 355II pulsed laser (pulse width: 10 ns; repetition rate: 20 Hz) as excitation source and the Hamamatsu R928 PMT combined with the Multi Channel Scaling (MCS) time resolved measuring card in the Edinburgh spectrometer (10μs time resolution). For temperature dependent measurements a liquid He cooled cryostat from Oxford Instruments was used.

Results and Discussion

Concentration Dependent Luminescence

To investigate the concentration dependent luminescence properties of $Mg_{1-x}Mn_xAl_2O_4$, a series of samples was made under identical synthesis conditions with x= 0.01, 0.02, 0.05, 0.1, 0.2 and 0.5. The materials came out of the tube oven as white powder for low-doped samples while at high doping concentrations (x>0.10) the body color was slightly yellowish. XRD powder diffraction confirmed that all samples were phase pure (SI Figure S4-1). The diffraction angles showed a continuous decrease for increasing Mn content as expected based on Vegard's law and the fact that the ionic radius of Mn^{2+} is larger than that of Mg^{2+} and thus the crystal unit cell expands upon increasing Mn-content. Note that in the $MgAl_2O_4$ host it is expected that Mn^{2+} mainly occupies the Mg^{2+} site (similar size, same charge) creating a tetrahedrally coordinated Mn.[44] Mn^{2+} emission has also been reported for Mn^{2+} on the Al^{3+} site in $Mg_{1-x}Mn_xAl_2O_4$.[45]

To characterize the Mn^{2+} luminescence for isolated Mn^{2+} ions, first PL and PLE spectra were recorded for $MgAl_2O_4$ doped with 1% Mn. In Figure 4-2 the PL spectrum is shown. Narrow band green emission peaking at 520 nm is observed, consistent with earlier reports. The emission band is assigned to the $^4T_1 \rightarrow {}^6A_1$ transition on Mn^{2+}. In addition there is a very weak sharp emission line at 680 nm. This is typical for Cr^{3+} at the Al^{3+} site and careful measurement of the position of the $^2E \rightarrow {}^4A_2$ zero-phonon line and vibronic structure show that these are identical to what has been reported for Cr^{3+} in $MgAl_2O_4$ providing evidence for the incorporation of a small amount of Cr^{3+} in our materials.[46] Cr is a common contaminant in the Al_2O_3 precursor. The recorded PLE spectrum of the green Mn^{2+} emission shows six distinct peaks, at 280, 350, 380, 425, 450 and 480 nm. These are all d-d transitions of the Mn^{2+} and can be assigned to transitions from the $^6A_1$ ground state to the $^4A_2(^4F)$, $^4E(^4D)$, $^4T_2(^4D)$, $^4A_1/E(^4G)$, $^4T_2(^4G)$ and $^4T_1(^4G)$ excited states, respectively. No broad emission around 650 nm is observed. Emission at this wavelength is typical for Mn^{2+} at the octahedral Al site.[45]

The concentration dependence of the luminescence was investigated by mea-

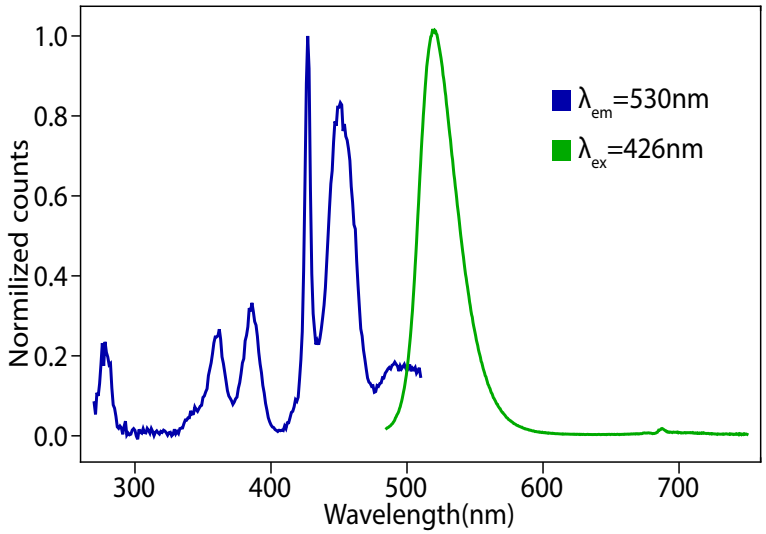

Figure 4-2. Photoluminescence (green) and excitation (blue) spectrum of $Mg_{0.99}Mn_{0.01}Al_2O_4$ at 300 K. The PL spectrum was recorded under 426 nm excitation, the PLE spectrum for 530 nm emission.

suring luminescence spectra for all Mn^{2+} concentrations over a wide spectral range, extending to 1200 nm. Note that in the past NIR emissions from highly Mn-doped samples may have been missed because of low sensitivity of detectors (photomultipliers) in the NIR. In Figure 4-3 the emission spectra are shown. The green 520 nm emission band increases in intensity up to 5% Mn^{2+} followed by a decrease above 10%. For the highest concentrations, 20 and 50% Mn^{2+}, the green emission is almost completely quenched. The emission maximum shifts from 518 to 526 nm upon raising the Mn^{2+} concentration from 1 to 50%. In the concentration region where the green emission is quenched, a NIR emission band around 830 nm is observed to increase with Mn-dopant concentration. The highest NIR intensity is found for the 50% dopant concentration. The present results are in good agreement with the trends observed for the visible and NIR emission in other host lattices where the NIR emission was assigned to exchange coupled Mn-pairs. Specifically, the spectra and relative intensities of visible and NIR emission are also consistent with results reported for concentration dependent Mn^{2+} luminescence in $MgAl_2O_4$.[21, 32]

In the inset of Figure 4-3, the excitation spectra of the green emission for the 1% Mn and the NIR emission in 50% doped $MgAl_2O_4$ are shown. The excitation spectra are similar and the assignment to Mn^{2+} d-d transition as discussed above can explain the features. The peak positions are almost identical while the excitation bands are broadened for the 50% doped host. The broadening can be explained by inhomogeneous broadening. The disorder in the Mg/Mn sublattice is maximized in the 50%/50% material and will give rise to varia-

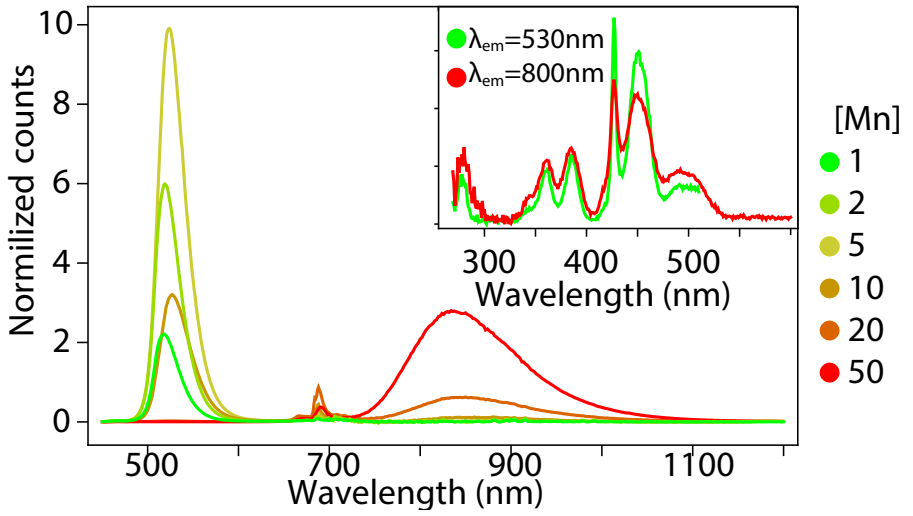

Figure 4-3. Emission spectra of $Mg_{1-x}Mn_xAl_2O_4$ for x=0.01,0.02,0.05,0.10,0.20,0.50, excited at 425 nm. From 450 to 800 nm the spectra were measured with a R928 detector and in the NIR region (600 to 1200nm) with a N7422 detector. The peak at ~680 nm was used to scale the spectra. The inset shows the excitation spectrum of the green emission of the 1%Mn and of the NIR emission of the 50% Mn material.

tions in the local crystal field splitting, induced by the difference in ionic radii for Mn and Mg. Variations in the local Mn-Mg distribution over nearest and possibly next-nearest neighbour lattice sites will thus give rise in differences in the crystal field splitting for Mn^{2+} and disorder is maximized in the host lattice with 50% Mn^{2+}.

To further investigate the origin of the NIR emission band, luminescence decay curves were recorded for both the green and NIR emission as a function of concentration following pulsed excitation (~10 ns pulse duration) at 420 nm. Excited state dynamics can give valuable information on the role of energy transfer processes. The results in Figure 4-4a for the green emission show that for 1 and 2 % Mn the decay curves are close to single exponential with a decay time of 6.1 ms for 1 and 2% and drops to 0.5 ms at 20% Mn. The 6.1 ms is in agreement with decay times reported for 1-2% Mn^{2+}-doped samples in Ref. [21] For concentrations of 5% and higher the decay becomes faster and increasingly non-exponential which can be explained by shortening of the life time by exchange coupling and, especially for higher Mn^{2+} concentrations, energy migration and transfer to trap centers. The decay curves for the NIR emission in Figure 4-4b also show decay on a ms time scale. The decay curves are non-exponential and decay times decrease for higher Mn^{2+} concentrations. The similar decay behavior observed for the NIR and green emission (non-exponential with an average decay time in the ms range) can be expected when the trap emission is populated by transfer from Mn^{2+} ions and the decay profile of the trap emission reflects the decrease in population of Mn^{2+} that feeds

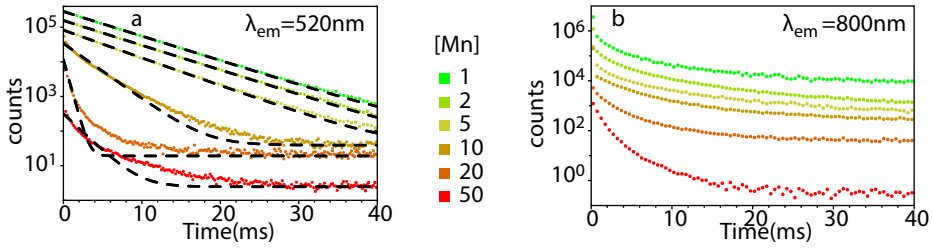

Figure 4-4. Luminescence decay curves of Mn^{2+} in $Mg_{1-x}Al_2O_4:Mnx$ (x=0.01,0.02,0.05,0.10,0.20,0.50) for pulsed λ_{ex}= 427nm excitation (curves are offset for clarity). (a) Decay curves for λ_{em}=520 nm, the dashed lines show the fit assuming mono exponential decay. (b) Decay curves for λ_{em}=830 nm.

the trap states.

Based on the concentration dependent luminescence measurements an alternative explanation for the NIR emission band can be given. Upon increasing dopant concentrations above 10% resonant energy transfer between Mn^{2+} dopant ions leads to concentration quenching. Due to the efficient energy transfer between neighbouring Mn^{2+} ions the excited state probes a larger volume and even in case of low concentrations of trapping sites, efficient energy transfer to trap states can occur. Especially above the percolation point (the concentration at which a 3D connected network of dopants is formed) efficient energy migration to traps occurs, leading to quenching of the dopant emission and, in the case of luminescent traps, a strong increase in trap emission. This phenomenon is well-known in the field of luminescent materials. [47–49] The concentration dependent luminescence properties for $MgAl_2O_4:Mn$ are consistent with this model: above 10% Mn^{2+} the NIR trap emission intensity rapidly increases while the green Mn^{2+} emission drops. The luminescence decay time of the Mn^{2+} donor decreases by migration mediated energy transfer to the trap states. The excitation spectrum for the trap emission is identical to that of the Mn^{2+} ions as the concentration of (and thus direct absorption by) the traps is very low. Following absorption by Mn^{2+} efficient transfer feeds the NIR emitting traps and this explains why the excitation spectrum for the NIR trap emission coincides with the Mn^{2+} absorption spectrum.

Note that in the earlier explanation (green emission from isolated Mn^{2+}, NIR emission from exchange coupled Mn^{2+} pairs) there is no clear explanation for the fast drop in decay time for the green emission. Isolated Mn^{2+} is expected to have a long ms decay time while the exchange coupled Mn-pairs have a faster decay by partial lifting of the selection rules. Also the similarity in excitation spectra is unexpected for the model in which the NIR emission is explained by exchange coupled Mn-pairs. Strong exchange coupling is required to explain the large redshift in emission and this large change in energy level structure should then also be reflected in changes in absorption transition energies. This is not observed. In other reports where strongly redshifted emission in concentrated Mn^{2+} phosphors is reported [26-35] also no corresponding signifi-

cant change in the excitation or absorption spectra is observed while it would be expected for such strong exchange coupling. Only for γ-MnS an additional 606 nm excitation band appeared in the excitation spectrum of the NIR but this can be due to direct excitation of the NIR emitting centers.[28]

Temperature dependent luminescence

To further elucidate the nature of the NIR emission in highly doped Mn^{2+} luminescent materials, temperature dependent measurements can help. Energy migration involves many consecutive energy transfer steps between neighbouring Mn^{2+} ions. Small variations in local environment give rise to small energy differences between the $^4T_1$ excited state of different Mn^{2+} ions. At room temperature these small energy differences can be easily compensated by absorption or emission of phonons, making resonant energy transfer possible. However, upon cooling to cryogenic temperatures, the excitation energy will be trapped at Mn^{2+} ions which have their $^4T_1$ excited state at lower energies. Further transfer to a Mn^{2+} neighbour with a higher energy $^4T_1$ state would require absorption of a phonon which is not available as the phonons are frozen out a cryogenic temperatures. Extensive research on energy migration for especially lanthanide ions has beautifully demonstrated how at low temperatures energy migration is hampered and emission from perturbed lanthanide ions is observed as a slightly red shifted sharp line emission.[50,51] Interestingly, also for concentrated Mn^{2+} thermally activated energy migration to NIR emitting trap centers has been reported.[52]

To investigate the role of energy migration in feeding the NIR emission in $Mg_{1-x}Mn_xAl_2O_4$ temperature dependent emission spectra down to cryogenic temperatures were performed for $MgAl_2O_4$:50% Mn sample. The emission spectra are shown in Figure 4-5. Upon cooling to 100 K there are no large changes but below 100 K a rapid increase in the green emission intensity observed while the NIR emission intensity decreases. The inset in Figure 4-5 shows the integrated emission intensities of the NIR and visible emission bands as a function of temperature, normalized to the intensity at 4 K. The temperature dependence is consistent with efficient energy migration over the Mn^{2+} sublattice at room temperature, feeding the NIR emitting traps, which is hampered upon cooling below 100 K. The NIR emission dominates above 100 K and shows a small decrease upon raising the temperature to 300 K, possibly by thermal quenching of the NIR luminescence.

To quantify the activation energy that is necessary to overcome these energy fluctuations an Arrhenius equation was used to fit the observed temperature dependence of green emission intensity, as shown with the dashed line in Figure 4-5. An effective ΔE of 200cm^{-1} was found. This value is consistent with what can be expected based on the broadening of the excitation bands for $Mg_{0.5}Mn_{0.5}Al_2O_4$ and also with earlier results by Güdel et al. on MnF_2 single crystals where it was shown that perturbations by Ca impurities could lower the energy levels of nearby Mn^{2+} ions by 250 cm^{-1}.[53] In Figure 4-6 the

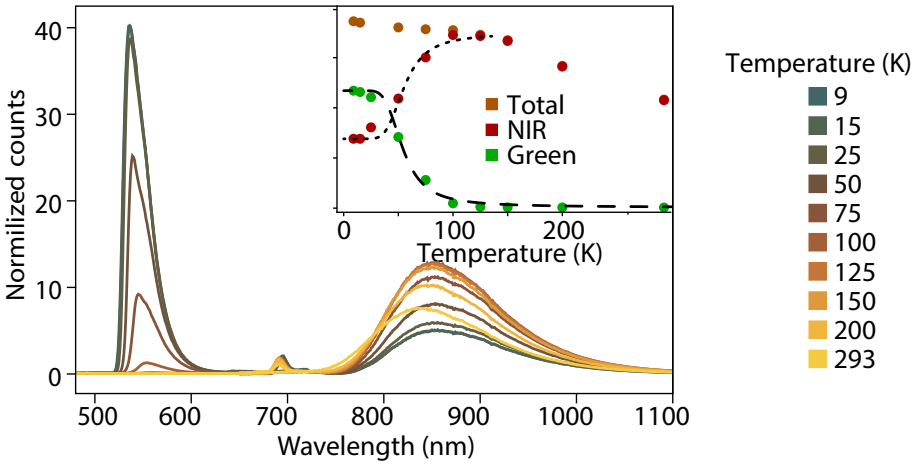

Figure 4-5. Temperature dependent emission spectra of $MgAl_2O_4$:50% Mn, λ_{ex}= 426nm. The inset shows the integrated intensity of the green and NIR emission bands. The dashed line shows the fit to determine the activation energy (ΔE of 200cm^{-1}) for energy migration. The dotted line is a visual guide to show that the NIR emission increases simultaneously with the decrease of the green emission

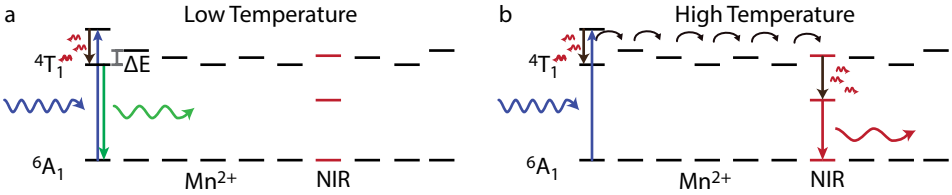

Figure 4-6. Schematic illustration of energy migration to NIR emitting trap centers. (a) At low temperature energy migration is hampered by the lack of thermal energy to bridge energy differences leading to trapping the excitation energy at Mn^{2+} sites with slightly lower $^4T_1$ state resulting in an enhanced green Mn^{2+} emission and reduced NIR trap emission. (b) Energy migration to NIR emitting centers at room temperature where the small energy differences of the $^4T_1$ states for neighbouring Mn^{2+} ions can be thermally overcome by lattice vibrations leading to dominant NIR emission.

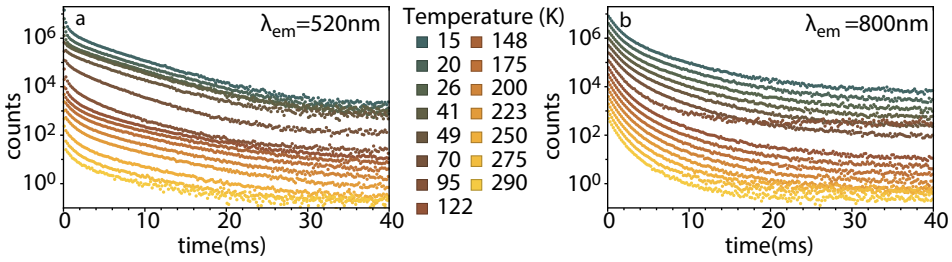

Figure 4-7. Luminescence decay curves of the (a) 520 nm and (b) 800 nm emission in $MgAl_2O_4$: 50% Mn following pulsed 427 nm excitation as a function of temperature

temperature dependent energy transfer is schematically depicted. At room temperature (Figure 4-6b) efficient energy transfer between Mn^{2+} neighbours allows for rapid energy migration to NIR emitting trap centers resulting in dominant NIR emission for concentrations above the percolation point where an interconnected 3D network of Mn^{2+} ions is formed. At cryogenic temperatures (Figure 4-6a) small energy differences between neighbouring Mn^{2+} ions hamper energy migration and result in a strong enhancement of the green Mn^{2+} emission.

The observed temperature dependence of the green and NIR emission is not consistent with the assignment of the green emission to isolated Mn^{2+} ions and the NIR emission to exchange coupled pairs. The concentration of isolated ions and exchange coupled pairs does not change with temperature and thus the strong increase of the green emission upon cooling from 100 K to 4 K cannot be explained by a model in which the green emission results from isolated ions and the NIR emission from exchange coupled pairs, especially for high Mn-doping concentrations where almost all Mn^{2+} ions are expected to be in pairs. A similar temperature dependence was previously even reported for fully concentrated Mn-system (e.g. MnS and $CsMnF_3$) where the isolated Mn^{2+} visible emission appeared upon cooling to 10 K. Clearly in a fully concentrated Mn^{2+} system all Mn^{2+} ions are in pairs and no isolated Mn^{2+} ions exist. For the $CsMnF_3$ material the observation of isolated Mn^{2+} emission at low temperature was attributed to competition between antiferromagnetic and ferromagnetic coupling interaction while for MnS no explanation was given for the observation of isolated Mn^{2+} visible emission upon cooling. In the $MgAl_2O_4$ system the NIR pair emission was assigned to pairs of Mn^{2+} ions on 'normal' four-coordinated Mg sites and six-coordinated Al^{3+} sites. Analysis of EXAFS data was used to determine that for 5% or less Mn^{2+} doping all Mn^{2+} was on IV-coordinated sites and for 10% or more Mn^{2+} ~8-10% of Mn^{2+} ions occupied octahedral VI-coordinated sites. This can explain an increase of isolated Mn^{2+} emission upon cooling by hampering energy migration to Mn-pairs at cryogenic temperatures, similar to the energy migration to NIR trap centers discussed above. Unfortunately, the evidence for a significant Mn^{2+} concentration in octahedral sites is inconclusive. The EXAFS data show poor fits and most importantly, no red Mn^{2+} emission typical for Mn^{2+} on octahedral sites can be observed for any Mn^{2+} concentration.

The temperature dependence of luminescence decay curves for the green and NIR emission in $MgAl_2O_4$: 50% Mn is shown in Figure 4-7. At low temperatures (<50 K) the decay curves are characterized by a single exponential tail and a fast initial decay. This shape is characteristic of single step energy transfer and limited or no energy migration. One-step energy transfer to the NIR emitting centers gives rise to faster initial decay for those Mn^{2+} ions close to a NIR center and the single exponential tail (with decay times longer than 6 ms) reflects the radiative decay for Mn^{2+} ions which are not in proximity to a NIR emitting center. Above ~50 K the decay in the tail becomes faster indicating an onset of energy migration that becomes faster as the temperature is raised

and results in more efficient energy transfer to NIR centers through energy migration, depopulating the green emitting excited states. The temperature dependence of the NIR emission is more complex. It is on time scales similar to the decay of the green emission, indicating that the observed decay dynamics are controlled by the feeding states, in agreement with energy migration from Mn^{2+} to the NIR emitting centers.

Influence of non-stoichiometry

The results and discussion presented above provide strong evidence that the broad NIR emission originates from trap centers. Excitation of Mn^{2+} and energy migration over the Mn^{2+} sublattice is followed by efficient energy transfer to the NIR emitting center. A candidate for the NIR center is Mn^{3+}. It is known that Mn^{3+} can show efficient NIR emission [52,54-57] in the 700 – 1000 nm spectral region and the 3+ valence state is a well-known for Mn. The broad band Red/NIR emission from Mn^{3+} is typically assigned to the $^1T_2 \rightarrow {}^5E$ emission but may also originate from the $^5T_2 \rightarrow {}^5E$ transition. To investigate if the NIR emitter is Mn^{3+}, non-stoichiometric samples doped with 10%Mn were synthesized while varying the amounts of MgO and Al_2O_3 precursor. It can be expected that excess Al_2O_3 will reduce the concentration of Mn^{3+} and that excess MgO will increase the Mn^{3+} concentration, based on the following equilibria reactions: [58]

$$3MgO \rightleftharpoons 2Mg'_{Al} + Mg^{\times}_{Mg} + 3O^{\times}_{O} + V^{\bullet\bullet}_{O}$$
$$3Al_2O_3 + V^{\bullet\bullet}_{O} \rightleftharpoons 4Al^{\times}_{Al} + 2Al^{\bullet}_{Mg} + 9O^{\times}_{O}$$
$$Mn^{\times}_{Mg} + V^{\bullet\bullet}_{O} \rightleftharpoons Mn'_{Mg} + V^{\bullet}_{O}$$

As Al is exclusively 3+ and Mg exclusively 2+, defect equilibria where is Mn is trivalent (either on a Mg^{2+} site or on a Al^{3+} site) will be shifted towards lower Mn^{3+} concentration in the presence of excess Al^{3+} ions while excess Mg^{2+} will shift the equilibria towards more Mn^{3+}.

The emission spectra in Figure 4-8 show indeed a strong increase in the NIR emission for 5% excess MgO and a decrease for 5 or 10% excess Al_2O_3.

The tentative assignment of the NIR emission to Mn^{3+} is further supported by investigating the luminescence of a 2% Mn-doped phosphor after synthesis in different environments. For this low concentration energy migration is hampered and the emission spectra reflect the concentrations of different ions, taking into account differences in absorption strength at the excitation wavelength. In the Supporting Information Figure S4-2 emission and excitation spectra are shown for synthesis in a strongly reducing N_2/H_2 atmosphere as well as an inert N_2 and oxidizing air atmosphere. For synthesis in N_2/H_2 green Mn^{2+} emission dominates. The phosphor fired in inert atmosphere shows a clear NIR emission band, in agreement with the formation of more Mn^{3+} in the less reducing atmosphere and assignment of the NIR emission to Mn^{3+}.

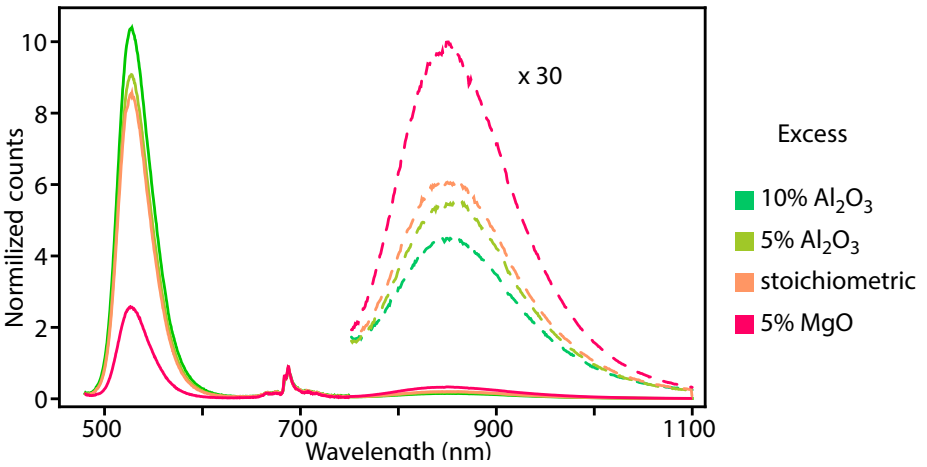

Figure 4-8. Emission spectra of $MgAl_2O_4$: 10% Mn synthesized with different excess of precursors. The NIR emission is also shown 30x enhanced for better visibility. The spectra were normalised at the 688nm emission peak.

The excitation spectrum of the NIR emission band reveals a weak absorption band around 460 nm that can be assigned to the $^5E \rightarrow {}^5T_2$ transition for Mn^{3+} and a strong band around 320 nm that can be assigned to a charge transfer band. Finally, following synthesis in even more oxidizing air also Mn^{4+} emission is observed showing the characteristic $^2E \rightarrow {}^4A_2$ narrow line emission of Mn^{4+} around 670 nm.

The assignment of the NIR emission to trivalent Mn^{3+} is in agreement with the experimental results. At higher dopant concentrations the strong increase in NIR emission is not only caused by enhanced energy migration over the Mn^{2+} sublattice but also, for a constant fraction on Mn being in the 3+ state, the absolute concentration of NIR emitting centers would increase at higher dopant concentrations giving rise to a sharp increase in NIR emission intensity for higher Mn-concentrations. Still, the identification of the NIR emitting trap as Mn^{3+} should be taken with some caution. NIR emission is also observed in undoped $MgAl_2O_4$,[59] this suggests that the NIR emission could also be caused by an intrinsic defect. It is notoriously difficult to unravel the nature of defects in luminescent materials and further research is needed to confirm the nature of the NIR emitting trap centers for the many phosphors in which broad band NIR emission is observed at high Mn-doping concentrations.

Conclusions

The origin of the NIR emission in highly Mn-doped phosphors was investigated. Earlier reports assign the NIR emission to exchange coupled Mn^{2+}-pairs in variety of host lattices. The reported spectral shifts are however more than 10 times larger than what can be expected based on exchange coupling parame-

ters for Mn^{2+}. Careful studies over wide Mn-concentration range in $Mg_{1-x}Mn_xAl_2O_4$ (x=0.01 – 0.5) indicate that energy migration towards NIR emitting trap centers is responsible for the NIR emission and not exchange coupled Mn-pairs. Temperature dependent measurement on $MgAl_2O_4$:50%Mn reveal a strong increase in the green emission intensity upon cooling to cryogenic temperatures, while the NIR emission intensity drops. This is consistent with energy migration that is hampered upon cooling as it requires thermal activation. The temperature dependence cannot be explained by a model in which exchange coupled Mn-pairs cause the NIR emission band in highly concentrated Mn-systems. Moreover, no redshifted absorption band is observed which would be expected for exchange coupled Mn-pairs. The NIR emitting center is tentatively assigned to Mn^{3+} and this assignment is supported by variations in the relative intensity of the NIR emission band in non-stoichiometric materials synthesized with excess MgO or Al_2O_3. Although the exact nature of the NIR emitting center is difficult to pinpoint it is evident that exchange coupled Mn-pairs cannot be responsible for the strongly redshifted emission in highly Mn-doped phosphors but that energy transfer to NIR emitting defects or impurities causes the NIR emission.

References

[1] Z. Xia, Q. Liu, Prog. *Mater. Sci.* **2016**, *84*, 59.
[2] M. A. van de Haar, M. Tachikirt, A. C. Berends, M. R. Krames, A. Meijerink, F. T. Rabouw, *ACS Photonics* **2021**, *8*, 1784.
[3] E. Song, Y. Zhou, X. B. Yang, Z. Liao, W. Zhao, T. Deng, L. Wang, Y. Ma, S. Ye, Q. Zhang, *ACS Photonics* **2017**, *4*, 2556.
[4] G. J. Hoerder, M. Seibald, D. Baumann, T. Schröder, S. Peschke, P. C. Schmid, T. Tyborski, P. Pust, I. Stoll, M. Bergler, C. Patzig, S. Reißaus, M. Krause, L. Berthold, T. Höche, D. Johrendt, H. Huppertz, *Nat. Commun.* **2019**, *10*, 1824.
[5] T. Senden, R. J. A. Van DIjk-Moes, A. Meijerink, *Light Sci. Appl.* **2018**, *7*, 2047.
[6] K. W. Houser, T. Esposito, *Front. Neurol.* **2021**, *12*, 25.
[7] S. Hariyani, J. Brgoch, *ACS Appl. Mater. Interfaces* **2021**, *13*, 16669.
[8] S. Fang, T. Lang, M. Cai, T. Han, *J. Alloys Compd.* **2022**, *902*, 163825.
[9] X. Qiu, Z. Luo, H. Jiang, H. Ding, Z. Liu, X. Chen, J. Xu, J. Jiang, *J. Am. Ceram. Soc.* **2020**, *103*, 5157.
[10] M. C. Giménez, M. Luxwolda, E. G. Van Stipriaan, P. P. Bollen, R. L. Hoekman, M. A. Koopmans, P. R. Arany, M. R. Krames, A. C. Berends, R. A. Hut, M. C. M. Gordijn, *Biology*. **2022**, *12*, 60.
[11] J. J. Casal, *Arab. B.* **2012**, *10*, e0157.
[12] J. Lai, J. Zhou, Z. Long, J. Qiu, D. Zhou, Y. Yang, K. Zhang, W. Shen, Q. Wang, *Mater. Des*. **2020**, *192,* 108701.
[13] An introduction to near infrared (NIR) spectroscopy | IM Publications Open, https://www.impopen.com/introduction-near-infrared-nir-spectroscopy, accessed: **Mar., 2021.**
[14] Q. Zhou, L. Dolgov, A. M. Srivastava, L. Zhou, Z. Wang, J. Shi, M. D. Dramićanin, M. G. Brik, M. Wu, *J. Mater. Chem. C* **2018**, *6*, 2652.
[15] B. Su, G. Zhou, J. Huang, E. Song, A. Nag, Z. Xia, *Laser Photon. Rev*. **2021**, *15*, 2000334.
[16] W. M. Yen, S. Shionoya, H. Yamamoto, Phosphor Handbook, *CRC Press*, **2018**.
[17] J. H. Schulman, *J. Appl. Phys.* **1946**, *17*, 902.
[18] A. J. van Bunningen, A. D. Sontakke, R. van der Vliet, V. G. Spit, A. Meijerink, *Adv. Opt. Mater*. **2023**, *11*, 2202794.

[19] A. D. Sontakke, A. J. van Bunningen, F. T. Rabouw, S. Meijers, A. Meijerink, *J. Phys. Chem. C* **2020**, *124*, 13902.
[20] P. J. McCarthy, H. U. Güdel, *Coord. Chem. Rev.* **1988**, *88*, 69.
[21] A. P. Vink, M. A. de Bruin, S. Roke, P. S. Peijzel, A. Meijerink, *J. Electrochem. Soc.* **2001**, *148*, E313.
[22] J. Si, L. Wang, L. Liu, W. Yi, G. Cai, T. Takeda, S. Funahashi, N. Hirosaki, R. J. Xie, *J. Mater. Chem. C* **2019**, *7*, 733.
[23] T. F. Soules, R. L. Bateman, R. A. Hewes, E. R. Kreidler, *Phys. Rev. B* **1973**, *7*, 1657.
[24] H. Masai, Y. Hino, T. Yanagida, Y. Fujimoto, Y. Tokuda, J. S. Kim, P. E. Jeon, J. C. Choi, H. L. Park, S. I. Mho, G. C. Kim, *Opt. Mater. Express*, **2015**, *5*, 617.
[25] I. Matsuyama, N. Yamashita, K. Nakamura, *J. Phys. Soc. Japan* **1989**, *58*, 741.
[26] E. Song, S. Ding, M. Wu, S. Ye, F. Xiao, S. Zhou, Q. Zhang, *Adv. Opt. Mater.* **2014**, *2*, 670.
[27] E. Song, J. L. Wang, D. C. Yu, S. Ye, Q. Y. Zhang, *J. Mater. Chem. C* **2014**, *2*, 8811.
[28] Z. T. Chen, E. H. Song, M. Wu, B. Zhou, Q. Y. Zhang, *Appl. Phys. Lett.* **2016**, 109.
[29] E. Song, J. Wang, S. Ye, X. B. Yang, M. Peng, Q. Zhang, L. Wondraczek, *Adv. Opt. Mater.* **2017**, *5*, 1700070.
[30] Z. Chen, E. Song, S. Ye, Q. Zhang, *J. Appl. Phys. 2017*, **122**, 213102.
[31] Z. Song, J. Zhao, Q. Liu, *Inorg. Chem. Front.* **2019**, *6*, 2969.
[32] E. Song, X. Jiang, Y. Zhou, Z. Lin, S. Ye, Z. Xia, Q. Zhang, *Adv. Opt. Mater.* **2019**, *7*, 1.
[33] X. Zhu, Y. Zhao, S. Zhang, J. Wu, D. Shao, E. Song, Q. Zhang, C. Yin, S. Ye, J. *Phys. Chem. C* **2021**, *125*, 27800.
[34] E. Song, M. Chen, Z. Chen, Y. Zhou, W. Zhou, H. T. Sun, X. Yang, J. Gan, S. Ye, Q. Zhang, *Nat. Commun.* **2022**, *13*, 1.
[35] X. Feng, L. Lin, R. Duan, J. Qiu, S. Zhou, *Prog. Mater. Sci.* **2022**, *129*, 100973.
[36] J. Ferguson, H. U. Güdel, E. R. Krausz, H. J. Guggenheim, *Mol. Phys.* **1974**, *28*, 893.
[37] P. J. McCarthy, H. U. Guedel, *Inorg. Chem.* **1984**, *23*, 880.
[38] C. R. Ronda, T. Amrein, *J. Lumin.* **1996**, *69*, 245.
[39] A. Morell, N. El Khiati, *J. Electrochem. Soc.* **1993**, *140*, 2019.
[40] C. Benecke, W. Busse, H. E. Gumlich, H. J. Moros, *J. Lumin.* **1988**, *40–41*, 627.
[41] P. De Visschere, K. Neyts, D. Corlatan, J. Van den Bossche, C. Barthou, P. Benalloul, J. Benoit, *J. Lumin.* **1995**, *65*, 211.
[42] L. R. Bradshaw, J. W. May, J. L. Dempsey, X. Li, D. R. Gamelin, *Phys. Rev. B* **2014**, *89*, 115312.
[43] J. Ferguson, H. U. Güdel, E. R. Krausz, H. J. Guggenheim, *Mol. Phys.* **1974**, *28*, 893.
[44] R. D. Shannon, *Acta Crystallogr. Sect. A* **1976**, *32*, 751.
[45] V. A. Dutov, A. N. Kiryakov, A. F. Zatsepin, A. V. Fokin, T. V. Dyachkova, A. P. Tytunnyuk, Y. G. Zainulin, *AIP Conf. Proc.* **2020**, *2313*, 030013.
[46] A. Ćirić, Z. Ristić, J. Periša, Ž. Antić, M. D. Dramićanin, *Ceram. Int.* **2021**, *47*, 27151.
[47] B. Henderson, I. G. F., Optical Spectroscopy of Inorganic Solids, *Oxford University Press, 1989*.
[48] G. Blasse, *Prog. Solid State Chem.* **1988**, *18*, 79.
[49] G. Blasse, B. C. Grabmaier, Luminescent Materials , *Springer-Verlag,* **1994.**
[50] J. P. M. van Vliet, D. van der Voort, G. Blasse, *J. Lumin.* **1989**, ***42***, 305.
[51] A. J. De Vries, M. F. Hazenkamp, G. Blasse, *J. Lumin.* **1988**, *42*, 275.
[52] O. Nijs, J. M. W. Verweij, G. Blasse, *Mater. Chem. Phys.* **1992**, *30*, 199.
[53] R. L. Greene, D. D. Sell, R. S. Feigelson, G. F. Imbusch, H. J. Guggenheim *Phys. Rev.* **1968**. *171*, 600
[54] S. Kück, S. Hartung, S. Hurling, K. Petermann, G. Huber, *Spectrochim. Acta - Part A Mol. Biomol. Spectrosc.* **1998**, *54*, 1741.
[55] L. Cornu, M. Duttine, M. Gaudon, V. Jubera, *J. Mater. Chem. C* **2014**, *2*, 9512.
[56] L. Marciniak, K. Trejgis, *J. Mater. Chem. C* **2018**, *6*, 7092.
[57] K. Petermann, G. Huber, *J. Lumin.* **1984**, *31–32*, 71.
[58] C. J. Ting, H. Y. Lu, *J. Am. Ceram. Soc.* **1999**, *82*, 841.
[59] N. Pathak, P. S. Ghosh, S. K. Gupta, S. Mukherjee, R. M. Kadam, A. Arya, *J. Phys. Chem. C* **2016**, *120*, 4016.

QR-Codes

Link to paper

Supporting Information

Supporting Information

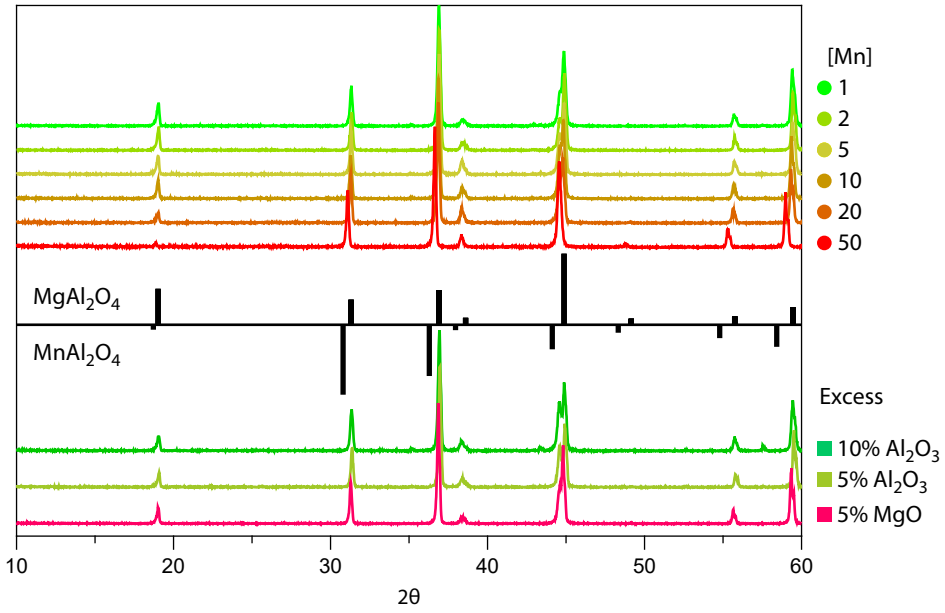

Figure S4-1. Diffractiograms of synthesized samples. On top the samples with increasing Mn concentrations. at the bottom the diffractograms of $MgAl_2O_4$: 10% Mn with excess precursor. In between the reference peaks for $MgAl_2O_4$ and $MnAl_2O_4$ are shown.

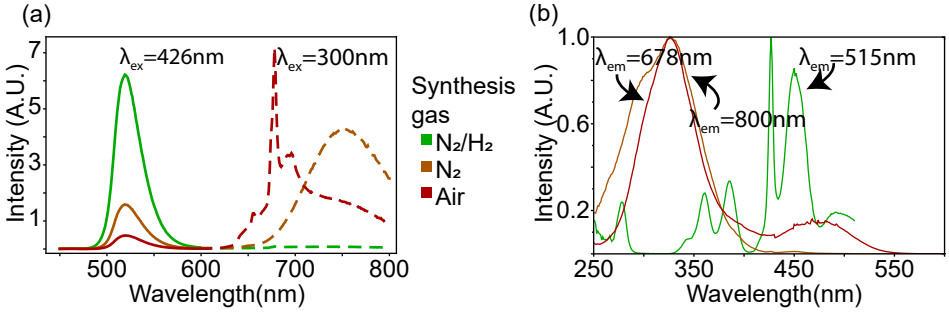

Figure S4-2. PL and PLE of $MgAl_2O_4$:2% Mn under different synthesis gasses. Dotted and full line in the PL (a) were measured using different detectors, so intensities of the NIR and visible part are not comparable. PLE spectra were normalised on their maximum intensity.

Chapter 5

New Hexagonal KRSF

Abstract

The efficient red emitting phosphor $K_2SiF_6:Mn^{4+}$ (KSF) is widely used for low power LED applications. The saturated red color and sharp line emission are ideal for application in backlight LEDs for displays. However, the long excited state lifetime lowers the external quantum yield (EQY) at high photon flux, limiting the application in (higher power density) lighting. Here we report on the synthesis of a new crystalline phase: hexagonal $(K,Rb)SiF_6:Mn^{4+}$ (h-KRSF). Due to the lower local symmetry the Mn^{4+} emission in this new host material shows a pronounced zero phonon line (ZPL), different from Mn4+ in the cubic KSF. The lower symmetry reduces the excited state lifetime and thus the loss of EQY under high photon fluxes and the spectral change also increases the lumen/W output. Temperature-dependent emission and lifetime measurements reveal a high luminescence quenching temperature of ~500 K, similar to KSF. The formation mechanism of h-KRSF was studied in situ by measuring the emission spectra of the precipitate in solution over time. Initially nanocrystalline cubic KRSF (c-KRSF) is formed which transforms into the microcrystalline hexagonal precipitate with a surprising exponential increase in transformation rate with time. The stability of the new phase was studied by temperature-dependent XRD and an irreversible transition back to the cubic phase was seen upon heating to temperatures above 200°C.

"You aren't doing it wrong, if nobody knows what you are doing."

Anonymous

Introduction

In the field of lighting and displays, the discovery of the blue light emitting diode (LED) marks the beginning of a revolution. Converting part of the blue LED output to longer wavelength light (green, yellow, orange or red) by a luminescent material (a phosphor) makes it possible to realize compact and efficient white light sources with a great flexibility in spectral distribution. The desired characteristics of a phosphor depend on the application. Lighting requires white LEDs (wLEDs) with a high efficacy (lumen/W output) and a high colour rendering index (CRI). The high brightness of wLEDs can only be realized using phosphors with emitters that have a high turnover rate (photons/s). In addition, the luminescence quenching temperature has to be high as the device locally heats up to 150 ^{0}C. In displays brightness is lower and this sets less stringent requirements on turnover rate and stability. However, phosphors with saturated colours with emission at specific wavelengths are preferred to extend the colour gamut while remaining efficient.

A successful red-emitting phosphor, especially for displays, is $K_2SiF_6:Mn^{4+}$ (KSF). The Mn^{4+} ion has the $3d^3$ configuration and in fluorides it shows sharp line emission around 620 nm due to vibronic $^2E \rightarrow {}^4A_2$ transitions. The narrow spectral distribution is ideal for displays. The luminescence of KSF was reported already back in 1973 but it was not until 2006 that the potential in LED lighting and displays was realized.[1,2] The spectral properties are superior to those of other red LED phosphors such as CASN:Eu^{2+}. The broad band red Eu^{2+} emission extends towards the NIR where the eye sensitivity is low. This reduces the lumen/W output. The narrow line emission around 620 nm of Mn^{4+} helps to extend the colour gamut in displays. Unfortunately, for higher power applications KSF is less suitable as the long emission lifetime (~10 ms) for the parity- and spin-forbidden $^2E \rightarrow {}^4A_2$ transition limits the turnover rate to ~100 photons/s per Mn^{4+} ion and thus lowers the external quantum yield (EQY) at higher photon fluxes.

The popular KSF phosphor has a cubic crystal structure and the Mn^{4+} ion is in a centrosymmetric octahedral coordination of fluoride ions. The inversion symmetry makes the parity selection rule strict and it can only be lifted by coupling with odd parity vibrations. As a result, the sharp emission lines observed are vibronic lines corresponding to ungerade vibrations that induce odd-parity crystal field components. The strictly forbidden zero-phonon line (ZPL) is not observed and the luminescence life time of the ^2E state is long. Later other Mn^{4+}-doped fluoride hosts were found with a hexagonal or trigonal crystal structures.[3–5] The lower local symmetry for the Mn^{4+} ion results in the appearance of a ZPL (induced by static odd parity crystal field components) in addition to vibronic lines. The emission lifetime for Mn^{4+} in these hosts is shorter and the higher eye-sensitivity at the ZPL wavelength is also

beneficial for the efficacy. Unfortunately, for all of these hosts the luminescence quenching temperature and/or stability were low and they could not replace KSF, in spite of the superior spectral properties.

There has been a search for Mn^{4+} phosphors similar to KSF but with a lower symmetry crystal structure to decrease the lifetime and induce a ZPL. Such a phosphor is reported here: hexagonal (K,Rb)SiF_6: Mn^{4+} (h-KRSF:Mn^{4+}). Normally K_2SiF_6 and Rb_2SiF_6 as well as their solid solutions form a cubic phase. Yet, here we show that under specific reaction conditions the mixed solid solutions can form in a stable hexagonal phase. Interestingly, the existence of the hexagonal crystal structure for KSF or KRSF has sporadically been reported. The crystal structure was described by Kolditz and Preiss in 1963[6], referring back to earlier reports from 1904.[7] In the mineralogy of fumaroles grains of 0.3 mm have been reported with the chemical formula K_2SiF_6 and hexagonal symmetry[8] while in 1952 hexagonal KSF was found when analysing chemicals of a decommissioned chimney that was used to drain sulphuric acid and hydrogen fluoride gases.[9] There are also a few recent examples on the hexagonal form of KSF. In 2015 the luminescence KSF:Mn^{4+} was measured at increasing pressure. Between 9 and 13 kbar a strong ZPL arises which does not disappear after decompression. This could be due the formation of nanocrystalline hexagonal KSF, but XRD measurements after decompression did not indicate a cubic-to-hexagonal phase transformation.[10] In 2014 hexagonal KSF:Mn^{4+} was synthesized, but no luminescence was observed.[11] So far no reports have been made that measured and verified Mn^{4+} in hexagonal KSF. For h-KRSF there is one patent that reports the existence and luminescence of this phase and describes the synthesis of KRSF:Mn^{4+} as a phosphor.[12]

In this paper we describe the reproducible synthesis of hexagonal KRSF:Mn^{4+}. We report the improved luminescence properties induced by the lower site symmetry for Mn^{4+} in the hexagonal phase and evaluate the advantageous properties such as a shorter luminescence decay time and a strong ZPL increasing the efficacy of the phosphor. We follow the formation of h-KRSF by measuring the Mn^{4+} emission to probe the phase transition from cubic to hexagonal and show how after a long induction period h-KRSF starts to form and the transformation rate of h-KRSF increases exponentially with time. Finally we determine the temperature stability of h-KRSF by measuring the back transformation to the cubic KRSF via temperature-dependent XRD and luminescence measurements.

Methods

Synthesis

The synthesis procedure for KRSF is inspired by previously reported methods for KSF. As Mn-precursor K_2MnF_6 was used. As this is not commercially available because of the low stability, it was synthesized as described by Roesky.[13]

Other chemical used were 40% HF and 30% H_2SiF_6, from Sigma Aldrich, KHF_2 from Strem Chemicals and RbF from Chempur.

For the typical synthesis of $KRbSiF_6$: 0.5% Mn^{4+}, 12 mg K_2MnF_6, 0.391 g KHF_2, and 0.523 g RbF were dissolved in 1.5 ml aqueous HF (48 vol%). In a second beaker, 1.5 ml of aqueous 30 wt% H_2SiF_6 was combined with 5 ml 48% HF. Upon combining the two solutions some turbidity was observed. To regain full dissolution of all precursors, ~20 ml aqueous HF was added until a clear solution was obtained. This solution was added to 4 times its volume of EtOH (~100ml). No precipitate was visible by naked eye but under illumination with a handheld violet laser (405 nm) the solution showed red luminescence. This indicates the formation of nanosized KRSF particles. The aqueous EtOH solution was left to evaporate for two days to a week in the fume hood. The amount of precipitate gradually increases during evaporation. After all the liquid has evaporated the solid material was washed with 3% H_2O_2 aqueous solution and subsequently with EtOH, after which it was dried at 100ºC for 1 to 2 hours. The hexagonal KRSF (h-KRSF) synthesized through this procedure contained 20 to 50 mole% of Rb. The K, Rb and Mn concentrations of the samples discussed below were measured with ICP-OES and values can be found in the Supporting Information Section S5-1.

For comparison also cubic KRSF (c-KRSF) was synthesized. Two different methods were employed. One involved immediate separation by decantation of the precipitate formed directly after the addition of H_2SiF_6 in the synthesis method described above. The second method was heating the hexagonal KRSF to 400 °C for 30 minutes.

Characterization

The powders were examined by using powder X-ray diffraction to determine phase purity. A Bruker D2 PHASER X-ray diffractometer with a Co source ($\lambda_{K\alpha}$ = 1.7902 Å) was used at 30 kV operating voltage and 10 mA current. The temperature-dependent X-ray diffraction measurements were performed with a Malvern Panalytical Aeris Research diffractometer equipped with an Anton Paar BTS 500 heating stage and a Cu K_α ($\lambda_{K\alpha}$ = 1.5418 Å) radiation source.

The K, Rb and Mn concentration in the phosphors were examined with inductively coupled plasma optical emission spectroscopy (ICP-OES). All measurements were performed on a Perkin Elmer Optima 8300DV spectrometer (Mn λ_{em}=257.610 nm, Rb λ_{em}=780.023 nm, and K λ_{em}=766.490 nm). Aqua regia was used to dissolve the phosphors.

Optical spectroscopy

Photoluminescence (PL) and PL excitation (PLE) spectra were recorded using an Edinburgh Instruments FLS 920 spectrofluorometer equipped with a 450 W Xe lamp as excitation source and a Hamamatsu R928 photomultiplier tube (PMT) detector. PL decay curves were recorded using a tuneable optical

paramagnetic oscillator (OPO) Opotek Opolette HE 355II giving ~1-5 mJ pulses in the visible or near infrared (pulse width: 10 ns; repetition rate: 20 Hz) as excitation source and the multi channel scaling (MCS) capabilities included in the Edinburgh spectrofluorometer. For temperature dependent studies a temperature-controlled stage from Linkam Scientific (THMS600) was built in the spectrofluorometer for measurements in a –190 °C to 450 °C temperature range.

The *in-situ* monitoring of the cubic-to-hexagonal phase transformation was performed with a custom build optical set-up. In short, the beaker containing the reaction mixture was illuminated from above with an OBIS LX 445 nm 45 mW laser with a fiber pigtail output. An AvaSpec-HSC 1024×58 TEC-EVO CCD spectrometer equipped with an optical fiber and a 472 nm longpass filter was used to collect the red emission on the side of the beaker to measure emission spectra at regular time intervals during the formation (for up to several days).

DFT calculations

To assess the stability of the cubic vs. hexagonal phase for KSF and KRSF, first-principles total energy calculations[14] were performed based on density functional theory (DFT)[15,16] using the Projector Augmented Wave (PAW) as implemented in Vienna ab-initio simulation package.[17,18] Frozen core approximation was combined with PAW and the valence electron configurations are $3s^2 3p^6 4s^1$ for K, $4s^2 4p^6 5s^1$ for Rb, $3s^2 3p^2$ for Si, $2s^2 2p^5$ for F. Exchange and correlation were treated with the generalized gradient approximation. [19] The wave functions were expanded in a plane-wave basis set with kinetic energy cut off of 600eV. 8×8×8 and 6×6×4 Monkhorst-pack *k*-points mesh were used for the integration in *k* space in the Brillouin zone for the cubic and hexagonal unit cell, respectively. The structural optimization were performed until each component of the interatomic force became less than 1.0×10^{-3} eV/Å.

Results and Discussion

Phase Identification

To investigate the crystal structure and phase purity of the different materials, after synthesis the dry powders were checked by measuring the x-ray diffractograms. In Figure 5-1 the diffractograms of the different powders are shown with their respective reference underneath.

In Figure 5-1 we can see that for all samples there is good agreement with the reference diffraction patterns. This shows that the different synthesis methods result in phase pure crystalline materials. For cubic KSF and RSF the crystal structure is well established and the reference diffractograms are well-known. For cubic KRSF the diffraction lines are at angles in between KSF

and RSF, as expected for a solid solution. A good agreement with the experimentally observed positions of diffraction lines was obtained by assuming an increase of 2% in lattice distances compared to the KSF reference. A slight increase is expected by the replacement of K by Rb as Rb (1.72 Å) is bigger than K (1.64 Å) causing a small expansion of the unit cell.[22]

The reference pattern of h-KRSF is based on earlier work on hexagonal KSF. In Ref. [6] the XRD pattern for h-KSF is reported and used to derive lattice parameters a=5.67 Å and c=9.24 Å. The diffraction pattern obtained here for KRSF is very similar. A good match is obtained for slightly larger lattice parameters a=5.78 Å and c= 9.42 Å providing convincing evidence for the formation of hexagonal $KRbSiF_6:Mn^{4+}$.

To evaluate the particle size and particle size distribution, SEM images were made of the final product. The SEM image in Figure 5-2 shows that the synthesis procedure used results in a homogeneous particle size distribution with an average particle size of ~30 µm.

Optical properties

To study the optical properties of Mn^{4+} in the new h-KRSF both PL and PLE spectra were measured for low-doped samples (0.1–0.5% Mn^{4+}). For comparison the spectra of Mn^{4+} in cubic KRSF, KSF and RSF were measured as well. In Figure 5-3 it is observed that all the PLE spectra have two relatively strong and broad excitations bands around 360 nm and 460 nm. The 460 nm band shows some sharp lines around 470 nm. These can be ascribed to Xe-lamp lines that are visible in spite of correcting the spectra for variations in the Xe-lamp intensity. A zoom-in for the area between 560 and 625 nm shows a multitude of weak and narrow excitation lines. The PLE spectra of the four samples are very similar with one exception: there is sharp extra peak at 621.5 nm for Mn^{4+} in h-KRSF. In the PL spectra (Figure 5-3c) again all spectra are very similar showing sharp emission lines at the same positions, with small shifts of ~0.5 nm to longer wavelengths from KSF to RSF. Again there is one exception: an extra peak at 621.5 nm for Mn^{4+} in the hexagonal form of KRSF.

Based on the Tanabe-Sugano diagram for $3d^3$ ions in octahedral symmetry, the excitation bands at 360 and 460 nm in the PLE spectra are assigned to the $^4A_2 \rightarrow {}^4T_1$ and $^4A_2 \rightarrow {}^4T_2$ transitions, respectively. In the zoom-in spectra, Figure 5-3b, the peaks observed from 560 to 595 nm are assigned to the vibronic lines of the $^4A_2 \rightarrow {}^2T_1$ transition and from 600 to 625 nm to vibronic excitation lines of the $^4A_2 \rightarrow {}^2E$ transition in the cubic modifications. For Mn^{4+} in inversion symmetry all $3d^3 \rightarrow 3d^3$ transitions are parity forbidden and coupling with odd-parity vibrations is required to partly lift the parity selection rule resulting in the observation of vibronic excitation and emission lines. In h-KRSF the Mn^{4+} ion is in a site with lower symmetry and static odd parity crystal field components allow for breaking the parity selection rule. As a result, also the purely electronic zero phonon transition can be observed. For the $^4A_2 \rightarrow {}^2E$ transition in h-KRSF this zero-phonon line (ZPL) is at 621.5 nm and is identical

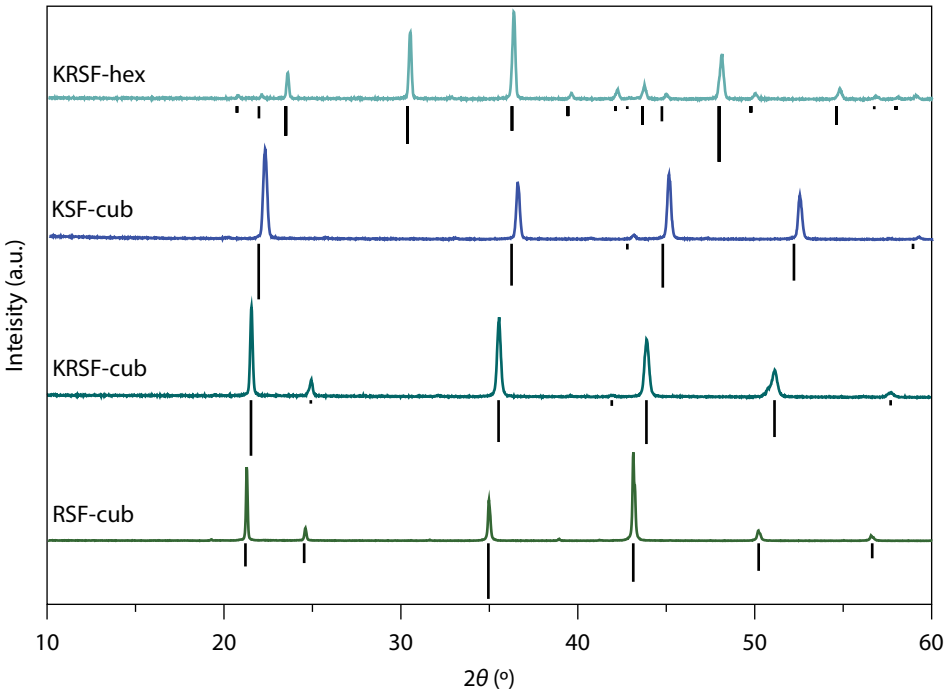

Figure 5-1. X-ray diffractogram of Mn^{4+}-doped fluorides. From top to bottom the diffractograms of hexagonal $KRbSiF_6$, cubic K_2SiF_6, cubic $KRbSiF_6$ and cubic Rb_2SiF_6 doped with 0.5% Mn4+ are shown. Below the experimental patterns, the reference patterns are plotted.[8,20,21] Note that these diffractograms are recorded using a Co X-ray source.

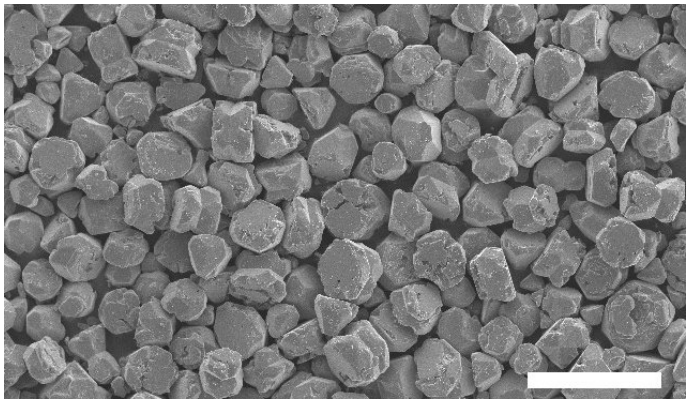

Figure 5-2. SEM image of synthesized hexagonal KRSF: 1.8% Mn^{4+}. Scale bar at the bottom is 100 µm. The average particle size is ~30 µm.

in the excitation and emission spectra. The positions of the vibronic emission lines in KSF (Figure 5-3c) are 597, 608, 613, 630, 635 and 648 nm, in agreement with earlier reports. The lines at 630, 635 and 648 nm are Stokes vibronic lines due to coupling with ν_6, ν_4 and ν_3 vibrations. The lines at 597, 608 and 613 nm are anti-Stokes vibronics at the same energy differences from the ZPL (that is hardly observed, except for h-KRSF) as the Stokes lines.

The change in local symmetry around the tetravalent ion in cubic KSF to hexagonal KSF is key for understanding the appearance of the ZPL. In the cubic phase the Si^{4+} atom (or the Mn^{4+}) is symmetrically surrounded by 6 equidistant fluorine ligands at 1.677 Å. In the hexagonal phase of KSF there is a slight distortion of the octahedron: 3 ligands are at a distance of 1.681 Å while the others are at a distance of 1.688Å.[8,20] The same deviation from inversion symmetry for Mn^{4+} can be expected in h-KRSF and explains why for the hexagonal phase a zero phonon line is observed and not for the cubic phases.

The enhanced ZPL is beneficial for the performance. The additional emission at ~620 nm where the eye sensitivity is higher increases the efficacy. The lu-

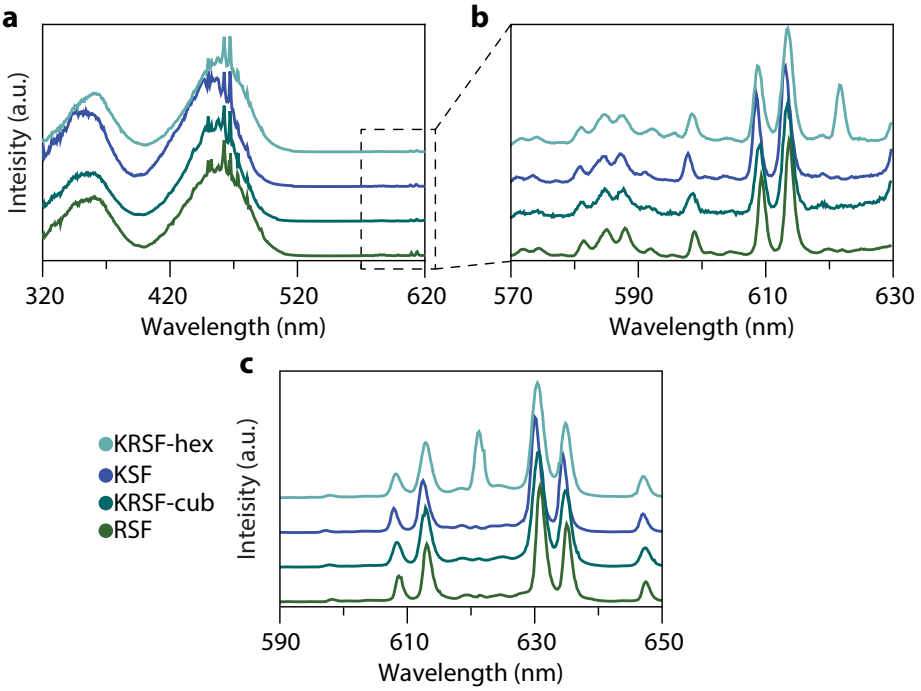

Figure 5-3. Photoluminescence excitation (PLE) and photoluminescence (PL) spectra of hexagonal $KRbSiF_6$ and cubic M_2SiF_6 (M = K and/or Rb) doped with 0.1-0.5% Mn^{4+}. (a) PLE spectra recorded at λem = 630 nm that show two spin-allowed $^4A_2 \rightarrow {}^4T_2$ and $^4A_2 \rightarrow {}^4T_1$ excitation bands centered at 460 and 360 nm respectively. (b) PLE spectra recorded for 648 nm emission, showing the spin-forbidden, vibronic $^4A_2 \rightarrow {}^2T_1$ and ^2E excitation lines. Multiple vibronic excitations are visible for both $^4A_2$, ^2E excitation (range 598nm-619nm) and the $^4A_2 \rightarrow {}^2T_1$ excitation (570–596 nm) (c) PL spectra of the $^2E \rightarrow {}^4A_2$ transition excited at 450 nm. Only for the hexagonal $KRbSiF_6$ samples the ZPL is clearly present at 621.5 nm, in excitation and emission.

minous response function has its maximum at 550 nm and drops to 1% of the maximum at 680nm. A higher fraction of the emission spectrum towards longer wavelengths reduces the efficacy. If we compare c-KRSF to h-KRSF, a smaller fraction of the emission is from the Stokes emission lines of 630, 636 and 648 nm. The additional emission intensity at ~620 nm results in an efficacy increase of 2.9% for h-KRSF compared to c-KRSF (see Supporting Information Section S5-2). In addition, deviation from inversion symmetry will also increase the $^4A_2 \rightarrow {}^4T_2$ absorption strength for the blue excitation wavelength at 450 nm. The increased absorption strength at 450 nm was not quantified but it is well known that also for spin-allowed $3d^n \rightarrow 3d^n$ transitions relaxing the parity selection rule increases the transition probability. To evaluate the efficiency of the new h-KRSF phosphor quantum yield measurements were done. A sample with 1.8 mole% Mn incorporated had an internal quantum yield of 91%. We consider this value to be very high as little effort was put into optimizing the synthesis.

For practical applications a wLED phosphor needs to be resilient to high temperatures and a humid atmosphere. To test the stability the luminescence of h-KRSF was measured after synthesis and this was compared to the luminescence after 48 h exposure to 85% humidity at 85°C. A KSF phosphor was measured simultaneously. For the h-KRSF a decrease in luminescence was seen of 16% which is considerably worse than the KSF which showed a loss of 1 to 2%. The relatively fast degradation of h-KRSF compared to KSF we attribute to the incorporation of Rb. Rb compounds tend to be more hygroscopic than K compounds, thus enhancing the degradation.[23] For practical application the stability needs to be improved e.g. by post-synthesis treatment, overcoating and/or encapsulation in a protective matrix using strategies that are also explored for KSF.[24,25] Reducing the Rb-content from 50% to 20% (a Rb-concentration for which the hexagonal phase can still be obtained, *vide infra*) may also enhance the stability. Further optimization is required to explore the potential of h-KRSF as a new LED phosphor. An initial test with h-KRSF phosphor in a w-LED shows promising results with a performance that is similar to a wLED with KSF.

Concentration dependent luminescence

The 450 nm absorption by Mn^{4+} in the $^4A_2 \rightarrow {}^4T_1$ absorption band involves a spin-allowed but parity-forbidden transition. As discussed above, the deviation from inversion symmetry in h-KRSF is expected to make the absorption stronger than in c-KRSF or KSF but this absorption is much weaker than for fully allowed transitions such as the $4f^n \rightarrow 4f^{n-1}5d$ transition in Ce^{3+} or Eu^{2+}. A high Mn^{4+} concentration is thus beneficial to reduce the amount of phosphor that is required to absorb sufficient blue LED light in a wLED. At the same time, a high dopant concentration can lead to concentration quenching. Energy transfer between neighbouring ions will cause migration of the excitation energy over the dopant sublattice. Especially above the percolation

point (where a 3D connected lattice of dopant ions is realized) the migrating excitation energy can probe a large volume in which there is a high probability to encounter a defect or impurity quenching site causing concentration quenching. Investigating the concentration dependence of the luminescence efficiency is therefore important and a concentration series of h-KRSF:Mn^{4+} x% (x=0.1 to 10) was synthesized. It is important to realize that the fraction of Mn^{4+} in the synthesis mixture is not the same as the fraction incorporated in the h-KRSF. Indeed, after evaporating the EtOH out of the reaction mixture darker coloured spots are visible within the dry powder. Washing with H_2O_2 removes these spots. Probably these spots were compounds with a high concentration of Mn that dissolve in H_2O_2. This also means that the fraction of Mn^{4+} incorporated in h-KRSF is lower than the nominal concentration. To check the actual Mn concentration, inductive coupled plasma optical emission spectroscopy (ICP-OES) measurements were done. The measurements show that 20 to 60% of the added Mn is actually incorporated (Supporting Information Section S5-3). The concentrations mentioned below always refer to actual concentrations in the phosphors as determined with ICP-OES.

To study the concentration-dependent optical properties both emission spectra and luminescence decay curves were measured for samples with Mn^{4+} concentrations varying between 0.1 and 10 mole%. In Figure 5-4a the emission spectra of samples with different Mn concentrations are shown under 450 nm excitation. The samples were diluted 10× (wt%) with optically inactive $BaSO_4$ to limit the pathlength of light through the h-KRSF phosphor and re-

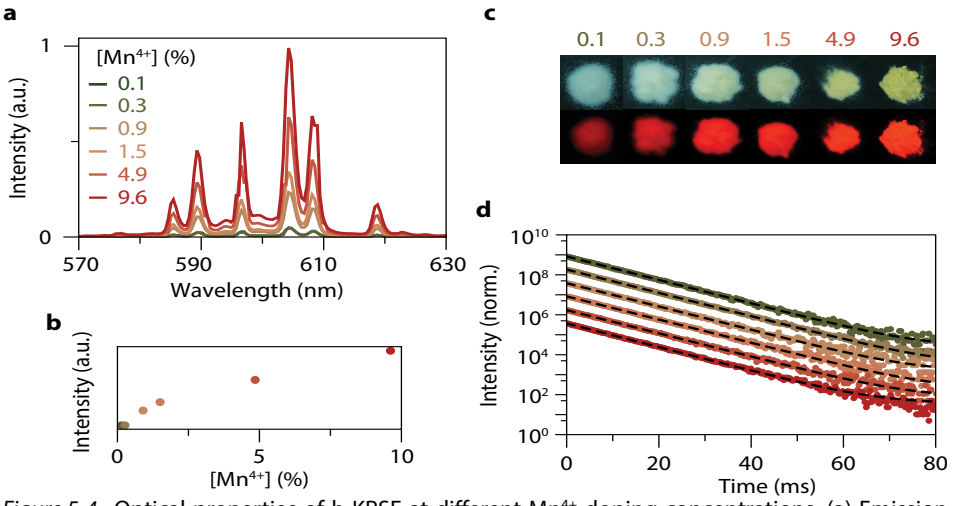

Figure 5-4. Optical properties of h-KRSF at different Mn^{4+}-doping concentrations. (a) Emission spectra of h-KRSF for different doping concentrations that range from 0.1–9.6 mole% with respect Si^{4+} (λ_{exc} = 450 nm). All samples are diluted 10× (wt%) with $BaSO_4$. (b) Integrated intensity of the emission spectra in panel a. The sublinear increase of emission intensity with [Mn^{4+}] is ascribed to saturation in the absorption of the blue excitation light. (c) Photographs of the undiluted KRSF samples under flashlight (top row) and UV (bottom row) illumination. (d) PL decay curves of the same samples as in panel a for ns pulsed excitation at 450 nm and emission at 630 nm. The dashed lines show the single-exponential fit to the experimental data.

duce saturation effects in blue light absorption. It can be seen that the intensity increases with increasing Mn concentration. The integrated intensities as function of Mn^{4+} concentration (Figure 5-4b) show a rapid increase at low concentrations (up to 1% Mn^{4+}) after which it levels off. This non-linear increase at high dopant concentrations has been observed before and is explained by saturation of blue light absorption. The integrated intensities of the undiluted phosphors show an even stronger levelling off with increasing Mn^{4+} concentration (Supporting Information Section S5-4). As the Mn^{4+} concentration increases a substantial part of the blue light is absorbed and the fraction of absorbed light no longer increases linear with Mn^{4+} concentration as is also evident from Lambert-Beers' law. Only for a low value of ε.c.l (molar extinction coefficient × concentration × path length) the fraction of absorbed light increases linear with concentration. This makes it difficult to determine if concentration quenching occurs based on concentration dependent emission intensities.

A better method to study concentration is measuring luminescence lifetimes. In case of non-radiative loss processes as a result of concentration quenching, the emission life time will decrease. Luminescence decay curves of the 630 nm emission after pulsed 450 nm excitation are shown in Figure 5-4b. A single exponential decay is observed for all concentrations and the decay times are constant ~ 6.2 ms. The single exponential decay curves and constant decay time indicates that no concentration quenching occurs up to at least 10% Mn^{4+}.

Temperature-dependent luminescence

The temperature stability of luminescence is an important aspect of wLED phosphors. Heat is generated by the LED chip and also by heat dissipation inherent to the conversion of a higher energy blue photon to green or red photons. The local temperature of a phosphor in wLEDs can easily reach 150 °C. The thermal quenching behavior is therefore crucial. Indeed, previously Mn^{4+}-doped fluorides have been found where the lower local symmetry also resulted in the desired observation of a strong ZPL and shorter emission life time but the poor thermal quenching behavior made these phosphors unfit for application in wLEDs.[3,5,26] The thermal quenching behavior of h-KRSF: 0.1% Mn^{4+} was therefore measured and compared with that of cubic KRSF: 0.1% Mn^{4+} and KSF: 0.5%: Mn^{4+}. The temperature dependence of the integrated emission intensities in the relevant high temperature region 373–700 K is shown in Figure 5-5. The corresponding emission spectra at different temperatures of the three samples are shown in the Supporting Information Section S5-5. When the temperature increases, the emission intensity remains constant until 450 K above which it starts to decrease.

Measuring emission intensity as function of temperature to probe thermal quenching can be complicated by intensity variations not related to thermal quenching, for example when the oscillator strength of the absorption transi-

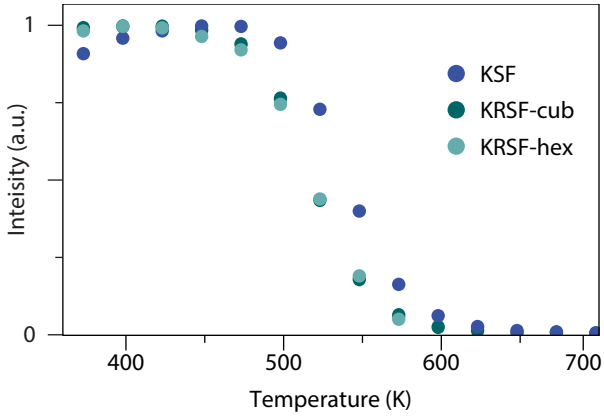

Figure 5-5. Integrated emission intensity as a function of temperature for cubic KSF and cubic and hexagonal KRSF doped with 0.1% Mn^{4+}.

tion is temperature-dependent. In addition, practical aspects such as changes in alignment, collection efficiency or excitation source intensity can give rise to intensity variations not related to thermal quenching. A fast and reliable method to determine the thermal quenching temperature is measuring the emission lifetime as a function of temperature. As non-radiative decay sets in, the emission lifetime shortens as the lifetime is the inverse of the sum of radiative and non-radiative decay rates. Therefore also lifetimes were measured as function of temperature for h-KRSF: 0.1% Mn^{4+} and c-KRSF: 0.1% Mn^{4+} and KSF: 0.5%: Mn^{4+} and are shown in Figure 5-6a. All the decay curves are single exponential. The lifetimes of the Mn^{4+} emission in the three different host lattices is shown as a function of temperature in Figure 5-6b. For all three host matrices it can be seen that the lifetime decreases slowly up till 450–480K after which the lifetime drops sharply, consistent with the temperature-dependent intensity measurements.

Before discussing the luminescence quenching temperature it is interesting to discuss differences in lifetimes for Mn^{4+} emission in the three compounds: the lifetime is longer for KSF and c-KRSF than for h-KRSF. As discussed above, the perfect octahedral coordination in the two cubic lattices imposes a strict parity selection rule. This does not only prevent the observation of a ZPL but also reduces the overall transition probability as the ZPL transition is forbidden. The room temperature emission lifetime is ~6 ms for Mn^{4+} in h-KRSF vs. ~8 ms in the cubic lattices. The shorter lifetime in h-KRSF is beneficial for application in wLEDs. As mentioned in the introduction, the long emission lifetime is a limiting factor in the total light output and prevents the application of KSF in high brightness wLEDs. The 25% shorter lifetime helps to improve the performance of h-KRSF in higher brightness sources although the lifetime is still long compared to that for emission in other wLED phosphors relying on d-f emission from Ce^{3+} (~40-80 ns) or Eu^{2+} (~1-2 µs).

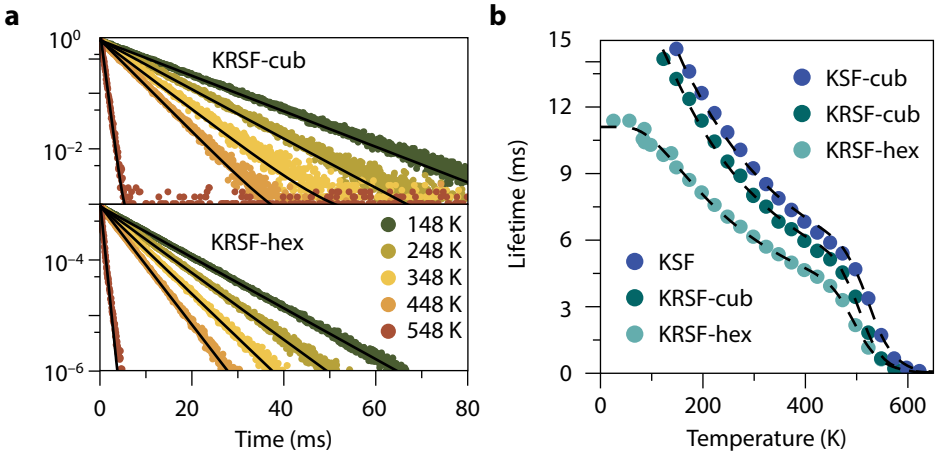

Figure 5-6. (a) PL decay measurements of Mn^{4+} emission in cubic (top) and hexagonal (bottom) KRSF, single-exponential fits to the data are shown in black. (b) Emission lifetime of the Mn^{4+} emission as a function of temperature in cubic KSF, c-KRSF and h-KRSF. All samples were excited at 450 nm and luminescence decay was recorded at 631 nm (KSF and c-KRSF) or 621 nm (h-KRSF).

In Figure 5-5 it is observed that the luminescence intensity is constant up until 450 K while the lifetime decreases gradually with temperature between 100 and 400 K (Figure 5-6b). This is an indication that the change in emission lifetime is not caused by temperature quenching. This is generally observed for ^2E emission of Mn^{4+} and explained by an increase in vibronic transition probabilities induced by a higher phonon occupation number *n*. It is well-established that the transition probability for Stokes vibronics scales with (*n*+1) and anti-Stokes vibronics with *n*.[26] The corresponding change in radiative lifetime as a function of temperature is described by:

$$\tau_r(T) = \frac{\tau_r(0)}{\coth(h\nu/2kT)} \tag{5.1}$$

Here (T) is the radiative lifetime at temperature *T* (in K), hν is the effective phonon energy and k_b is the Boltzmann constant. This equation describes the emission lifetime before temperature quenching sets in at 450 K. Temperature quenching for Mn^{4+} has been shown to occur via the $^4T_2$ state with an activation energy *ΔE*. Together with temperature dependence for the radiative decay time from Equation (5.1) the expression for the lifetime as a function of temperature is:

$$\tau(T) = \frac{\tau_r(T)}{1 + \frac{\tau_r(T)}{\tau_{nr}} e^{-\Delta E/kT}} \tag{5.2}$$

where τ_{nr} is the non-radiative decay time which is typically in the order of picoseconds, the time scale of vibrations. We can now use equations 5.1 and 5.2

to find the quenching temperature T_{50}, defined as the temperature at which . The T_{50} temperatures determined in this way for KSF, c-KRSF and h-KRSF were found to be 530, 510 and 503 K, respectively. All temperatures are sufficiently high to prevent thermal quenching in wLEDs. There is a small decrease in T_{50} from KSF to KRSF. The thermal luminescence quenching mechanism has been shown to occur by thermal crossover to the $^4A_2$ state via the $^4T_2$ state. The lower the energy of the $^4T_2$ state, the lower the quenching temperature will be. The slightly lower T_{50} values for KRSF are consistent with a small red shift (from 452 nm is KSF to ~ 458 nm in c-KRSF) of the $^4T_2$ excitation band. The small redshift may be related to slightly larger distances to the F^- ligands in compounds with increasing Rb content which lowers the crystal field splitting.[26]

Formation mechanism

The formation mechanism of the h-KRSF is intriguing. The method was found serendipitously: the addition of extra aqueous HF to dissolve the initial precipitate followed by the addition of ethanol (EtOH) was meant to precipitate a random mixed phase K/Rb system to investigate the role of disorder in a more distant cation (K/Rb) coordination sphere on the Mn^{4+} luminescence. Interestingly, the absence of a ZPL in c-KRSF shows that deviations from inversion symmetry by disorder in the second (K/Rb) coordination sphere are too small to effectively relax the parity selection rule, as was the original goal of the research project. When the EtOH addition did not result in precipitation, the solution was left to evaporate for several days and the new h-KRSF phase was found. It is interesting to obtain better insight in the formation mechanism of h-KRSF. Therefore, to follow the formation of h-KRSF emission spectra were recorded during the evaporation process. A 445 nm laser was used to illuminate the reaction beaker (as shown in the Supporting Information Section S5-6) while the emission spectra were recorded at regular time intervals over a period of days by a simple fiber-coupled CCD spectrometer. The results are shown in Figure 5-7. Immediately after pouring the reaction mixture in the EtOH the solution shows emission spectra typical of the cubic phase with vibronic Stokes and anti-Stokes emission lines, but no ZPL. The solution remains transparent after mixing, indicating the formation of 50-100 nm nanocrystals. No precipitation is observed, however, blue excitation shows that much of the c-KRSF immediately concentrates in the lower part of the beaker. The presence of the typical Mn^{4+} spectrum without a ZPL in the initially formed clear solution indicates that nanocrystalline c-KRSF is formed. The characterization and optical properties of nanocrystalline KRSF (and KSF) deserves further study but is beyond the scope of this work. Stabilizing the KRSF nanocrystals may be interesting for applications where nanocrystalline KSF offers advantages over the conventional microcrystalline material.

To follow the transformation from cubic to hexagonal KRSF, the emission spectra as recorded over time are shown in Figure 5-7. The formation of

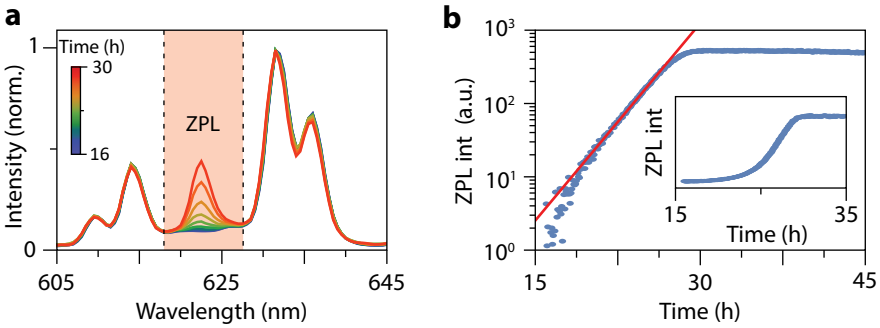

Figure 5-7. In-situ emission spectroscopy measurements to follow hexagonal KRSF:Mn^{4+} formation. (a) A selection of emission spectra recorded between 16 and 30 hours after pouring the precursor mixture into EtOH. During this time the ZPL intensity increases strongly, indicating the transition from c-KRSF to h-KRSF. (b) Logarithmic plot of the integrated emission intensity of the ZPL peak, corrected for "background" signal as recorded before 16 h. The integration limits are indicated by the highlighted area in panel a. A single exponential function is fitted to the data between 16 and 26 hours after mixing and is plotted in red. The inset shows the corrected ZPL intensity between 15 and 35 hours in a linear plot.

h-KRSF is probed by monitoring the intensity of the ZPL. No ZPL is present in the cubic phase and by integrating the 618 to 627 nm range the ZPL intensity is measured by subtracting the background measured in spectra recorded immediately after the addition to EtOH. The integrated ZPL intensity increases over time and shows a peculiar time dependence. There is a delay in the formation and only after ~15 h the formation of h-KRSF starts and a small ZPL appears. The relative intensity of the ZPL increases, first slowly and then rapidly until all c-KRSF is transformed into h-KRSF. The rapidly increasing transformation rate can be well-described by exponential growth: when plotted on a logarithmic scale vs. time the ZPL intensity increase is linear. This behavior is typically observed, also when reaction conditions are changed. There is always a delay time (induction period) before the formation of h-KRSF starts and after that the ZPL intensity increases exponentially with time. The reaction conditions were varied by changing the K/Rb ratio and the alcohol used. The minimum fraction of Rb required to form the hexagonal phase is 20% for the synthesis procedure followed, resulting in part hexagonal and part cubic KRSF. For all the different alcohols used (from methanol to butanol) formation of h-KRSF was observed. The induction period varied and was longer for a lower Rb content (Supporting Information Section S5-7).

Before discussing the formation mechanism, it is good to evaluate the thermodynamic stability of the hexagonal vs. cubic phase. To test this, first temperature-dependent XRD was used. Diffractograms from 17.5 to 24.0° (2θ) were measured. This range was chosen because in this area there are peaks that distinctively belong to either the cubic or hexagonal KRSF. After each measurement the sample was heated by 10K and the next diffractogram was measured. The results between 18 to 19° 2θ are shown in Figure 5-8 and the full pattern (17.5 to 24.0° 2θ) is shown in the Supporting Information Sec-

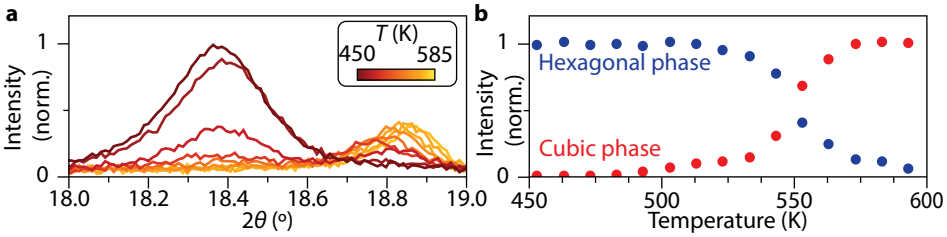

Figure 5-8. Monitoring the stability of hexagonal KRSF with temperature-dependent XRD measurements. (a) Selection of diffractograms measured between 450 and 585 K. The peak at 18.85 ° corresponds to the hexagonal phase ((002) reflection) and the peak at 18.4° corresponds to the cubic phase ((111) reflection). (b) Integrated intensity underneath the peaks corresponding to the hexagonal (blue) and cubic (red) phase of KRSF with temperature intervals of 10 K. Note that for recording these diffractograms a Cu Kα (λKα = 1.5418 Å) X-ray source is used.

tion S5-8. Upon heating above 500K the peaks at 18.85° and 20.1° 2θ (from h-KRSF) diminish and then disappear while the peaks at 18.4° and 21.2° 2θ (from c-KRSF) increase in intensity and then remain constant above 570K. After cooling down to RT the peaks at 18.8° and 20.1° 2θ do not reappear.

The transformation from the hexagonal to cubic indicates that at higher temperatures the cubic phase is the most stable phase. The observation that the peaks at 18.85° and 20.1° 2θ do not reappear upon cooling shows that the transformation is irreversible. Note that this is different from K_2MnF_6 for which the cubic phase is not stable at RT. Heating hexagonal K_2MnF_6 to 440°C transformed the crystals to the cubic phase but after storing the crystals at room temperature they transformed back to the hexagonal phase.[27] To test whether c-KRSF transforms back to h-KRSF at lower temperatures several experiments were done: the material was kept for months at 253K and RT, cubic material was heated for one month at 373 K and also heated and then slowly cooled from 573 to 435K in 90 hours. No XRD peaks of h-KRSF were found in any of the diffractograms recorded afterwards indicating that c-KRSF is the stable phase around and above RT. The XRD results were confirmed by luminescence measurements which showed no ZPL at 621.5 nm and only the emission spectra typical of c-KRSF.

Based on the observations so far one can only speculate on the formation mechanism of h-KRSF. Initially, when the aqueous solution is added to the EtOH nanosized c-KRSF particles are formed. Precipitation at the bottom of the beaker occurs gradually during the evaporation. Possibly, the decreased alcohol content destabilizes the nanocrystals and induces particle growth. At the same time it can destabilize the surface of the nanoparticles. It is known that difference in solvent changes the surface-solvent interaction and can affect the obtained crystal structure of polymorphic materials.[28,29] A high surface area may induce the transformation to a structure with a higher density and thus less surface area.[30] This can explain the transformation to h-KSF, as h-KSF has a higher reported density than c-KSF (2.87 vs. 2.746 g/cm^3). Once particles transform to the hexagonal phase these can serve as seeds that grow

at the expense of dissolving c-KRSF nanoparticles and give rise to an exponential increase of the fraction of h-KRSF over c-KRSF with time. A similar rapid increase in conversion rate was recently observed by some of us in the transformation of cubic (α-phase) $NaYF_4$ nanocrystals to larger hexagonal (β-phase) $NaYF_4$ nanocrystals.[31] We were able to model this transformation by taking into account a distribution in reaction (dissolution/growth) rates for nanoparticles, first resulting in a bimodal size distribution followed by an increasingly rapid transformation to large and monodisperse β-phase crystallites with time, similar to what is observed in Figure 5-7b.

To obtain better insight in and evidence for a formation mechanism, further studies such as combined *in situ* WAXS and SAXS measurements are required to follow particle size and crystallinity in time and relate these to the time-dependent luminescence properties. Indeed, also other mechanisms have been reported where an induction period is followed by a rapidly increasing transformation rate, for example the transformation of ferrihydrite to goethite or hematite nanocrystals.[32] two-line ferrihydrite gradually transforms to more thermodynamically stable and more crystalline phases, such as goethite and hematite. This temperature- and pH-dependent transformation can play an important role in the sequestration of metals and metalloids adsorbed onto ferrihydrite. A comprehensive assessment of the crystallization of two-line ferrihydrite with respect to temperature (25, 50, 75, and 100 °C) Alternatively, autocatalysis can explain an exponential growth of the phase transformation rate. This mechanism has been extensively studied in for example α/β-Sn.[33]

A final challenge is the formation of hexagonal KSF free of Rb, especially since the presence of Rb can be linked to a lower stability of the phosphor under the extreme conditions experienced in wLEDs. To lower the amount of Rb, the synthesis of h-KRSF was done with different K/Rb ratios. Lowering the Rb-fraction resulted in longer induction periods and slower formation of h-KRSF. For 40% and 30% Rb still a complete transformation to h-KRSF was observed. For 20% Rb there was no complete transformation (For details, see Supporting Information Section S5-9) while for 10% and 0% Rb, no formation of h-K(R)SF could be observed (no increase in ZPL intensity). However, based on earlier reports on the synthesis of h-KSF by Kolditz in 1963 and Gossner in 1904,[6,7] and the observation of h-KSF in Refs. [10] and [11] and it is evident that h-KSF can be obtained and it is worthwhile pursuing a synthesis method to realize the synthesis of h-KSF doped with Mn^{4+} with superior performance as a wLED phosphor.

To understand the role of the Rb in the formation of hexagonal KRSF DFT calculations were done to determine the formation energy of cubic and hexagonal Rb_2SiF_6, $KRbSiF_6$, and K_2SiF_6. The results are shown in the Supporting Information

S5-9. To quantify how stable the hexagonal phase is compared to the cubic phase, the formation energy of the hexagonal phase was subtracted from the cubic phase. The calculations show that in all cases the cubic phase is more stable. However, it can be seen that K_2SiF_6 and Rb_2SiF_6 have a much stronger preference for the cubic phase as the energy difference between the cubic and the hexagonal phase is 43 meV and 71 meV per unit cell respectively, while it is only 9 meV for the $KRbSiF_6$. This confirms that for the mixed K/Rb composition it is easier to form the hexagonal phase.

Conclusion

The luminescence of Mn^{4+} in a new hexagonal phase of $KRbSiF_6$ is reported. The optical properties have clear advantages over those for Mn^{4+} in the cubic KSF. The deviation from inversion symmetry allows for the observation of a strong zero-phonon line and shortens the luminescence lifetime for Mn^{4+}. This improves the lumen/W efficacy, increases the absorption strength and reduces saturation at high blue photon fluxes. The quenching temperature of the Mn^{4+} luminescence in the hexagonal phase is very high and comparable to that in the cubic phase (>500K). High quantum yields (>90%) are realized without synthesis optimization but the stability is less, probably due to the large fraction of Rb. The h-KRSF is synthesized by adding precursors dissolved in water to an excess volume of ethanol followed by slow evaporation of the ethanol. The formation mechanism is intriguing and was studied by continuously measuring luminescence spectra of the (nano)particles in the reaction volume. After an induction period of ~15 hours the precipitate started to transform to the hexagonal phase with an exponentially increasing transformation rate. After 8 hours it was fully transformed. The stability of the hexagonal phase was tested by temperature-dependent XRD and luminescence measurements showing that above 200 ^{0}C h-KRSF transforms back to c-KRSF. The higher efficacy, shorter luminescence lifetime and high quenching temperature make the hexagonal phase superior to cubic KSF, especially if a Rb-free synthesis route for pure h-KSF can be found to match the stability of c-KSF.

References

[1] A. G. Paulusz, *J. Electrochem. Soc.* **1973**, *120*, 942.
[2] E. V. Radkov, L. S. Grigorov, A. A. Setlur, A. M. Srivastava, **2009**. US7497973B2
[3] S. Yan, *ECS J. Solid State Sci. Technol*. **2020**, *9*, 106004.
[4] Y. K. Xu, S. Adachi, *J. Appl. Phys.* **2009**, *105*, 119
[5] S. Adachi, *J. Lumin.* **2018**, *197*, 119.
[6] L. Kolditz, H. Preiss, *Zeitschiift fur Anorg. und Allg. Chemie* **1963**, 196, 245.
[7] B. Gossner, Zeitschrift für Krist. *Cryst. Mater*. **1904,** *38*, 110.
[8] C. M. Gramaccioli, I. Campostrini, *Can. Mineral.* **2007**, *45*, 1275.
[9] M. E. Denaeyer, D. Ledent, Bull. *la Société française Minéralogie Cristallogr*. **1952**, *75*, 231.
[10] A. Lazarowska, S. Mahlik, M. Grinberg, C. C. Lin, R.-S. Liu, *J. Chem. Phys.* **2015**, *143*, 134704.

[11] L. Lv, X. Jiang, S. Huang, X. Chen, Y. Pan, *J. Mater. Chem. C* **2014**, *2*, 3879.
[12] V. Weiler, W. Schnick, P. J. Schmidt, M. A. Seibald, **2016**. US10153406B2
[13] H. W. Roesky, Efficient Preparations of Fluorine Compounds, *John Wiley And Sons*, **2012**
[14] M. Bockstedte, A. Kley, J. Neugebauer, M. Scheffler, *Comput. Phys. Commun.* **1997**, *107*, 187.
[15] P. Hohenberg, W. Kohn, *Phys. Rev.* **1964**, *136*, B864.
[16] W. Kohn, L. J. Sham, *Phys. Rev.* **1965**, *140*, A1133.
[17] G. Kresse, D. Joubert, *Phys. Rev. b* **1999**, *59*, 1758.
[18] G. Kresse, J. Furthmüller, *Phys. Rev. B* **1996**, *54*, 11169.
[19] J. P. Perdew, K. Burke, M. Ernzerhof, *Phys. Rev. Lett.* **1996**, *77*, 3865.
[20] R. D. Shannon, *Acta Crystallogr.* **1976**, *32*, 751.
[21] J. Rienmüller, J. Bandemehr, F. Kraus, *Zeitschrift für Naturforsch. B* **2021**, *76*, 559.
[22] J. H. Loehlin, A*cta Cryst C* **1984**, *40*, 570.
[23] B. H. W. S. de Jong, H. T. J. Supèr, R. M. Frijhoff, A. L. Spek, G. Nachtegaal, *Z. Kristallogr.* **2000**,*215*, 397
[24] H. Nguyen, C. C. Lin, R. Liu, *Angew. Chemie* **2015**, *127*, 11012.
[25] Y.Y. Zhou, E.H. Song, T.T. Deng, Q.-Y. Zhang, *ACS Appl. Mater. Interfaces* **2018**, *10*, 880.
[26] T. Senden, R. J. A. van Dijk-Moes, A. Meijerink, *Light Sci. Appl.* **2018**, *7*, 2047.
[27] H. F. Sijbom, R. Verstraete, J. J. Joos, D. Poelman, P. F. Smet, *Opt. Mater. Express* **2017**, *7*, 3332.
[28] H. Chu, X. Li, G. Chen, W. Zhou, Y. Zhang, Z. Jin, J. Xu, Y. Li, *Cryst. Growth Des.* **2005**, *5*, 1801.
[29] C. Stoica, P. Verwer, H Meekes, P. J. C. M. van Hoof, F. M. Kaspersen, E. Vlieg, *Crystal Growth & Design* **2004**, *4*, 4, 765
[30] D. Croker, B. K. Hodnett,*Cryst. Growth Des.* **2010**, *10*, 6, 2806
[31] P. T. Prins, J. C. van der Bok, F. T. Rabouw, A. Meijerink, *Angew. Chem.Int.* Ed**2023**,*62*, e20230508
[32] S. Das, M. J. Hendry, J. Essilfie-Dughan, Environ. *Sci. Technol.* **2011**, *45*, 268.
[33] B. Cornelius, S. Treivish, Y. Rosenthal, M. Pecht, *Microelectron. Reliab.* **2017**, *79*, 175.

Section S5-1. Determination of [K], [Rb] and [Mn] with ICP-OES

The concentration of Mn^{4+} in the KRSF host material is determined with respect to the combined K^+ and Rb^+ concentration. Because these three elements were all present in a single multi-element calibration solution, only one calibration curve had to be prepared. Therefore, the (K+Rb)/Mn ratio was used to determine the actual doping concentration of Mn^{4+}.

Table S-5-1. The concentration of K, Rb and Mn in hexgonal $K_xRb_xSi_{1-x}Mn_xF_6$: x% Mn^{4+} as determined with ICP-OES. The concentration of K, Rb and Mn are determined at em=766.490 nm, em=780.023 nm and em=257.610 nm respectively. Note that the concentration of K increases with increasing Mn doping concentrations because the Mn precursor is K_2MnF_6.

Feed [Mn] (%)	[K]	[Rb]	[Mn] (%)
0.5	1.10	0.90	0.13
1	1.14	0.86	0.14
2	1.17	0.83	0.27
5	1.26	0.74	0.90
7	1.27	0.73	1.50
10	1.29	0.71	4.86
20	1.43	0.57	9.61

Section S5-2. Luminous efficacy

The luminous efficacy (Lm/W) of cubic KRSF, hexagonal KRSF, and cubic KSF are calculated and compared with each other. The spectra of these materials are shown in figure S5-2 and are normalized with respect to their integral. In the same figure the photopic eye responsivity curve is plotted in black, highlighting the advantage of Mn^{4+}-doped fluorides and hexagonal KRSF:Mn^{4+} in particular. In the CCD spectrometer and PMT detectors used in our research, the number of counts as a function of wavelength is proportional to the number of photons that are registered by the detector. As energy is proportional to 1/ λ the measured intensity needs to be converted into energy by dividing all measured intensities by its corresponding wavelength. With the corrected spectrum, the luminous efficacy of the Mn-doped fluorides is calculated between 580 and 680 nm:

$$\text{Luminous Efficacy} = \frac{\int_{580}^{680} V(\lambda)\Phi_\lambda d\lambda}{\int_{580}^{680} \Phi_\lambda d\lambda} \qquad \text{(S 5-1)}$$

Where V(λ) is the eye responsivity curve and is the radiant flux in W/nm. The numerator of the fraction describes the luminous flux and the denominatordescribes the radiant flux. Based on this calculation the luminous efficacy of hexagonal KRSF is determined to be 1.2 % higher than for c-KSF and 2.9 % higher than for c-KRSF.

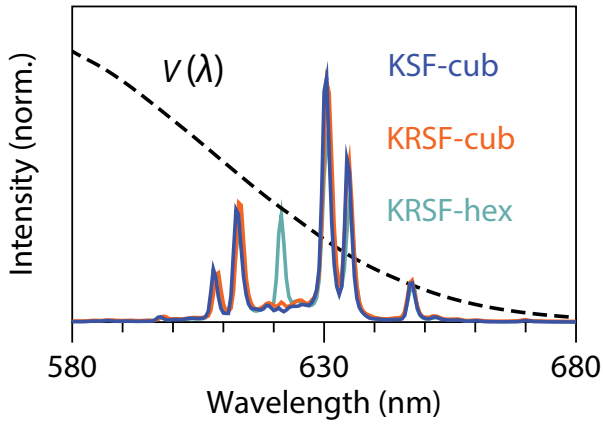

Figure S5-2. Normalized emission spectra of cubic KSF, cubic KRSF and hexagonal KRSF plotted with the eye reponsivity curve V (λ). Because the emission redshifts a little going from KSF to KRSF, the luminous efficacy improvement is slightly larger for h-KRSF to c-KRSF than for h-KRSF to c-KSF.

Section S5-3. Incorporation of [Mn^{4+}] in KRSF determined with ICP measurements

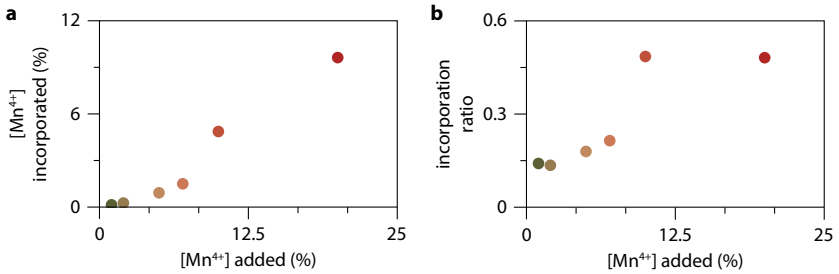

Figure S5-3. Incorporation of Mn^{4+} in h-KRSF. (a) Incorporation into the host lattice as a function of feed concentration. (b) Incorporation ratio as a function of feed concentration.

Section S5-4. Emission intensity as a function of [Mn^{4+}] – diluted and undiluted

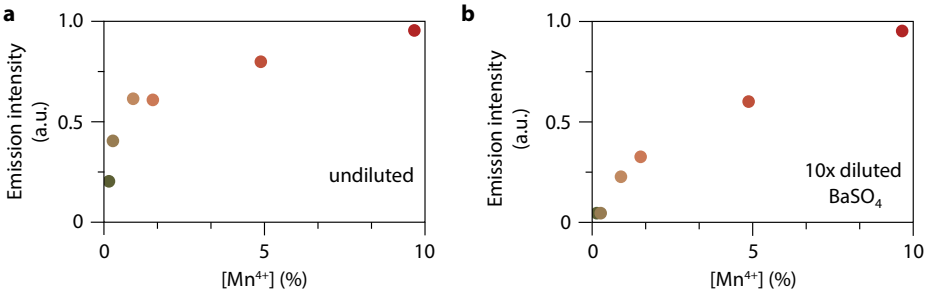

Figure S5-4. Emission intensity as a function of [Mn^{4+}]. (a) Integrated emission intensity between 580–680 nm as a function of [Mn^{4+}] in KRSF. (b) Same as in panel a, but for samples that are diluted (weight dilution) 10 with $BaSO_4$ in order to reduce the effect of blue light exctinction on the measured emission intensity. Even though in both measurements the emission intensity does not increase linearly as a function of [Mn^{4+}], the behavior becomes much more linear by diluting the samples. This observation, in addition to the constant lifetime as a function of [Mn^{4+}] (figure 5-4d in the main text) shows that concentration quenching does not play an important role up to 10 % Mn^{4+}.

Section S5-5. Temperature-dependent emission spectra

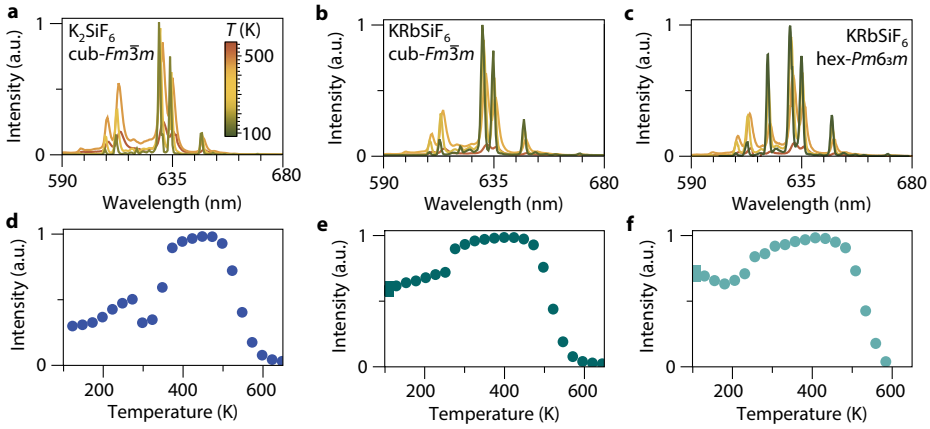

Figure S5-5. Temperature-dependent emission spectra and integrated emission intensities for cubic KSF, cubic KRSF and hexagonal KRSF between 100 and 650 K. (a–c) A selection of emission spectra between 100 and 600 K for all three samples. (d–f) Integrated intensity of the spectra between 590 and 680 nm. Note that the temperature range for hexagonal KRSF does not extend beyond 600 K, as it is fully converted into cubic KRSF at that temperature.

Section S5-6. Experimental set-up in-situ emission

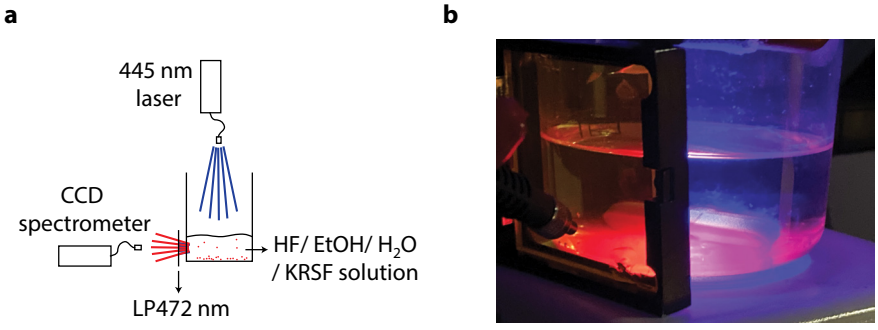

Figure S5-6. Schematic and photographic depiction of the experimental set-up for tracking the growth of hexagonal KRSF. (a) Schematic depiction of the optical set-up. (b) photograph of the set-up with the fiber-coupled spectrometer visible on the left hand side, after the 472nm LP filter.

Section S5-7. Influence of K/Rb ratio and choice of antisolvent

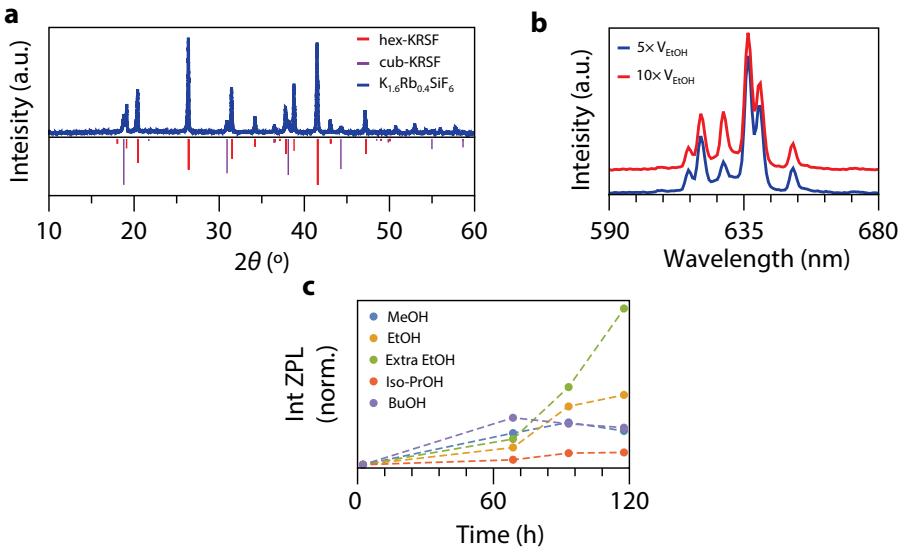

Figure S5-7. Influence of the K/Rb ratio and the choice of antisolvent on the formation of h-KRSF. (a) XRD pattern of $K_{1.6}Rb_{0.4}SiF_6$ doped with 0.1% Mn^{4+}, synthesized with protocol described in the methods section. The XRD pattern matches with both the cubic and hexagonal phase of KRSF. (b) Upon pouring the K/Rb=0.2 reaction mixture into extra EtOH, the full cubic-to-hexagonal transformation takes place again (red spectrum). Using the "standard" amount of EtOH does not result in a full conversion (blue spectrum). (c) The conversion from the cubic to the hexgonal phase for $K_{1.6}Rb_{0.4}SiF_6$takes place over a time period that is roughly 5 times longer than that of the K/Rb=1 synthesis. If the regular amount (5x excess) of EtOH is used no full conversion is obtained. Probably because all the EtOH has evaporated before full conversion has taken place. The effect of other alcohols was investigated as well. All tested alchohols other than EtOH performed worse in terms of the cubic-to-hexagonal phase transformation for the $K_{1.6}Rb_{0.4}SiF_6$ It is unclear whether this is an effect of the interaction between the particles and the alcohol or the evaporation speed.

Section S5-8. Temperature-dependent XRD measurements

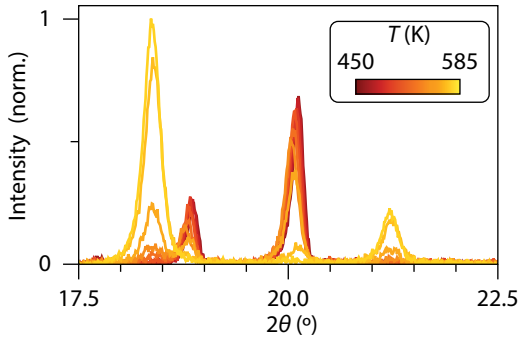

Figure S5-8. Full range T-dependent XRD pattern. The peak intensity values shown in figure 5-8b in the main text are determined based on both the cubic and the hexagonal peaks in this pattern.

Section S5-9. Ab-initio DFT calculations on phase stability in hexagonal and cubic KSF, KRSF and RSF

	Fm-3m	P63mc	P-3m1	E (Fm-3m – P63mc)
KSF	–46.6430	–46.6003	–46.5225	–0.043
KRSF	–46.5118	–46.5029	-	–0.009
RSF	–46.4435	–46.3724	–46.2780	–0.071

Values in eV.

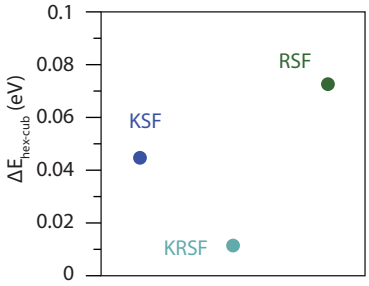

Figure S5-9. Results for ab-initio DFT calaculations for the formation energy per unit cell of cubic, hexagonal and trigonal KSF, KRSF and RSF. Details of the calcualtions can be found in the methodology section of the main text.

Chapter 6

Temperature quenching of Cr^{3+} in solid solutions

Abstract

Blue absorbing near infrared (NIR) emitting phosphors are a promising class of materials for phosphor converted NIR LEDs, which can be used in compact NIR spectrometers. Preferably, these phosphors have a broad emission spectrum and show negligible luminescence quenching at LED operating temperatures (100°C). Here, we investigated $ASc(Si_{1-x}Ge_x)_2O_6$ (A=Li/Na, x=0,0.2,0.4,0.6,0.8,1) solid solutions doped with Cr^{3+} to tune and optimize the emission maximum and bandwidth to cover the full 700 to 1100 nm range. With increasing Ge content an emission redshift was observed, along with emission band broadening at intermediate Ge/Si ratio, which is explained by disorder around Cr^{3+} in the second coordination sphere (mixed Si/Ge). Temperature dependent emission spectra and luminescence decay curves were measured between 90K and 670K to determine the quenching temperature T_Q. With increasing Ge content T_Q drops from 550K to below 400K. Interestingly, Cr^{3+} emission in the highly symmetric site in $LiScSi_2O_6$ shows a strongly temperature dependent lifetime before thermal quenching sets in. DFT calculations on $LiScSi_2O_6$ indicate that asymmetric vibrations at the Sc site are involved and calculated phonon energies were confirmed by measuring FTIR. Our study indicates that a solid solution is a promising way to increase the emission band width. However, with increasing Ge content T_Q decreases. An optimum Ge-content in $LiSc(Si_{1-x}Ge_x)_2O_6:Cr^{3+}$ is x=0.2-0.4 as it redshifts the NIR band maximum close to 900 nm and offers a FWHM bandwidth around 180 nm, while keeping the thermal quenching temperature high enough for application in NIR-LEDs.

"Wie het zelfde anders zegt,
zegt iets anders. "

*"He who says the same differenty,
says something different"*

Paul Scholten

Introduction

The discovery of the efficient blue (In,Ga)N-based LED has revolutionized the lighting industry. In the development of better phosphor converted white light LEDs an important focus is on narrow band red and green phosphors to enhance the colour quality and overall efficiency of the LEDs. Beyond this traditional quest for more efficient lighting with better colour rendering, new fields are emerging. An upcoming field is human centric lighting aimed at spectral shaping of the LED output to realize health benefits, for example through phosphors with a cyan emission colour to influence the circadian rhythm. Control over the spectral distribution of LED lighting is also important in horticulture as plant growth can be optimized by the lamp spectrum, also including emission wavelengths outside the visible range as plants respond to wavelengths in the near infrared (NIR).[1] Another upcoming application in NIR LEDs concerns chemical sensing. Vibrational overtones of organic molecules are in 700-1500nm spectral window and NIR absorption spectroscopy can be used to monitor the presence and concentrations of (bio-)molecules.[2,3] Broadband NIR sources can be used for spectral scanning to observe and analyse these absorption lines. This results in a non-destructive and facile chemical analysis method. This technique has great potential in applications such as healthcare, agriculture, or food.

Traditionally incandescent lamps are used in NIR spectrometers. However, their short life-span (<2000 hours), large size and low efficiency make them unattractive. Recent developments are focussed on phosphor-converted NIR LEDs (pc-LEDs) based on spectral conversion of blue LED light to NIR emission by broadband NIR emitters. The pc-LED broadband emitters provide a compact and efficient broadband NIR source for bio-chemical sensing. Miniaturization using NIR pc-LEDs combined with compact CCD-type spectrometers will allow for cheap sensing functionalities that can be incorporated in portable devices and mobile phones. The performance of the NIR pc-LED strongly depends on the NIR phosphor and presently Cr^{3+} is the most widely explored activator for broadband NIR emitting phosphors owing to its ability to provide broadband NIR emission with excellent efficiency.

The desired properties of phosphors for NIR pc-LEDs include an emission wavelength between 700 and 1000 nm (or longer wavelengths if combined with detectors other than crystalline silicon), broad band width, preferably close to 200 nm, strong absorption in the blue and limited thermal quenching of the emission up to at least ~100 ^{o}C.[4] Cr^{3+} ticks most of these boxes as it can have a broadband $^4T_2 \rightarrow {}^4A_2$ emission, typically centred between 750 to 900 nm and bandwidths between 100 and 150 nm, depending on the local environment and has broad band d-d absorption in the cyan or blue making it suitable for pc-LEDs. A problem is however thermal quenching of the $^4T_2 \rightarrow {}^4A_2$

emission that often sets in well below 100 °C. From the Tanabe-Sugano diagram for the $3d^3$ configuration it is clear that a small crystal field splitting is required to have the $^4T_2$ level as the lowest excited state (giving broad band emission) and not the ^2E level which gives a sharp line emission around 700 nm.

A few years ago, Osram light AG was the first to introduce pc-LED product that shows broadband NIR emission based on Cr^{3+} NIR phosphor(s). This device has an efficiency of 7-8%, [4] which leaves room for improvement. Many studies have appeared since and show that thermal quenching is an issue for Cr^{3+} NIR phosphors. The local ligand coordination is important but also the second coordination sphere affects the Cr^{3+} luminescence quenching temperature. For example, research by Małysa et al.[5] on Sc garnets has shown that the local environment in the first and second coordination sphere is crucial to the quenching temperature. Broad band $^4T_2 \rightarrow {}^4A_2$ emission is essential but even for Cr^{3+} in several hosts not showing the ^2E line emission, the crystal field is still too large resulting in a $^4T_2$ emission band that is at higher in energy (towards 750nm) than desired.[5–8] Other hosts have a more desirable emission towards 900nm [9] but suffer from temperature quenching of the luminescence. Unfortunately, there is trend for Cr^{3+} emission to show lower thermal quenching temperatures upon red shifting the emission and upon band broadening, as can be understood from the configurational coordinate diagram (larger offset between ground state and excited state and lower excited state energy lead to a lower quenching temperature T_Q). This opposite relation between the desired thermal quenching temperature on the one hand and the emission maximum and bandwidth on the other, make it challenging to find a phosphor that meets all requirements. Amongst several hosts explored for Cr^{3+} broadband NIR emission, recently the clinopyroxenes $LiScSi_2O_6$ and $NaScSi_2O_6$ have shown good thermal stability up until 100-150°C while still the emission maximum is at wavelengths above 850nm.[10, 11] Pyroxenes are a group of minerals with the formula $XYSi_2O_6$ where X and Y are different metal ions. The structures consist of layers of silicate chains sandwiched between layers of metal cations.

In this research we focus on the $(Li,Na)Sc(Si_{1-x}Ge_x)_2O_6 : Cr^{3+}$ system. By varying the Si and Ge, the influence of the second coordination sphere on the emission of Cr^{3+} can be studied. The peak position as well as the FWHM of the Cr^{3+} emission is studied as function of the Ge concentration with the goal to optimize emission wavelength and FWHM. By introducing disorder, inhomogeneous broadening can increase the emission band without affecting the offset in the configurational coordinate diagram. We study the effect of the solid solutions on the thermal quenching of the luminescence. Two series of phosphors are investigated: $LiSc(Si_{1-x}Ge_x)_2O_6$, $NaSc(Si_{1-x}Ge_x)_2O_6$ both doped with 1% Cr. A relatively low Cr^{3+} concentration is used to avoid Cr-Cr interactions at neighbouring Sc sites. Our composition and temperature dependent measurements show that substituting part of the Si by Ge is beneficial for the FWHM (broader) and emission maximum (redshift) but lowers the lumines-

cence quenching temperature, making the optimum composition a trade-off between the different performance parameters.

Materials and methods.

For the synthesis of the samples Li_2CO_3 (MERCK, >99%), $NaCO_3$(Sigma Aldrich, >99,95), $Sc_2(C_2O_4)_3{\cdot}5H_2O$. (Scandium oxalate, precipitated from dissolved Sc-metal), SiO_2 (Amorphous Silica Pore Size 6nm, Sigma Aldrich, >99,9%), GeO_2 (highways International, 6N), Cr_2O_3 (Merck, 99,9%) was used. Two series were made for $LiSc(Si_{1-x}Ge_x)_2O_6$: 1% Cr^{3+} and $NaSc(Si_{1-x}Ge_x)_2O_6$: 1% Cr^{3+} (with x= 0,0.2,0.4,0.6,0.8,1). It is assumed that the Cr^{3+} substitutes on the Sc^{3+} position. The precursors were mixed for about 15 minutes in stoichiometric amounts using an agate pestle and mortar with sufficient acetone to wet the powder. For the $LiSc(Si_{1-x}Ge_x)_2O_6$ samples 10 mole% extra Li_2CO_3 was added as a flux. The synthesis was done by heating the precursors to 1100 ^oC under air atmosphere and annealed for 8 hours. Nano porous silica was necessary to maximize the contact surface of the micro grains. Scandium oxalate was used to increase the reactivity of Sc^{3+} ions and accelerate the synthesis.

The powders were examined using powder X-ray diffraction for its phase purity. A Phillips PW1729 X-ray generator, Cu source was used at 40 kV operating voltage and 20 mA current. The step size resolution was 0.02° 2θ. The photoluminescence (PL) spectroscopy was performed by using an Edinburgh Instruments FLS-920 fluorescence spectrometer. The PL and PL excitation (PLE) spectra were recorded using a 450 W Xe lamp as excitation source and a Hamamatsu H5509 photomultiplier tube (PMT) detector. PL decay measurements were performed by using a tuneable optical paramagnetic oscillator (OPO) Opotek Opolette HE 355II pulsed laser (pulse width: 10 ns; repetition rate: 20 Hz) as excitation source, and the emission was recorded by a Hamamatsu R928 PMT detector. For temperature dependent studies a temperature-controlled stage from Linkam Scientific (THMS600) was used for measurements in a -190°C to 450°C temperature range.

For the FTIR absorption measurements the samples were pressed into KBr pellets by mixing 1mg of sample with 200mg of dry KBr. FTIR measurements were performed with a Bruker Vertex 70. Spectra were recorded from 400 cm^{-1} to 4000 cm^{-1}, with a KBr beam splitter, a DLaTGS D301 detector, and a mid IR source.

First-principles total energy calculations[12] were performed based on density functional theory (DFT) [13,14] using the Projector Augmented Wave (PAW) as implemented in Vienna ab-initio simulation package[15,16]reliable, and minimizes the number of order (Formula presented. Frozen core approximation was combined with PAW and the valence electron configurations are $1s^22s^1$ for Li, $3s^23p^63d^14s^2$ for Sc, $3s^23p^2$ for Si, $2s^22p^4$ for O. Exchange and correlation were treated with the generalized gradient approximation.[17] The wave

functions were expanded in a plane-wave basis set with kinetic energy cut off of 600eV. 6×6×6 Monkhorst-pack *k*-points mesh were used for the integration in *k* space in the Brillouin zone for the primitive unit cell. The structural optimization were performed until each component of the interatomic force became less than 1.0×10^{-3}eV/Å. Phonon energy calculations were carried out using the density functional perturbation theory[18, 19] and PHONOPY software[20] A supercell of 2x2x2 and 2x2x2 Monkhorst-pack *k*-points mesh were used for phonon energy calculations.

Results

The as-synthesized samples were visually inspected and exhibit a clear trend in sample body colour as a function of composition. For both series of samples, phosphors with a high Ge concentration are pink while the Si rich sample are light green in colour (supporting information, Figure S6-1). This change of colour represents the differences in crystal field and covalency as Si is substituted with bigger Ge ions in the lattice. This causes a shift of the Cr absorption bands to lower energies. The body colour is used in the figures to identify the composition of samples by varying the colour from pink (Ge) to green (Si) and colour shades between pink and green for results obtained for the (Si,Ge) solid solutions.

XRD

$LiScSi_2O_6$ (LSS), $LiScGe_2O_6$(LSG), $NaScSi_2O_6$(NSS) $NaScGe_2O_6$(NSG) are all isostructural. When looking at the XRD patterns in tabl 6-1 one notices that for both the LSS/LSG and the NSS/NSG series the peaks shift to lower 2θ angles with increasing Ge concentration, for example the (3 1 0) peak shifts from 31° to 30° in LSS/LSG and from 30.5°-29.5° in the NSS/NSG series. The shift to lower 2θ with increasing Ge is expected as a result of lattice expansion for increasing Ge content (with a larger 0.39 Å ionic radius for Ge^{4+} vs. 0.26 Å for Si^{4+} [21]). The continuous shift indicates that a solid solution is formed with Si and Ge mixed homogeneously throughout the matrix. Some weak extra peaks for the $LiScSi_2O_6$ sample can be seen around 2θ = 24°. We attribute this to $Li_2Si_2O_5$. Full XRD patterns are available in the supporting information (Figure S6-2.).

The crystal structure is composed of alternating layers of tetrahedrally coordinated Si^{4+}/ Ge^{4+} and layers with octahedral Sc^{3+} and polyhedral Na^{+} or Li^{+}, as can be seen in Figure 6-2. The Sc ions have two Sc nearest neighbours giving rise to one dimensional strings through the crystal. On either side of the string there are Na or Li atoms. These Na or Li atoms together with tetravalent cations atoms create a cylindrical channel though the crystal. The cylindrical structure may enhance ion diffusion and would explain the relative low temperature (1100 °C) needed for the synthesis where most silicates require temperatures above 1200°C.

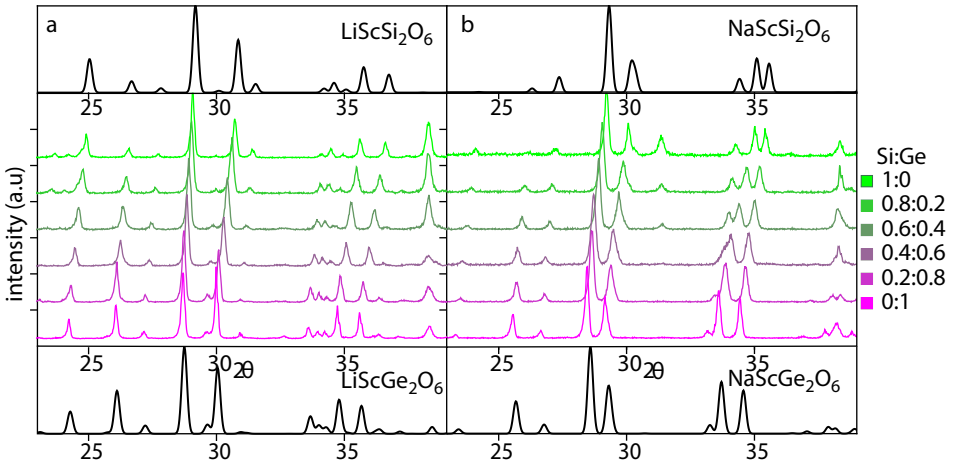

Figure 6-1. X-ray powder diffraction patterns of: (a) $LiSc(Si_{1-x}Ge_x)_2O_6$:1%$Cr^{3+}$with the reference of $LiScSi_2O_6$ (LSS)[45] and $LiScGe_2O_6$ (LSG)[46]shown above and below. (b) $NaSc(Si_{1-x}Ge_x)_2O_6$:1%$Cr^{3+}$with the reference of $NaScSi_2O_6$(NSS) [32] and $NaScGe_2O_6$ (NSG)[33]shown above and below.

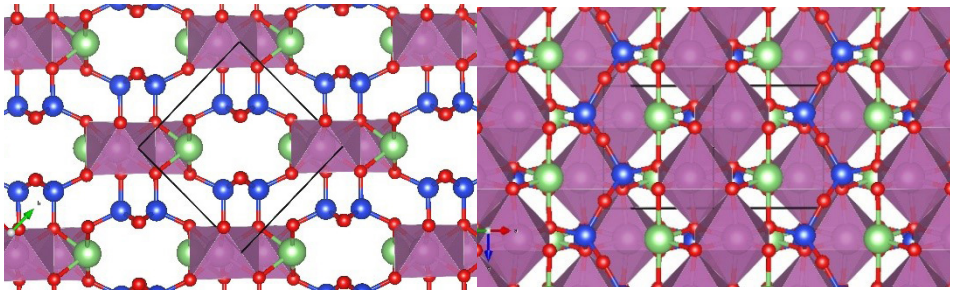

Figure 6-2. Crystal structure of $LiScSi_2O_6$ perpendicular to the c axis. Green: Li, Blue: Si, Red: O Purple: Sc. One can observe layers of tetrahedral silicate groups alternating with layers of Li and Sc. In b a perpendicular projection of a is shown. Here we can clearly see the strings of interconnected octahedral Sc ions separated by Li atoms

To investigate the role of the host composition on the luminescence properties, emission spectra of Cr^{3+} in LSS, LSG, NSS and NSG were recorded and are shown in Figure 6-3. The NIR emission has a peak maximum around 860 nm in the silicates and it redshifts to 900 nm for Cr^{3+} in the germanates. For the photoluminescence excitation (PLE) spectra three clear bands are observed, one just above 300 nm and around 480 nm and 700 nm. These observations are in agreement with earlier results for the luminescence of Cr^{3+} in $NaScSi_2O_6$ and $LiScSi_2O_6$[10,11,22]The 700 nm band shows some interesting features with some dips around the band maximum. Comparing the intensity of the 480 and the 700 nm peak we observe that the 480 nm peak is relatively stronger than the 700 nm peak for the germanate samples. The luminescence spectra can be un-

derstood using the d^3 Tanabe Sugano diagram. The broadband emission is the $^4T_2 \rightarrow {}^4A_2$ emission. The bands at 320, 480 and 700 nm in the PLE spectra can be assigned to the transition from the $^4A_2$ ground state to the $^4T_1(^4P)$, $^4T_1(^4F)$ and $^4T_2$ (^4F) excited states. The small dips in the $^4A_2 \rightarrow {}^4T_2$ excitation band around 700 nm are explained by Fano anti-resonance due to mixing of the $^4T_2$ state with resonant $^2T_1$ and ^2E states [23, 24]

In Figure 6-4 the luminescence spectra of Si-Ge solid solutions are shown. Both for the LSS/LSG series as well as the NSS/NSG series the band maxima redshift with increasing Ge content, as is also plotted in Figure 6-4d. The full width at half maximum (FWHM) of the emission bands for both series initially increase with Ge content, level off and then decrease again for the pure Ge sample (Figure6-4c). The redshift of the emission peak with an increase in Ge is explained by a weaker crystal field upon substituting Si with the larger Ge which lowers the energy difference between the $^4T_2$ and $^4A_2$ states. The weaker crystal field cannot simply be explained by a change in Cr-O distance. Based on the XRD data the average O-Sc distances *d* have been calculated: NSS 2.102 Å (±0.068), NSG 2.106 Å (±0.065), LSS 2.107 Å (±0.084) and LSG 2.109 Å (± 0.078). The slight increase in Sc-O (and thus Cr-O) distance upon substituting Si by Ge cannot explain the redshift through the Cr – Ligand distance dependence of the CF splitting Δ_O. The very small difference in *d* and the theoretical d^5 dependence of Δ_O would only cause a redshift less than 1%. Clearly, covalency effects play a role as will be discussed below. The variation FWHM of the Cr^{3+} emission bands for the solid solutions are explained by an increase of disorder in the second coordination sphere where a mixed Si/Ge coordination is varies for different Cr^{3+} ions and causes variations in the emission band maximum (shifting to longer wavelengths for a Ge-rich coordination). This gives rise to inhomogeneous broadening and the sum of all the emission spectra is observed in the spectrum as a broadened band. The largest FWHM is realized for $LiSc(Si_{1-x}Ge_x)_2O_6$:1%Cr^{3+} with x=0.4-0.8. The FWHM of 0.28 eV corresponds to ~180 nm FWHM around 880 nm which is much larger than for other Cr^{3+} based NIR phosphors where typical values for the FWHM of the $^4T_2$-$^4A_2$ emission band range from 100 to 150 nm [6,24–26]

To determine the PL peak maxima, the spectra were converted to an energy scale, [27] after which a Gaussian fit was done using the data points between 1.55 and 1.31eV (800 and 950 nm) as shown in Figure6-4a and 6-4b. This helps to determine peak positions even though it is important to realize that the theoretical peak shape is not Gaussian. The peak maximum shows a clear dependence on Ge content. For Cr^{3+} in LSS the emission is at slightly shorter wavelength (850 nm) then for NSS (870 nm) but with increasing Ge content the peak positions redshift to almost the same wavelength (900 nm). A shift in $^4T_2 \rightarrow {}^4A_2$ emission is often related to the Sc-O distance[5, 28] The difference in band maximum between LSS and NSS cannot be explained by only a variation in distance as the change in Sc-O is ~0.5%: 2.102 to 2.107 Å for LSS and NSS respectively. Also, here changes in covalency contribute to the redshift in NSS.

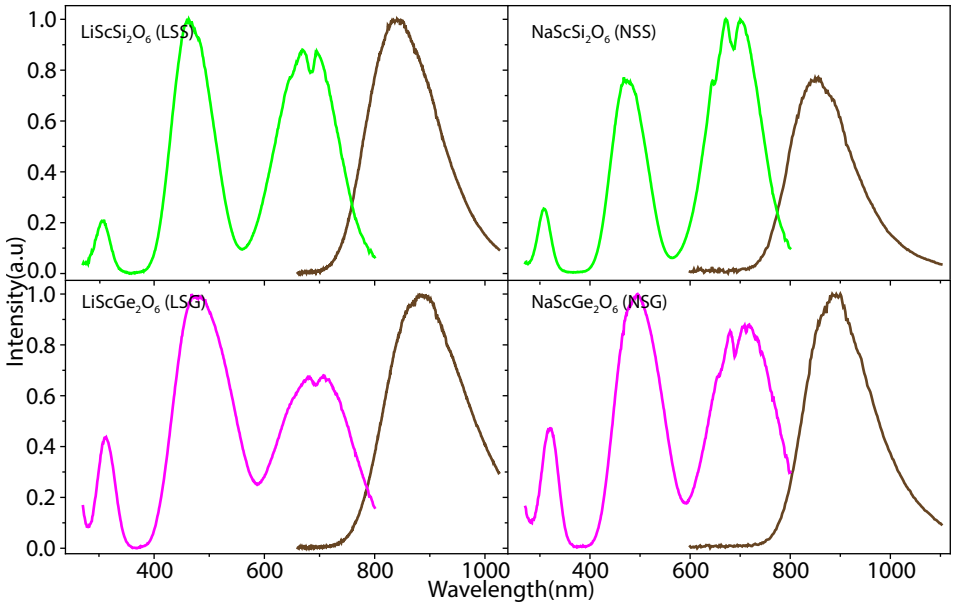

Figure 6-3. PL and PLE spectra of LSS, NSS, LSG, NSG doped with 1% Cr3+ measured at room temperature. The PL curves are shown in brown and are excited at 480 nm. The PLE curves, green or pink, are measured for 900nm emission.

To further investigate the role of cation substitution on the optical properties of Cr^{3+}, the PLE spectra were analysed to determine the crystal field and Racah parameters. After converting the spectra to an energy scale [27] the peak positions of the $^4A_2$ to $^4T_1(^4F)$ and $^4T_2$ excitation bands were determined by fitting to a Gaussian. From these peak positions, the crystal field parameter Dq (note Δ_O = 10 Dq) and Racah parameter B were found using the Tanabe-Sugano diagrams (Figure 2-2).[29] The results are shown in Table 6-1. Some interesting trends can be observed for the pure compounds and solid solutions. With increasing Ge content, the crystal field splitting decreases. For the $NaSc(Si_{1-x}Ge_x)_2O_6$ series Dq drops from 1,443cm^{-1} to 1,398 cm^{-1} and for $LiSc(Si_{1-x}Ge_x)_2O_6$ from 1,469 to 1,436 cm^{-1} . The Racah parameter B also lowers as a function of Ge content, from 670 cm^{-1} to 610 cm^{-1} for $NaSc(Si_{1-x}Ge_x)_2O_6$ and from 665cm^{-1} to 608 cm^{-1} for $LiSc(Si_{1-x}Ge_x)_2O_6$. Increasing Ge content increases the covalent bonding character, and this decreases the crystal field strength and gives a stronger nephelauxetic effect (smaller B). These effects are in line what is observed by B Małysa in and $Sr_{1-x}Ca_xSc_2O_4$:Cr^{3+}. With increasing concentration of the smaller cation Ca^{2+} cation the Dq value increased. Similarly in $CaAl_{12}O_{19}$/$SrAl_{12}O_{19}$, $YAl_3(BO_3)_4$ / $GdAl_3(BO3)_4$, $YSc_3(BO_3)_4$ / $GdSc_3(BO_3)_4$ the Dq is the highest for the smaller ion and the B parameter is larger[28,30,31]which emit one ultraviolet (UV. For example, in $Sr_{1-x}Ca_xSc_2O_4$:Cr^{3+} the crystal field splitting Dq increases with Ca-content while B increases. In $Sr_{1-x}Ca_xSc_2O_4$ a significant decrease in in Sc-O distance

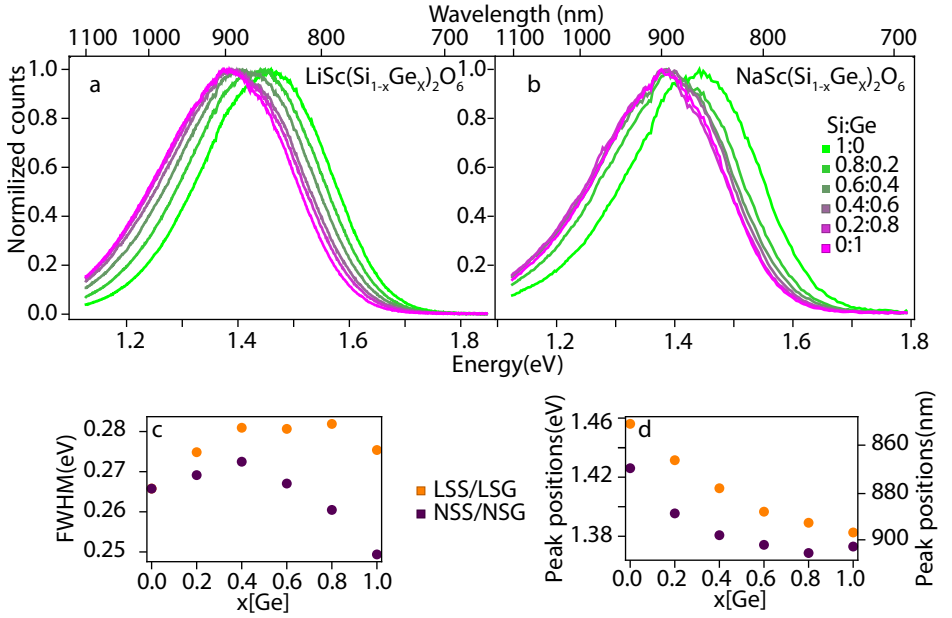

Figure 6-4. PL spectra of (a) $LiSc(Si_{1-x}Ge_x)_2O_6$:1%Cr^{3+} and (b) $NaSc(Si_{1-x}Ge_x)_2O_6$:1%Cr^{3+} solid solutions. All the spectra were obtained by exciting at 480nm at room temperature. (c) The full width half max (FWHM) of both the series as a function of Ge content (d) emission peak positions as determined by fitting to a Gaussian.

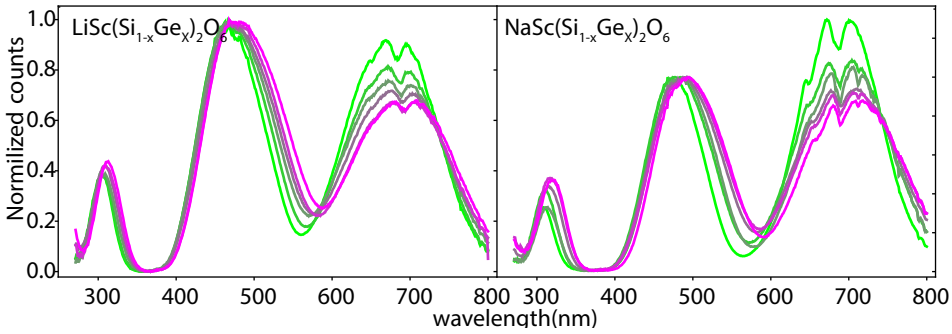

Figure 6-5. PLE spectra of $LiSc(Si_{1-x}Ge_x)_2O_6$:1%Cr^{3+} and $NaSc(Si_{1-x}Ge_x)_2O_6$:1%Cr^{3+} solid solutions. All the spectra were obtained by monitoring emission at 900nm at room temperature

Table 6-4. Crystal field parameters (10 Dq) and Racah parameter (B) as obtained from the PLE spectra for the 12 different samples of $NaSc(Si_{1-x}Ge_x)_2O_6$ and $LiSc(Si_{1-x}Ge_x)_2O_6$ at room temperature.

Sample	$^4A_2 \rightarrow {}^4T_2(cm^{-1})$	$^4A_2 \rightarrow {}^4T_1(cm^{-1})$	10Dq/B	B (cm^{-1})	Dq (cm^{-1})
NSS	14440	20840	21.7	665	1443
x=0.2	14300	20560	22.1	648	1432
x=0.4	14240	20390	22.5	633	1424
x=0.6	14160	20210	22.8	620	1414
x=0.8	14080	20060	23	611	1405
NSG	13990	19950	23	608	1398
LSS	14650	21200	21.8	674	1469
x=0.2	14590	20920	22.8	643	1466
x=0.4	14530	20760	23.2	629	1459
x=0.6	14450	20590	23.5	618	1452
x=0.8	14370	20440	23.4	609	1425
LSG	14290	20260	24.1	596	1436

explains the increase in Dq for higher Ca^{2+} content, which at the same time makes the bonding more ionic, explaining the increase in B. Note that, as discussed above, changes in the average Sc-O distance $NaSc(Si_{1-x}Ge_x)_2O_6$ and $LiSc(Si_{1-x}Ge_x)_2O_6$ are less than 1 pm and are too small to explain the shift in excitation and emission bands.[32,33]

Finally, it is interesting to observe that the ratio between the $^4T_1$ to $^4T_2$ peaks changes with Ge concentration. The ratio of $^4T_2$: $^4T_1(^4F)$ for LSS/ LSG goes from 0.9 to 0.7 and for the NSS/NSG system from 1.3 to 0.9. The relative intensity of the $^4T_1(^4P)$ increases along with that of the $^4T_1(^4F)$ band. This change in $^4T_1$ to $^4T_2$ ratio is often observed but has not received much attention.[5,28] A very strong change was reported by Back et al. for Cr^{3+} in two polymorphs of Ga_2O_3, a high symmetry α-phase and a lower symmetry β-phase [34]The PLE showed a tremendous difference in the $^4T_1$: $^4T_2$ excitation intensity ratio (1:3 for α, 2:1 for β)[34] and was explained by the influence of admixture of ^2E and $^2T_1$ states in the overlapping (resonant) $^4T_2$ states. Whether this explanation is correct or not requires further research. Symmetry does seem to play a role. To quantify the deviation from perfect octahedral symmetry the angles between the oxygen atoms around the scandium position were analysed. The six O atoms will have fifteen interatomic distances and directions (twelve nearest neighbours and three opposing distances). The angles between all the vectors (105 in total) were compared to the angles a perfect

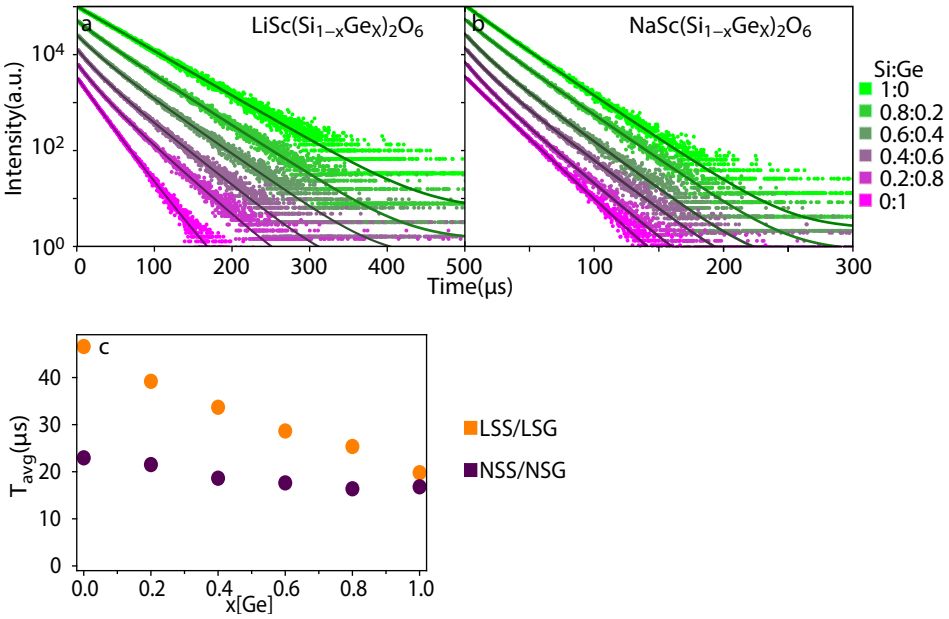

Figure 6-6. Decay curves at room temperature of (a) $LiSc(Si_{1-x}Ge_x)_2O_6$:1%Cr^{3+} solid solutions and (b) $NaSc(Si_{1-x}Ge_x)_2O_6$:1%Cr^{3+} solid solutions. Excited at 480nm and monitored at 800nm. The solid lines show the fits

octahedron would have and the average angle deviation for each compound was calculated to be for LSS 2.201°, LSG 2.775°, NSS 2.777°, NSG 3.360°. We can see that the deviation from perfect octahedral symmetry becomes stronger from LSS to LSG and from NSS to NSG and is accompanied by an increase in relative intensity of both $^4T_1$ bands. Similar results were seen $Ca_{1-x}Sr_xSc_2O_4$. With increasing Sr content, the $^4A_2 \rightarrow {}^4T_1$ increases. The $SrSc_2O_4$ has more distorted Sc sites with respect to $CaSc_2O_4$.[28] An opposite trend is observed in $Bi_2Al_{4-x}Ga_xO_9$:Cr^{3+} but here also the bandgap (smaller for the gallate) and ionic radius of the cation site for Cr^{3+} (larger in the gallate) changes which will affect the breaking of the parity selection rule [35] The analysis presented suggests that breaking the parity selection rules by deviations from inversion symmetry is more pronounced for the $^4A_2 \rightarrow {}^4T_1$ than for the $^4A_2 \rightarrow {}^4T_2$ transition but further research to fully understand the strong variations of the $^4A_2 \rightarrow {}^4T_1$ to $^4A_2 \rightarrow {}^4T_2$ absorption strengths is needed.

In Figure 6-6 luminescence decay curves are shown for the $^4T_2$ emission in the various samples. Emission decay dynamics are insightful to obtain radiative decay rates which are, especially for symmetry forbidden transitions, dependent on the coordination symmetry. Typically, luminescence decay can be described with a single exponential function. In solid solutions the local environment can differ between luminescing ions, and this gives rise to deviations from single exponential decay. A bi-exponential fit provides a good approximation and therefore the emission decay curves for Cr^{3+} in the solid

(Si,Ge) solutions was fitted to:

$$I(t) = A_1 e^{-t/\tau_1} + A_2 e^{-t/\tau_2} + C \quad (6.1)$$

Here *I(t)* is the intensity as a function of time, A_1 and A_2 are pre-exponential factors and τ_1 and τ_2 represent the emission lifetimes of differently coordinated Cr^{3+} ions and *C* takes background noise into account. The average lifetime can be calculated using:

$$\tau_{\text{avg}} = \frac{A_1\tau_1^2 + A_2\tau_2^2}{A_1\tau_1 + A_2\tau_2} \quad (6.2)$$

In Figure 6-6c luminescence lifetime for the Cr^{3+} emission is plotted as function of composition. The lifetimes are longer in the Li-based samples. With increasing Ge content, the lifetime decreases, and this effect is stronger for the Li series. The longest emission lifetime observed for the highest symmetry coordination (LSS), as expected. The decrease in lifetime with Ge content is consistent with lowering of the symmetry and an increase in the covalent character which lowers the energy of opposite parity states favouring admixture to break the parity selection rule.

Based on the optical characterization of the two series of samples, it is evident that for application in a NIR-LED the $LiSc(Si_{1-x}Ge_x)_2O_6$ samples with a Ge content around 50% are the most promising based on the largest FWHM combined with a favourable emission maximum around 880-900 nm. An important condition is however that the luminescence quenching temperature must remain high, preferable above 100 °C. For sensing applications, the intensity is not as high as in high power w-LEDs for lighting where phosphor temperatures can reach 150°C. Still, thermal quenching can be an issue and in the next section the role of (Si,Ge) mixing on the thermal quenching behaviour is investigated.

Temperature dependence

To investigate the thermal quenching of the NIR luminescence first the emission intensity was measured as a function of temperature for Cr^{3+} in $LiScSi_2O_6$ and $NaScSi_2O_6$ under 460 nm excitation. The results are shown in Figure 6-7. The intensity starts to diminish above ~ 125 °C with a T_{50} (temperature at which the intensity drops to 50% of the maximum) around 250 °C, consistent with previous studies.[10,22] This high T_{50} for long wavelength Cr^{3+} emission (maximum between 850 and 900 nm) is favourable for application. Typically, high quenching temperatures for broad band $^4T_2$ emission are observed for shorter wavelength Cr^{3+} emission while longer wavelength NIR emission has lower T_{50} values. The high T_{50} combined with redshifted emission make Cr^{3+}-doped $LiScSi_2O_6$ and $NaScSi_2O_6$ promising for application in NIR-LEDs.

Measuring emission intensity as function of temperature to probe thermal quenching can give deviations, for example when the oscillator strength of the absorption transition is temperature dependent giving rise to intensity

variations not related to thermal quenching.[36,37] In addition to fundamental problems also trivial aspects such as changes in alignment, collection efficiency or excitation source intensity can give rise to intensity variations not related to thermal quenching. A fast and reliable method to determine T_{50} is measuring the emission lifetime as a function of temperature. As non-radiative decay sets in, the emission lifetime shortens. Temperature dependent lifetime measurements were done on all compounds between -190 and 450°C. In the SI lifetime measurements are shown with the fits from which the (average) lifetime was determined. In Figure 6-8 the temperature dependence of the Cr^{3+} emission life times is plotted for both $NaSc(Si_{1-x}Ge_x)_2O_6$ and $LiSc(Si_{1-x}Ge_x)_2O_6$.

For the $NaSc(Si_{1-x}Ge_x)_2O_6$ series we observe that emission lifetimes are constant up to a certain temperature above which τ rapidly drops. From the temperature dependence the T_{50} values were determined and plotted as a function of Ge content in Figure 6-6c. It is evident that increasing the Ge-content lowers the T_{50} values. To fit the temperature dependence of emission life times, a sigmoidal fit was done: [38]

$$\tau(T) = \frac{\tau(0)}{1 + Ae^{-\Delta E/kT}} \tag{6.3}$$

Here τ (*0)* is the lifetime a 0K, assumed to be equal to the lifetime measured at ~80-100K, *A* is a pre-factor often associated with an attempt rate and ΔE is the activation barrier for non-radiative decay to the ground state. A single sigmoidal fit was unsatisfactory for the solid solutions. It can be argued that a multi sigmoidal fit is necessary because the local environment of Cr^{3+} varies from ion to ion in the mixed (Si,Ge) samples. A two sigmoidal fit turned out to be sufficient and was used to determine the T_{50} by using as shown in Figure 6-8. The T_{50} decreases from 539 K to 356K upon replacing Si by Ge.

For the LSS/LSG series the temperature dependence of the emission lifetime shows a slow decrease prior to the fast drop around 400 K. This is interesting as the intensity does not drop until 450K (see Figure 6-7). This increase in lifetime upon cooling to cryogenic temperatures is also observed for Cr^{3+} emission in solid solutions, albeit less pronounced as the Ge content increases. Similar observations have been made for Cr^{3+} emission in other high symmetry crystals with long emission lifetimes at low temperatures, e.g. in garnets where the lifetime at room temperature is close to 70 μs.[39] A similar behaviour has also been observed for Mn^{4+} where it was shown that thermal occupation of odd parity vibrational modes contribute to relaxing the parity selection rule at elevated temperatures.[40] The temperature dependence follows:

$$\tau_r(T) = \frac{\tau_r(0)}{\coth(h\nu/2kT)} \tag{6.4}$$

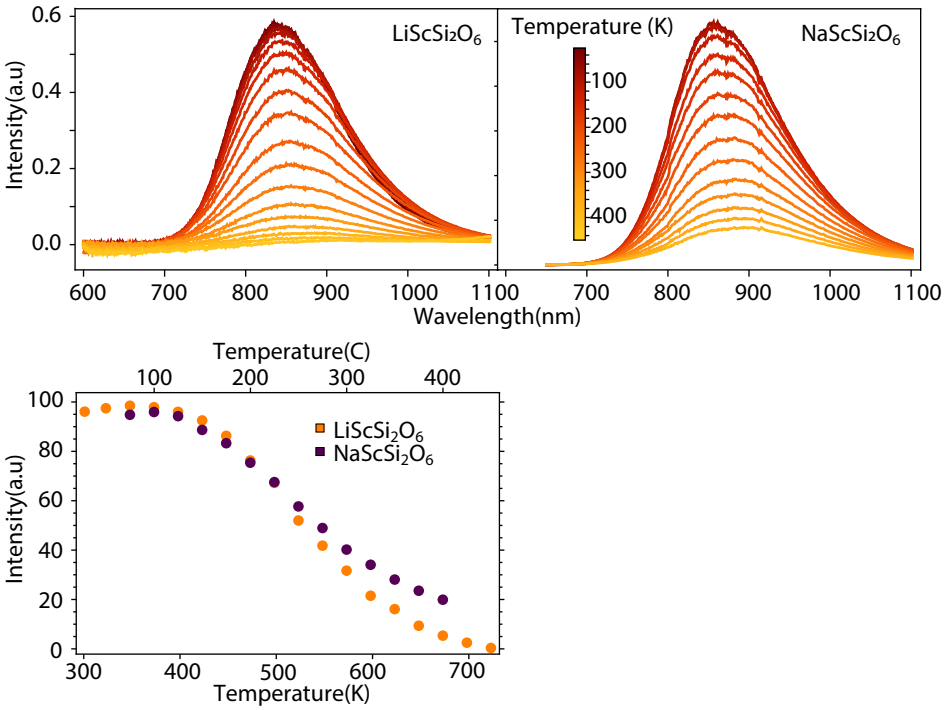

Figure 6-7. Temperature dependent emission spectra of $LiScSi_2O_6$ and $NaScSi_2O_6$ doped with 3.5% Cr^{3+} for 460 nm excitation. The bottom figure shows the integrated emission intensity as a function of temperature.

With $\tau_r(T)$ the radiative lifetime as a function of temperature and $\tau_r(0)$ is the radiative lifetime at 0K. hν is the effective energy of odd-parity phonon modes and k is the Boltzmann constant. The measured lifetime is determined by the sum of radiative and non-radiative decay rates. Therefore, the equation for to the temperature dependence of the radiative decay time in Eq. (6,4) needs to be incorporated in the sigmoidal fit Eq. (6,3):

$$\tau(T) = \frac{\tau_r(T)}{1 + \frac{\tau_r(T)}{\tau_{nr}} e^{-\Delta E/kT}} \qquad (6.5)$$

The decrease in lifetime by phonon coupling at elevated temperatures as is observed for Cr^{3+} in LSS but not in NSS, can be understood from the much stricter parity selection rule in the higher symmetry coordination in LSS. The radiative decay time at 4 K is almost 60 µs in LSS vs. 20 µs in NSS. The static odd-parity crystal field components already relax the selection rule in NSS and the additional contribution from thermally populated odd parity vibrations is not significant. Upon increasing the Ge-content, the low temperature radiative decay rate in the $LiSc(Si_{1-x}Ge_x)_2O_6$ series increases and a single sigmoidal fit can be used to determine the T_{50} for LSG. To model the temperature dependence for LSS/LSG solid solutions taking into account both the dis-

order in Si/Ge coordination and the temperature dependence of the radiative decay rate gives too many fit parameters. Either equation 5 or a bi-sigmoidal fit gave a reliable fit with similar outcomes for T_{50}. A bi-sigmoidal fit was used for the $LiSc(Si_{0.2}Ge_{0.8})_2O_6$ and Eq. (6.5) was used for $LiSc(Si_{1-x}Ge_x)_2O_6$ were x=0,0.2,0.4,0.6. The fits are shown in the SI. Using Eq. (6.5) LSS gives a vibrational energy hν of 203 cm^{-1}. This is a very reasonable value as low phonon energy phonon in these clinopyroxenes are around 200 cm^{-1}[41] and are typical for Sc-O or Cr-O stretching vibrations. Note that asymmetric stretching or bending vibrations in the $[CrO_6]$ can be expected to distort the inversion symmetry and break the parity selection rule to increase the radiative decay rate. The higher energy stretching vibrations in the SiO_4 or GeO_4 groups will give rise to smaller distortions for Cr^{3+}. The T_{50} values for Cr^{3+} in the LSS/LSG series decrease from 553K to 393K changing the Ge content from 0 to 100%.

The variations in quenching temperatures can be understood using the well-known configurational coordinate diagram. Previous research has shown that the dominant temperature quenching mechanism for $^4T_2$ emission from Cr^{3+} is cross-over to the $^4A_2$ ground state by thermal population of higher vibrational levels [6,24,25,42,43]bio-imaging, and modern agriculture, in which the development of NIR-emitting phosphors with large full width at half maximum (FWHM. A larger off-set between ground and excited state parabola lowers the thermal activation energy for this process. Also, a longer wavelength emission (smaller energy difference between ground and excited states) lowers the barrier for non-radiative relaxation. For the Li containing samples the quenching temperatures are higher, both for the germanate and the silicate series. The smaller Li cation creates more rigid crystal structure due to its higher ionic character resulting in a smaller offset between the ground and excited state parabola and thus a higher thermal quenching temperature. Similarly, the more covalent bonding in the germanates vs. the silicates explains the lower T_{50} values with increasing Ge content resulting in a larger offset between ground and excited state, in addition to a redshift of the emission which also contributes to lowering T_{50}.

The optical spectroscopy experiments on Cr^{3+} luminescence in $NaSc(Si_{1-x}Ge_x)_2O_6$ and $LiSc(Si_{1-x}Ge_x)_2O_6$ show that the emission band broadens and redshifts towards 900 nm by partial replacement of Si ion by Ge ions. Both effects are advantageous for application NIR-LEDs where broad band emission between 700 and 1100 nm is desired. However, increasing the Ge-content lowers the thermal quenching temperature which is a drawback for application. Based on the experimental results, an optimum Ge-content is 20-40% which gives rise to an appreciable redshift and broadening while keeping the thermal quenching temperature high enough for application in NIR-LEDs. In addition, a favourable characteristic of the $NaSc(Si_{1-x}Ge_x)_2O_6$ and $LiSc(Si_{1-x}Ge_x)_2O_6$ is the one-dimensional character with small nearest neighbour distances of 3.3 Å for Cr^{3+} in the one direction and nearest neighbour distance of 5.6 Å and 7.7Å in the other dimension. This gives rise to one-dimensional energy migration and hampers three-dimensional energy migration leading to concentra-

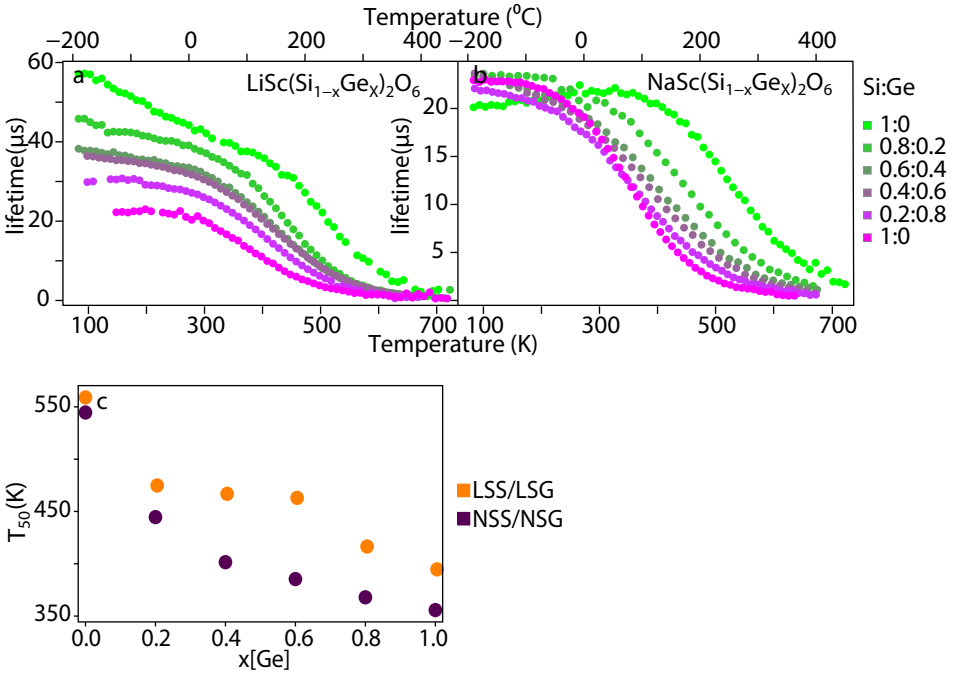

Figure 6-8. Average lifetime of $LiSc(Si_{1-x}Ge_x)_2O_6$:1%Cr^{3+}(left) and $NaSc(Si_{1-x}Ge_x)_2O_6$:1%Cr3+ (middle) as a function of temperature. From green to purple we go from Silica rich samples to Germanate rich samples. Note the difference in scale on y-axis. On the right the T_{50} values are shown as a function of Ge content.

tion quenching at high Cr^{3+} concentrations. Incorporating high Cr^{3+} concentrations without quenching is favourable to enhance the absorption strength.

FTIR/DFT

Infrared active phonons can facilitate parity forbidden d-d transitions such as the $^4T_2$ to $^4A_2$ transition in LSS by temporary inducing odd parity crystal field components. This can explain the temperature induced shortening of the $^4T_2$ to $^4A_2$ emission lifetime in LSS between 100 and 400 K as phonon modes are thermally occupied. To map the energies of phonons in the various host lattices, Fourier Transform Infrared (FTIR) absorption spectroscopy were recorded on undoped NSS/LSS/NSS/NSG.

In the IR absorption we observe that the germanates have similar spectra and in parallel the silicates also have similar spectra. The silicates have two groups of peaks, one below 700 cm^{-1} and a second group between 800 and 1200 cm^{-1}. For the germanates both groups are shifted to lower energies, the first group of peaks ending around 600 cm^{-1} and the second group situated between 700 and 900 cm^{-1}. The high energy vibrations are assigned to lo-

cal modes in the silicate and germanate groups. Si-O stretching vibrations are typically observed around 1000 cm^{-1}. As Si is lighter than Ge the energy required for the vibration is higher. For the Ge-O stretching vibrations are around 800 cm^{-1}. Replacement of Li with Na in both samples causes only minor changes. The replacement of Si with Ge has more influence on the lower energy vibrational modes than replacing Na with Li.

To further investigate the phonon energies, DFT calculations were made on $LiScSi_2O_6$ and $LiScGe_2O_6$. Experimentally determined structures($LiScSi_2O_6$: ICSD #55172 for C2/c, #152075 for $P2_1/c$, $LiScGe_2O_6$: #430516 for $P2_1/c$) are used as initial geometries. For C2/c phase of $LiScGe_2O_6$, the optimized structure of $LiScSi_2O_6$ is used as an initial structure because of no experimental structure data. The atomic structures were fully optimized by minimizing the electronic total energy and Hellmann-Feynman forces.[44] In $LiScSi_2O_6$, no energy difference between C2/c and $P2_1/c$ structure is observed. However, $P2_1/c$ structure is stable in $LiScGe_2O_6$. This result agrees with experimental observations. After the structural optimization of the unit cell the phonon dispersion was calculated for both hosts.

In Figure 6-10 the phonon energies at the Γ point are overlaid with the FTIR of the respective compound. There is good agreement between the experimentally observed and calculated vibrational energies. The gap in vibrational states between 700 and 800cm^{-1} for LSS and between 600 and 700cm^{-1} for LSG agrees with the calculations. The calculated phonon energies extend to 1050 cm-1 for the silicate and to 850 cm-1 for the germanate, again in line with the experimental results. The absorption tail above the highest energy phonons is attributed to multi phonon absorption (combination bands).

It is also interesting to investigate if the observed temperature dependence of the $^4T_2$-$^4A_2$ emission lifetime for Cr^{3+} in $LiScSi_2O_6$ is consistent with energies for odd-parity local modes. The temperature dependence was modelled using equation 4 and the fit gave a phonon energy hν of 202 cm^{-1} (see SI for the fit). The various low energy vibrations were inspected by monitoring the displacements of the atoms, via the xyz jmol files (see SI for the files for LSS/LSG). The 8th lowest phonons clearly create a strong asymmetry on the Sc site, the calculated energy of this vibration is 167 cm^{-1}. The next vibration that distorts the centre of inversion symmetry around Sc significantly are 13 and 14th vibrations, the calculated energies of these vibrations are cm^{-1} 234 and 238 cm^{-1}, respectively. The higher energy levels will have less importance as the phonon population decreases exponentially with increasing energy. As these values correspond well with the effective phonon energy of the fit 202 cm^{-1} this serves as evidence that asymmetric vibrations involving the Cr^{3+} ion and surrounding ligands are responsible for the shortening of the lifetime with increasing temperature for Cr^{3+} in the highest symmetry coordination in LSS.

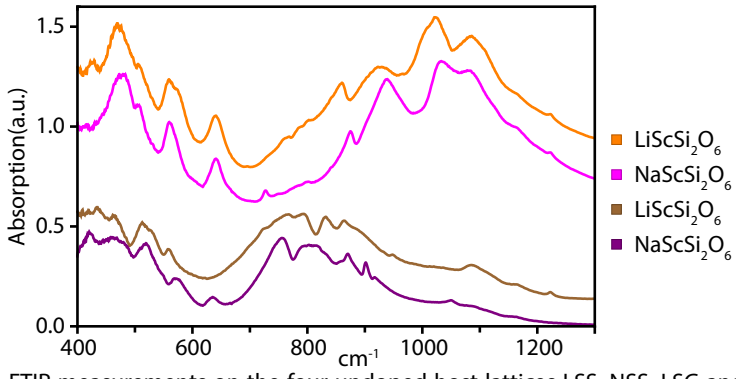

Figure 6-9. FTIR measurements on the four undoped host lattices LSS, NSS, LSG and NSG. The vertical offset was introduced for easy comparison.

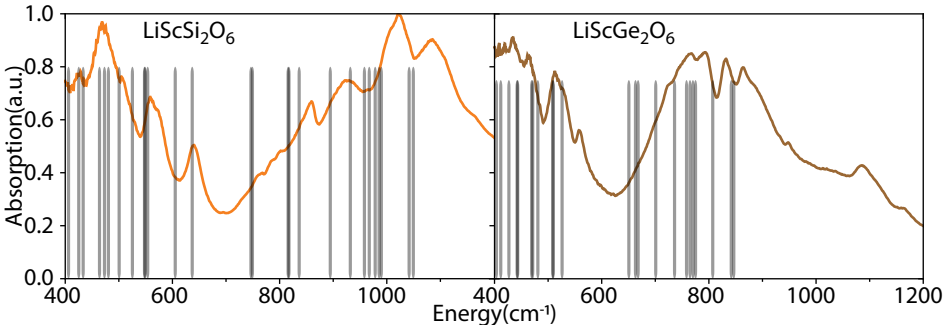

Figure 6-10. FTIR absorption measurements of LSS and LSG. The black lines indicate the phonon energies determined using DFT calculations.

Conclusion

Better blue excitable phosphors with broad band NIR emission are needed for compact light sources in new NIR sensing applications. Both $LiSc(Si_{1-x}Ge_x)_2O_6$ and $NaSc(Si_{1-x}Ge_x)_2O_6$ doped with Cr^{3+} are promising materials with efficient broad band NIR emission and high luminescence quenching temperatures. The role of partial replacement of Si by Ge on the $^4T_2$-$^4A_2$ emission has been investigated aimed at tuning the NIR emission to longer wavelengths and broadening the NIR emission output. Disorder in the second coordination sphere for mixed Si-Ge compositions broadens the NIR emission band to almost 200 nm. Addition of Ge however also lowers the luminescence quenching temperature. The trends in thermal quenching behaviour can be understood by thermally activated cross-over from the $^4T_2$ excited state to the $^4A_2$ ground state. The optimum spectral properties for application in NIR LEDs are found for in $LiSc(Si_{1-x}Ge_x)_2O_6:Cr^{3+}$ with 20 to 40% of Ge having broad band (FWHM ~180 nm) emission around 900 nm with a thermal quenching temperatures well above 100°C. In addition, the role of symmetry in the temperature dependence of ratio of $^4T_1/^4T_2$ absorption bands has been discussed indicating the ratio increases for lower symmetry coordination.

References

[1] P. M. Pattison, J. Y. Tsao, G. C. Brainard, B. Bugbee, *Nature* **2018**, *563*, 493.
[2] J. Lai, J. Zhou, Z. Long, J. Qiu, D. Zhou, Y. Yang, K. Zhang, W. Shen, Q. Wang, *Mater. Des.* **2020**, *192*, 108701.
[3] An introduction to near infrared (NIR) spectroscopy | IM Publications Open, https://www.impopen.com/introduction-near-infrared-nir-spectroscopy, accessed: **Mar., 2021.**
[4] OSLON® P1616, SFH 4737, https://www.osram.com/ecat/OSLON® P1616 SFH 4737/com/en/class_pim_web_catalog_103489/prd_pim_device_10751075/.
[5] B. Malysa, A. Meijerink, T. Jüstel, *J. Lumin.* **2018**, *202*, 523.
[6] L. Zhang, D. Wang, Z. Hao, X. Zhang, G. Pan, H. Wu, J. Zhang, *Adv. Opt. Mater.* **2019**, *7*, 1900185.
[7] S. Miao, Y. Liang, Y. Zhang, D. Chen, S. Yan, J. Liu, X.-J. Wang, *J. Mater. Chem. C* **2022**, *10*, 994.
[8] D. Huang, H. Zhu, Z. Deng, H. Yang, J. Hu, S. Liang, D. Chen, E. Ma, W. Guo, *J. Mater. Chem. C* **2021**, *9*, 164.
[9] S. Kück, L. Fornasiero, E. Mix, G. Huber, *J. Lumin.* **2000**, *87–89*, 1122.
[10] Q. Shao, H. Ding, L. Yao, J. Xu, C. Liang, Z. Li, Y. Dong, J. Jiang, *Opt. Lett.* **2018**, *43*, 5251
[11] Y. Duan, Y. Liu, G. Zhang, L. Yao, Q. Shao, *J. Rare Earths* **2021**, *39*, 1181.
[12] M. Bockstedte, A. Kley, J. Neugebauer, M. Scheffler, *Comput. Phys.Commun.* **1997**, *107*, 187.
[13] P. Hohenberg, W. *Kohn, Phys. Rev.* **1964**, *136*, B864.
[14] W. Kohn, L. J. Sham, *Phys. Rev*. **1965**, *140*, A1133.
[15] G. Kresse, J. Furthmüller, *Phys. Rev. B* **1996**, *54*, 11169.
[16] G. Kresse, D. Joubert, *Phys. Rev. B* **1999**, *59*, 1758.
[17] J. P. Perdew, K. Burke, M. Ernzerhof, *Phys. Rev. Lett.* **1996,** *77*, 3865.
[18] S. Baroni, P. Giannozzi, A. Testa, *Phys. Rev. Lett.* **1987**, *58*, 1861.
[19] X. Gonze, *Phys. Rev. A* **1995**, *52*, 1086.
[20] A. Togo, I. Tanaka, *Scr. Mater.* **2015**, *108*, 1.
[21] R. D. Shannon, *Acta Crystallogr. Sect. A* **1976**, *32*, 751.
[22] Y. Yan, M. Shang, S. Huang, Y. Wang, Y. Sun, P. Dang, J. Lin, *ACS Appl. Mater. Interfaces* **2022**, *14*, 8179.
[23] U. Fano, *Phys. Rev.* **1961**, *124*, 1866.
[24] S. Adachi, *J. Lumin*. **2021**, *234*, 117965.
[25] S. Miao, Y. Liang, Y. Zhang, D. Chen, X. J. Wang, *ACS Appl. Mater. Interfaces* **2021**, *13*, 36011.
[26] Z. Jia, C. Yuan, Y. Liu, X.-J. Wang, P. Sun, L. Wang, H. Jiang, J. Jiang, *Light Sci. Appl.* **2020**, *9*, 86.
[27] J. Mooney, P. Kambhampati, *J. Phys. Chem. Lett*. **2013**, *4*, 3316.
[28] B. Malysa, A. Meijerink, W. Wu, T. Jüstel, *J. Lumin.* **2017**, *190*, 234.
[29] Y. Tanabe, S. Sugano, *J. Phys. Soc. Japan* **1954**, *9*. 766
[30] G. Wang, H. G. Gallagher, T. P. J. Han, B. Henderson, *J. Cryst. Growth* **1996**, *163*, 272.
[31] Z. Nie, J. Zhang, X. Zhang, X. Ren, W. Di, G. Zhang, D. Zhang, X. J. Wang, *J. Phys. Condens. Matter* **2007**, *19*, 076204.
[32] F. C. Hawthorne, H. D. Grundy, *Can. Mineral.* **1977**, *15*, 50
[33] E. A. Genkina, B. A. Maksimov, V. A. Timofeeva, A. B. Bykov, *J. Struct. Chem.* **1985**, *26*, 136.
[34] M. Back, J. Ueda, H. Nambu, M. Fujita, A. Yamamoto, H. Yoshida, H. Tanaka, M. G. Brik, S. Tanabe, *Adv. Opt. Mater*. **2021**,*9*, 2100033.
[35] D. Chen, X. Chen, X. Li, H. Guo, S. Liu, X. Li, *Opt. Lett.* **2017**, *42*, 4950.
[36] T. Senden, R. J. A. Van Dijk-Moes, A. Meijerink, *Light Sci. Appl.* **2018**, *7*, 2047.
[37] D. Böhnisch, J. Rosenboom, A. García-Fuente, W. Urland, T. Jüstel, F. Baur, *J. Mater. Chem. C* **2019**, *7*, 6012.
[38] A. M. Srivastava, H. A. Comanzo, S. Camardello, S. B. Chaney, M. Aycibin, U. Happek, *J. Lumin.* **2009**, *129*, 919.

[39] G. Özen, *Opt. Commun.* **2000**, *183*, 493.
[40] T. Senden, E. J. van Harten, A. Meijerink, *J. Lumin.* **2018**, *194*, 131.
[41] P. Vignola, N. Rotiroti, F. Hatert, D. Bersani, S. Andò, S. Varvello, *Can. Mineral.* **2019,** *57*, 489.
[42] J. Xiang, J. Zheng, X. Zhao, X. Zhou, C. Chen, M. Jin, C. Guo, Mater. *Chem. Front*. **2022**, *6*, 440.
[43] T. Gao, W. Zhuang, R. Liu, Y. Liu, C. Yan, X. Chen, Cryst. *Growth Des.* **2020**, *20*, 3851.
[44] R. P. Feynman, *Phys. Rev.* **1939**, *56*, 340.

QR-Codes

Link to paper

Supporting Information

Supporting information

Figure S6-1. $NaSc(Si_{1-x}Ge_x)_2O_6$: Cr1% from left to right were x=1.0, 0.8, 0.6, 0.4, 0.2, 0.0 direct after annealing

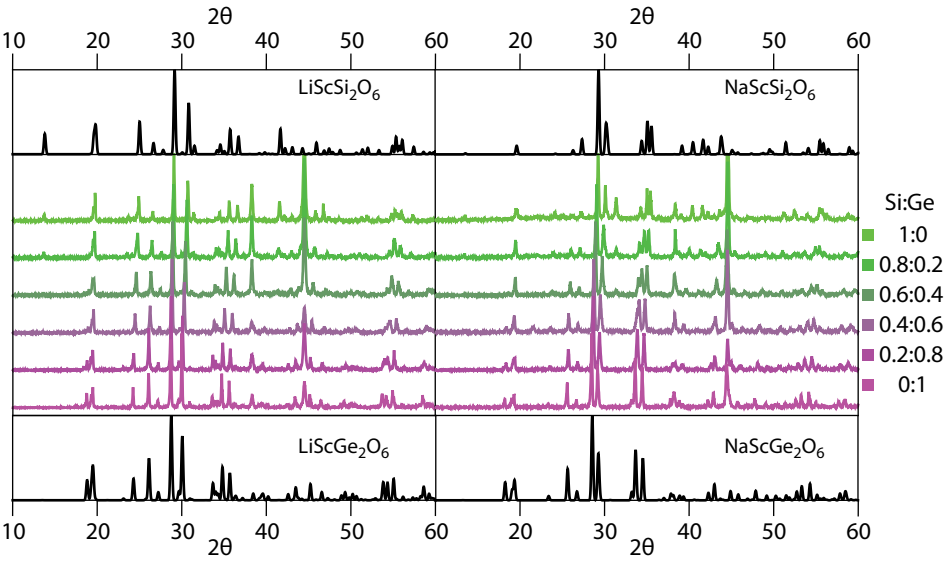

Figure S6-2. Full XRD diffractograms of: $LiSc(Si_{1-x}Ge_x)_2O_6$:1%$Cr^{3+}$with the reference of $LiScSi_2O_6$(LSS) and $LiScGe_2O_6$ (LSG) shown above and below. $NaSc(Si_{1-x}Ge_x)_2O_6$:1%$Cr^{3+}$with the reference of $NaScSi_2O_6$(NSS)and $NaScGe_2O_6$ (NSG) shown above and below.

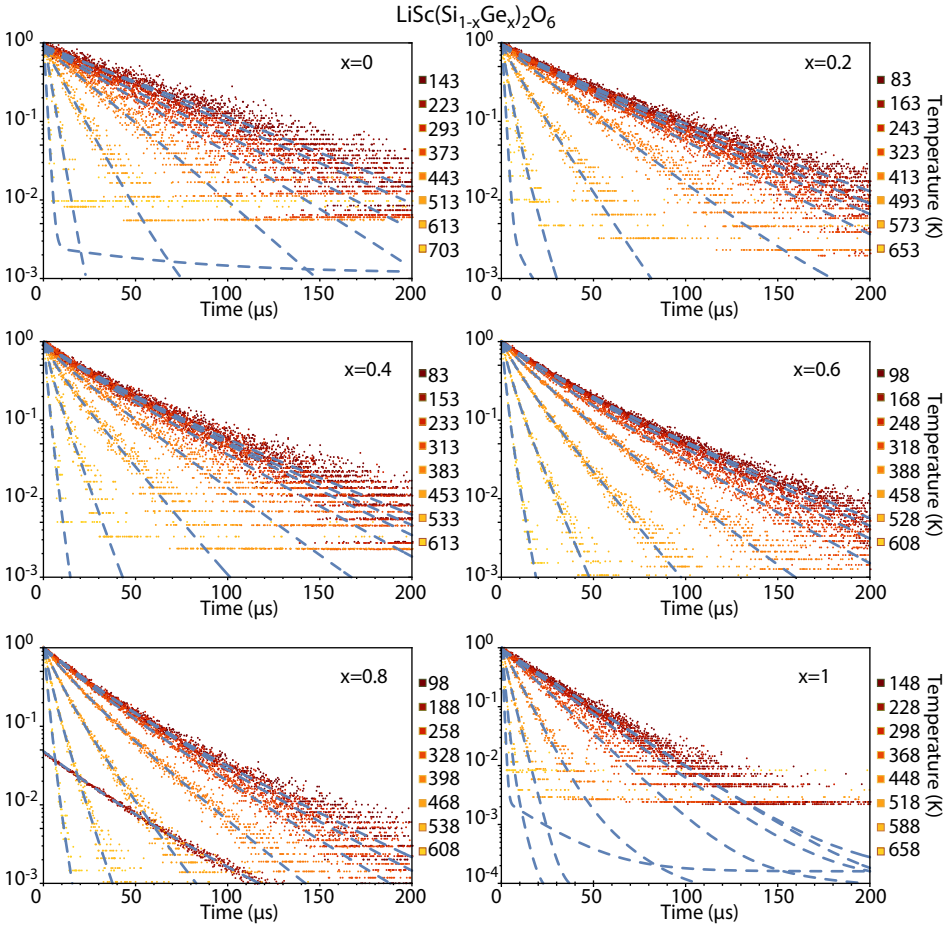

Figure S 6-3. Excerpts of the T dependent lifetimes of $LiSc(Si_{1-x}Ge_x)_2O_6$:1%Cr^3. Excited at 480nmm measured at 800nm

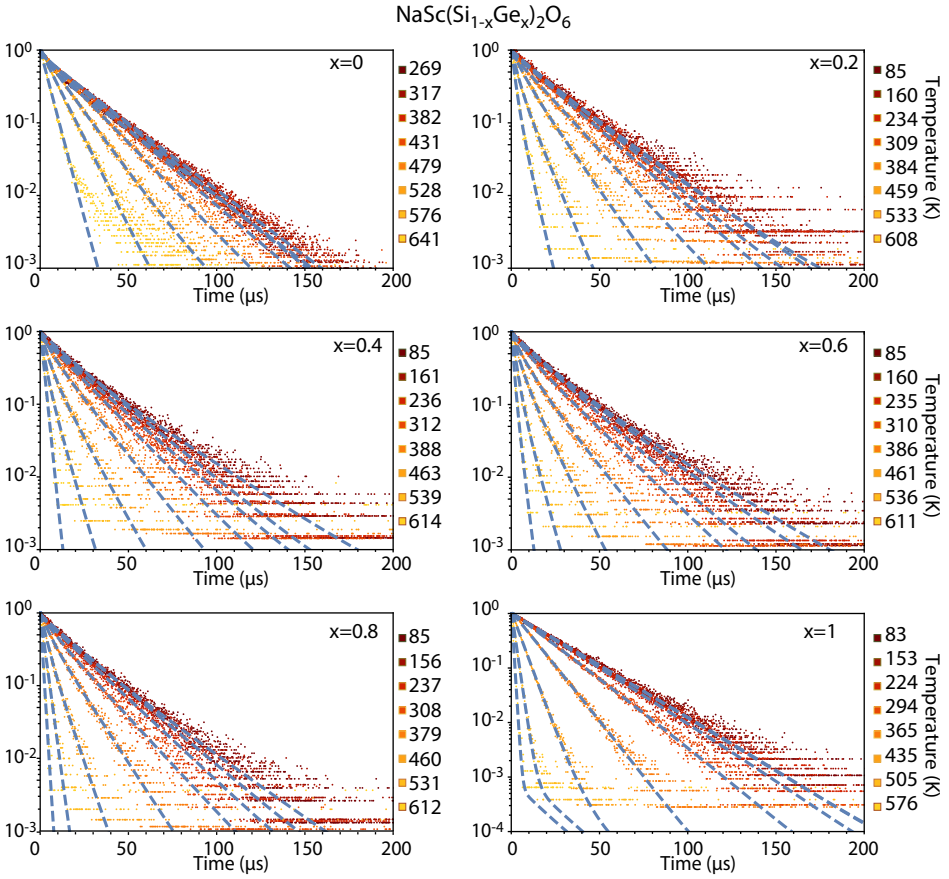

Figure S6-4. Excerpts of the T dependent lifetimes of $NaSc(Si_{1-x}Ge_x)_2O_6$:1%Cr^{3+}. Excited at 480nmm measured at 800nm.

Table S6-1. Deviation from a perfect octahedral coordination of the oxygens surrounding the scandium site. The axes are the distances of opposing oxygens atoms, while the edges are the distances of the nearest oxygen atoms. Between every couple of oxygen atom there is a vector. All possible angles between these vectors were compared to what they should be in a perfect octahedron (either 0º or 45º or 60º or 90 º). Then the average deviation per angle was determined. To determine these distances and angles the following cif files of the following ICSD collection codes the ICDS database: $NaScSi_2O_6$: #14263, [1] $NaScGe_2O_6$ #22503,[2] $LiScSi_2O_6$ #55172,[3] Li Sc Ge_2O_6 #430516.[4]

Host	angle deviation degree	Mean axes(Å)	stdev axes (Å)	Mean edges(Å)	Stdev edges(Å)
LSS	2.201	4.199	0.011	2.968	0.113
LSG	2.775	4.204	0.019	2.971	0.140
NSS	2.777	4.183	0.002	2.964	0.105
NSG	3.360	4.188	0.026	2.969	0.140

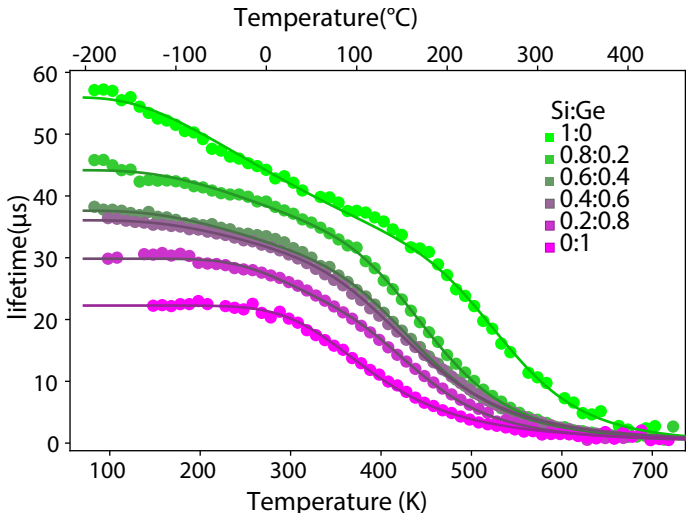

Figure S6-5. Fitted lifetime $LiSc(Si_{1-x}Ge_x)_2O_6$:1%Cr^{3+} samples as a fumction of temperature. The solid line through the dots is the used fit, The $LiScSI_2O_6$ and $LiScGe_2O_6$ were done with a single sigmoidial fit while the solid solution were fitted with a bisigmoidial fit. The parameters from the fit are shown in Table S6-2 and S6-3

Table S6-2. Parameter entries for fits when using equation 6-5

Sample	τ_0(µs)	τ_{nr}(µs)	hν (cm^{-1})	ΔE (cm^{-1})	T_{50}(K)
LSS	56.0	9.7×10^{-5}	202.6	4817	553
LSS x=0.2	44.2	8.1×10^{-4}	252.1	3443	473
LSS x=0.4	37.6	1.9×10^{-3}	250.5	3044	465
LSS x=0.6	36.1	4.7×10^{-3}	264.5	2739	461

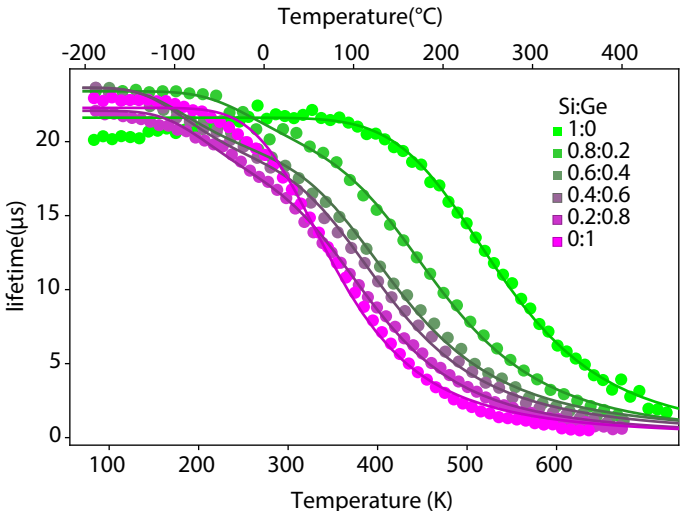

Figure S6-6. Fitted lifetime $NaSc(Si_{1-x}Ge_x)_2O_6$:1%Cr^{3+} samples as a fumction of temperature. The solid line through the dots is the used fit, The $NaScSI_2O_6$ and $NaScGe_2O_6$ were done with a single sigmoidial fit while the solid solution were fitted with a bisigmoidial fit. The parameters from the fit are shown in Table S6-3

$$\tau(T) = \frac{X_1\tau(0)}{1 + A_1 e^{-\Delta E_1/kT}} + \frac{X_2\tau(0)}{1 + A_2 e^{-\Delta E_2/kT}} \qquad \text{(S 6-1)}$$

Table S6-3. Parameter entries for fits when using single sigmoidial or bi sigmoidial fit, equation S6-1

Sample	τ_0(µs)	X_1	X_2	A_1	A_2	ΔE_1 (cm^{-1})	ΔE_2 (cm^{-1})	T_{50}(K)
NSS	21.6	-	-	5562	-	3234	-	539
x=0.2	23.4	0.79	0.21	2255	674	2552	1274	450
x=0.4	23.0	0.72	0.28	1558	130	2239	856	406
x=0.6	23.0	0.70	0.30	1677	164	2191	863	390
x=0.8	21.5	0.65	0.35	2355	325	2224	1070	374
NSG	22.3	-	-	1087	-	1728	-	356
LSS x=0.8	29.8	0.65	35	20343	1059	3074	1547	414
LSG	22.2	-	-	1454	-	1989	-	393

Table S6-4. Calculated lattice constants versus experimental determined lattice constants of $LiScSi_2O_6$ and of $LiScGe_2O_6$ ICSD#152079,[3] ICSD#55172,[3] ICSD#430516.[4]

Com-pound	$LiScSi_2O_6$				$LiScGe_2O_6$		
Space group	C2/c(15)		$P2_1/c(14)$		C2/c(15)	$P2_1/c(14)$	
Z	2		4		2	4	
	calc.	expt.	calc.	expt.	calc.	calc.	expt.
a(Å)	9.921 (+1.14%)	9.809	9.922 (+1.19%)	9.805	10.071	10.171 (+1.72%)	9.998
b	9.079 (+1.46%)	8.948	9.074 (+1.39%)	8.949	9.289	9.204 (+1.09%)	9.104
c	5.412 (+1.01%)	5.358	5.404 (+0.86%)	5.358	5.510	5.524 (+1.14%)	5.462
β(deg.)	110.66	110.42	110.648	110.39	108.177	109.553	109.24
V(Å^3)	456.11 (+3.49%)	440.72	455.25 (+3.31%)	440.68	489.74	487.26 (+3.81%)	469.38

[1] F. C. Hawthorne, H. D. Grundy, *The Canadian Mineralogist.* **1977**.
[2] E. A. Genkina, B. A. Maksimov, V. A. Timofeeva, A. B. Bykov, *J. Struct. Chem.* **1985**, *26*, 136.
[3] H. D. Grundy, **1973**, *2*, 2615.
[4] M. Ai, G. J. Redhammer, G. Roth, **2004**, *219*, 278.
[5] G. Hofer, J. Kuzel, K. S. Scheidl, G. Redhammer, R. Miletich, *J. Solid State Chem.* **2015**, *229*, 188.

Chapter 7

Conclusion and Outlook

"... und alles, was man weiss, nicht bloss rauschen und brausen gehört hat, lässt sich in drei Worten sagen."

"... and whatever a man knows, whatever is not mere rumbling and roaring that he has heard, can be said in three words"

Ferdinand Krünberger

Conclusion and Outlook

The luminescence properties of various transition metal ions in inorganic host lattices have been studied in this thesis, with a strong emphasis on their temperature-dependent behavior also in relation with application as phosphors in white light LEDs for lighting and broad band NIR LEDs for sensing. The following paragraphs present an overview of the key results from each chapter. This is followed by an outlook on future research topics and challenges.

Chapter 3 of this thesis reports on the elucidation of the thermal luminescence quenching mechanism of Mn^{2+} ions. The study reveals that Mn^{2+} luminescence is quenched through thermally assisted photoionization (PI), where an electron from the excited state of Mn^{2+} can escape to the conduction band at elevated temperatures causing luminescence quenching. The investigations involve measurements and analysis of the temperature-dependent luminescence properties of Mn^{2+} in 20 different host matrices, including emission intensity and luminescence lifetime measurements as a function of temperature. Additionally, thermally stimulated luminescence measurements were performed on Mn^{2+}-doped AlN, $MgGa_2O_4$, $ZnGa_2O_4$, and Zn_2SiO_4 following illumination at a wide range of temperatures. These results showed that the TSL signal increased for illumination temperatures in the same temperature range where luminescence quenching of Mn^{2+} was observed under direct excitation. This provides strong evidence that PI is the operative quenching mechanism. A clear correlation between bandgap and quenching temperature indicates that for all host materials, Mn^{2+} luminescence quenches via thermally assisted photoionization. To verify that PI was the quenching mechanism and not thermal crossover (TC), the full width at half maximum (FWHM) of the Mn^{2+} emission in different host materials was compared to the quenching temperature. No correlation was found while for the TC mechanism a broader bandwidth is expected to result in lower quenching temperatures. The combined TSL measurements and correlation with bandgap to the luminescence quenching temperature provide clear evidence that Mn^{2+} quenches via thermally assisted photoionization. This information helps in the design of Mn^{2+} phosphors with high thermal quenching temperatures of the luminescence.

Chapter 4 of the thesis explores the near-infrared (NIR) emission observed in materials with high concentrations of Mn^{2+}. Many recent papers report strongly red-shifted Mn^{2+} emission and attribute this near infrared (NIR) emission to exchange coupled Mn^{2+} pairs. This explanation is controversial as it is not consistent with exchange coupling strengths previously obtained

from careful optical and magnetic studies. An alternative explanation for the observation of strongly redshifted emission in concentrated Mn^{2+} phosphors is energy migration to an impurity ion or trap that is responsible for the NIR emission. Energy migration to this NIR emitting center is facilitated at high Mn^{2+} concentrations. To investigate this hypothesis, $MgAl_2O_4$ doped with 1 to 50% Mn^{2+} was synthesized and the emission and excitation spectra were measured. The results showed a clear increase in the NIR peak intensity with increasing Mn concentration. Upon cooling the sample with 50% Mn to cryogenic temperatures a simultaneous decrease of NIR and an increase in green Mn^{2+} emission was observed. This supports the explanation where energy migration is responsible for the NIR emission as energy migration is hampered at cryogenic temperatures while the concentration of exchange coupled pairs is not temperature dependent. Excitation spectra for the NIR emission were measured and show excitation peaks at the same positions as those in excitation spectra of the normal green Mn^{2+} emission, in line with energy migration over the Mn^{2+} sub lattice to NIR emitting traps. For strongly exchange coupled pairs a shift in the position of excitation bands and additional excitation bands are expected for exchange coupled pairs, especially since the spectral shifts reported for the NIR emission in various host lattices are very large (3400 – 6800 cm^{-1}) which can only be explained by very strong exchange coupling that would also affect the excitation spectra. To further investigate the origin of the NIR emission, $MgAl_2O_4$ doped with 10% Mn^{2+} and varying amounts of MgO and Al_2O_3 precursor were synthesized. The results showed that an increase in MgO led to a corresponding increase in the NIR emission, indicating that possibly Mn^{3+} is the impurity responsible for the NIR emission in this host material.

Chapter 5 discusses the discovery of a new Mn^{4+}-doped crystallographic phase: hexagonal-$KRbSiF_6$ (KRSF). This new phase was found serendipitously while attempting to improve the optical properties of K_2SiF_6 doped with Mn^{4+} (KSF), a widely used red-emitting LED phosphor for display applications due to its sharp line emission around 620 nm enabling a wide color gamut. However, the long emission lifetime of the Mn^{4+} emission causes KSF to suffer from droop effects at higher photon fluxes. To reduce the droop and also to increase lumen/W efficacy, disorder was introduced into the crystal structure by synthesizing solid solutions of K_2SiF_6, Rb_2SiF_6, and Cs_2SiF_6 in which a mixed K/Rb or Rb/Cs second coordination sphere of Mn^{4+} could potentially distort the inversion symmetry for Mn^{4+} resulting in an increased transition probability for the zero-phonon line (ZPL). Aqueous solutions of H_2SiF_6/K_2MnF_6 and KF/RbF/CsF were mixed and precipitated in ethanol. During the synthesis of $KRbSiF_6$, the precipitate was left for a week, and it was found that it had transformed from the cubic to the hexagonal phase. The optical properties of the hexagonal phase of KRSF were compared to both cubic KRSF and cubic KSF. Mn^{4+} in the hexagonal phase has a strong zero-phonon line (ZPL) that distinguishes it from the cubic phase and can be understood from a deviation of inversion symmetry in the first F^- coordination sphere. Additionally, the lifetime of the Mn^{4+} emission in the hexagonal phase is shorter (~6 ms) than that

of the cubic phase (~8 ms). The increased ZPL has some additional benefits, such as a 3% increase in luminous efficacy and the shorter emission lifetime results in less droop effects. The temperature-dependent properties were also investigated, and a similar high quenching temperature just over 500 K was found for Mn^{4+} in both KRSF phases. The increase in the ZPL intensity of Mn^{4+} emission in the precipitate was monitored over several days to quantify the formation of the hexagonal phase as a function of time. After an induction period of ~15 hours the ZPL appeared indicating that the precipitate started to transform to the hexagonal phase. In the next ~10 hours an exponentially increasing transformation rate resulted in fully transformed hexagonal KRSF. The mechanism behind the exponentially increasing transformation rate is intriguing and further *in situ* studies and modelling are needed to understand the phase transformation kinetics.

Chapter 6 discusses the impact of solid solutions on the emission bandwidth (FWHM) and luminescence quenching temperature of Cr^{3+}. The near infrared (NIR) emission between 700 to 1000 nm is promising for NIR-based sensing. A product is irradiated with a wide range of wavelengths, and the reflected NIR radiation is detected using a CCD spectrometer to extract chemical information by the analysis of the intensity distribution of the reflected NIR radiation. This is different from the incident NIR spectrum as a result of absorption by overtone vibrational modes of organic molecules in the product. To achieve a broad spectrum required for NIR sensing, a NIR phosphor which can convert blue or red LED light to NIR radiation is typically used. Cr^{3+} has broad band emission in the NIR in a low crystal field. The bandwidth can be further increased by incorporating Cr^{3+} into a solid solution to create disorder. However, for a NIR phosphor to be useful in a device, it must function at elevated temperatures as the LED chip can get very hot. In this chapter the influence of solid solutions of $NaSc(Si,Ge)_2O_6$ and $LiSc(Si,Ge)_2O_6$ on the FWHM and the luminescence quenching temperature of Cr^{3+} emission were investigated. The solid solutions have a broader emission than the pure compounds, but increasing the relative Ge content of the solid solutions reduces the quenching temperature from 550K to 350K. Therefore, creating solid solutions to enhance the performance of these broad band NIR phosphors based on Cr^{3+} emission is a trade-off between a broader emission and a lower quenching temperature.

Outlook

The relationship between the luminescence quenching mechanism of Mn^{2+} and the band gap of the material is clearly demonstrated in Figures 3-3 to 3-5 of Chapter 3. To refine the model and provide even stronger evidence for the thermally activated photoionization mechanism it is important know the position of the Mn^{2+} ground state in the bandgap. A method previously explored for lanthanide ions involves measurements to locate the ground state and to place it in a vacuum-referred binding energy diagram (VRBE). It is interesting

to perform similar measurements for Mn^{2+} as this allows for the determination of the absolute energy distance between the bottom of the conduction band and the $^4T_1$ level of Mn^{2+}. To construct a VRBE with Mn^{2+}, the band gap of the material and the distance to the vacuum level must be determined. This requires PLE spectra going into the vacuum ultraviolet for undoped samples as well as ultraviolet photoelectron spectroscopy (UPS) measurements.

Strong evidence for thermally activated photoionization is the mechanism responsible for luminescence quenching was obtained from TSL curves recorded at different charging temperatures. However, for many Mn^{2+}-doped phosphors no signal was obtained during the TSL measurements. This can be due to traps being too deep to be emptied or because shallower traps are emptied quickly at the charging temperature, thereby preventing the charging process (trap filling). Indeed, to correlate a TSL signal with the PI quenching mechanism, one has to be lucky to have traps with right trap depths present in the phosphor. By using photo-stimulated luminescence (PSL) following charging at different temperatures, much deeper traps can be probed. While PSL curves are often difficult to interpret, in this case, the nature of the traps is irrelevant, and only the filling of the traps in the temperature range where luminescence quenching occurs is important. For samples that did not produce a TSL signal, PSL may be a promising alternative. It is also less susceptible to blackbody radiation and can access a wider range of trap depths.

Chapter 5 describes the transformation of KRSF from its cubic phase to the hexagonal phase in a mixture of water and ethanol, but the mechanism behind the transformation and its exponentially increasing rate remained unclear. One hypothesis is that this is an autocatalytic process, where the hexagonal phase facilitates the formation of more hexagonal phase, as observed in metallic Sn where the β phase transforms exponentially to the α phase at -40°C. [1] The complete transformation from cubic to hexagonal KRSF takes approximately 8 hours, similar to the transformation in Sn. The cubic particles are in the micro meter size range and are precipitated from a suspension of nanocrystalline KRSF during the transformation. Alternatively explanations may be sought in analogy to recent observations of the transformation of cubic α-$NaYF_4$ nanoparticles to hexagonal β-$NaYF_4$ where a difference in growth and dissolution reactivity was able to explain the exponentially increasing transformation rate. Further studies using *in situ* x-ray scattering techniques during the transformation may be used to provide a better understanding of the transformation mechanism.[2] In addition, the initial formation of nanocrystalline Mn^{4+} doped KRSF is interesting and deserved further attention. Lanthanide doped insulator nanocrystals and transition metal semiconductor nanocrystals have been studied in the past two decades and form interesting classes of materials both from a fundamental and applied point of view. Recently lanthanide doped semiconductor nanocrystals (especially halide perovskites) are receiving more attention and it would be interesting to also explore transition metal insulator nanocrystals, also for sensing applications. The higher sensitivity of the outer 3d orbitals vs. the inner 4f orbitals of lan-

thanides may give the 3d transition metal doped nanocrsytals an advantage over lanthanide doped insulator nanocrystals.

From an application point of view, Chapter 5 raises interesting questions on the potential of hexagonal K(R)SF in white light LEDs. The research indicated that the hexagonal phase of KRSF is notably more susceptible to humid environments compared to the cubic KSF. The underlying reason for this is uncertain, and it is not clear whether it is due to the Rb content and if lowering the Rb fraction would help to improve the stability. An investigation comparing cubic and hexagonal KRSF would help to clarify the factors that affect phase stability, by distinguishing the role and contributions of the constituent elements and the crystal structure. Finally, it should be possible to synthesize pure $K_2SiF_6:Mn^{4+}$ in the hexagonal phase as this polymorph has been identified and synthesized in the past century, albeit not doped with Mn^{4+}.[3,4] If synthesis under ambient conditions do not work out, high pressure conditions may be a route to create a narrow band LED phosphor which is superior to KSF.

In Chapter 6 Cr^{3+} doped phosphors were proposed as a viable source for NIR light for chemical analysis by measuring vibrational overtones of organic molecules. $NaSc(Si,Ge)_2O_6$ and $LiSc(Si,Ge)_2O_6$ doped with Cr^{3+} have a strong and broad emission at wavelengths between 700 and 1000 nm and a relatively high quenching temperature and are thus excellent phosphors in this NIR range. The detectors that are presently associated with chemical analysis and sensing are typically crystalline silicon based CCD detectors. These detectors are able to detect wavelength up to ~1000 nm. Another interesting region for NIR sensing lies in the area of 1000 to 1700nm. This region of the NIR is in many cases preferred as the lower overtones have a stronger absorption in the 1000 to 1700 nm part of the NIR as it includes second vibrational overtones of organic molecules while the 700-1000nm region encompasses the weaker absorbing third or higher overtones. There is recent development in the better NIR detectors in the 1000-1700 nm range which may enable cheap and sensitive sensors for this alternative NIR window.

Clearly, NIR sensing in the 1000-1700 nm range requires also an efficient broad band excitation source in this wavelength range. A real promising future for transition metal doped phosphor lies in this type of NIR emitting phosphors. In the region of 1000 to 1700 nm Co^{2+} and Ni^{2+} doped phosphors have shown to have broadband emission. [5–7] Phosphors based on these 3d transition metals are likely to be superior to lanthanide based phosphor or quantum dot phosphors as they have a broad emission which is impossible to obtain for 4f-4f transitions in lanthanides. NIR emitting quantum dots can have broad band emission but they suffer from stability issues. The major downside of Ni^{2+} and Co^{2+} based phosphors is that their emission is mostly quenched at room temperature. [5–7] Understanding of the quenching mechanism of these ions is still lacking and new insights can aid in the development of stable NIR emission in the region of 1000 to 1700nm from 3d transition metal doped phosphors.

For the lighting industry there still is the need for new phosphors to improve

the color rendering, color gamut and efficacy of white light LEDs for lighting and displays. For green emission a narrower band phosphor is desired that does not show degradation over time. Currently a popular green emitting phosphor is Eu^{2+}-doped β-SiAlON. The green emission band has a FWHM of 55 nm. The broadness of the band lowers the color quality and efficiency in screens. Alternatively green emitting quantum dots can be used while there is also research on narrower band Eu^{2+} emission. In chapter 3 several highly stable compounds emitting in the green part of the spectrum show a significant lower FWHM of their emission e.g $ZnAl_2O_4:Mn^{2+}$ and $ZnGa_2O_4:Mn^{2+}$ which both have a FWHM below 25 nm. Although these compounds have a very poor absorption in the blue part of the spectrum, they show the potential of transition metal based phosphors for narrow green emission. The holy grail is to find an efficient blue absorbing sensitizer for the narrow band green Mn^{2+} emission. The small energy difference between the blue absorption at 450 nm and green emission around 520 nm leaves very little room for a sensitizer to absorb in the blue and emit at wavelengths overlapping with Mn^{2+} excitation lines. With the rapid development of more efficient violet and near-UV LEDs the window for sensitization widens and more options are available for sensitization of narrow band Mn^{2+} emission. It remains challenging as the spin- and parity forbidden character of the transitions on Mn2+ requires energy transfer via exchange interaction which is only efficient at very short distances.

There is even more room for improvement in the field of red phosphors which are essential for warmer white LEDs. The phosphors that are currently added for an extra red component are either Ca-SiAlON or SLA. The former has a broad emission peak where a significant proportion of the emission is above 650 nm where the eye sensitivity is extremely low. On the other hand SLA has a far narrower peak but has limited chemical stability and slowly degrades over time. Again Mn^{2+}-based phosphors as $AlN:Mn^{2+}$ have a narrow red emission and are chemically inert. Again, the downside of these materials is the extreme poor absorption in the blue part of the spectrum.

For high power applications where red light is desired as for example in projectors for large screens, lighting with improved color rendering in large sport stadiums and the automotive industry no reliable orange/red emitting phosphor has been found to date. For these high power density applications the desired phosphor needs to have a fast turnover rate to prevent serious droop effects. This can only be realized for emitters with short emission lifetimes. The parity forbidden 4f-4f transitions of lanthanides and spin- and parity forbidden 3d-3d transitions of transition metal ions have lifetimes in the hundreds of µs to several ms range which is too long for these application. Quantum dots offer a solution as the emission life times are in the ns range. However, these high power applications also involve high temperatures and combined with the extreme excitation densities (exceeding 10 W/mm^2) the quantum dots rapidly degrade. Even for mid-power LED applications it is challenging to stabilize CdSe and InP QDs. Only Ce^{3+} in garnet phosphors have so far shown a combination of the high turnover rate (as a result of the ~50-70

ns emission life time) and high stability required for these application. Alternative stable Ce^{3+} based phosphors with orange/red Ce^{3+} emission and a high luminescence quenching temperature are another active field of phosphor research. This thesis has shed new light on the luminescence of transition metal ions for LEDs but it is evident that the quest 'LEDs make light better' continues.

[1] B. Cornelius, S. Treivish, Y. Rosenthal, M. Pecht, *Microelectron. Reliab.* **2017**, *79*, 175.
[2] P. T. Prins, J. C. van der Bok, T. P. van Swieten, S. O. M. Hinterding, A. J. Smith, A. V. Petukhov, A. Meijerink, F. T. Rabouw, *Angew. Chemie - Int. Ed.* **2023**, *62,* e2023050.
[3] B. Gossner, *Zeitschrift für Krist. - Cryst. Mater.* **1904**, *38*, 110.
[4] C. M. Gramaccioli, I. Campostrini, *Can. Mineral.* **2007**, *45*, 1275.
[5] L. P. Sosman, A. Dias Tavares, T. Abritta, *J. Phys. D. Appl. Phys.* **2000**, *33*, L19.
[6] Z. Zhao, C. Bocker, C. Liu, C. Rüssel, L. Li, C. Lin, *Opt. Lett. Vol. 40, Issue 22, pp. 5263-5266* **2015**, *40*, 5263.
[7] C. Matuszewska, L. Marciniak, *J. Lumin.* **2020**, *223*, 117221.

Chapter 8

Nederlandse Samenvatting

“ Als ik zou willen dat je het begreep,
had ik het wel beter uitgelegd”

“If I had the intention for you to understand it,
I would’ve explained it better”

Johan Cruijf

Lichtbronnen maken het ons mogelijk om activiteiten te ondernemen ook na zonsondergang. Om deze reden wordt de ontdekking van vuur als een belangrijke stap gezien voor de ontwikkeling van de moderne mens. Waar kaarsen en olielampen de essentiële lichtbronnen waren in de afgelopen 6000 jaar van de menselijke geschiedenis, zijn sinds ruim 100 jaar elektrische lichtbronnen niet meer weg te denken in onze moderne maatschappij. Met de huidige klimaatcrisis is het echter essentieel dat deze lichtbronnen een hoge efficiëntie hebben om de CO_2 uitstoot van de mens te minimaliseren. Sinds de uitvinding van de lamp is de efficiëntie van lichtbronnen sterk verbeterd. Oude gloeilampen hebben een efficiëntie van slechts 5%. Dit betekent dat 5 procent van de elektrische energie die men erin stop werkelijk wordt omgezet naar energie in de vorm van zichtbaar licht. TL buizen, of fluorescentie lampen hebben een efficiëntie van typisch 20%. Moderne LED lampen hebben daarentegen een efficiëntie van 30% of meer. Niet alleen is een LED lamp veel efficiënter in elektriciteitgebruik, een LED lamp hoeft ook veel minder vaak vervangen te worden. De levensduur van een LED lamp is typisch meer dan 30 000 uur, veel langer dan zijn traditionele voorgangers. Toch is er nog steeds ruimte voor innovatie in termen van kleurweergave en energie-efficiëntie. In dit proefschrift hoop ik bij te dragen aan een beter begrip van de natuurkundige fenomenen die een rol spelen in het verlies van efficiëntie, en daarmee aan de uiteindelijke verbetering van deze lampen.

Om een idee te krijgen waar mijn onderzoek over gaat is het belangrijk om te begrijpen wat licht is en hoeveel energie het heeft. Vervolgens zal ik uitleggen hoe atomen licht kunnen absorberen en uitzenden. Daarnaast is het belangrijk om te begrijpen hoe atomen kristalstructuren vormen. Deze aspecten zal ik eerst beschrijven. Daarna zal ik van elk hoofdstuk uitleggen wat erin ontdekt is.

Licht is het deel van het elektromagnetisch spectrum dat wij als mens kunnen zien. Het bestaat uit deeltjes: fotonen. Deze fotonen gedragen zich ook als golven wanneer ze door de ruimte bewegen. Hoeveel energie een foton heeft wordt bepaald door de golflengte. De golflengte is de afstand tussen de maxima van twee golven (zie figuur 8-1). De energie en golflengte zijn omgekeerd evenredig met elkaar: hoe langer de golflengte, hoe lager de energie van een foton en wordt de golflengte twee keer zo kort dan wordt de fotonenergie twee keer zoveel.

Met onze ogen kunnen wij mensen alleen golflengtes waarnemen tussen de 400 en 700 nanometer (een nanometer is één miljoenste van een millimeter). Wij zien fotonen met een golflengte van 450 nanometer als blauw, fotonen van 520 nanometer zien we als groen en 620 nanometer als rood. Bij kortere golflengtes dan 400 nm komen we in het ultraviolette gebied, deze golflengtes zijn schadelijk voor onze huid en als bescherming kleurt onze huid bruin. In-

dien we de golflengte nog veel korter maken en dus de energie van de fotonen groter maken dan komen we uit bij Röntgenstraling. Aan de andere kant van het lichtspectrum, zijn er fotonen met een langere golflengte dan rood. Dit kennen we als infrarood (denk aan de warmtelampen op terrassen in de winter). Voor nog langere golflengtes spreken we over microgolven en als je de golflengte nog langer maakt (in de orde van centimeters tot meters) komen we bij radiogolven. Iedere vorm van deze straling, van Röntgenstraling tot radiogolven, bestaat dus uit hetzelfde soort fundamentele deeltjes: fotonen die met de lichtsnelheid door de ruimte bewegen.

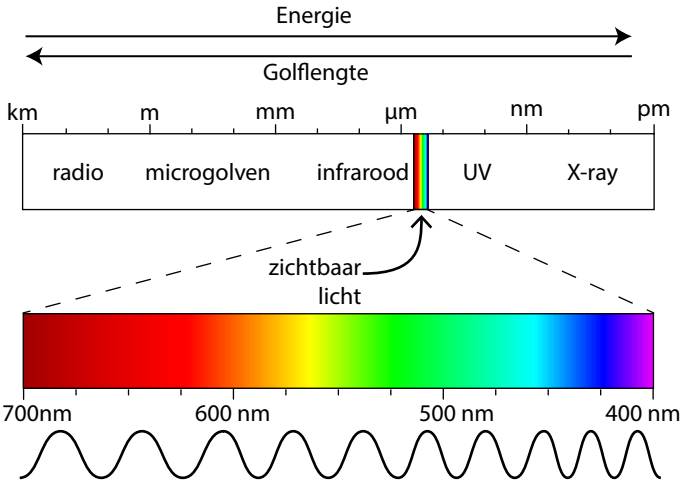

Figuur 8-1. Schematische weergave van het elektromagnetisch spectrum. Kortere golflengte betekent meer energie. Het deel van elektromagnetisch spectrum dat wij als mensen kunnen waarnemen is maar een fractie van alle electromagnetische straling.

Om te begrijpen hoe een stof licht kan omzetten moet men weten dat in atomen negatief geladen elektronen rond een positief geladen kern 'vliegen' en elk een andere baan of orbitaal hebben. Voor een atoom zijn er evenveel negatief geladen elektronen rond de kern als positieve ladingen ('protonen') in de kern. Als er meer of minder elektronen zijn spreken we van een ion dat negatief of positief geladen is. De elektronen kunnen de ruimte rondom een kern op verschillende manieren vullen. De manier waarop de ruimte gevuld wordt bepaalt de energie van dat atoom. De verschillende manieren waarop de orbitalen gevuld worden door de elektronen worden elektronenconfiguraties genoemd. Eén van deze configuraties zal de laagste energie hebben. Dit noemen we de grondtoestand van het atoom. In principe zijn atomen onder normale omstandigheden in de grondtoestand. Als je de elektronen op een andere manier over de orbitalen wilt verdelen dan moet je energie in het systeem steken. Licht is één van de manieren om energie aan een atoom te geven. Nadat er licht is geabsorbeerd, is de configuratie waarin de elektronen

zijn energetisch ongunstiger dan de grondtoestand. Elke configuratie die niet de grondtoestand is wordt een aangeslagen toestand genoemd. Alles in het universum heeft de behoefte om terug te gaan naar de grondtoestand, zo ook deze atomen. Nu is het mogelijk om van de aangeslagen toestand terug te vallen naar de grondtoestand en dit kan gebeuren door middel van het uitzenden van een foton. Door het juiste atoom of ion te kiezen in de juiste omgeving kun je bepalen welk licht er nodig is om naar de aangeslagen toestand te gaan en welk licht eruit komt bij het terugvallen naar de grondtoestand. Het uitzenden van licht door middel van het terugvallen vanuit een aangeslagen toestand terug naar de grondtoestand staat bekend als luminescentie. Stoffen die luminesceren worden ook wel fosforen genoemd.

In dit proefschrift heb ik specifiek bestudeerd hoe fosforen fotonen met een hoge energie absorberen en deze 'omzetten' naar fotonen met een lagere energie vooral in het zichtbare gebied van het spectrum. In dit geval zijn de fosforen vaste anorganische materialen, stoffen die, anders organische ma-

Figuur 8-2. Fruit analogie van hoe een kristal structuur er uit ziet. Elke vrucht representeerd een ander atoom. **links boven:** Sinasappellen die zich periodiek herhalen zoals atomaire kristallen. **rechtboven:** een met appel gedoteerd kristal rooster. **Links onder:** limoen en sinasappelen in een zout structuur. **rechts onder:** een met perzik gedoteerd zout kristal structuur.

terialen, niet vooral de elementen koolstof en waterstof bevatten. Typische voorbeelden hiervan zijn zout, staal en steen. De atomen of ionen in anorganische vaste stoffen stapelen zich in de ruimte in een bepaald patroon. De vorm van dit soort patronen kun je bijvoorbeeld zien bij de groenteboer wanneer het fruit is opgestapeld (zie figuur 8-2). Je kunt je voorstellen dat als je atomen hebt van verschillende groottes het patroon anders kan worden. Afhankelijk van de grootte van de atomen zijn er verschillende stapelingspatronen mogelijk zijn. Dit patroon waarin de posities van atomen of ionen zich herhalen om zo de ruimte te vullen heet de kristalstructuur.

Een atoom bestaat uit een kern omringd door elektronen maar kan ook extra elektronen opnemen of afstaan en zoals hierboven beschreven een ion worden. Elk atoom heeft een zekere affiniteit om meer of minder elektronen om zich heen te hebben. Zo wil zuurstof graag twee extra elektronen en calcium is niet zo geïnteresseerd in zijn twee buitenste elektronen. Als deze twee atomen samen komen zal zuurstof de elektronen van calcium overnemen. We spreken van een anion als het atoom meer elektronen heeft en van een kation als het minder elektronen heeft. Bij een verbinding van anionen en kationen spreken we over een zout. Dit is een verwijzing naar tafelzout dat uit natrium en chloride bestaat. Chloor pakt hierbij één elektron van een natrium atoom af. De hoeveelheid negatieve elektronen ontvangen of afgestaan door het ion wordt genoteerd als superscript bij het element. In het geval van calcium en zuurstof in het vorige voorbeeld schrijft men dat als volgt: Ca^{2+} en O^{2-}.

In kristallijne anoroganische stoffen zijn atomen of ionen gestapeld in een zich herhalend patroon. Interessant is nu dat het mogelijk is om een deel van de atomen of ionen te vervangen door een ander atoom of ion zonder dat het herhalend patroon onderbroken wordt. Belangrijk hierbij is dat het atoom of ion dat het reguliere atoom of ion vervangt vergelijkbaar is in grootte en lading. Een typisch voorbeeld waarbij een deel van de atomen vervangen wordt, zijn legeringen zoals brons waar zink deels koper vervangt of roestvrij staal waar chroom atomen ijzer atomen vervangen om de roestvorming tegen te gaan. Een voorbeeld van een zoutstructuur waarbij ionen vervangen worden is Himalaya zout waar een kleine fractie van de natrium is vervangen door ijzer. De ijzerionen geven het zout de bekende roze kleur. Het bewust vervangen van een klein deel van de ionen door een ander ion heet doteren. In dit proefschrift doteer ik kationen met specifieke optisch actieve ionen die in de zoutstructuren efficiënt licht kunnen omzetten van een hoge naar een lage energie. De luminescerende materialen die zo ontstaan zijn fosforen die kunnen worden gebruikt in bijvoorbeeld lampen en beeldschermen.

Fosforen zijn essentieel voor LED (light emitting diode) lampen. De diode in een LED lamp zet elektriciteit om naar blauw licht. De ontdekking van de blauwe LED begin jaren ’90 veroorzaakte een revolutie in de verlichtingsindustrie. Wit licht bevat alle kleuren van de regenboog. Blauwe fotonen hebben de hoogste energie en door een deel van deze fotonen om te zetten naar groen, geel, oranje en/of rood licht kan wit licht gemaakt worden. In een witte LED

lamp wordt er op de blauwe chip een laagje van fosforen aangebracht. Door de combinatie van de luminescentie van de fosforen en doorgelaten blauwe diode emissie zendt de LED lamp wit licht uit. Dit proefschrift gaat over fosforen en hoe de kristalstructuur invloed heeft op de luminescentie eigenschappen van mangaan en chroom ionen. Het doel is om begrip omtrent fosforen te verbeteren.

Uitdagingen in de verlichtingsindustrie zijn o.a. het ontwikkelen van efficiënte smalbandige (kleurzuivere) groene en rode fosforen voor verlichting en beeldschermen. De eerste generatie witte LED-lampen gaf ongezellig koud wit licht. Dit is opgelost door een rode fosfor toe te voegen maar de veel gebruikte rode fosforen zenden een deel van het licht uit in het dieprode gebied waar onze ooggevoeligheid laag is en dit vermindert de efficiëntie van LED lampen. Ook voor de kleurweergave van beeldschermen is er ruimte voor verbetering aangezien beeldschermen (nog) niet in staat zijn alle kleuren correct weer te geven. Daarnaast worden compacte en efficiënte LEDs ingezet voor de ontwikkeling van nieuwe technologie zoals het gebruik van nabij infrarood licht om producten te analyseren, bijvoorbeeld op versheid of samenstelling van voeding. Hiervoor is er behoefte aan een fosfor die juist breedbandige infraroodstraling uitzendt. In dit proefschrift worden de luminescentie-eigenschappen van de overgangsmetaalionen Mn^{2+}, Mn^{4+} en Cr^{3+} in diverse fosforen bestudeerd om bij te dragen aan een beter begrip van de luminescentie eigenschappen en toepassing ervan in nieuwe LED lichtbronnen.

Thermische luminescentie doving van tweewaardig mangaan (hoofdstuk 3)

Hoewel LED lampen niet erg warm worden tijdens gebruik, blijkt dat de temperatuur van de fosfor direct boven de blauwe chip lokaal kan oplopen tot wel 150^{0}C. Bij deze hoge temperaturen verliezen veel fosforen luminescentie-efficiëntie. Verschillende natuurkundige mechanismen kunnen dit verklaren en voor veel stoffen is bekend welk mechanisme verantwoordelijk is voor de temperatuurdoving. Echter, voor Mn^{2+} was dit nog onbekend. Door naar veel verschillende zouten te kijken, allemaal gedoteerd met een kleine fractie mangaan, en te bestuderen bij welke temperatuur de luminescentie dooft is bepaald wat het doofmechanisme is.Twee mechanismes voor temperatuurdoving van luminescentie zijn bekend:

Mechanisme 1: Vanuit de aangeslagen toestand kan het ion terugkeren naar de grondtoestand door licht uit te zenden (stralend verval) of door alle energie om te zetten in warmte (niet-stralend verval). Voor luminescerende ionen is er vaak een barrière om terug te vallen zonder licht uit te zenden. Bij hogere temperatuur heeft het ion meer energie waardoor het makkelijker deze barrière kan overbruggen en wordt de kans op niet-stralend verval alsmaar groter. Op een gegeven moment is de kans groter om niet stralend terug te vallendan de kans om terug te vallen via luminescentie en dooft de luminescentie.

Mechanisme 2: Nadat het lichtgevende ion in de aangeslagen toestand is, kan één elektron in het ion de energie van de warmte gebruiken om te ontsnappen naar hoge energieniveaus van het kristal. Hierdoor wordt het elektron mobiel in het kristal en kan daardoor ergens anders in het zout ingevangen worden. Zodra dit elektron is verdwenen, is het ion ook niet meer in de aangeslagen toestand en dooft de luminescentie.

Belangrijk is dat bij mechanisme 1 de lokale interacties rondom het ion heel belangrijk zijn terwijl bij mechanisme 2 het draait om interactie van het ion met de rest van het hele kristal. Bij mechanisme 2 worden elektronen elders in het kristal ingevangen. Wanneer de fosfor opgewarmd wordt, kunnen deze elektronen terugkomen bij het lichtgevende ion en dan licht uitzenden. De fosfor fungeert als het ware als een batterij, waarbij licht in combinatie met warmte de fosfor opladen. Verwarmen van de opgeladen fosfor in het donker zorgt ervoor dat de energie weer vrij komt in de vorm van het uitzenden van licht. Dit verschijnsel wordt thermoluminescentie genoemd.

Als we waarnemen dat een fosfor ophoudt met licht uitzenden in hetzelfde temperatuurgebied waarin we het zout opladen is dat een bewijs voor mechanisme 2. Daarnaast verwacht je voor mechanisme 2 dat de dooftemperatuur hoger is als de energieniveaus van het kristal hoger in energie liggen. Voor mechanisme 1 wordt verwacht dat de luminescentie dooftemperatuur lager wordt als de emissieband breder is. In het totaal hebben we naar twintig verschillende kristalroosters gekeken gedoteerd met Mn^{2+} en bepaald op welke temperatuur de luminescentie dooft. Er was een duidelijke toename in dooftemperatuur als kristal energieniveaus hoger in energie waren en er was geen verband met de breedte van de emissieband. In vier van deze structuren waar energieopslag mogelijk was, zagen we bovendien dat de luminescentiedoving bij dezelfde temperaturen plaatsvond als waarbij we het materiaal konden opladen. Hieruit concluderen we dat voor Mn^{2+} mechanisme 2 de oorzaak is van de doving van luminescentie op hoge temperatuur.

Infrarood emissie bij hoge concentratie mangaan (hoofdstuk 4)

Het afgelopen decennium verscheen er een toenemend aantal wetenschappelijke artikelen waarin beweerd wordt dat mangaanparen in het infrarood uitzenden, in plaats van in het groen. Met paren worden twee Mn^{2+} ionen bedoeld die vlak bij elkaar zitten (naaste buren in het kristalrooster). Bij een toenemende Mn^{2+} concentratie komt de infrarood piek omhoog. Op basis hiervan werd geredeneerd deze afkomstig moet zijn van Mn^{2+} paren omdat er bij een hoge concentratie een grotere kans is dat twee Mn^{2+} ionen naast elkaar zitten. Dat laatste is juist maar bewijst niet dat de infrarood emissie van de Mn^{2+}-paren komt. Nauwkeurig onderzoek uit eerdere jaren toonde aan dat de verschuiving in emissiegolflengte voor deze paren klein is. Een andere verklaring lijkt dus noodzakelijk om deze infrarood emissiepiek bij hoge mangaan concentraties te verklaren.

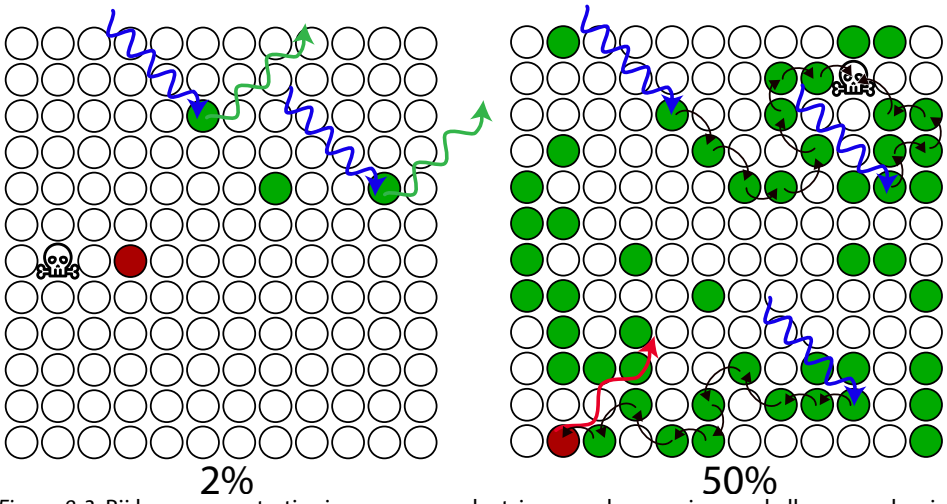

Figuur 8-3. Bij lage concentraties is er geen verplaatsing van de energie en zal alles groen luminescceren. Bij hoge concentraties kunnen infrarood luminescerende centra gevonden worden. Daarnaast zal bij een hoge een groot deel verdwijnen op locaties waarbij de energie zonder luminescentie kan terugvallen.

In hoofdstuk 4 wordt beschreven dat energiemigratie naar infraroodemitterende defecten een betere verklaring is. Ionen die hetzelfde zijn kunnen energie overdragen aan hun buren. Bij hoge concentraties is er een grote kans dat elk ion twee of meer dezelfde ionen in zijn omgeving heeft. Er vormt zich een netwerk van ionen. Als een ion in de aangeslagen toestand is kan het makkelijk de energie overdragen naar een buurion. Deze kan op zijn beurt weer een volgend buurion activeren en zo kan de aangeslagen toestand als het ware migreren door het zout. Hoe hoger de concentratie hoe sneller en effectiever die energiemigratie is. Als er nu een ander soort luminescerend centrum in het zout zit die deze energie kan opvangen dan ontstaat er een soort trechter effect waarbij alle geactiveerde Mn^{2+} ionen uiteindelijk de energie overdragen naar dit defect of verontreiniging. Als deze licht uitzendt in het infrarood dan krijg je een toename in infrarood emissie met een toename van de mangaanconcentratie. In hoofdstuk 4 worden experimenten beschreven waarbij door variatie in Mn concentratie, temperatuur en synthesemethode wordt aangetoond dat de infrarood emissie bij hoge Mn^{2+} concentraties niet afkomstig is van Mn-paren maar van infrarood emitterende defecten.

Hexagonaal KRSF (hoofdstuk 5)

Beeldschermen bestaan uit pixels in drie verschillende kleuren: rood, groen en blauw. De fosfor voor het rode licht heeft weinig ruimte voor verbetering, het is een bijna perfecte balans tussen een zuivere rode kleur en hoge efficiëntie. De fosfor die gebruikt wordt in beeldschermen staat bekend als KSF, een afkorting voor de elementen waaruit het bestaat: kalium, silicium en fluor. Wederom is in deze structuur mangaan als lichtgevend element toe-

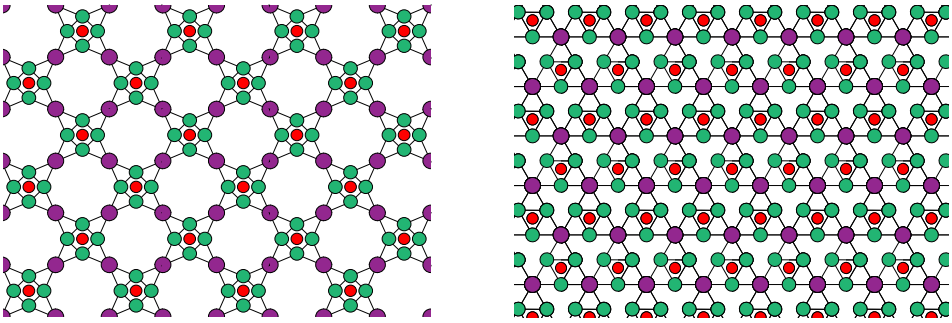

Figuur 8-4. 2D weergave van de twee verschillende 'patronen' waarin KSF in kan voorkomen. Paars zijn Kalium atomen, groen zijn fluor atomen en rood zijn silicium atomen. De silicium atomen kunnen vervangen worden met mangaan, dit zorgt ervoor dat de stof mooi rood kan luminesceren. Een belangrijke voetnoot: in werkelijkheid stapelen atomen zich op in drie dimensies om die reden zijn er een aantal simplificaties in dit model vertoont.

gevoegd maar nu als vierwaardig kation: Mn^{4+}.

Een nadeel van de rode Mn^{4+} emissie is echter de lange levensduur van de aangeslagen toestand. Deze is vele milliseconden en dit beperkt het aantal fotonen dat per seconde kan worden uitgezonden. Voor lichtbronnen met een hoge helderheid is KSF daarom niet geschikt en het wordt daarom niet toegepast in witte LED lampen. Bij het bestuderen van wat er zou gebeuren als een deel van de kalium vervangen zou worden door het grotere element rubidium leek een synthese mislukt. Het product was in de zuurkast achtergelaten zodat gevaarlijke stoffen van de synthese zouden wegdampen. Toen de stof een week later toch maar geanalyseerd werd, bleek dat er een nieuwe verbinding te zijn ontstaan. Normaal KSF heeft een kristalstructuur die zich herhaald in een vierkant patroon maar in deze nieuwe variant herhalen de atomen zich in een zeshoekig patroon (zie figuur8-4).

De luminescentie van Mn^{4+} in deze nieuwe structuur heeft als voordeel dat er meer fotonen per seconden kunnen worden omgezet van blauw naar rood en ook is de lichtopbrengst 2 á 3 % hoger dan voor Mn^{4+} in het traditionele KSFm omdat de rode luminescentie net iets beter zichtbaar is voor het menselijk oog. Een interessante en opmerkelijke ontdekking bij de vorming van deze nieuwe verbinding was dat de omvorming van vierkante naar zeshoekige structuur pas plaatsvond na een lange opstarttijd. Het is dus een spontane reactie, maar het is pas spontaan na één dag. Vervolgens neemt de omzettingssnelheid exponentieel toe in de tijd. Het precieze mechanisme voor de omvorming dat deze waarnemingen kan verklaren is niet opgehelderd maar er zijn eerder vergelijkbare waarnemingen gedaan voor andere reacties waarbij de kristalstructuur van een stof verandert.

Chroom voor nabij infrarood licht (hoofdstuk 6)

Een nieuw onderwerp in de LED-industrie zijn nabij-infrarood lichtbronnen voor chemische analyse. Nabij infrarood is het gebied van het elektromagnetisch spectrum waar fotonen net iets minder energie hebben dan voor rood licht, dus net onzichtbaar voor ons maar wel belangrijk voor bijvoorbeeld plantengroei. Moleculen zoals suiker, water, vet en eiwitten absorberen zwak specifieke golflengtes in dit gebied van het spectrum. Door met een nabij infraroodlamp te schijnen op een product (een appel, graan, reep etc.) en de intensiteit als functie van de golflengte van het gereflecteerde licht te meten, kan door analyse van bij welke golflengtes hoeveel geabsorbeerd is bepaald worden welke moleculen er in je product zitten en in welke concentratie. Dit kan erg nuttig zijn voor bijvoorbeeld de kwaliteitscontrole van voedsel en deze functionaliteit zou wellicht, met een compacte nabij infrarood LED in combinatie met een mini spectrometer, in mobiele telefoons ingebouwd kunnen worden.

Om een nabij infrarood LED te maken is er een fosfor nodig die zo veel mogelijk verschillende golflengtes nabij infrarood uitzendt. Het chroom ion Cr^{3+} kan afhankelijk van de kristalstructuur breedbandig nabij infrarood licht uitzenden dat zeer geschikt is voor deze toepassing. In hoofdstuk 6 proberen we de Cr^{3+} emissie zo breedbandig mogelijk te maken. Als je twee kristalroosters van verschillende atoom soorten hebt die erg op elkaar lijken dan kun je deze mengen om zo een nieuw rooster te maken. Dit soort stoffen heten vaste stof oplossingen omdat het ene element als het waren opgelost is in de omgeving van het andere element.

Als we dus nu kijken naar verschillende Cr^{3+} ionen in zo een gemengd rooster, zal elk Cr^{3+} ion een net iets andere omgeving hebben en hierdoor bij een iets andere golflengte luminesceren. Door de wanorde in het rooster neemt de bandbreedte van de emissie toe. Zoals besproken in hoofdstuk 3 worden LED-lampen lokaal erg warm en kan de fosfor stoppen met luminesceren. In hoofdstuk 6 bespreek ik hoe het maken van een vaste stof oplossing invloed heeft op de bandbreedte en op temperatuurdoving van de nabij infrarood luminescentie van Cr^{3+}. Er worden twee fosforen bekeken, één met een lage dooftemperatuur en één met een hoge dooftemperatuur. Door deze twee stoffen met elkaar te mengen nam de breedte van het uitgezonden golflengtegebied toe. Echter, bij het toevoegen van de stof met de lage dooftemperatuur aan de stof met de hoge dooftemperatuur daalde ook de dooftemperatuur. Er werd een optimale mengverhouding gevonden waarbij de dooftemperatuur voldoende hoog was en er significante verbreding van het nabij infrarood emissiespectrum werd verkregen.

Vooruitzicht

Evident is dat er nog veel ruimte is voor meer onderzoek in dit veld. In hoofdstuk 4 werd gesproken over de infrarood emissie van een defect, wat de chemische origine is van dit defect is nog onbevestigd. In hoofdstuk 5 werd een stof gemaakt met een andere structuur dan zijn voorganger. Hoe deze stof zich omvormt van kubische naar de hexagonale structuur is nog onduidelijk.

Daarnaast is er nog potentie voor nieuw onderzoek naar andere overgangsmetaal ionen. In hoofdstuk 6 werd over chroom gesproken als een ion voor nieuwe technologieën voor bijvoorbeeld chemische analyse. Twee andere overgangsmetalen, kobalt en nikkel (Co^{2+} en Ni^{2+}), zouden voor deze applicaties ook gebruikt kunnen worden. Het licht dat deze ionen uitzenden is typisch verder in het infrarood wat beter is voor deze technologie. Echter bij lage temperaturen verliezen ze al heel veel luminescentie efficiëntie. Vaak zijn deze stoffen op kamertemperatuur al volledig uitgedoofd. Het is dus belangrijk om uit te zoeken wat het dovingsmechanisme is voor beide overgangsmetaalionen. Met dit begrip zou men makkelijker fosforen met deze ionen kunnen vinden die weinig doving vertonen bij hogere temperaturen.

Op basis van dit proefschrift is er meer duidelijkheid over de luminescentie van de overgangsmetaalionen Mn^{2+}, Mn^{4+} en Cr^{3+}. Er is echter nog voldoende ruimte voor nieuw en meer onderzoek naar overgangsmetaal luminescentie.

Chapter 9

Appendices

“ I wanna thank me,
for just being me all the times ”

Snoop Dogg

Chapter 9

Acknowledgements

Throughout my years as a PhD student I had to honor and the pleasure to work with an abundance of beautiful colleagues and students It is but right to thank them for their contribution and/or support over the years.

Allereerst wil ik al mijn studenten bedanken die de moeite en tijd genomen hebben om bij mij een project te doen: Tobias, Denny, Sam, Philipp, Kees, Cos, Jan, Larse, Vincent Benning, Mark, Marco, Rick, Ruben, Vincent Spit. Het was een genoegen voor mij om jullie te onderwijzen in spectroscopie en phosphoren. Door jullie te onderwijzen moest ik mezelf dwingen de onderwerpen in kwestie op een hoog niveau te begrijpen. Het harde werken van jullie kant is erg gewaardeerd. Een paar keer heeft de bijdrage van jullie significant bijgedragen aan een publicatie. In het speciaal wil ik bedanken Larse, Tobias en Phillipp die alle drie, driekwart jaar of langer, met mij hebben moeten doorbrengen. Phillipp het was fijn met zo een vrolijke student te hebben mogen samenwerken. Enorm veel dank aan Tobias die het meeste experimenteel werk van hoofdstuk 4 op zijn schouders heeft genomen. Larse, iemand begeleiden die zo gemotiveerd is, ook al gaan de experimenten nergens heen, die zo goed voor zijn eigen experimenten kan zorgen, een luxe die ik niet gewend was.

Het allerbelangrijkst is natuurlijk de grote professor die het allemaal mogelijk heeft gemaakt Andries Meijerink. Ik waardeerde enorm hoe begripvol je was de paar keer dat er persoonlijke problemen waren. je creëert een plek waar je (PhD) studenten zich veilig voelen. Nooit kreeg ik te horen dat ik te weinig data had of dat we echt wel in LSA moesten publiceren. Veel van mijn PhD collega's klaagde constant over de nare omstandigheden die door hun promotor vaak gecreëerd werd. Ik kreeg soms zelfs het idee hierdoor dat ik mijn PhD verkeerd deed omdat ik me niet gestrest of slecht voelde. Het is ook erg fijn als je humor gewaardeerd word. Waar menigeen vond dat mijn presentaties misschien te onserieus waren, spoorde jij me aan bij mijn olijke manier van presenteren te blijven. Als ik het me goed herinner had je me al vier keer willen ontslaan, heel fijn dat je het hebt gehouden bij een ferme waarschuwing, ik zal mijn best doen de titel van je leerstoel te onthouden.

Office mates:

अतुल, आम्हा दोघांना एकाच प्रोजेक्टवर ठेवले होते, मला एकत्र काम करण्याची थोडी भीती वाटत होती कारण आम्ही एकाच ऑफसिमध्ये असू आणि कोणीतरी सतत माझ्या खांद्यावर पाहण्याची कल्पना मला आवडली नाही | सुदैवाने तुम्ही त्या अर्थाने परिपूर्ण सहकारी होता, तुम्ही नेहमी मैत्रीपूर्ण, छान आणि आश्वासक आहात | तुम्हाला दुसरा गुरू म्हणून तुम्हाला असल्याने तुम्हाला खूब चांगले वाटले कारण अँन्ड्रसि कष्टुल्लक प्रश्नांना चडिवण्यासाठी खूब व्यस्त असायचा |

मला वाटते की तुम्ही खरे तज्ज्ञ आहात हे समजायला मला थोडा वेळ लागला | तुमची नम्र वृत्ती आणि सहनशीलता तुमच्या बुद्धिमत्तेवर मुखवटा घातली आहे | तूर्मि स्पेक्ट्रोस्कोपीमध्ये नरियात करण्याव्यतरिक्त मला खात्री आहे की तूर्मि मला जीवनाचे बरोबर धडी शिकिवले आहेत | गेल्या अनेक वर्षे तुम्ही वेगवेगळ्या देशांमध्ये काम केले आहे | प्रत्येकाची स्वतःची पूर्णपणे वेगळी संस्कृती आहे. यामुळे तुम्हाला लोकांच्या वेगवेगळ्या प्रेरणा आणि कठीण प्रक्रियांची जाणीव झाली आहे | तूर्मि मला हे सांसारिक ज्ञान पोचवण्यात यशस्वी झाला. मी तुम्हाला, तुमची पत्नी आणि मुलाला जगातील सर्व शुभेच्छा देथे |

Thomas jij bent zo een gevalletje: een fijn persoon zodra je hem leert kennen. De eerste paar jaar bestond onze collegialiteit met name met het complimenteren van elkanders fit/mathematica script en nog belangrijkere ons ongenoegen over slecht werkenden studenten uitspreken. Ik ben nog steeds dankbaar dat jij mij gedwongen hebt om een keertje een student ferm toe te spreken op zijn veel ver te gaande laksheid op het lab. Als natuurwetenschapper leer je te weinig hoe je niet over jezelf heen te laten lopen. Gelukkig heb je mij hierin gementord. Daarnaast staat mij bij dat wij graag roddelde over jan en alleman. Frustraties over andere mensen en het snobisme van de Amsterdammer konden altijd veilig binnen de contreien van het gesloten kantoor besproken worden.

Когда я начинал работать в CMI, я боялся, что я, со своей болтовней, буду слишком отвлекать коллег в кабинете или даже всю исследовательскую группу. А когда к нам в лаборатории пришел Вася, эта боязнь полностью исчезла. Он постоянно общался по видеосвязи с коллегами, друзьями или родственниками в России и так затмил любые другие виды отвлечения. С того момента, что Вася решил перестать быть в видеозвонках дольше пяти минут, он начинал интересные научные обсуждения, чтобы убедиться, что никто не сосредотачивался на работе. Вася, год, когда ты работал с нами в кабинете, был замечательным. Несмотря на иногда возможные отвлечения, ты привнес жизнь в нашу лабораторию и, в частности, в наш кабинет.

バシリの退社後、オフィスには突然と静寂が訪れました。涌井博士は蛍光体の専門家になる為、２年間滞在しておりました。　私は早くも涌井博士を下の名前の「貞一」と呼ぶようになりました。後ほど分かったことですが、日本で下の名前で呼ばれるのは滅多にないことらしく、許可していただきありがとうございます。しかし残念ながら、働き始めて３か月が経過した後、全世界的にコロナが大流行するようになり、翌年からはほとんどオンラインで連絡を取り合うことになりましたが、彼のご自宅でヨーロッパの文化を取り入れていることを見ることができ、とても素敵でした。カモノハシペリーや、アルバート・ハイン社（スーパーマーケットチェーン）のハムスターのぬいぐるみが背景に映っているのを何度も目にすることができました。何度もお伝えすることになりますが、お陰様でオランダの良さに気づくことができました。そして、オランダと日本での計り知れないほどの親切さやおもてなしに大変感謝致します。近い将来、日本もしくはオランダでお会いできることを心から願っております。

Dan Jur; ik weet tot de dag van vandaag niet of ik me schuldig moet voelen over de uitspraak dat je te goed uitzag om onderzoek te kunnen doen. Ik ben vooral blij dat ik me over mijn eerste impressie van jou heb heengezet. Ik vond Arkabarka geweldig, terwijl thomas zijn uitgebreide ontbijt met gepocheerd ei en geglazuurd bacon at, keken wij uit met een bakje yoghurt over de Donau. Op het lab was het fijn om met jou samen te werken. Bij het KRSF project wist je een veilige omgeving te creeëren. Elke keer dat ik paranoia werd wist jij met een enkele zin het gevaar uit mijn hoofd te praten. Jur je word niet alleen gewardeerd als collega, maar ook als vriend. Je bent me nog een paar pakken stroopwafels te goed, maar dat kan ik je denk ik wel vergeven.

Als laatste kantoorgenoot Maaike. Ik denk dat jij meer mentale steun hebt geleverd tijdens de eindsprint dan enig ander persoon. Misschien vind je jezelf niet inherent vriendelijk maar in mijn hoofd sta je hoog op de lijst van mensen met een goed hart.

Collegues

Some colleagues I want to highlight, in particular: Raimon, Soarsia, Serena, and Ian, Markus Liudmyla and Dechao

Raimon, quan vas arribar a l'oficina, jo estava acabant el doctorat i no tenia cap intenció de socialitzar-me amb cap persona nova. Però la teva felicitat i espontaneïtat eren difícils d'ignorar i, abans que me n'adonés, ja estaves a la meva taula de sopar gairebé dues vegades al mes per jugar a jocs de taula

A big shout out goes to Saoirsé who was my favourite person to distract in the first few years of my PhD. It is always amazing if you have someone who genuinely thinks you are funny and is able to crack some more jokes on the same horrible level.

Serena, mi ricordo vivamente che, quando ero appena stato nominato membro del Comitato per i Borrel, sei venuta da me dicendo: "c'è un grosso problema con questo Gruppo qui: la gente non beve!". Da quel momento ho capito che sarei stato in buona compagnia! Durante la pandemia sei stata davvero la mia salvezza. La tua ospitalità e la tua ottima cucina hanno reso più tollerabili i lockdown

Pedro, você me fez perceber que todo super nerd ou geek é capaz de ser divertido e sociável. Além das nossas visitas semanais à tricolore, nós fomos sob quaisquer condições climáticas, o que deu à minha semana um senso de propósito. Muito obrigado

Ian, seu malandro, tu és um verdadeiro amigo, tanto que não há forma de expressar o quão sortudo me sinto por te ter conhecido. Eu tinha uma pequena ideia de quão horrível a culinária Holandesa era antes de teres chegado, mas as tuas queixas constantes sobre 'boterhammen' Holandês mostraram-me

quão grave a situação é. Numa tentativa desesperada de te fazer apreciar um pouco mais a comida na Europa, fomos numa viagem pela França. E, apesar de estarmos em plena pandemia, conseguimos rimo-nos o suficiente sobre o debate entre “coronatine” ou “petit virus au corona”.Eu gostei imenso do nosso contacto no dia-a-dia. Desejo sinceramente tudo do melhor para ti e que nos continuemos a encontrar.

Markus, dein Charakter ist geprägt von einer faszinierenden Kombination aus Güte und Intelligenz. Wann immer ich dich fragte, um die Fundamente der Spektroskopie zu diskutieren, warst du bereit mir dein Gehör zu schenken und mir, ohne zu prahlen, fachkundig Antwort zu geben. Es ist beneidenswert, dass du lesen über Wissenschaft zum Hobby gemacht hast. Es macht mich froh, dass diese ganze Wissenschaft den Deutschen in dir nicht ausmerzen konnte: Deine Lust auf Bier ist unversiegbar. Ich habe unglaublich viel von dir gelernt und durch unsere Gespräche blieben Leuchtstoffe und Spektroskopie immer interessant. Vielen Dank!

Люда, ти дуже добросерда і, напевно, ти людина з найширшою посмішкою у світі. Мені дуже сподобався час, який ми провели у США. Я пам›ятаю, як я подав тобі велику порцію супу. Це було не тому, що ти була бідна, а тому, що в тебе не було часу готувати для себе. Сподіваюся, тепер ти знайшла для цього час. Бажаю тобі всього найкращого в ці важкі часи.

在我攻读博士学位的第二年，我去了中国，就像任何一个欧洲人一样，我不知道这两个截然不同的土地的文化差异。幸运的是，我身边有德朝，他很友善地向我展示了中国生活的细节与由来。我甚至可以在他家里睡一个多星期。在让我沉迷于中国的饮食文化方面，德朝也是一位很棒的向导。每顿饭我都吃一些我以前从未见过的东西，而且所有的东西都非常美味。我衷心感谢禹德朝的友善和热情款待

Ofcourse I want to thank all the other people related to my research this includes the supporting staff: Peter, Ramon, Linda, Silvia and Stephan. The other PIs: Daniel, Ingmar, Celso,Machtold, Zeila. And then all the other PhD students and (longterm) visiting scientist: Annelies, Annelisa, Anne, Auke, Marie-Anne, Rian, Robin, Frederico, Jesper, Pierre, Jan, Christiaan, Tim, Thomas Gardenier, Peter Jacobse, Lei, Jintao, Marlou, Maryam, Bas, Elleke, Carlo, Ricardo, Pim, Hao en Shuai. Ook wil ik graag bedanken de bravelingen: Freddy, Sander, Mark en Vincent, die dagelijks mijn kantoor ruimte binnendrongen om dan wel ping pong batjes te pakken dan wel om mij of mijn kantoorgenoten aftelijden van het werk. Dit was vaker gezellig dan vervelend.

Nichia

私の博士号取得の軌跡を語る上で、最も重要で不可欠だったのは、日亜化学工業株式会社の存在です。お陰様でこの４年半の間、蛍光体の研究を楽しむことができました。貴社なしでは当プロジェクトの資金調達は不可能であったと思います。特に山下 恵祥様 、中嶋 正次様 、 細川 昌治様には大変お世話になりました。マイエリンクと私が阿南市に訪問した際、とても温かく迎えていただき、誠にありがとうございます。日本で皆様から頂いた親切さと幸せな思い出は、私の心にずっと残っております。アチュールと私を経済面で支えていただくほか、科学的な面でも徹底的にサポートして頂きました。特に、涌井貞一博士とのやりとりはとても勉強になりました。全てにおいて、皆様と一緒に仕事ができたことを本当にうれしく思います。

Buiten werk om:

Buiten het Ornstein laboratorium zijn er uiteraard ook mensen die hun stempel op mij en daardoor ook op deze thesis hebben gedrukt. Allereerst wil ik mijn vaste clique hier in Utrecht bedanken: Bas, Max en Joep. Zonder jullie geen gezelligheid en plezier, en zonder gezelligheid en plezier geen animo om ook maar iets te doen in het leven. Jullie zijn een fijne afleiding als het aankomd op onderwerpen die niet gaan over spin baan koppeling en de invloed van symmetrie op de overgang van $^6A_1$ naar de $^4T_2$ (hoe mooi ik dat soort onderwerpen ook vind).

I also want to thank Erik and Shu-Hua. Erik, I really enjoyed having you around the house for the first three years of my PhD (the time at the Salamancapad was also great). 書華，我很怕有你做室友，但事實證明，你做室友也是一種幸福

Ook belangrijk is natuurlijk mijn familie. Mijn papa Bert en mijn mama Susan, die hun best gedaan hebben (hoop ik) om mij op te voeden tot de vrolijke wetenschapper die ik geworden ben. Dan mijn allerliefste broer die mij in mijn tiener jaren op het juiste pad getrokken had. Zonder hem was ik waarschijnlijk de eerste 5 miljoen cijfers van het getal van Euler uit mijn hoofd aan het leren.

Am letzte mochte ich gerne mein liebe Fabienne danken für die letzten Jahre die wir zusammen erlebt haben. Es ist schön um du in meinem Leben zu haben. Ich freue mich nach unserer Zeit zusammen in ‘Gruun’.

List of publications

Chapter 5

Luminescence and formation of cubic and hexagonal $(K,Rb)_2SiF_6:Mn^{4+}$

Arnoldus J. van Bunningen , Jur de Wit, Sadakazu Wakui, Andries Meijerink

Not yet published

Chapter 4

Understanding enormous redshifts in highly concentrated Mn^{2+} phosphors

Arnoldus J. van Bunningen, Simon Tobias Keizer and Andries Meijerink

J. Mater. Chem. C, 2023, 11, 8961

Chapter 3

Luminescence Temperature Quenching in Mn^{2+} Phosphors

Arnoldus J. van Bunningen, Atul D. Sontakke, Ruben van der Vliet, Vincent G. Spit, Andries Meijerink

Adv. Optical Mater.2023, 2202794

Chapter 6

Temperature quenching of Cr_{3+} in $ASc(Si_{1-x}Ge_x)_2O_6$ (A=Li/Na) solid solutions

Arnoldus J. van Bunningen,Atul D. Sontakke, Sadakazu Wakui, Andries Meijerink

Optical Materials .2022,128, 112433

Patent

LIGHT EMITTING DEVICE

WAKUI SADAKAZU [JP]; MURAZAKI YOSHINORI [JP]; SONTAKKE ATUL DNYANESHWAR [NL]; VAN BUNNINGEN ARNOLDUS JACOBUS [NL]; MEIJERINK ANDRIES [NL]

EP4086323A1

Highly luminescent $Gd_2O_2S:Er^{3+},Yb^{3+}$ upconversion microcrystals obtained by a time- and energy-saving microwave-assisted solid-state synthesis

Ian P. Machado , Jur de Wit , **Arnoldus J. van Bunningen**, Cássio C.S. Pedroso, Lucas C.V. Rodrigues , Hermi F. Brito, Andries Meijerink

Journal of Alloys and Compounds ,2023,942 16908

Fermi surface and band structure of Ti_2SnC as observed by angle-resolved photoemission spectroscopy

Damir Pinek, Takahiro Ito, Kanji Furuta, **Arnoldus J. van Bunningen**, Patrick Le Fèvre, François Bertran, and Thierry Ouisse

Phys. Rev. B ,2021104, 195118

Exciton interaction with Ce^{3+} and Ce^{4+} ions in $(LuGd)_3(Ga,Al)_5O_{12}$ ceramics

Vasilii Khanin, Ivan Venevtsev , Kirill Chernenko, Vladimir Pankratov, Konstantin Klementiev, Thomas van Swieten, **Arnoldus J. van Bunningen**, Ivan Vrubel, Roman Shendrik, Cees Ronda, Piotr Rodnyi, Andries Meijerink

Journal of Luminescence ,2021,237 118150

Mn^{2+} activated Ca-α-SiAlON – broadband deep-red luminescence and sensitization by Eu^{2+}, Yb^{2+} and Ce^{3+}

Atul D. Sontakke, **Arnoldus J. van Bunningen**, Sadakazu Wakui and Andries Meijerink

Mater. Adv., 2021,2, 2075

Understanding and tuning blue-to-near-infrared photon cutting by the Tm^{3+}/Yb^{3+} couple

Dechao Yu, Ting Yu, **Arnoldus J. van Bunningen**, Qinyuan Zhang, Andries Meijerink, Freddy T. Rabouw

Light Sci Appl 2020, 9, 107

Unraveling the $Eu^{2+} \rightarrow Mn^{2+}$ Energy Transfer Mechanism in w-LED Phosphors

Atul D. Sontakke, **Arnoldus J. van Bunningen**, Freddy T. Rabouw, Sam Meijers, and Andries Meijerink

J. Phys. Chem. C 2020, 124, 13902

Single Au Atom Doping of Silver Nanoclusters

Marte van der Linden, **Arnoldus J. van Bunningen**, Lucia Amidani, Maarten Bransen, Hebatalla Elnaggar, Pieter Glatzel, Andries Meijerink and Frank M. F. de Groot

ACS Nano 2018, 12, 12751

Insights into the Synthesis Mechanism of Ag_{29} Nanoclusters

Marte van der Linden, **Arnoldus J. van Bunningen**, Mario U. Delgado-Jaime, Blanka Detlefs, Pieter Glatzel, Alessandro Longo, Frank M. F. de Groot

J. Phys. Chem. C 2018, 122, 49, 28351

Characterisation, degradation and regeneration of luminescent Ag_{29} clusters in solution

Marte van der Linden, Arjan Barendregt, **Arnoldus J. van Bunningen**, Patrick T. K. Chin, Dominique Thies-Weesie, Frank M. F. de Groot,Andries Meijerink

Nanoscale, 2016, 8, 19901

Structure sensitivity of Cu and CuZn catalysts relevant to industrial methanol synthesis

Roy van den Berg, Gonzalo Prieto, Gerda Korpershoek, Lars I. van der Wal, **Arnoldus J. van Bunningen**, Susanne Zægsgaard-Jørgensen, Petra E. de Jongh ,Krijn P. de Jong

Nat Commun 2016,7, 13057

Chapter 9

List of presentations

ICL 2020

Spectral broadening and temperature quenching of Cr^{3+} in $LiSc(Si,Ge)_2O_6$ and $NaSc(Si,Ge)_2O_6$ solid solutions

Changchun (online), China, 29-July-2021

Leopold-Franzens-Universität Innsbruck visit

Temperature quenching in tetrahedral coordinated Mn^{2+}

Innbruck, Austria, 16-Mar-2022

ICOOPMA-Eurodim

Some like it cool: Thermal Luminescence quenching in Mn^{2+}

Gent, Belgium, 5-July-2022

ICOM 2022

Thermal Luminescence quenching in Mn^{2+}

Belgrade, Serbia, 2-Sept-2022

DPC 22

Understanding the giant emission redshift in concentrated Mn^{2+} phosphors

Wrocław, Poland, 5-Sept-2022

Nichia Visit

Experimental techniques for optical spectrometry

Anan, Japan, 15-Nov-2022

Kyoto University visit

Thermal Luminescence quenching in Mn^{2+}

Kyoto, Japan, 17-Nov-2022

Over de auteur

Naud (Arnoldus) van Bunningen werd geboren in 1992 in Maastricht, hier heeft hij de eerste 18 jaar van zijn leven doorgebracht. Op het gymnasium van het Sint maartencollege interes-seerde hij zich in toneel, wiskunde, scheikunde en filosofie. In 2011 besloot hij een studie scheikunde te doen in Utrecht. Dit werd vervolgd met een master nanomaterials aan dezelf-de universiteit. Tijdens deze master heeft hij een half jaar stagegelopen bij een onderzoeks-groep van de universiteit van Grenoble, Hier ontdekte Naud zijn passie voor vastestofchemie. Na zijn master gaf hij een jaar lang les op het eerstejaars laboratorium van de universiteit Utrecht. Hierna is hij begonnen promotie scriptie over fosforen, het resultaat daarvan heeft u nu in u handen.

Naud houd zich in zijn vrije tijd bezig met bordspellen, een beetje sport (bolderen en wielrennen) en van het leven genieten met vrienden. Hij heeft daarnaast een interesse in wereldgeschiedenis, aardwetenschappen, populaire wetenschap, het correct toekennen van citaten en Wikipedia browsen.